Development of widefield nitrogen-vacancy centre microscopy for application to condensed matter systems

Scott Eric Lillie

orcid.org/0000-0001-6787-0949

Doctor of Philosophy

January 2021

School of Physics,

The University of Melbourne,

Australia

Submitted in total fulfillment of the

requirements for the degree of

Doctor of Philosophy

Abstract

Microscopy based on the nitrogen-vacancy centre in diamond is an emerging technology that may soon find regular application in characterising a broad range of systems. The development of nitrogen-vacancy microscopy has been benchmarked by key proof-of-concept experiments, each demonstrating the great potential of the technique, without necessarily delivering unique insights into the system studied. In this thesis, we aim to further the development of this emerging technology by applying it to study a range of delicate and complex condensed matter test systems. Specifically, we take a widefield approach which utilises a dense ensemble of near-surface nitrogen-vacancy centres to image magnetic and electric fields over a 100 μm field of view with diffraction-limited resolution and good sensitivity. In each application presented, we study physics both intrinsic to the test systems and arising from their interaction with our imaging technique. These observations inspire refinements to our approach that enhance the utility of the technique.

Chapter 1 reviews the physics underpinning microscopy with nitrogen-vacancy centres in diamond, and surveys key achievements in the literature. Chapter 2 details our approach to widefield nitrogen-vacancy microscopy. Chapter 3 applies widefield magnetic imaging to ultrathin depositions of nanoparticles on the diamond surface. We observe a strong magnetic noise associated with metallic depositions, even when the deposited material is less than 1 nm thick. This study demonstrates the great sensitivity of widefield nitrogen-vacancy microscopy, allowing the detection of minute sample volumes. Chapter 4 studies magnetic and electric fields associated with graphene field-effect transistors fabricated on the diamond surface. We demonstrate current density mapping under different doping conditions, a significant extension of device studies published at the time, and identify strong electric fields associated with the gating that affect both the spin resonances

and photoluminescence of the sensing ensemble. These first two studies motivate the use of a deeper and thicker nitrogen-vacancy ensemble that protects against the short-range noise contributed by the metallic nanoparticles, which mimic common contaminants, and protects the sensing layer from device-related electric fields.

Chapter 5 extends our widefield imaging technique to low temperatures (4 K) by incorporating a closed-cycle cryostat into the apparatus, which we use to study a low-critical-temperature system, superconducting niobium wires. By imaging Abrikosov vortices and superconducting transport at various laser powers, we quantify local heating in the sample caused by the excitation laser. This observation motivates a refined nitrogen-vacancy imaging substrate that includes a reflective metallic layer at the diamond surface and an insulating oxide layer, onto which the target sample is deposited. This design mitigates the local heating caused by the excitation laser, an essential component of the imaging technique, and leaves the sample electrically isolated, facilitating advanced studies of low-temperature physics. Chapter 6 deploys this refined nitrogen-vacancy substrate to characterise the magnetic properties of two free-standing ultrathin ferromagnetic materials. We directly quantify the layer-dependent magnetisation of a van der Waals ferromagnet, VI_3; a capability lacking in established characterisation techniques. Finally, we identify a threshold size (20 nm) below which a non-layered ultrathin material, magnetite, ceases to show ferromagnetism. This thesis furthers the development of widefield imaging using nitrogen-vacancy centres in diamond, enabling a range of future applications.

Declarations

This is to certify that:

(i) the thesis comprises only original work towards the Doctor of Philosophy except where indicated in the preface;

(ii) due acknowledgement has been made in the text to all other material used; and

(iii) the thesis is fewer than the maximum word limit in length, exclusive of tables, maps, bibliographies and appendices.

I authorize the Head of the School of Physics to make or have made a copy of this thesis to any person judged to have an acceptable reason for access to the information, i.e., for research, study or instruction.

Scott Lillie

April 24, 2021

Preface

The work presented in this thesis spans a number of experimental research projects undertaken by the Quantum Sensing Group under the supervision of Prof. Lloyd Hollenberg and Dr. Jean-Philippe Tetienne at the University of Melbourne from January 2017 until March 2020. Each of these projects benefited from the input of numerous researchers within our group and from external collaborations. Here we explicitly detail the contribution of these individuals to work presented in the following chapters.

Chapter 1 is an original introduction to the literature of quantum sensing and imaging. Figure elements adapted from the literature are acknowledged explicitly in their accompanying captions. Chapter 2 motivates and introduces our experimental approach to widefield imaging with nitrogen-vacancy centres in diamond. The methods here were developed by the ongoing efforts of our research group, as informed by the literature. Most of the nitrogen-vacancy-containing diamonds used throughout the thesis were initially prepared by Dr. Jean-Philippe Tetienne. The SRIM simulation used to determine the vacancy profile arising from a 100 keV $^{12}C^{-}$ implant was performed by Dr. Brett C. Johnson and originally published in Ref. [1]. The widefield optical apparatus follows a design originally used by Dr. David Simpson, described in Ref. [2].

Chapters 3, 4, and 5 cover the major experimental works of this thesis. The experiments and analysis presented were performed by the author under the supervision of Dr. Jean-Philippe Tetienne and Prof. Lloyd Hollenberg. All sample preparation, data acquisition and analysis was performed by the author with regular input from the extended Quantum Sensing Group, unless stated otherwise. In chapter 3 we study ultrathin depositions of metallic nanoparticles deposited on the diamond surface. The first inox steel depositions, which are not presented in the chapter, were originally charac-

terised with the help of Dr. Torben Daeneke and Dr. Ali Zavabeti (RMIT University), as this contamination emerged from attempts to use our NV-diamond imaging to study atomically-thin metal oxides synthesised by their group. The EDSX analysis of one of these original inox steel depositions (see appendix A.1.2) was done by Dr. Jean-Philippe Tetienne using facilities at the Bio21 Institute. In chapter 4, the design of graphene field-effect transistors was led by Dr. Nikolai Dontschuk. The device fabrication was shared by the author and Dr. Dontschuk, with the exception of the atomic-layer deposition of the gate oxide, which was done solely by Dr. Dontschuk at the Melbourne Centre for Nanofabrication. The ODMR-based electric field imaging of the devices was performed with the assistance of Dr. David Broadway. Electric field simulations were performed by Dr. Daniel Creedon using COMSOL. In chapter 5, the superconducting Nb wires were fabricated by Dr. Nikolai Dontschuk. LabVIEW routines used to electrically characterise the Nb wires were programmed by Sam Scholten. Our understanding of the vortex clustering and temperature-dependent current paths in the Nb wires were informed by discussions with Dr. Stephan Rachel and Sebastian Wolf at the University of Melbourne.

Chapter 6 summarise studies of two ultrathin ferromagnetic materials. The VI_3 studied was fabricated and deposited onto our NV-diamond substrates by Prof. Lan Wang and his team at RMIT University. The ultrathin magnetite studied was synthesised by Prof. Vipul Bansal, Aviraj Ingle, and their team at RMIT University. The NV imaging of VI_3 flakes was performed primarily by Dr. Jean-Philippe Tetienne and Dr. David Broadway, but is reported here briefly to demonstrate the refined approach to widefield NV imaging informed by the work of this thesis. The NV imaging of magnetite flakes was performed by the author, and the AFM imaging of magnetite was performed by the author and Aviraj Ingle.

Throughout my candidature I have been supported by an Australian Government Research Training Program Scholarship. The research itself has been funded by the Australian Research Council (ARC) through Grants DE170100129, CE170100012, LE180100037, DP190101506, and FL130100119. Parts of this work was completed using facilities at the Melbourne Centre for Nanofabrication in the Victorian Node of the Australian National Fabrication Facility, and the Materials Characterization and Fabrication Platform at the University of Melbourne.

Acknowledgements

This work was principally carried out on the stolen land of the Wurundjeri and Boon Wurrung people of the Kulin Nation. I pay my respects to their Elders past, present, and emerging. Sovereignty of these lands has never been ceded.

Throughout my PhD, I have had the pleasure of working with a large group of talented and affable researchers. I thank Jean-Philippe Tetienne for his attentive supervision during my candidature. His passion and drive for excellence is always balanced with compassion and kindness. Lloyd Hollenberg has been a key role model for myself and many in the School of Physics at the University of Melbourne. Lloyd is a great team leader with an keen eye for the big picture. It has been a pleasure working with Lloyd and his team. Jeffrey McCallum, as chair of my advisory committee, has been a great support and source of good humor, always ready to lend a sympathetic ear. Many of the logistical bumps inherent to research life were smoothed by the dedicated work of Rose Cooney. Thanks, Rose! My time in the University of Melbourne cleanroom would have been far more stressful and far less fruitful without the presence of Nikolai Dontschuk. Nik is an invaluable asset to any research team, doubly so when things get tough. A special thanks is reserved for David Broadway who has been a keen collaborator and friend throughout my candidature. What a fun time we had. The senior researchers in and adjacent to the quantum sensing team have all offered their advice, expertise, and friendship in various combinations. Thanks to David Simpson, Alastair Stacey, Liam Hall, Mina Barzegaramiriolya, Brett Johnson, and Daniel Creedon.

The student contingent of the quantum sensing group is one of its great strengths, making the office and lab welcoming spaces even when research is a struggle. Thanks to all the quantum sensing students for your camaraderie, especially David Broadway, Julia

McCoey, Robert de Gille, Daniel McCloskey, Alex Healey, Erin Grant, Sam Scholten, Di Wang, Alister Chew, and Ella Walsh. Thank you to fellow PhD students within the physics community Will Lawrie, Danielle Holmes, and Greg White for their friendship. As a great progenitor of typos, the readability of this manuscript owes much to my kind team of proofreaders. Thanks to all of Di Wang, Alex Healey, Erin Grant, Robert de Gille, Nikolai Dontschuk, Sam Scholten, and Ella Walsh for their service.

The support of friends and family outside of the physics community has been as essential to my completion as that from within. Thanks to all my close friends for their time, comfort, and care over the past four years. Thanks to my immediately family Barbara Mans, David Lillie, and Colin Mans for their constant support and encouragement. And finally, thanks to my partner Sarah McDonald, who, in additional to her endless support and encouragement, has been an outstanding office mate and housemate over the past year.

Publications

1. S. E. Lillie, D. A. Broadway, J. D. A. Wood, D. A. Simpson, A. Stacey, J.-P. Tetienne, and L. C. L. Hollenberg, "Environmentally Mediated Coherent Control of a Spin Qubit in Diamond," *Physical Review Letters*, 118, 167204 (2017).

2. D. A. Broadway, S. E. Lillie, N. Dontschuk, A. Stacey, L. T. Hall, J.-P. Tetienne, and L. C. L. Hollenberg, "High precision single qubit tuning via thermo-magnetic field control," *Applied Physics Letters*, 112, 103103, 2018.

3. D. A. Broadway, N. Dontschuk, A. Tsai, S. E. Lillie, C. T.-K. Lew, J. C. McCallum, B. C. Johnson, M. W. Doherty, A. Stacey, L. C. L. Hollenberg, and J.-P. Tetienne, "Spatial mapping of band bending in semiconductor devices using in situ quantum sensors," *Nature Electronics*, 1, 502-507, 2018.

4. S. E. Lillie, D. A. Broadway, N. Dontschuk, A. Zavabeti, D. A. Simpson, T. Teraji, T. Daeneke, L. C. L. Hollenberg, and J.-P. Tetienne, "Magnetic noise from ultrathin abrasively deposited materials on diamond," *Physical Review Materials*, 2, 116002, 2018.[1]

5. J.-P. Tetienne, R. W. De Gille, D. A. Broadway, T. Teraji, S. E. Lillie, J. M. McCoey, N. Dontschuk, L. T. Hall, A. Stacey, D. A. Simpson, and L. C. L. Hollenberg, "Spin properties of dense near-surface ensembles of nitrogen-vacancy centers in diamond," *Physical Review B*, 97, 85402, 2018.

6. J.-P. Tetienne, D. A. Broadway, S. E. Lillie, N. Dontschuk, T. Teraji, L. T. Hall, A. Stacey, D. A. Simpson, L. C. L. Hollenberg, "Proximity-induced Artefact in Magnetic Imaging with Nitrogen-Vacancy Ensembles in Diamond," *Sensors*, 18, 1290, 2018.

7. J.-P. Tetienne, N. Dontschuk, D. A. Broadway, S. E. Lillie, T. Teraji, D. A. Simpson, A. Stacey, and L. C. L. Hollenberg, "Apparent delocalization of the current density in metallic wires observed with diamond nitrogen-vacancy magnetometry," *Physical Review B*, 99, 014436, 2019.

8. D. A. Broadway, B. C. Johnson, M. S. J. Barson, S. E. Lillie, N. Dontschuk, D. J. McCloskey, A. Tsai, T. Teraji, D. A. Simpson, A. Stacey, J. C. McCallum, J. E. Bradby, M. W. Doherty, L. C. L. Hollenberg, and J.-P. Tetienne, "Microscopic Imaging of the Stress Tensor in Diamond Using in Situ Quantum Sensors," *Nano Letters*, 19, 7, 4543-4550, 2019.

9. S. E. Lillie, N. Dontschuk, D. A. Broadway, D. L. Creedon, L. C. L. Hollenberg, and J.-P. Tetienne, "Imaging graphene field-effect transistors on diamond using nitrogen-vacancy microscopy," *Physical Review Applied*, 12, 024018, 2019.[1]

10. S. E. Lillie, D. A. Broadway, N. Dontschuk, S. C. Scholten, B. C. Johnson, S. Wolf, S. Rachel, L. C. L. Hollenberg, and J.-P. Tetienne, "Laser Modulation of Superconductivity in a cryogenic widefield nitrogen-vacancy microscope," *Nano Letters*, 20, 3, 1855-1861, 2020.[1]

11. D. A. Broadway, S. C. Scholten, C. Tan, N. Dontschuk, S. E. Lillie, B. C. Johnson, G. Zheng, Z. Wang, A. R. Oganov, S. Tian, C. Li, H. Lei, L. Wang, L. C. L. Hollenberg, and J.-P. Tetienne, "Imaging domain wall reversal in an ultrathin van der Waals ferromagnet," *Advanced Materials*, 32, 39 2003314, 2020.

12. D. A. Broadway, S. E. Lillie, S. C. Scholten, D. Rohner, N. Dontschuk, P. Maletinsky, J.-P. Tetienne, and L. C. L. Hollenberg, "Improved current density and magnetisation reconstruction through vector magnetic field measurements," *Physical Review Applied*, 14, 024076, 2020.

[1] Publications contributing to the work of this thesis.

Contents

List of figures

Introduction

Modern life is overrun with sophisticated electronic devices that have emerged from the concerted efforts of scientists and engineers over the past sixty years. These solid-state devices play a role is every aspect of our lives, helping us work with ever greater efficiency, connecting us with friends and family around the world, offering new platforms for creative expression and an abundance of new media. A key ingredient of this spectacular progress has been the continuous development of tools to characterise the physical properties of these devices and their associated materials with ever better precision. To solve the grand challenges of today (e.g. ever increasing energy/data consumption) and invent the electronic devices of tomorrow, further improvements and innovations in the domain of characterisation are needed.

This thesis reports on the development of one such innovation, derived from the advent of quantum technology. It relies on the nitrogen-vacancy centre in diamond, a quantum sensor first demonstrated over a decade ago, which is harnessed to realise a new type of microscope capable of multi-modal imaging with an unprecedented combination of sensitivity, resolution, and experimental flexibility. The nitrogen-vacancy centre is an atomically-sized, photoluminescent defect in diamond with a unique electronic structure that facilitates optical polarisation and readout of its electronic spin state, and coherent manipulation by resonant microwave fields. The robust coherence times of the electronic spin states permit good sensitivity of nitrogen-vacancy centres across a broad range of environmental conditions, from room temperature down to cryogenic temperatures. The centre's good sensitivity to magnetic, electric, temperature and strain fields, combined with its optical initialisation and readout, allow nitrogen-vacancy-based microscopy to image these fields in a quantifiable manner. In this thesis we take a so-called "widefield"

approach the NV-diamond microscopy, which relies on a dense layer of near-surface of nitrogen-vacancy centres in a diamond substrate that are optically addressed in parallel. Samples of interest here are deposited or fabricated on the diamond surface, allowing rapid, diffraction-limited imaging of the sample over a large field of view.

This thesis presents original research in the development and application of wide-field imaging techniques using nitrogen-vacancy centres in diamond to a variety of devices and materials within the realm of condensed matter physics. In particular, this thesis makes several important original contributions to the field by applying widefield nitrogen-vacancy microscopy to metallic-nanoparticle depositions, graphene-field effect transistors, superconducting niobium wires, and ultrathin magnetic materials. The study of metallic nanoparticles reveals significant magnetic noise associated with such depositions that was previously unreported in the literature. Our study of graphene field-effect transistors represents a significant advance in the complexity of devices studied with nitrogen-vacancy microscopy at the commencement of that project, and reveals an unexpected accumulation of charge at the diamond interface. The feasibility of imaging low-critical-temperature systems is demonstrated by our study of superconducting niobium wires, where we achieve minimally invasive imaging over the largest field of view reported in the literature under such conditions. Finally, our characterisation of ultrathin free-standing magnets demonstrates the great utility of nitrogen-vacancy microscopy to this emerging field and paves the way for future studies of ultrathin heterostructures. These advances bring this emerging technology one step closer to deployment in academic and industrial laboratories around the world, where it may facilitate development of the materials and devices of tomorrow.

1

Quantum sensing and imaging with nitrogen-vacancy centres in diamond

The nitrogen-vacancy (NV) centre in diamond is the physical system at the heart of all studies presented in this thesis. In order to implement NV sensing and imaging techniques, we first need to understand the physics underlying their function and make clear the inherent capabilities and limitations. Ultimately, we wish to apply these techniques to study systems extrinsic to the diamond host, namely, condensed matter phenomena that can be measured by some steady-state signature. In principle this can be achieved using a small subset of the available NV sensing techniques. The full suite of NV sensing techniques, however, is a valuable resource for extracting additional information from a sample of interest and is one of the key advantages of the system. For this reason, we start with a comprehensive overview of NV sensing.

This chapter begins with a brief definition of quantum sensing to highlight the properties of the NV centre that qualify it as a quantum sensor, and includes a brief comparison to other quantum sensors such that the unique advantages of NV sensing can be appreciated. Then, the NV centre in diamond is introduced in detail, including its photoluminescence properties, and its electronic and spin-state structure which underpin its sensing capabilities. The most common sensing modes are introduced, including optically detected magnetic resonance - the most widely utilised technique in this thesis - but also more sophisticated coherence-based measurements. The chapter finishes with a review of some of the key achievements in NV sensing and imaging including state-of-the-art applications in nuclear magnetic resonance, hyperpolarisation, quantum information technologies, transport measurements, and other condensed matter and biophysics applications. Understanding the key achievements of NV sensing and imaging, demonstrates the value of the system as a quantum sensor and suggests the future direction of NV research and technology. This understanding gives context to the goal of this thesis: to use NV measurements to characterise condensed matter phenomena via an associated field.

1.1 Quantum Sensing

Quantum sensing refers broadly to the controlled interaction of a quantum system with its environment such that a physical quantity associated with that environment can be measured. The use of a quantum sensor over a classical sensor is typically motived by

the greater sensitivity and precision offered by quantum sensors, in addition to the length scales they can probe. The quantum system of choice, i.e. the quantum sensor, and the nature of its interactions dictate which quantities can be measured at what sensitivity. There are many physical systems that classify as quantum sensors, each with their own advantages and limitations, but they all share common attributes. Here, we follow the instructive review of Degen, et al. [3], which enumerates four key criteria required of any quantum system if it is to function as a quantum sensor. They are:

1. The system has discrete and resolvable energy levels, which can be addressed as a two-level system, though more complex systems are admissible.

2. The system needs to be reliably initialised into some known quantum state and have a mechanism by which its state can be read out.

3. The systems can be coherently manipulated by a time-varying field.

4. The system interacts with a time-varying quantity of interest, such as a magnetic or electric field, which results in a shift in the energy levels of the system.

The NV centre in diamond is one system that meets the above criteria. It has discretised electron spin-state energy levels, which can often be simplified to a two-level system. The spin state is reliably intialised following illumination with visible light and the state can be read out by collecting the subsequent photoluminescence. The spin state of the system can be coherently controlled using a microwave field resonant with one of the spin-state transition frequencies. The energy of these spin states shift in response to magnetic and electric fields via Zeeman and Stark effects respectively, which allows for the detection of static, time-varying, and fluctuating fields with an appropriate control scheme. The details of the NV centre and its sensing protocols will be introduced in sections 1.2 and 1.3.

The NV centre is just one example of a system that satisfies the quantum sensor criteria above. Alternative systems that can be used as quantum sensor include other solid-state spins such as phosphorus donors in silicon and quantum dots, superconducting circuit devices such as flux qubits and super-conducting quantum interference devices (SQUIDs), and atomic systems such as Rydberg atoms, trapped ions, and atomic vapour

cells. The physics underlying each of these systems dictates the quantities they are capable of sensing. For example, the electron or nuclear magnetic moments of solid-state spin qubits make them naturally good magnetic field sensors, as for atomic vapour cells. Superconducting circuit devices are similarly good magnetic field sensors as magnetic fields alter Aharonov-Bohm phase or superpositions of super-current in SQUIDs and flux qubits respectively [3]. Rydberg atoms and trapped ions on the other hand are extremely good sensors of electric fields due to strong coupling with their electrons, but also magnetic fields via the Zeeman effect on their spin sub-levels [3]. Each of these systems have their own unique advantages and disadvantages. SQUIDs, for example, have excellent sensitivity to magnetic fields, typically down to $\mathrm{fT}/\sqrt{\mathrm{Hz}}$ for bulk systems [4] and can image at sub-micron spatial resolutions with single electron-spin sensitivity using scanning nano-SQUIDS [5]. Their requirement to be below the critical temperature of the superconducting material, however, limits imaging conditions to cryogenic temperatures. This can be overcome if the SQUID is separated and isolated from the sample, but this comes at the expense of spatial resolution, as is the case of bulk SQUID magnetometry. Similar obstacles are encountered for solid-state spin qubits, such as phosphorous donors in silicon which are impractical to use above 10 K [6], and trapped ions and Rydberg atoms which require operation in vacuum.

The NV centre in diamond, though not excelling in any single criteria, is an attractive sensor because of its flexibility. Although its sensitivity to magnetic fields does not compete with that of SQUIDs, it has good sensitivity (down to a few $\mathrm{nT}/\sqrt{\mathrm{Hz}}$ for ac signals [7] and tens of $\mathrm{nT}/\sqrt{\mathrm{Hz}}$ for dc signals [8]) which is maintained across a broad range of experimental conditions [9]. In addition to magnetic field sensing, NV centres can be used to sense and image electric, strain, and temperature fields, with moderate sensitivities of $200\,\mathrm{V/cm}/\sqrt{\mathrm{Hz}}$ [10], tens of $\mathrm{MPa}/\sqrt{\mathrm{Hz}}$ [11], and a few $\mathrm{mK}/\sqrt{\mathrm{Hz}}$ [12] respectively. These capabilities, in addition to the many sensing modes accessible to NV centres, allow multiple aspects of a sample to be investigated with little infrastructure. The spatial resolution of NV imaging is typically optical resolution limited to a few hundred nanometres [1], but by scanning single and small ensembles of NV centres, spatial resolutions down to approximately 100 nm can be achieved [13, 14]. This combination of features make NV sensing well suited to imaging mesoscopic phenomena that may vary

over a broad temperature range, or that demand ambient or non-invasive conditions.

1.2 The nitrogen-vacancy colour centre in diamond

Now that the key properties which qualify the NV centre in diamond as a quantum sensor have been introduced, the physics underlying these properties can be explored in detail. This section covers the fundamental physics which govern the NV centre in diamond. It begins with a brief description of the centre's geometry within the carbon diamond lattice. The various NV charge states and their photoluminescence properties are introduced, with a discussion of the challenges in stabilising the NV^- charge state, the only state viable as a quantum sensor. The electronic structure of the NV^- state, which is key to the optical initialisation and readout of the NV spin state, is described in detail. Finally, the Hamiltonian that governs the NV ground-state spin levels is introduced, with a focus on the Zeeman and Stark terms that dictate their sensitivity to magnetic and electric fields respectively.

The NV centre in diamond is a photoluminescent, atomically-sized defect comprised of a substitutional nitrogen atom and an adjacent vacancy situated in the tetrahedral carbon lattice [15]. The centre belongs to the C_{3v} point group, giving it a trigonal pyramidal symmetry. The nitrogen atom, a group V donor in diamond, is covalently bound to its three neighbouring carbon atoms leaving an unbound electron pair at the site. The vacancy is host to three dangling bond originating from its three neighbouring carbon atoms. The metastable NV^- charge state is formed by capturing a sixth electron at the defect site, where the extra electron is typically sourced from a nearby donor such as substitutional N. The NV^- is the only charge state viable as a quantum sensor (see section 1.2.1).

The axis connecting the substitutional nitrogen atom to the adjacent vacancy, referred to as the NV axis, can be oriented along either of the four $\langle 111 \rangle$ crystal orientations. This is shown in a conventional unit cell diagram, figure 1.1(a), where there are four candidate vacancy sites for a given substitutional nitrogen site. The NV axis is the quantisation axis of the NV^- spin states in the absence of strong magnetic or electric fields. The orientation of this NV axis for a given centre therefore dictates its directional

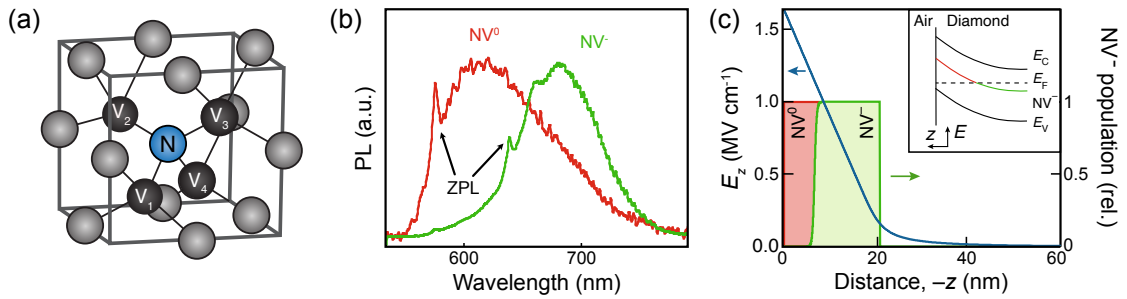

Figure 1.1: The NV centre in diamond, photoluminescence and charge states. (a) Conventional unit cell of diamond featuring a single NV centre, which is comprised of a substitutional nitrogen atom (N, blue) and an adjacent lattice vacancy (black). For a given substitutional N, there are four candidate vacancy sites (V_1, V_2, V_3, V_4). (b) Photoluminescence (PL) spectrum of NV^- (green) and NV^0 (red) charge states showing their respective zero-phonon lines (ZPL) at 637 nm and 575 nm. Both spectra are dominated by phonon-side bands. This figure is reproduced from Ref. [17]. (c) Relative population of the NV^- and NV^0 charge states near the diamond surface due the large electric field, E_z, that airses from band bending (inset). This figure is adapted from Ref. [18].

sensitivity to external fields, which is greatest for magnetic fields parallel the NV axis and electric fields perpendicular to the NV axis. This directionality allows these quantities to be reconstructed vectorially, a capability not open to all quantum sensors that can be advantageous in certain applications [16].

1.2.1 Charge states and photoluminescence spectrum

The NV centre in diamond can exist in a number of charge states, the most common of which are the neutral NV^0 and the negatively charged NV^- states. As outlined previously, the NV centre is a multi-electron system comprised of two electrons from the group V donor nitrogen, and one unpaired electron from each of the three dangling carbon bonds surrounding the vacancy site. In this arrangement the centre is neutrally charged, NV^0, and despite being a photoluminescent spin-1/2 defect, cannot function as a quantum sensors as it lacks a mechanism by which its spin state can be optically read out [15]. Capturing an additional electron from the diamond lattice gives the negative charge state, NV^-, the properties of which satisfy all quantum sensing criteria. Throughout this thesis, given the focus on quantum sensing applications utilising the NV^- spin states, the term "NV" refers to the NV^- charge state unless explicitly labeled otherwise.

The dominant NV^- and NV^0 charge states can be distinguished by their photoluminescence profiles. Each charge state has a distinct optical zero-phonon line (ZPL), 637 nm for NV^- and 575 nm for NV^0 [15], but their photoluminescence is dominated by phonon side-bands. The photoluminescence spectrum of each species are shown in figure 1.1(b). For quantum sensing applications, NV photoluminescence is typically filtered to collect between $680 - 730$ nm, improving the signal-to-noise ratio by targeting more of the sensitive NV^- photoluminescence and excluding some of the insensitive NV^0 photoluminescence that is present in any ensemble measurement and even single NV measurements due to charge state switching.

Given the dependence of quantum sensing applications on the capture and retention of a sixth electron at the defect site, there are many factors to consider when fabricating a NV diamond to maximise the NV^-/NV^0 charge state ratio in a sample. These factors include the level of doping in the diamond lattice, usually dictated by the density of nitrogen or other species incorporated into the diamond by implantation or growth, the depth of the sensing layer, annealing strategies, the diamond surface treatments and termination, and the presence of other defects that may compete with NV^- for its sixth electron [18–26]. Details specific to the fabrication of NV diamond samples used in this thesis will be covered in chapter 2. Charge state sensitivity to depth is illustrated in figure 1.1(c), where we see NV^0 become the dominant change state close to the diamond surface due to the large electric field associated with band bending at the diamond-air interface.

The factors outlined above dictate the equilibrium charge state balance in a diamond substrate, however, the charge state of a given NV centre can change dynamically during and between measurements. The light source used to stimulate the NV photoluminescence plays a key role in these dynamics, where both the wavelength and power of the excitation laser influence the interconversion between the NV^- and NV^0 charge states, and ionization to other charge traps [25,27–29]. Typical NV sensing experiments use a 532 nm wavelength laser to stimulate photoluminescence, as this strikes a good balance between efficient excitation of NV^- and minimal ionisation to NV^0 [15]. Despite best design practices in NV diamond fabrication and control, dynamic charge state switching is intrinsic to any NV experiment due to coupling of the centre to neighbouring defects and electronic states [30]. The sixth NV^- electron is free to tunnel to neighbouring defect at any point during a

measurement sequence, which, depending on the measurement, may have implications for the subsequent data analysis and should always be considered [31]. In section 1.3.1, the use of photoluminescence imaging based on the NV^0/NV^- charge state ratio to probe electric fields within the diamond will be discussed.

1.2.2 Electronic structure of NV^-

The electronic structure of the NV center is key to its use as a quantum sensor. Here, the structure is reviewed as relevant to sensing and imaging applications in the absence of external magnetic, electric, or strain fields, and hence omits further details such as the hyperfine interaction with the nitrogen nucleus. This description is summarised in figure 1.2(a), and is informed by Refs. [32, 33].

The NV centre features a spin-triplet ground state, $^3A_2$, and a spin-triplet excited state, ^3E, that are energetically separated by 1.945 eV. This energy splitting gives rise to the 637 nm zero-phonon line (ZPL) from the ground to excited state transitions. These triplet states have three spin sub-level projections, $m_s = 0, \pm 1$, which are quantised relative to the NV axis. Two singlet states exist between the ground and excited states. The higher energy singlet state, $^1A_1$, is separated from the lower, ^1E, by 1.190 eV. Radiative decay between these singlet states results in infrared photoluminescence with a 1042 nm ZPL. The addition of fine structure lifts the degeneracy of the spin sub-levels in the ground and excited triplet states. In the ground state, $^3A_2$, this results in a zero-field splitting between the $m_s = 0$ and the degenerate $m_s = \pm 1$ states of 2.87 GHz at room temperature, where the latter are higher in energy. This structure is mirrored in the excited state (notwithstanding orbital splitting which can effectively be ignored in most sensing scenarios), ^3E, but with a smaller zero-field splitting of 1.42 GHz.

The visible range photoluminescence and absorption of the NV centre is due to the cycling between the ground and excited states. Excitation from the ground state, $^3A_2$, to the excited state, ^3E, is spin preserving and can be achieved non-resonantly via phonon mediated processes. In most experiments, this is achieved using a 532 nm laser which gives efficient excitation and good spin polarisation, which can be as high as 90% [27]. Direct relaxation from the excited state to the ground state is similarly spin preserving,

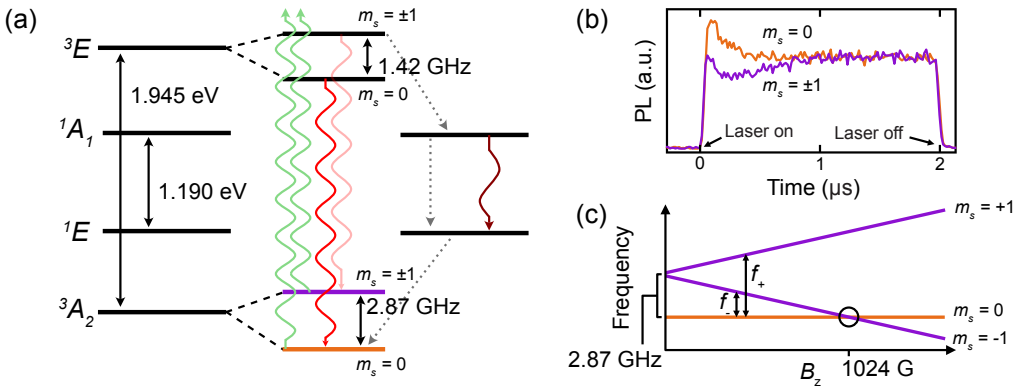

Figure 1.2: Spin-state dependent photoluminescence and optical pumping. (a) Energy-level structure of the NV centre as described in the text. The left and right-hand sides of the diamond show the structure before and after including spin-spin interactions. Energy/frequency differences are labeled with solid double-headed arrows. Radiative and non-radiative transitions are denoted by wavy and dotted arrows respectively. This diagram is based on Ref. [33]. (b) Time-resolved photoluminescence for a single NV centre in the $m_s = 0$ (orange) or $m_s = \pm1$ (purple) states when the excitation laser is turned on. The spin-state-dependent photoluminescence is due to the optical cycling shown in (a). The system is repumped to the $m_s = 0$ state after 1 μs. (c) Zeeman effect acting on the ground-state spin sub-levels for a magnetic field applied along the NV axis, B_z. The resonance frequencies at a given applied field strength are denoted by f_- and f_+. The GSLAC occurs at $B_z \approx 1024\,\mathrm{G}$ when the $m_s = 0$ and $m_s = -1$ states approach degeneracy.

with most of the photoluminescence emitted in the phonon side-band (650-720 nm), as mentioned in 1.2.1.

The ability to initialise and read out the NV spin state is facilitated by relaxation from the excited state to the ground state via the singlet states. Relaxation from the excited state, ^3E, to the higher energy singlet state, ^1A, is non-radiative, however, only the $m_s = \pm1$ spin sub-levels of the excited state couple efficiently to this singlet state. Further relaxation to the lower energy singlet state, ^1E, can occur radiatively about the 1042 nm ZPL, and non-radiatively. Relaxation from the metastable ^1E state to the ground-state triplet, $^3A_2$, is again non-radiative, but mainly couples to the $m_s = 0$ ground-state spin sub-level. This relaxation pathway therefore results in a lower on average NV photoluminescence from the $m_s = \pm1$ spin states as compared to the $m_s = 0$, which only undergoes radiative decay from the excited state to the ground state. This pathway also gives a mechanism by which the NV spin state can be initialised to the $m_s = 0$ state, as

repeated excitation of electrons in the $m_s = \pm 1$ state will pump the population towards the $m_s = 0$ state. These transitions are denoted in figure 1.2(a).

The lifetimes and branching ratios of each of these states set the time scales over which optical spin polarisation and readout occur, in addition to the degree of spin-state polarisation that can be achieved. The lifetime of the ^3E excited state and $^1A_1$ singlet state are short as compared to the metastable ^1E state, which has a lifetime upwards of 100 ns [34, 35]. This shelving in the metastable singlet state is therefore a limiting step in the re-pumping of the NV spin state. For a single NV centre excited at optical saturation, maximum spin polarisation is typically achieved after 1 μs, as shown in figure 1.2(b). Reports on the degree of spin polarisation at room temperature vary, but polarization above 90% has been reported [15, 27]. For the widefield imaging application pursued by this thesis, limited laser power means that the NV ensemble is excited far below optical saturation. The implications for sensitivity of widefield ensemble imaging will be discussed in chapter 2.

1.2.3 The NV ground-state spin Hamiltonian

The electronic structure of the NV center facilitates the initialisation and readout of the discrete and resolvable ground-state spin sub-levels upon illumination and collection of visible light. These properties satisfy the first two criteria required to qualify the NV centre as a quantum sensor. To satisfy the remaining criteria, which are the ability to coherently manipulate the state of the quantum system and for it to be able to interact with a time-varying quantity of interest, we must look to the Hamiltonian which governs the NV ground-state spin sub-levels.

The NV ground-state is a spin-1 system with three spin sub-level projections, $m_s = 0, \pm 1$, which denote projections along the NV axis in the absence of magnetic or electric fields. By convention, this quantisation axis is labeled the z-direction. The sensitivity of the nitrogen-vacancy centre to both magnetic and electric field, but also temperature and strain, is governed by the ground-state spin Hamiltonian. The Hamiltonian can be

written as

$$\mathcal{H}/h = D(T)(S_z^2 - S(S+1)/3) + \gamma_{\mathrm{NV}}\mathbf{B}\cdot\mathbf{S} + d_{\parallel}[E_z + e_z(\hat{\sigma})]S_z^2 + d_{\perp}[E_x + e_x(\hat{\sigma})](S_xS_y + S_yS_x) + d_{\perp}[E_y + e_y(\hat{\sigma})](S_x^2 - S_y^2), \tag{1.1}$$

where h is the Planck constant, $\mathbf{S} = (S_x, S_y, S_z)$ are the spin-1 Pauli matrices, $\gamma_{\mathrm{NV}} = 28.035(3)\,\mathrm{GHz/T}$ is the reduced isotropic NV-electron gyromagnetic ratio [36], and $d_{\parallel} = 0.035\,\mathrm{kHz\,m/V}$ and $d_{\perp} = 1.73\,\mathrm{kHz\,m/V}$ are the parallel and perpendicular electric susceptibility parameters respectively [10, 37, 38]. The Hamiltonian contains a temperature dependent zero-field splitting term, $D(T)$, which gives the 2.87 GHz offset between the $m_s = 0$ and $m_s = \pm 1$ states at room temperature due to spin-spin interactions. Note that here the (x, y, z) is the reference frame specific to each defect with the z direction being the symmetry axis discussed previously. There exists an equivalent spin Hamiltonian for the excited state, differing most notably by a zero-field splitting which is approximately half the value of that in the ground state, 1.42 GHz at room temperature [39]. The excited state is typically not used for sensing given its short coherence time and state lifetime as compared to the ground state [40].

The effect of a magnetic field, $\mathbf{B} = (B_x, B_y, B_z)$, on the spin states is described by the Zeeman term, $\gamma_e\mathbf{B}\cdot\mathbf{S}$, which gives the greatest splitting of the $m_s = \pm 1$ sub-level when the magnetic field is in the z direction, i.e. along the NV axis. This is illustrated in figure 1.2(c). Stark terms dictate the response to electric fields, $\mathbf{E} = (E_x, E_y, E_z)$, and the effective electric fields which manifest from crystal stress, $\mathbf{e}(\hat{\sigma}) = (e_x(\hat{\sigma}), e_y(\hat{\sigma}), e_z(\hat{\sigma}))$, where $(\hat{\sigma})$ is the stress tensor. Note that in general, the magnetic, electric, strain and temperature fields may all be time-dependent, which permits the measurement of these quantities in both static and dynamic scenarios with appropriate control sequences.

The sensitivity to time-dependent magnetic fields can be exploited to coherently control the NV spin state. A state that has been optically initialised in the $m_s = 0$ state can be magnetically driven between the $m_s = 0$ state and either of the $m_s = \pm 1$ by applying an oscillating magnetic field resonant with the relevant transition frequency [41, 42]. This induces coherent Rabi cycling between the levels and allows arbitrary super-position of the two states to be prepared (see section 1.3.3). For simplicity, the NV spin state is

often treated as a two-state system comprised of the $m_s = 0$ state and whichever of the $m_s = \pm 1$ state is relevant, reducing the Hilbert space dimension from three to two. This simplification allows the familiar Bloch sphere picture to be used to understand the effective two-state system where population and phase between the two states can be represented by polar and azimuthal angles on a three dimensional unit sphere. Note that a two-state system between the $m_s = \pm 1$ states can be considered, but that this two-state system can only be manipulated by a mechanical resonance [43], given it is forbidden by magnetic dipole radiation.

The relatively poor sensitivity of NV spin states to electric fields as compared to magnetic fields are dictated by the pre-factors of the Zeeman and Stark terms in the spin Hamiltonian. For example, to achieve a 1.0 MHz shift of the $m_s = 0$ to $m_s = -1$ transitions via the Zeeman effect requires an on-axis magnetic field (i.e. the z-direction) of only 0.36 G. To achieve the same shift via the Stark effect perpendicular to the NV axis (say in the x-direction), an electric field strength of 0.58 kV/m is required. Achieving this same shift in frequency via the temperature dependent zero-field splitting requires a temperature change of 13.4 K [44]. This is the reason that the NV is favoured primarily as a magnetometer, as is the case for most of this thesis. The additional sensitivity to electric fields, strain, temperature must be considered in any NV experiment to ensure that a signal is not falsely attributed to a magnetic interaction, however, this sensitivity can often reveal supplemental information about a sample of interest and investigate phenomena that may not have been anticipated.

Finally, a brief note on the hyperfine interaction between the NV electron spin and the nuclear spin of the nitrogen. This hyperfine interaction will be mostly ignored throughout this thesis as the measurements presented are taken in magnetic field and microwave power regime in which it can be ignored. In general, however, the addition of the nuclear spin, I, and electron spin, S, angular momentum introduces hyperfine structure to the ground and excited-state spin sub-levels. If the substitutional nitrogen is ^{14}N, for which $I = 1$, there are three hyperfine projections for each electron spin sub-level, $m_s = 0, \pm 1$ and $m_I = 0, \pm 1$. Each of these projections shift the energy of the electron spin sub-level by $m_I \times 2.2$ MHz, a shift that can be observed in ODMR in a low microwave power regime [45]. For nitrogen ^{15}N, which has a nuclear spin $I = 1/2$, there are two

hyperfine projections for each electron spin sub-level, $m_s = 0, \pm 1$ and $m_I = \pm 1/2$. This results in a shift of the electron spin sub-levels, and hence the ODMR transition frequencies of $m_I \times 3.1\,\mathrm{MHz}$ [45, 46]. The nuclear spin state is typically not affected by the optical cycling of the centre or manipulations of the electron spin state. The relative abundances of ^{14}N and ^{15}N are 99.6% and 0.4% respectively. For this reason, enriched ^{15}N sources are often used in the fabrication of NV centres such that they can be distinguished from naturally forming NV and substitutional N centres by their hyperfine structure [45].

This hyperfine structure has more serious implications for the electron spin states at what are known as the ground-state level anti-crossing (GSLAC) and excited-state level anti-crossing (ESLAC), which occur when the $m_s = -1$ sub-level approaches the $m_s = 0$ sub-level as the magnetic field increases in the ground and excited states respectively. For a magnetic field applied in the z-direction, i.e. along the NV axis, these occur around field strengths of 1024 G and 512 G, given the 2.87 GHz and 1.42 GHz zero-field splittings of the ground and excited states respectively. In these regimes, the hyperfine coupling is comparable to the energy splitting between the electron spin-state sub-levels, which leads to polarisation of the nuclear spin via the ground to excited state cycling and anti-crossings of the spin sub-levels [46–49]. For the scope of this thesis, we will be working under a bias magnetic field of less than 300 G, however, these effect need to be considered for applications that require NV electron spin transitions to be on the order of MHz, some of which rely on the anti-crossing dynamics [50–54].

1.3 Sensing modes and coherent control

One of the great advantages of NV-based sensing and imaging is the plurality of sensing modes accessible with a relatively simple infrastructure. The previous section established the physics underlying the preparation and readout of the NV spin state, and the Hamiltonian that governs the interaction of these spin states with local environmental quantities. With this foundation that qualifies the NV centre as a quantum sensor, the details of key sensing and imaging modes using NV centres in diamond can be discussed. These sensing modes include schemes for static magnetic, electric, strain and temperature fields based of reading out the NV spin-transition frequencies, and more advanced techniques to measure

time-varying quantities via the NV relaxation times.

1.3.1 Photoluminescence imaging

The majority of NV experiments rely on the preparation, manipulation, and readout of NV spin state by a coordinated series of laser and microwave pulses to quantitatively measure some aspect of the environment. Direct measurement of the NV photoluminescence, however, can be a useful sensing technique in its own right that reveals information about the environment in a fast and efficient manner, although this often comes at the expense of quantitative measurement. Here we outline how direct photoluminescence measurements can be used to probe electric fields via their influence of the NV charge state ratio, and systems that give a near-field optical coupling with the NV centres.

Section 1.2.1 highlighted the two dominant charge states of the NV centre, NV^- and NV^0, and their distinguishable photoluminescence profiles. The NV^-/NV^0 charge state is sensitive to a number of environmental parameters, some of which are fixed upon fabrication and preparation of the host diamond, such as the level of doping, surface termination or geometry [55]. Electric fields arising from surface termination are particularly relevant for near-surface NV sensing applications. Strong electric fields persist tens of nanometres below the diamond surface due to charge transfer from the diamond into an adsorbed acceptor layer, as illustrated in figure 1.1(c) [18,26]. This charge transfer depletes NV^- of its sixth electron, shifting the charge balance in favour of NV^0 and therefore changing the photoluminescence spectrum. The extent of charge transfer and resultant band bending in the diamond is influenced by the chemical surface termination of the diamond. Raw photoluminescence measurements have been used to image hydrogen surface termination which enhances this charge transfer, giving more NV^0 than NV^- as compared to more commonly used oxygen terminated diamond surfaces [18, 19].

The NV charge state ratio and resulting photoluminescence can also be altered dynamically by entities extrinsic to the diamond, such as gate structures fabricated on the diamond surface and gates associated with nearby devices of interest. For example, direct electrostatic gating of NV centres has been employed to controllably switch the NV charge state, as determined by photoluminescence measurements, using both electrolytic and solid

state [56,57] gate electrodes. Nanoscale gate electrodes have also been used to ionise single NV centres to the non-photoluminescent NV^+ charge state to extend nuclear coherence times [58]. In chapter 4, we shall see how electric fields associated with graphene field-effect transistors at the diamond surface affect the charge state balance of the sensing ensemble. Simple photoluminescence measurement lend insight to the diamond-device interface that is not offered by other measurements [59].

Quantifying the electric field responsible for such changes in the NV charge state balance is non-trivial given that this effect is often mediated by surface acceptor layer, which is not well understood, and the subsequent band bending into the diamond. This saturation can be modeled in an equilibrium condition, but extending the model to reflect dynamics introduced by the excitation laser is additionally challenging. For this reason, direct photoluminescence measurements are best used for qualitative sensing and imaging of electric fields. Electric fields can be quantified by spin-resonance measurements of NV^-, however, as will be shown in chapter 4, this has its own limitations and biases due to the poor sensitivity of NV^- spin states to electric field.

In addition to revealing information about electric fields via their effect on the NV charge state, direct measurements of the NV photoluminescence can report on changes to the diamond interfaces [60] and near-field coupling to local systems (plasmon modes) as for any emitter [61, 62]. Förster resonant energy transfer is a well studied example of near-field, non-radiative coupling in NV centres. Here, the photoluminescence lifetime of an NV centre is reduced as the optical excitation non-radiatively couples to a nearby system where it is dissipated. This has been observed between single NV centre and single organic molecule [63], and also 2D graphene which extends the Förster radius to a range of 20 nm given its sheet-like nature [64]. This effect allows graphene to be observed by a direct photoluminescence measurement when placed directly on the diamond surface, provided that some volume of the sensing layer is within the 20 nm Förster radius of the surface [59, 65]. For this effect to be used as a quantitative sensing protocol for near-field couplings, reliable control of the NV-to-sample distance must be achieved to measure the effect across the Förster radius and be compared to a model [64]. In practice, this effect is a simple way to distinguish the presence of a target material at the diamond surface that may not be distinguishable due to a change in reflectance or refractive index, as shown in

chapters 3 and 4.

1.3.2 Optically detected magnetic resonance

Optically detected magnetic resonance (ODMR) is the mostly widely used measurement throughout this thesis. ODMR is a relatively simple technique that measures the electron spin resonance frequencies in the NV ground state that can be driven by magnetic dipole transitions, namely the $m_s = 0$ to $m_s = -1$ and $m_s = 0$ to $m_s = +1$ transitions. These transition frequencies shift in response to magnetic, electric, and strain fields according to the ground-state spin Hamiltonian (equation 1.1). Therefore, by measuring these transition frequencies with ODMR, these fields can be quantitatively reconstructed using a model of the spin Hamiltonian.

In its most basic implementation, an ODMR measurement can be made by continuous application of a microwave field in parallel with a continuously applied laser field. The microwave field has a variable frequency, f_{MW}, which is swept across some range encompassing the NV electron spin-transition frequencies, f_{NV}. The laser field pumps the NV electron spin into the $m_s = 0$ state when this microwave field is out of resonance and stimulates the photoluminescence of the NV centre as outlined in section 1.2.2. As the varying microwave field frequency comes into resonance with an NV spin-transition frequency, the collected photoluminescence decreases as the NV spin state is driven from the bright $m_s = 0$ state, to either of the dark $m_s = \pm 1$ states. As the microwave frequency is brought out of resonance with the spin transition frequencies, the laser re-pumps the NV to the $m_s = 0$ state. This approach to ODMR is known as continuous wave (CW) ODMR. Though simple to implement, this scheme limits the sensitivity of the measurement due to competition between the spin-state driving of the microwave field and the re-pumping of the laser field. This ultimately reduces the photoluminescence contrast of the measured transition frequency and/or increases the resonance line width, which both contribute to reduce the sensitivity. Despite this, we will see CW scheme implemented in chapter 5 to facilitate ODMR measurements under low laser power.

To improve upon the CW scheme, microwave and laser fields can be pulsed in succession and their durations optimised to maximise sensitivity. This pulse scheme is

shown in figure 1.3(a), with a Bloch sphere illustration of its effect on the NV state when $f_{\mathrm{MW}} = f_{\mathrm{NV}}$. An ODMR spectrum acquired by this technique is shown in figure 1.3(b). The details of implementing pulsed ODMR, particularly in the context of widefield NV imaging, will be discussed in chapter 2, including a derivation of the measurement sensitivity and discussion of the analysis and fitting of the acquired spectra. Quantitatively determining magnetic, electric, temperature or strains fields from an ODMR spectrum requires fitting the acquired spectrum to extract the NV spin-transition frequencies, and relating them to a model of the spin Hamiltonian. This will be described in detail in chapter 2.

Although the energy of the NV ground-state spin sub-levels are sensitive to time-dependent fields, ODMR is capable of measuring only static or steady-state manifestations of these field. This is due to the need to repeat the sequence many times and average the signal to improve the signal-to-noise ratio which is limited by the poor photon-collection efficiency. The temporal resolution of ODMR is therefore limited to a few milliseconds, which is roughly the sum of microwave-pulse durations across the number of repetitions required to give a signal-to-noise ratio greater than one in an optimised system. Variation of the spin-transition frequency due to fields fluctuating on timescales shorter than this are overlooked by the measurement. To usefully probe these fluctuating fields, we have to encode these fluctuations in either the relative phase or population of our NV state.

1.3.3 Coherent control of the NV spin state: Rabi cycling

Measuring the ground-state spin resonances of single NV centres by ODMR at room temperature first highlighted the system's value as a magnetometer [66]. However, it was not until coherent control of the NV spin state was demonstrated that its full potential as a quantum sensor was revealed [41, 42]. Here, the coherent control of the NV spin state on exposure to a microwave field resonant with one of the ground-state spin transitions is described. This controlled interaction induces Rabi cycling between the target spin states, allowing reliable preparation and manipulation of arbitrary super-position states. This functionality opens up a range of additional sensing schemes where the phase accumulation of these states can be used as a resource to probe dynamic phenomena.

Rabi cycling of the NV spin state emerges from the Zeeman term in the ground-

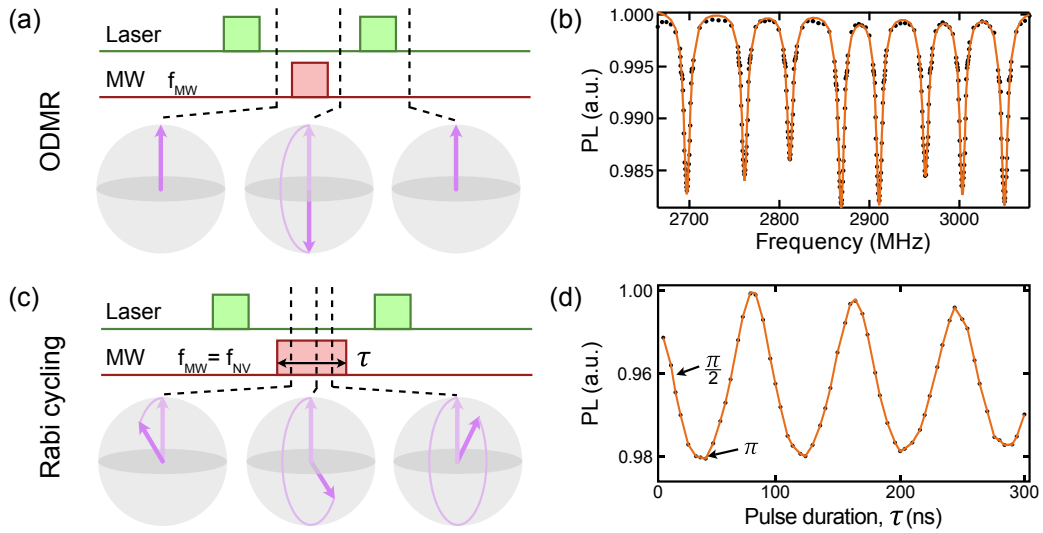

Figure 1.3: Pulsed ODMR and coherent control. (a) ODMR pulse sequence featuring initialisation and read out laser pulses, separated by a microwave pulse. The microwave frequency, f_{MW}, is varied across a chosen range and the pulse duration, is tuned to give maximum photoluminescence contrast across the resonances. The affect of the sequence on the NV state when $f_{\mathrm{MW}} = f_{\mathrm{NV}}$ is shown below, where the north pole represents the bright $m_s = 0$ state, and the south pole represents the resonant $m_s = \pm 1$ state. (b) ODMR spectrum taken from an NV ensemble under a bias field that separates of each of the two resonance from the four NV axis orientations. The orange line is a sum-of-eight-Lorentzian fit. (c) Rabi cycling pulse sequence, which is identical to the ODMR sequence expect that the microwave frequency is fixed to one of the resonances, $f_{\mathrm{MW}} = f_{\mathrm{NV}}$, instead varying the pulse duration, τ,which causes the state vector to rotate azimuthally, varying the population of the two target states. (d) Rabi cycling data taken by resonantly driving one of the transitions seen in (b), with $\pi/2$ and π-pulse durations labeled. The orange line is a guide to the eye.

state spin Hamiltonian (equation 1.1) when coupling the magnetic component of resonant microwave field that is perpendicular to the NV axis to the spin state. This resonant magnetic field component rotates the eigenstates of the system, causing the population to cycle between the targeted spin states, for instance, the $m_s = 0$ and $m_s = 1$ states. In practice, these fields are applied by driving an alternating current through a strip-line or resonator close to the target NV centres. This gives a linearly polarised oscillating magnetic field that can induce Rabi cycling between both the $m_s = 0$ and $m_s = -1$ states, and the $m_s = 0$ and $m_s = +1$ states when resonant with the relevant transition frequency, with Rabi frequencies up to gigahertz [67]. Circularly polarised microwave fields can be used to selectively drive only one of the transitions depending on handedness of the

polarisation [68,69]. It is also possible to mechanically drive the magnetic-dipole-forbidden transition between the $m_s = \pm 1$ state by using a time varying strain field. This has the added benefit of extending coherence times given the two-level system's insensitivity to magnetic noise [43].

The Rabi formula governing these magnetic dipole transitions can be derived semi-classically from the spin Hamiltonian by considering a microwave field with magnetic component of the form, $\mathbf{B}(t) = B_1 \sin(\omega_{\mathrm{MW}} t)\hat{x}$, where B_1 is the field strength and ω_{MW} is the angular frequency of the microwave field. Here, the magnetic field is explicitly oriented along the x-axis, i.e. perpendicular to the NV axis. For an arbitrarily oriented field, the projection perpendicular to the NV axis is taken given that components parallel to the NV axis do not induce a rotation of the spin-state vector. Presuming that the NV spin state is intialised in the $m_s = 0$ state, and invoking the rotating wave approximation, the coherent evolution of the spin state is governed by the general Rabi equation,

$$P_{|\pm 1\rangle}(t) = \left(\frac{\Omega}{\Omega'}\right)^2 \sin^2\left(\frac{\Omega' t}{2}\right), \tag{1.2}$$

where $P_{|\pm 1\rangle}(t)$ is the probability of finding the NV in the target state, $m_s = \pm 1$, at time t, and Ω' is the generalised Rabi frequency. The generalised Rabi frequency, $\Omega' = \sqrt{\left(\omega_{\mathrm{NV}} - \omega_{\mathrm{MW}}\right)^2 + \Omega^2}$, depends on the detuning between the angular microwave and angular spin-transition frequencies, ω_{NV}, and the natural Rabi frequency, which is related to the amplitude of the driving microwave field, $\Omega = \gamma_e B_1/\sqrt{2}$. The probability of finding the NV in the $m_s = 0$ state is simply $P_{|0\rangle}(t) = 1 - P_{|\pm 1\rangle}(t)$. Note that the Rabi cycling described above does not persist infinitely, and will decay due to interaction of the system with the environment, giving a statistical mixture of the target sub-levels. The characteristic time scale of the decay is approximately the rotating-frame decay time, $T_{1\rho}$.

Coherent Rabi oscillations are most relevant to this thesis in that they allow the microwave pulse duration to be optimised in pulsed-ODMR measurements, maximising the spin-state population inversion on resonance, and hence the contrast and sensitivity of the measurement. This duration is known as π pulse as it rotates the NV state vector by π radians in the Bloch sphere picture. ODMR measurements are tuned iteratively in this fashion, using some initial choice of microwave pulse time and power to first identify the

spin-transition frequencies. A Rabi measurement is then made using a sequence identical to that of pulsed ODMR except that the microwave frequency is fixed to the resonance and the pulse duration is varied instead, as shown in figure 1.3(c). Plotting the readout photoluminescence versus microwave pulse duration shows the Rabi cycling, and permits the calibration of microwave pulse duration to the corresponding state-rotation, as shown in figure 1.3(d).

Though primarily a tool for calibrating rotations of the NV state-vector, Rabi oscillation measurements can be used as a sensing mode. Changes to the decay time scale of Rabi oscillation have been used to detect magnetic noise from ion species [70], and measuring Rabi frequency when cycling is mediated by neighbouring spins indicates the coupling strengths of the NV to those spins [51]. Additionally, mapping variations in Rabi frequency can reveal changes in the microwave field which may be due to a sample of interest, as will be the case in chapter 5 [1]. The real value of coherent and long-lived Rabi oscillation of the NV spin state, however, is the ability prepare and manipulate superposition states, whose coherent phase evolution can be used to measure time-varying signals with great sensitivity. This will be covered in section 1.3.5.

1.3.4 Ramsey interferometry (T_2^*)

The most simple sensing technique that relies on coherent phase evolution of a superposition state is Ramsey interferometry [7, 36, 71]. The technique involves preparing a superposition state that is left to freely accumulate phase over some time interval. The accumulated phase is then mapped to a measurable quantity such as the population of the bright and dark states in the NV. This is in contrast to bulk free-induction decay measurements in conventional ESR which typically rely on inductive measurement. The technique, much like ODMR, is used principally to measure quasi-static fields with similar sensitivity.

Ramsey sequences for NV centres are bookended by intialisation and readout laser pulses as in ODMR. Following the initilisation of the NV to the $m_s = 0$ state, the NV is driven to an equal superposition of the $m_s = 0$ and $m_s = +1$ states, for example, by application of a $\pi/2$-pulse, i.e. $|\psi\rangle = |0\rangle \rightarrow |\psi\rangle = 1/\sqrt{2}(|0\rangle + |+1\rangle)$. Here, the

state accumulates phase at the Larmor frequency of the qubit state, which is related to the energy splitting between the superimposed states. After some free precession time, τ, the accumulated phase, $\phi = \omega_{\mathrm{NV}}\tau$, is mapped back to population by application of a second $\pi/2$-pulse. In practice, it is only the relative phase accumulated between the state and the microwave axis under the rotating wave approximation, i.e. $\Delta\phi = (\omega_{\mathrm{NV}} - \omega_{\mathrm{MW}})\tau$, that is mapped to a population, $P_0 = \sin(\Delta\phi)$. For this reason, the microwave frequency is deliberately detuned from the NV resonance, and it is this detuning that dictates the oscillation observed as the free-precession time is varied. Measuring the oscillation frequency of a Ramsey signal can therefore be used to infer the average splitting between the superimposed states, and hence quantify static fields at the site of the NV via the spin Hamiltonian.

Time-varying fields at the NV site lead to a variance in the accumulated phase upon repeated measurement at a given free-precession time. As the precession time increases, so does the variance in accumulated phase, resulting in a decay of the free-induction oscillation as the evolution time increases. Inhomogeneities across a measured ensemble also give a variance in the accumulated phase, and subsequent decay of the free-induction/Ramsey signal. The characteristic time scale of this decay, T_2^*, ultimately limits the sensitivity of the measurement. This same time scale is related to the intrinsic linewidth of the ODMR peak, and hence the techniques measure static fields to similar sensitivities. Using Ramsey interferometery to measure changes in this decay time scale can give insight into the temporal and spatial inhomogeneities at a single NV site, or across a measured ensemble, however, more sophisticated sequences can be employed to tune the NV's sensitivity to fields varying over a target time scale.

1.3.5 Decoherence and dynamical decoupling based detection (T_2)

As outlined in the previous section, the Ramsey sequence relies on the coherent accumulation of phase in a superposition state to detect the static, or rather, time-averaged energy difference between the two superimposed states. Variations in this energy difference both during and between the measurement cause decoherence of the accumulated phase, limiting the measurement sensitivity. Advanced control sequences, however, can be employed

to protect the state from some of this variation by filtering the noise spectrum to which the state is subjected. This filtering, often referred to as dynamical decoupling, has the benefit of extending the NV coherence time throughout the measurement sequence and allows spectroscopy to be performed on the noise spectrum by varying the filter. This is the basis of many NV-based ESR and NMR applications [72–74]. The simplest of these dynamical decoupling sequences is the spin-echo sequence, which refocuses dephasing/decoherence arising from quasistatic variations.

The spin-echo measurement is identical to the Ramsey sequence apart from its inclusion of a π pulse in the middle of the sequence, equidistant from the two $\pi/2$ pulses, as shown in figure 1.4(a). This additional pulse refocuses dephasing of the state arising from field variations that are quasistatic with respect to the sequence, i.e. those that vary between repetitions of sequence, but not during, or static variations across an ensemble of measured spins. The resulting signal is therefore sensitive to fields varying within the measurement sequence. In the case where the evolution time is short, and hence dephasing minimal, the state is returned to the pumped state by the final $\pi/2$ pulse. As the evolution time increases, so does the variance of the phase, and dephasing results in less of the population returning to the bright state. Spin-echo envelopes decay exponentially as the evolution time increases, with a characteristic decay time known as the spin-spin dephasing time, or T_2. An example spin-echo decay is shown in figure 1.4(b) for a diamond similar to those used in chapters 3 and 4. The spin-echo sequence effectively increases the coherence time of the system by decoupling it from quasi-static variations [75].

The spin-echo sequence is the simplest example of such a decoupling sequence. More sophisticated dynamical decoupling sequences can be realised by including additional π pulses that repeat periodically between the bookending $\pi/2$ pulses. Rotations about multiple microwave axes can make the sequence more robust to pulse errors and detunings, and hence schemes such as the XY8 pulse sequence are applied in preference to Carr-Purcell-Meiboom-Gill (CPMG) sequences [76]. These decoupling sequences effectively apply a filter function to the noise spectrum experienced by the system. Broadly, this filtering selects for time-varying signals that match the periodicity of the decoupling sequence, maximising the variance of accumulated phase by the sensor due to these signals, while correcting the dephasing due to other periodic noise. When decoupling sequence is

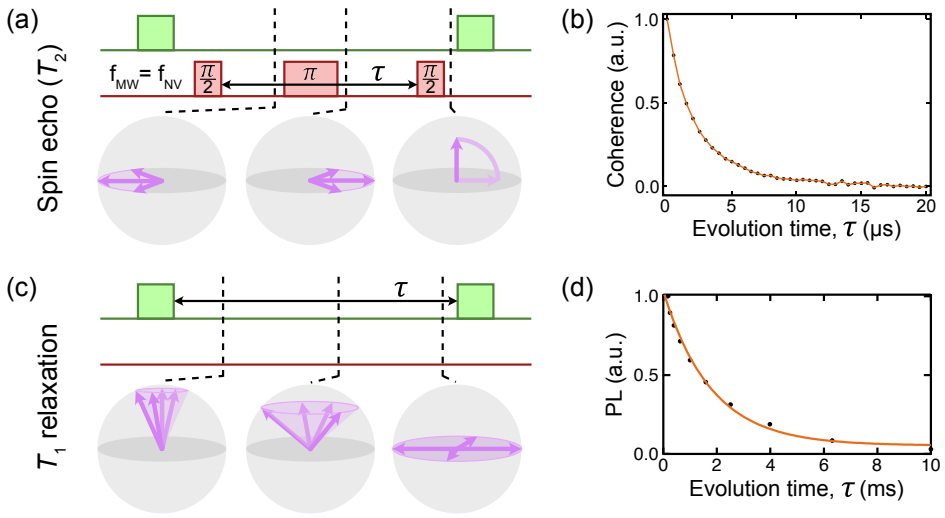

Figure 1.4: Decoherence and relaxation-based sensing modes. (a) Spin-echo (T_2) pulse sequence for decoherence-based sensing. Initialisation and readout laser pulses bookend a microwave pulse sequence featuring two $\pi/2$-microwave pulses, separated by a total evolution time τ, and a central π pulse. The π pulse refocuses dephasing that is symmetric about the sequence, and the final $\pi/2$ pulse maps the remnant dephasing to a population difference, as illustrated in the Bloch sphere diagram. (b) Spin-echo-decay data (black points) measured across and NV ensemble with $T_2 \approx 3\,\mu$s. The (orange) line is guide to for the eye. (c) All-optical T_1-relaxation sequence. The optically-pumped $m_s = 0$ state is left to relax freely for an evolution time, τ, before being read out. As τ increases, the state ensemble evolves to a mixture of the $m_s = 0, \pm 1$ states. (d) T_1-relaxation data from an NV ensemble (black points) with a single-exponential fit (orange) giving $T_1 \approx 1.79\,$ms.

synchronous with a regular ac signal, such as that due to Larmor precession of nuclear spin species, the coherence is collapsed/revived as the phase variance of the NV in this scenario is minimsed/maximised. Such revivals are seen most commonly in NV spin-echo measurements due to the surrounding ^{13}C bath [75, 77]. These sequences can be used to detect nuclear spin species external to the diamond by locking the decoupling sequence periodicity to their Larmor precession frequency [78]. Key achievements and extension of this approach to sensing are covered in section 1.4.1.

1.3.6 Spin-lattice relaxation sensing (T_1)

The phase decoherence of the NV centre is not the only state resource that can be used to sense and image dynamic phenomena. The relaxation of the NV population from some

non-equilibrium state towards thermal equilibrium can be used to measure fluctuating fields that introduce noise at the qubit transition frequency, in addition to phonon activity. This relaxation, referred to as spin-lattice relaxation, is commonly used to detect magnetic noise associated with unpaired electron spins in various ion species, and hence has found application in both condensed matter and biophysics sensing applications [47, 50, 79–85].

Measuring spin-lattice relaxation is particularly simple given it concerns only the NV spin-state population rather than phase as for decoupling measurements. Spin-lattice relaxation can be measured all-optically by first pumping the NV to the bright $m_s = 0$ state, leaving the system to relax freely for some time, τ, and then reading out the degree of relaxation with a subsequent laser pulse, as shown in figure 1.4(c). As the evolution time is increased, the state migrates further towards the equilibrium state, a statistical mixture of the $m_s = 0, \pm 1$ sub-levels at room temperature. This decay is typically exponential with a characterisitic decay time, T_1, known as the spin-lattice relaxation time. In practice, T_1 measurements are normalised by an additional measurement, which applies a π pulse at the end of the evolution time to reference the measured photoluminescence to the dark $m_s = \pm 1$ states, extracting the spin-dependent photoluminescence decay and removing common mode variations from the measurement. A T_1-decay curve measured in this fashion is shown in figure 1.4(d). T_1-based imaging features heavily in chapter 3 where we use it to interrogate magnetic noise from thin metallic depositions on the diamond surface.

Measuring the coherence and relaxation times of a single NV centre or ensemble prior to their application to sensing or imaging determines the sensitivity of measurements to follow. For example, at long native T_1 in an NV ensemble means that a given noise contribution from a sample of interest will result in a greater proportional change in the T_1 time than if the background T_1 were shorter, and is hence more easily detected. Similarly, NV centres with longer T_2 coherence times allow phase contribution from an ac signal of interest to be accumulated over a longer total evolution time, and hence signals with smaller amplitudes can be detected against the background decoherence. For the ensemble measurements presented in this thesis, these coherence considerations must be balanced with the total photon count from the sensing volume, which usually scales inversely with T_1 and T_2, and spin-dependent optical contrast. The balancing of these factors will be discussed in chapter 2 in relation to the fabrication of dense, near-surface, NV-ensemble-

diamond substrates for widefield magnetic imaging.

1.4 State of the art in nitrogen-vacancy sensing and imaging

The previous section introduced the fundamentals at play in most NV sensing and imaging experiments. This toolkit has been developed over the past two decades by the efforts of many groups in the NV research community. One of the key goals in developing this toolkit has been to apply the various sensing and imaging techniques to probe systems of interest external to the diamond. The aim of this thesis is ultimately to make such a contribution, applying NV diamond imaging techniques to study various condensed matter systems. To give context to the original work presented in the following chapters, this chapter concludes with a survey of key achievements in NV-sensing applications to both condensed matter and biological systems. The various approaches to applied NV imaging and sensing discussed in the following sections are illustrated in figure 1.5. The achievements showcased here, though by no means exhaustive, demonstrate the potential use of NV imaging to research communities outside of quantum sensing.

1.4.1 Application to condensed matter systems

The application of NV imaging and sensing to condensed matter systems is the primary concern of this thesis and has been a focus for much of the NV research community. The work of this thesis looks primarily at imaging static or steady-state magnetic fields associated with materials and devices on the diamond surface, typically in an ultrathin to two-dimensional regime. Here, we survey other key achievements in this vein, including the use of NV centres to study the magnetic properties of materials such as two-dimensional ferromagnets and superconductors. Transport phenomena have been studied by various NV sensing techniques including ODMR detection of the Ørsted field associated with charge transport in nearby devices, and T_1-relaxation measurements to probe magnetic noise associated with carrier collisions. Application of NV centres to the detection of electron and nuclear spins by advanced dynamical decoupling and coherence based measurements are discussed, topic of keen interest to NMR and magnetic resonance imaging studies. The excellent review published by Casola, et al., covers many of these topics in

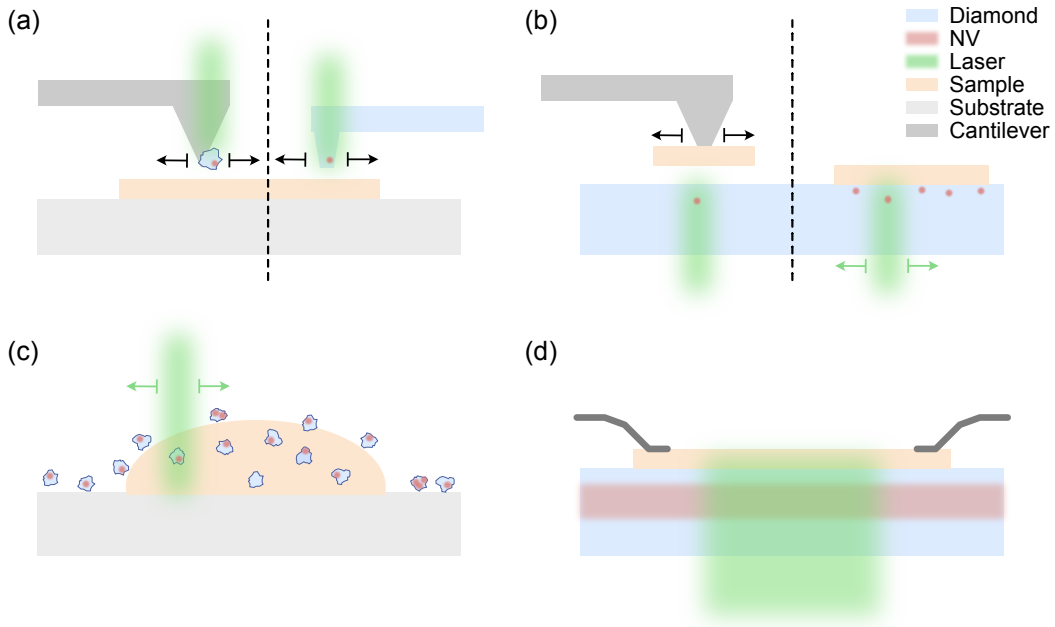

Figure 1.5: Experimental approaches to applied-NV imaging and sensing. (a) Scanning-NV imaging is achieved using either an NV nanodiamond (blue) adhered to the tip of an AFM cantilever (left-hand side), or using an NV-diamond (blue) cantilever (right-hand side). Imaging is achieved by scanning the cantilever across a sample of interest (orange) which may be deposited on a substrate of choice (grey). The laser (green) remains focused on the NV centre (red). (b) Imaging can be achieved using single NV centres in a bulk diamond substrate by scanning the sample of interest relative to the diamond. Alternately, if sensing can be achieved at discrete points across a sample by depositing it on a sparse array of single NV centres which may vary in depth. (c) Dispersions of NV nanodiamonds can be used for discrete sensing across a range of sample, including in vivo sensing for biological applications. (d) Widefield-NV-diamond imaging uses a dense ensemble of near-surface NV centres (red) in a diamond substrate (blue) with a broad laser beam to image a large field of view in parallel. Samples may be deposited/fabricated directly on the diamond surface where electrical contact can be made (dark grey).

detail [86].

The study of ferromagnetic materials is an obvious application of NV sensing and imaging given its good sensitivity to magnetic fields across a broad temperature range. A simplified ODMR type measurement of single NV centres scanned over nickel nanostructures was one of the first demonstrations of magnetic material imaging using NV centres [87]. Since then, scanning single NV centres have been used to study domain wall structure and dynamics in ferromagnetic nanowires [88], magnetic textures including vortex cores [89], non-collinear anti-ferromagnetic ordering [90], and skyrmions [91–93]. These types of experiments initially used NV nanodiamonds adhered to the tip of an atomic force microscope (AFM), but more recently have utilised purpose-fabricated single-crystal diamond AFM tips containing NV centres for greater reliability and performance [94, 95]. Ferromagnetic spin waves have been measured using stationary single-NV centres in a diamond upon which ferromagnetic material is fabricated [96, 97]. Similar studies of ferromagnetic materials have been undertaken using widefield imaging, including imaging of magnetic hard disks [2], and ferromagnetic grains in geologically relevant samples [98].

Ferromagnetism in two-dimensional materials is a recently observed phenomenon that NV imaging is particularly well suited to studying. The small volume of ferromagnetic material in a two-dimensional sample inhibits the use of conventional characterisation techniques such as bulk-SQUID magnetometry, which requires a large sample volume to reach their superior sensitivities. Magneto-optical Kerr effect microscopy was used in the first measurements of ferromagnetic two-dimensional van der Waals [99, 100], however, it relies on the sample having some degree of spin-orbit coupling. NV microscopy on the other hand, requires only that the stray magnetic field of the sample be within the sensitivity limits of the technique, which is true for most ferromagnetic materials (typical spin density of $1\,\mu_{\mathrm{B}}/\mathrm{nm}^2$). The use of NV imaging in this field was first demonstrated by studying chromium triiodide (CrI_3) with scanning single NV centres, providing high-spatial resolution and even revealing a mechanically induced shift from ferromagnetic to anti-ferromagnetic inter-layer coupling in a bilayer sample [14]. Our group has similarly applied NV imaging to two-dimensional ferromagnetism in vanadium triiodide (VI_3) using a widefield imaging configuration to study domain boundary formation and migration of a large number of flakes in parallel [101]. This work and a further application of NV imaging

to thin, un-layered magnetite samples will be discussed in chapter 6.

Superconductors are similarly well suited to analysis by NV sensing and imaging techniques due to their strong response to magnetic fields [102]. The Meissner effect, for example, has been studied in a range of superconductors via its reduction of the stray field in proximity to the material [103–108]. Abrikosov vortices in type-II superconductors have been imaged in both scanning and widefield NV experiments [13,95,109]. Chapter 5 of this thesis contributes to this field, studying a low critical temperature type-II superconductor to test the feasibility and consequences of performing widefield NV imaging over a 100 μm field of view for a temperature critical condensed matter system [1].

NV sensing can also be used to interrogate charge transport phenomena via their associated magnetic fields. For bulk charge transport in conventional currents, the steady state Ørsted field can be measured by nearby NV centres using the ODMR measurement outlined in section 1.3.2. This has been demonstrated in several systems including metallic wires [60], mono-layer graphene [65] and carbon nanotubes [110]. In the case where transport is confined to a two-dimensional material, a current density map can be recreated from the measured Ørsted field [65], a technique that has been used to investigate viscous flow in graphene [111]. Chapter 4 of this thesis applied this same technique in an attempt to map the current density in graphene field-effect transistors under different doping conditions. Thermal collisional of charge carriers in conductors can also be studied using NV sensing, as the fluctuating magnetic field associated with such collisions reduce the NV spin-lattice relaxation time. This interaction has been used to study conductivity in metals via the Johnson noise [112, 113] and also electron-phonon instability in graphene [114].

Finally, one of the most sought after applications of NV sensing is the detection and imaging of small numbers of electron and nuclear spins. The NV centre, as a quantum sensor, is sensitive to order or magnitude smaller numbers of spins, at greater spatial resolution than conventional bulk electron and nuclear spin spectrometers, although this is often as the cost of spectral resolution. Detecting these small numbers of spins typically relies on the dynamical decoupling sequences outlined in section 1.3.5, that are tuned to optimise sensitivity to either the Larmor frequency of the target spins or to a driven modulation of the target species. Single electron spins have been measured in this manner

by driving the electron spin synchronous to an XY8 sequence driven on the NV [115]. Nuclear spins have been detected both by driving the target proton spins in parallel with an NV spin-echo sequence [116] and by simply driving the NV in XY8 sequence to detect hydrogen spins in a volume as small as $(5\,\mathrm{nm})^3$ [78]. This latter technique has been applied to perform NMR spectroscopy of ^{11}B, ^{10}B, and ^{14}N spin species present in a mono-layer of hexagonal boron nitride (h-BN) at the diamond surface [117], and has been implemented in widefield NV experiment to map spin species at the diamond surface via the NMR signature [118, 119].

Recently, the spectral limitation of this technique has been advanced by so-called Qdyne sequences. In these techniques, the decoupling sequence is repeated synchronously with some external clock [120,121], narrowing the spectral resolution to the coherence time of the clock, rather than that of the NV centre [120, 121]. Synchronising this sequence to the precession of nuclear spin species, which have significantly longer coherence times than the NV electron spin, has allowed chemical shifts to be measured by NV measurements of micron-scale sample volumes external to the diamond [122]. Extensions of these techniques have achieved imaging of a cluster of 27 nuclear spins, albeit internal to the diamond [123]. Such progress has renewed hopes for single molecule NMR imaging [124], though much work is needed to replicate these achievements with a spin system external to the diamond. The usefulness of NV centres for NMR and ESR sensing applications is such that systems are now accessible to researchers outside of NV physics [125].

1.4.2 Applications in biophysics

The non-toxicity of diamond, combined with its chemical inertness and the compatibility of NV sensing with ambient conditions has motivated the use of NV centres as sensors in biological systems. These applications range from simply using NV-containing nanodiamonds as photoluminescent nano-probes, to taking full advantage of the NV spin-state structure and performing ODMR and T_1-relaxometry measurements. Approaches to biological sensing with NV centres vary. Some use NV-nanodiamond to disperse around a biological system of interest or even embed within the system, such as living cells. Other approaches use a dense array of NV centres in a diamond substrate upon which biological

systems can be deposited or cultured. Here we review some of the key achievements in biological sensing applications across these approaches.

Nanodiamonds containing NV centres, despite having generally worse spin-coherence properties than their bulk counterparts, allow NV centres to be embedded in biological systems, to perform in situ sensing. This was first achieved in living human HeLa cells where nanodiamonds containing single NV centres have been used to track their movement and orientation within the cell over many hours using repeated ODMR measurements in a small bias field [126]. A full suite of quantum measurements (T_2^*, T_2, and T_1) were also demonstrated in this environment [126]. Similar ODMR-based measurements have been made to perform nanometre-scale thermometry within living cells [127], using sensitivity of the NV spin state to temperature with nanodiamond to enhance spatial resolution [12]. Dispersions of nanodiamond have also been used to measure intra-cellular temperatures [128].

NV measurements have also been implemented in widefield NV imaging configurations for applications in biophysics, mostly to detect magnetic signatures. Widefield ODMR measurements have been used to image living magnetotactic bacteria deposited on the diamond surface [129]. These measurements can be used to probe biomineralisation in harvested biological samples, such as teeth of chiton species, which contain magnetite [85]. Notably, NV measurements can probe both the static magnetic fields from the mineralised magnetite and fluctuating fields originating from pre-mineralised iron species, in a single experiment [85].

Indeed, relaxation based NV measurements are particularly applicable to biological sensing. Both T_1 and T_2 based relaxation imaging can be applied to detect relatively small concentrations of biologically relevant electron spin species, including copper [128], iron [80], gadolinium [130], manganese [70], depending on the nature of their spin fluctuations. Changes to the T_1-relaxation times of single NV centres in nanodiamond have been observed from only a few proximal gadolinium spin labels in a lipid bi-layer [81]. Diamond substrates are similarly useful in these applications as the biological sample of interest can be deposited on or brought close to the surface. Gadolinium labeled cell walls have been imaged by T_1-relaxation of a dense NV ensemble in this fashion, as for magnetic ions in a microfluidic channel [79]. Similar measurement of single NVs in diamond pillars

have been used to map ferritin in single cells scanned over the pillar [131]. The usefulness of relaxation based imaging can be extended to other target molecules by functionalising the diamond surface with molecules that host appropriate spin noise sources, that then responds to the target molecule which itself may not be a spin-noise source.

1.5 Summary

This chapter has introduced the NV centre in diamond and addressed its qualification as a quantum sensor. The distinct advantages of the NV centre over competing quantum sensors have been discussed, namely its good sensitivity to magnetic fields and its broad range of suitable sensing conditions, which allow a variety of systems to be interrogated in a minimally invasive fashion. The physics underlying the NV centre has been introduced, including the geometry of the defect, and the unique electronic energy level structure of the NV^- charge state that allows optical intialisation and readout of the electron spin state. The NV ground-state spin Hamiltonian, which ultimately dictates what the NV centre can be used to measure and with what sensitivity, was introduced in detail, highlighting the key terms that allow for magnetic, electric, strain, and temperature fields to be detected.

Having established the underlying physics of the system, many of the key measurement and control techniques of the system were introduced. These included ODMR, the most widely used technique in this thesis, which can be used to measure the NV ground-state spin resonance, and hence quantify local fields of interest. Coherent control of the NV spin state via Rabi cycling was introduced, which facilitates the preparation of superposition states that can be used to detect time-varying quantities via their effect on the NV spin coherence times. Measurement of the NV spin-population relaxation time, or T_1 time, was introduced as a technique to detect magnetic signals fluctuating in the range of NV ground-state spin-transitions frequencies. Finally, the chapter concluded with a survey of key achievements in NV sensing using these techniques, as applied to condensed matter and biological systems, two fields of keen interest to NV applications.

While this chapter has covered the governing principles of each measurement, the details of implementing these techniques in practice have not yet been addressed. The following chapter, now that the fundamentals of the system have been established, will

describe the construction and preparation of a widefield NV diamond imaging system. This implementation is common to all of the original research projects covered in the remainder of the thesis.

2

Experimental methods of widefield nitrogen-vacancy imaging

The NV centre in diamond is a robust and adaptable sensor that can be used to investigate a wide range of physical systems. As outlined in the previous chapter, this adaptability has given rise to a range of strategies implementing NV sensing and imaging. These include using large diamond substrates with either single or ensembles of NV centres to study systems intrinsic and extrinsic to the diamond host, dispersions of NV nanodiamonds to image within or around systems of interest, and using nanodiamond or fabricated diamond tips containing NV centres for scanning imaging measurements. Each of these approaches are advantageous in certain applications.

The aim of this thesis is to achieve imaging, primarily magnetic, of condensed matter systems over a wide field of view. To achieve this goal, single crystal diamond substrates with dense ensembles of NV centres are used, with the system of interest to be deposited or fabricated on the diamond surface. In this chapter, the process and motivation behind the fabrication of these NV diamond substrates and their subsequent imaging are elucidated. The question of sensitivity ultimately guides the design of NV-diamond samples, and therefore, this chapter begins with a derivation of the sensitivity of ODMR measurements, which are the basis of most imaging exhibited in the following chapters. The broad strategies used across the NV community to produce NV diamond sensors are reviewed, including approaches to diamond growth, nitrogen doping, NV formation via vacancy creation and annealing, and surface treatments. The methods specific to this thesis, which were developed by our research team throughout my candidature, are summarised in detail as related to the derived expression for ODMR sensitivity. Finally, we introduce the apparatus used to interrogate the fabricated NV diamond samples; the custom-built widefield diamond microscope. The optical set-up used to illuminate the NV ensemble with the excitation laser and collect subsequent photoluminescence in widefield configuration is reported, including the accompanying microwave circuitry and control scheme that allows the measurements introduced in section 1.3 to be implemented. These methods are common to all of the projects to follow. Exceptions to these methods are noted in subsequent chapters.

2.1 ODMR Sensitivity

The methods used to fabricate and measure an NV-diamond sample ultimately depend on the desired application. The goal of this thesis is to develop widefield magnetic imaging using NV ensembles and apply it to model systems such that the viability of the technique can be assessed and the methods refined. ODMR measurements of the NV-ensemble's spin resonance frequencies are the basis of this imaging technique, and hence, parameters influencing the sensitivity of such a measurement must be considered prior to fabricating NV-diamond imaging sensors. To identify these parameters, an expression for the measurement sensitivity must be derived.

The sensitivity of any measurement technique can be determined by deriving the minimum detectable signal yielded by a unity signal-to-noise ratio [3, 8, 24]. In ODMR, the desired signal is a measured change in the accumulated photoluminescence due to a dc shift in magnetic field, δB. This signal is given by $\frac{\partial I_{\mathrm{PL}}}{\partial B} \times \delta B \times \Delta t$, where I_{PL} is the photon count rate under the given measurement sequence, and Δt is the integration time. The change in photoluminescence count rate due to the shift in magnetic field, $\frac{\partial I_{\mathrm{PL}}}{\partial B}$, is related to the relative optical contrast and linewidth of the resonance, C and Δf respectively, and the reduced gyromagnetic ratio of the NV electron spin, $\gamma_e = 2.80\,\mathrm{MHz/G}$. For microwave frequencies maximally sensitive to a shift of the resonance, the change in count rate is well approximated as $\frac{\partial I_{\mathrm{PL}}}{\partial B} \approx \gamma_e C I_{\mathrm{PL}}/\Delta f$, assuming $C << 1$, as illustrated in figure 2.1, given the approximately Lorentzian resonance shape. The photoluminescence noise associated with the measurement is generally photon-shot-noise limited, and hence the noise is given by $\sqrt{I_{\mathrm{PL}} \times \Delta t}$. Taking a unity signal-to-noise ratio and an integration time $\Delta t = 1\,\mathrm{s}$ by convention, the minimum detectable dc magnetic field strength, i.e. the sensitivity, is given by

$$\eta_{dc} = \frac{\Delta f}{\gamma_e C \sqrt{I_{\mathrm{PL}}}}. \tag{2.1}$$

Equation 2.1 indicates that the sensitivity of the magnetic imaging based on ODMR measurements benefits from an enhancement of the optical contrast and count rate of the measured ensemble, and a narrowing of the resonance linewidth. As will be shown in the

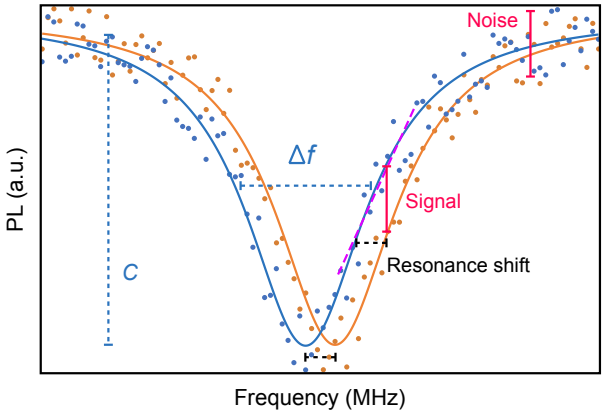

Figure 2.1: Illustration of ODMR sensitivity. Here we consider two mock-data sets (blue and orange points) that are offset from each other in frequency due to a small change in dc magnetic field, δB. An example Lorentzian fit to each line is included as a guide (blue and orange solid lines). The data sets are accumulated for a set integration time. The resonance shift is given by $\delta f = \gamma_e \delta B$. The corresponding change in photoluminescence at the most sensitive point in frequency is approximated by $\frac{C I_{\mathrm{PL}}}{\Delta f} \times \delta f$, where C and Δf are the relative contrast and linewidth of the resonance respectively, and I_{PL} is the maximum photoluminescence count rate. The noise level, which grows in time as $\sqrt{I_{\mathrm{PL}} \Delta t}$, is indicated by the scattering of points about the resonance baseline. The expression here is visualised in frequency, but this is easily converted to magnetic filed by scaling with the NV electron gyromagnetic ratio, γ_e.

following section, these parameters cannot be independently optimised, and so a balance must be struck between them. For example, the photon count rate can be increased by incorporating a higher density of nitrogen into the diamond, but this comes at the expense of broadening the resonance linewidth due to dipolar interactions between adjacent NV centres or NV centres and neighbouring nitrogen species/paramagnetic defects [24, 132]. The balancing of these effects is discussed in section 2.2.1.

In the limit of ODMR linewidths approaching the intrinsic ESR linewidth, $\Delta f \approx 1/T_2^*$, the sensitivity expression for ODMR resembles that of Ramsey interferometry [8]. In practice, the ODMR linewidths of the NV ensembles used in this thesis are not always at the T_2^* limit, however, ODMR is favoured over Ramsey measurements given its more simple implementation and the fact that many of our target signals are well above the sensitivity floor. ODMR also enables vector magnetometry to be performed by measuring multiple NV families in parallel, whereas Ramsey would require a series of measurements to achieve this vector capability. Ramsey sequences could be more streamlined by employing

a simple slope detection rather than integrating over the full free-induction decay, however this introduced the risk of mis-identifying fields that shift the slope detection by a whole period.

In practice, the minimum detectable signal often varies from the figure of merit derived above due to a range of experimental limitations. For example, in our magnetic imaging experiments, a floor of minimum detection is usually reached after a few hours of photoluminescence accumulation due to instabilities of the system including drifting of the stage, sample, and optics, which all alter the photoluminescence collection. The figure of merit is also not representative of the manner in which we extract resonance frequencies from a data set, where we fit a multi-peak-Lorentzian function to the data rather than looking at a change in accumulated photoluminescence at a single point (see section 2.4). In practice, the minimum detectable field strength for a given ODMR-based magnetic image will be determined empirically by the pixel-to-pixel noise. The sensitivity derived in equation 2.1, however, allows us to compare measurements across and within different physical systems, and identifies the key parameters to be considered in the design of a magnetic imaging suitable NV sample.

2.2 Fabrication of nitrogen-vacancy diamond samples for widefield imaging applications

Now that the parameters relevant to establishing good ODMR sensitivity have been identified, the process of fabricating viable magnetic imaging sensors based on NV-diamond substrates can be discussed. The fabrication of any NV-diamond substrate for magnetic imaging can be achieved by a variety of methods. Broadly, each of these multi-step processes must include a method of incorporating nitrogen into the diamond substrate, which may occur during synthesis of the diamond or after the fact by ion implantation. Depending on the method of nitrogen doping, an additional irradiation step may be required to create vacancies within the doped region at a density comparable to that of the nitrogen. Following this, an annealing step is required to improve the conversion of nitrogen dopant to NV centres by mobilising lattice vacancies at high temperature. This step has the added benefit of repairing lattice damage that may be detrimental to NV performance.

Finally, some form of cleaning or surface treatment may be included in preparation for imaging or further fabrication/deposition of target systems on the diamond surface.

All of these steps have implications for the sensitivity of ODMR based imaging and must be considered cautiously. This section begins by reviewing key approaches and findings of the wider NV research community regarding NV diamond fabrication. This includes the various strategies for nitrogen doping, post-doping irradiation, annealing, and surface treatments or cleaning. Following this insight, the methods used by our research team to produce diamond substrates with a high density of near-surface NV centres are detailed.

2.2.1 Nitrogen doping

Nitrogen is a naturally occurring dopant in diamond that forms a number of defects within the lattice. The NV centre in diamond is one such defect, however, there also exist substitutional nitrogen (often referred to as the P1 centre), dual-nitrogen defects, nitrogen interstitials, nitrogen-vacancy-hydrogen defects and nitrogen multi-vacancy complexes [133, 134]. Many of these are paramagnetic defects, owing to the fifth valence electron of the group-V donor, and are therefore detrimental to the coherence properties of NV^- centres at high densities and also undermine its charge stability [24,30]. The widefield imaging applications presented in this thesis, require a dense (more than $10^{11}\,cm^{-2}$ to give greater than 100 NV centres per optically resolvable area) near-surface ensemble (within 100 nm of the surface depending on the target signal) of NV centres, whose sensitivity is not compromised by doping related defects or proximity to the surface. The method of nitrogen incorporation is fundamental to satisfying these criteria.

Broadly, there are three methods by which nitrogen can be introduced into a diamond lattice. The first relies on the incorporation of nitrogen during diamond synthesis in a high-pressure high-temperature (HPHT) environment. Here, single crystal diamonds are grown on seed crystals at pressures from $5-6\,GPa$ and temperatures between $1300-1600\,°C$ with use of a metal catalyst [134]. The final nitrogen content can be controlled by the addition of nitrides to the growth medium [134]. The density of nitrogen achieved in this growth can range from several ppb to ppm, and increasingly, the

presence of undesired dopants and defects has been minimized [134, 135]. This method, however, gives little control over the distribution of nitrogen in the resulting crystal and therefore their use is limited to niche applications such as bulk magnetometry or single NV experiments when the incorporated nitrogen density is low [41, 42, 51, 136]. Control over the final NV sensing volume is achievable, however, when the technique is coupled with post synthesis irradiation as will be discussed in section 2.2.2.

The second method involves the introduction of nitrogen gas into a vapour mixture during diamond growth by chemical vapour deposition (CVD). This method uses a gas-phase carbon source, typically $\sim 1\%$ methane in a hydrogen plasma, to grow diamond on a substrate in a highly non-equilibrium process [134]. Adding a nitrogen vapour to the reactor mixture, typically N_2, incorporates nitrogen into the diamond with minimal damage to the lattice [134]. The slow growth rate of CVD, which can be as low as 0.1 nm/min, allows the density and depth distribution of the incorporated nitrogen to be controlled by selectively switching on/off the nitrogen vapour source during growth, achieving delta-doping specificity where only a few atomic layers of the lattice are subject to doping [137–139]. Nitrogen can be incorporated at densities larger than 100 ppm or excluded from the diamond altogether in well isolated systems [132]. Isotopically purified diamond can be grown by CVD using an enriched carbon source, which can benefit the coherence properties of NV centres by removing magnetic noise otherwise present due to the ^{13}C spin bath [7, 140–142]. The kinetics of diamond growth by CVD can be exploited to form preferentially aligned NV centres in the crystal by selecting an appropriate crystal growth plane and finely controlling the temperature, which can be advantageous in certain applications [143, 144]. One drawback of CVD growth is the limited nitrogen to NV conversion due to the incorporated hydrogen forming nitrogen-vacancy-hydrogen defects [133].

The final method is to incorporate nitrogen into the diamond crystal post-synthesis by implanting nitrogen ion species into the diamond substrate. This method allows the limits to nitrogen density incorporation by CVD to be aggressively overcome, at the expense of precise control over the depth distribution and preservation of the diamond lattice [45,145,146]. Here the mean depth of implanted nitrogen is determined by the implantation energy, but the distribution necessarily features some straggle due to the stochastic

nature of ion scattering [147, 148]. Ion implantation causes considerable damage to the target lattice, which is advantageous in that vacancies are created within the lattice by the same process by which the nitrogen is incorporated, but is otherwise detrimental to NV performance due to the paramagnetic defects that are created such as divacancies, vacancy chains, and dangling bonds [24]. Some of these defects and damage sites can be mended by annealing the crystal [24, 149]. Isotopically enriched ion sources of ^{15}N can be used to distinguish NV centres formed by the implanted nitrogen from those formed by naturally occurring ^{14}N by measuring their hyperfine structure in ODMR, should a distinction be necessary [45].

The ideal depth of an NV ensemble beneath the diamond surface is dependent on the target signal. For example, if the aim is to detect fluctuating magnetic fields from electron or nuclear spin-species external to the diamond, the ensemble depth is best kept to a few 10s of nanometers given the $1/r^3$ fall off of such dipolar magnetic fields. Ensembles too close to the diamond surface, however, suffer from charge instability as NV^0 becomes the dominant charge state due to the surface mediated band-bending [18, 26]. The insensitive NV^0 photoluminescence adds noise to photoluminescence signal of the remaining NV^-, which, despite being close to the surface, may result in a reduced sensitivity than if the ensemble was slightly deeper in the diamond. For the type of NV diamond samples used for widefield magnetic imaging in chapters 3 and 4 of this thesis, the dc and ac sensitivities do not vary greatly for nitrogen implant energies between 4 keV and 14 keV (mean depths of 10 nm and 30 nm respectively) as the ensemble is already dominated by noise within the implant layer, as shown in figure 2.2(a) [24]. NV^- centres whose coherence properties are not limited by noise originating from the doped region suffer from exposure to magnetic and electric noise associated with the surface at shallow depths [150–153]. If the target phenomena is a steady-state magnetic field associated with a ferromagnetic flake or transport current, greater NV depths are acceptable as these fields decay on the lateral length scale of the material or device, which can be up to microns [101]. Experiments probing phenomena intrinsic to the diamond, such as coupling to neighbouring nuclear spins [123, 154, 155], are best done in the diamond bulk far from the surface, with a low nitrogen density such that the coherence properties of the centre are protected from surface noise and have greater charge stability.

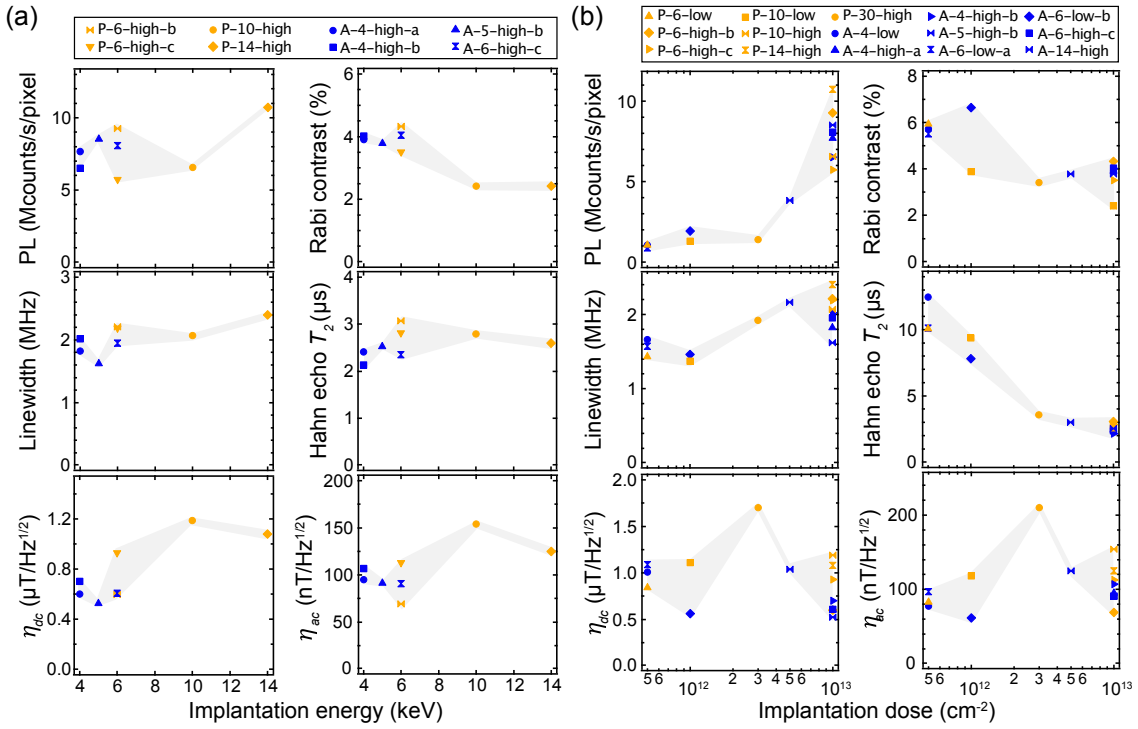

Figure 2.2: Magnetic-sensitivity parameters as a function of implantation energy and dose. (a) Coherence and optical properties of eight diamonds with dense near surface NV ensembles and their subsequent ac and dc magnetic sensitivities, η_{dc} and η_{ac} respectively, as a function of N^+ implantation energy. Optical properties include the photoluminescence count rate (PL), and optical contrast between spin-states as extracted from a Rabi measurement (Rabi contrast). These properties represented quantities I_{PL} and C in equation 2.1. The coherence properties include the ODMR linewidth, Δf in equation 2.1, and T_2 decay time as measured by a Hahn echo measurement. (b) The same properties and resulting sensitivities for fifteen diamond samples as a function of N^+ implantation dose. This figure is a reproduction of one published in Ref. [24]. The sample labels denote, in order, polished or as-grown surfaces (P or A), the implantation energy (in keV), and high or low-temperature annealing (950 °C or 1200 °C), with the lowercase letter distinguishing identically fabricated samples.

The density of incorporated nitrogen is similarly application dependent. For widefield ODMR, the sensitivity scales with the CW photon count rate of the ensemble (equation 2.1), and therefore, a higher nitrogen density should lead to an increased count rate following N to NV conversion, and hence lower sensitivity. However, there is a trade-off between NV density and the EPR linewidth due to dipolar interaction with NVs and neighbouring nitrogen-based paramagnetic defects. For the type of NV diamond samples used for widefield magnetic imaging in chapters 3 and 4 of this thesis, the overall sensitivity is largely independent of the nitrogen density with an implant dose between $0.5 \times 10^{12} - 1.0 \times 10^{13}\,\mathrm{cm}^{-1}$, as enhanced count rates are mitigated by the increased linewidths and reduced optical contrasts as shown in figure 2.2(b) [24]. The methods outlined above are equally applicable for single-NV experiments provided the density of incorporated nitrogen is such that on average there is only one NV centre per optically resolvable volume, $\Delta x \times \Delta y \times \Delta z \approx 300\,\mathrm{nm} \times 300\,\mathrm{nm} \times 1\,\mu\mathrm{m}$, where the lateral dimensions are diffraction limited and the z-dimension is the typical depth of a confocal microscope imaging plane. Single-NV experiments often use an istopically purified carbon environment to extend coherence times, as the noise in such samples is not dominated by large densities of nitrogen-related defects [7].

2.2.2 Converting N to NV: Vacancy creation and annealing

Successfully incorporating nitrogen into single crystal diamond is the first step to producing a viable NV-diamond sensing or imaging chip. Once nitrogen has been incorporated into the diamond lattice, the goal is to convert as much of the incorporated nitrogen into sensing-viable NV centres. This requires the formation of vacancies in the lattice if they are not produced in abundance by the nitrogen doping method, which must then be allowed to migrate towards substitutional nitrogen centres to form NV centres. Additional steps may be required to produce a greater quantity of NV^- as compared to insensitive NV^0.

Diamonds subjected to nitrogen incorporation by ion implantation typically do not require additional processing to increase the number of vacancies within the doped region [139]. Even the low-energy implantations of $^{15}\mathrm{N}^+$ between $1 - 10\,\mathrm{keV}$, which give mean

nitrogen depths between $2 - 20\,\text{nm}$, create 10 to 100 vacancies per implanted ion [156]. For diamonds doped with nitrogen during CVD or HPHT synthesis, post-doping vacancy creation is required to enhance the final NV centre density within the doped region. This is typically achieved by implantation of ion species such as ^{12}C or He^+ at energies of $10 - 100\,\text{keV}$ to create numerous vacancies per implanted ion [132, 157, 158]. These ion species are favoured given that, aside from the implantation damage, they do not form paramagnetic defects within the lattice. Heavy irradiation of nitrogen-doped samples fabricated by CVD can achieve NV densities of $10^{17}\,\text{cm}^{-3}$, close to the maximum achievable by irradiation of HPHT synthesized diamonds (approximately $10^{18}\,\text{cm}^{-3}$) [132, 159, 160]. Irradiation with electrons, protons, and even laser light can also increase conversion from N to NV by damaging the lattice and creating vacancies [138, 159–162].

Annealing is a near-universally employed technique to improve N to NV conversion and the resulting NV spin properties. As outlined previously, the purpose of high-temperature annealing post-nitrogen doping and vacancy creation is twofold: first, to mobilise vacancies such that they combine with substitutional nitrogen, thereby increasing the NV yield for a doping density; and second, to repair damage to the diamond lattice that may have been caused during doping and irradiation. Annealing under vacuum or in an inert gas environment around $800\,^\circ\text{C}$ is typically used to improve NV yield, given that vacancies within the lattice become mobile at $600\,^\circ\text{C}$ [162–164]. However, annealing at higher temperatures between $1000 - 1200\,^\circ\text{C}$ has been shown to improve NV coherence properties across a range of NV densities, which is attributed to annealing out additional paramagnetic defects such as divacancies and vacancy chains [24, 149, 164]. Recently, our research team showed that high-temperature annealing at temperatures $1100 - 1200\,^\circ\text{C}$ significantly improves the linewidth and spin properties of dense near-surface NV ensembles for this reason [24]. Additional steps can be taken during the annealing step to further increase the NV yield. For example, ensuring that the vacancy sites are charged upon annealing prevents the formation of vacancy chains and clusters, improving both NV yield and coherence times [22].

2.2.3 Cleaning up: Surface termination and processing

After producing a good yield of NV centres by some combination of doping, irradiation, and annealing, the last thing to consider, particularly for external sensing applications that rely on near-surface ensembles of NV centres, is the surface termination. As highlighted in section 1.2.1, the NV charge state is sensitive to the presence of acceptor states at the diamond surface which may compete with the NV^- for its sixth valence electron that makes sensing possible. The various fabrication procedures outlined in the previous sections have different implications for the diamond surface termination.

Samples grown by CVD emerge with hydrogen terminated surface owing to the hydrogen plasma present during growth [18,141]. This can be advantageous to electrical applications that rely on the conductivity of the two-dimensional electron gas formed near the surface of hydrogen-terminated diamond, however, it necessarily precludes the existence of near-surface NV^- for sensing applications due to the significant band bending near the surface [18,165]. Oxygen terminated surfaces are generally favoured by most NV applications due to the enhanced NV^- charge stability as compared to hydrogen-terminated surfaces. Oxygen terminated surface can be achieved by either soft-plasma treatments [18, 21] or an"oxygen annealing" or "oxygen burn" process in which the sample is heated to between 450 °C and 550 °C in an oxygen-rich environment [24]. This additional "oxygen burn" has been demonstrated to improve the NV^- charge stability at low densities (implantation doses $< 10^9\,\mathrm{cm}^{-2}$) [17, 23, 166, 167] and even improve coherence times [168] regardless of the initial surface termination. The common understanding is that this additional "oxygen burn" step removes sp^2 defects and other charge traps/paramagnetic defects at the diamond surface, and hence improves charge stability and coherence properties regardless of the initial termination. However, our research group has shown that no substantial improvement is observed following oxygen annealing in dense near-surface ensembles, and indeed, such a process introduces broadband magnetic noise [24]. This complex and defect-density-dependent interplay between surface terminations, defects, and near-surface NV centres necessitates a cautious approach to NV-diamond fabrication. Alternate plasma treatments can be used to further improve the charge stability of near-surface NV centres. For example, fluorine terminated diamonds, produced via CF_4 or SF_4 plasma treatment

in a microwave plasma reactor, has been observed to increase the stability of the NV^- charge state in near-surface NV ensembles and single NV centres [20, 141, 169].

Acid cleaning of the diamond surface may be necessary depending on the preceding fabrication. Acid treatments are commonly used to remove organic and graphitic compounds at the diamond surface that may arise from any of the doping or annealing steps preceding, and also to strip fabrication at the surface and reuse valuable NV diamond substrates. Common acid cleaning techniques include pirahna (sulphuric acid and hydrogen peroxide heated to $\sim 90\,^{\circ}\mathrm{C}$), triacid (boiling mixture of equal parts sulfuric, nitric and perchloric acids), and "Bristol boil" (boiling mixture of sulfuric acid and sodium nitrate) [18, 21, 24]. As will be shown in chapter 3, "Bristol boiling" the diamond successfully removes sparse metallic depositions from the diamond surface that may arise from handling of the diamond or previous fabrication and surface contamination [170].

2.2.4 Our approach to fabricating widefield imaging NV diamond chips

Having outlined the general trends used in the field to produce NV diamond for a broad range of applications, the methods employed to produce the samples used in this thesis can be summarised. These processes were developed by the collective work of our research team during and preceding my candidature, as guided by the literature of the broader NV research community. For explicit contributions on this topic, refer to the preface.

The diamond samples used in this thesis were produced by one of two methods. The first, Method A, implants nitrogen ions into an electronic-grade CVD substrate ([N] $< 1\,\mathrm{ppb}$) to form a near-surface NV ensemble. Note that some of the diamond used had an extra 1-μm-thick layer grown on top of the electronic-grade substrate before the implant. This extra layer was ^{12}C enriched which is useful for NMR applications but is not critical to the applications explored in this thesis. This overgrowth is responsible for the diamond pyramids or hillocks seen in figure 2.3(a). The low nitrogen content in the bulk diamond gives these substrates a clear and colourless quality. The electronic-grade CVD substrates were 50-μm-thick plates purchased from Diamond Delaware Knives (DDK), which are produced by polishing thicker plates sourced from Element Six. The substrates arrive as $4\,\mathrm{mm} \times 4\,\mathrm{mm}$ but are laser cut into $2\,\mathrm{mm} \times 2\,\mathrm{mm}$ plates for cost-effectiveness. The purified

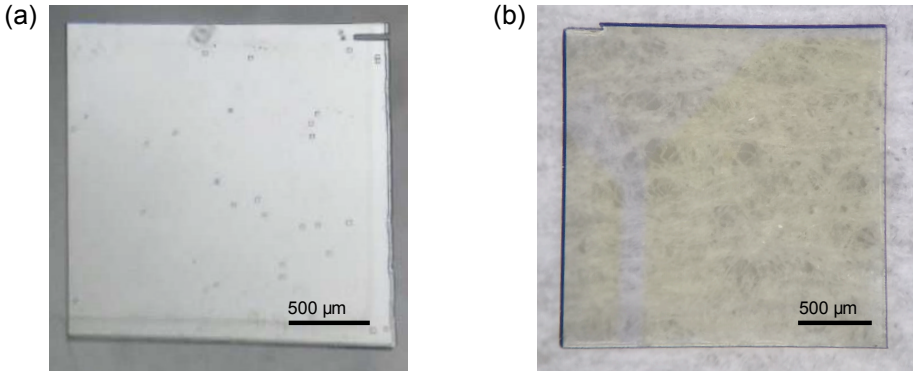

Figure 2.3: NV-diamond samples from two fabrication methods. (a) Diamond sample produced by Method A, an electronic-grade CVD diamond implanted with 6 keV N^+ at a fluence of $1 \times 10^{13}\text{cm}^{-2}$. The diamond is 2 mm $\times$2 mm $\times$30 μm. The sample surface is as-grown, showing visible growth pyramids at the surface up to 10 μm laterally. (b) NV diamond sample produced by Method B, an HPHT synthesized type Ib diamond ($[\text{N}] \sim 100$ ppm) implanted with 100 keV ^{12}C ions with a $1 \times 10^{12}\,\text{cm}^{-2}$ dose to create vacancies near the surface. Growth sectors boundaries are visible indicating different incorporation of nitrogen during growth between the highly doped regions (yellow) and the less doped regions (transparent). The diamond is 2.2 mm $\times$2.2 mm $\times$50 μm with a polished surface with roughness less than 5 nm Ra.

top layer was grown in a CVD reactor by T. Teraji (NIMS, Japan) with a ^{12}C purity of $99.95 - 99.998\%$ with minimal nitrogen content to ensure low defect concentration and consequent spin-noise spectrum [142]. Ion implantation was performed by INNOViON, implanting $2-6$ keV N^+ at a fluence of $1 \times 10^{13}\,\text{cm}^{-2}$, giving nitrogen density profiles with mean depths below 20 nm. NV diamond substrates produced by this method are used in the experiments presented in chapter 3 and 4. This method is summarised in figure 2.4(a).

The second method, Method B, uses an HPHT diamond substrate with a large native nitrogen concentration throughout the crystal and subsequent implantation of $^{12}C^-$ ions to form vacancies close to the diamond surface. The HPHT substrates used are 50-μm-thick type Ib single crystal diamonds ($[\text{N}] \sim 100$ ppm) with {100}-oriented faces, purchased from DDK. These samples appear yellow in colour due to the high nitrogen content, as shown in figure 2.3(b). Vacancies were created by irradiating the diamond substrates with $^{12}C^-$ ions accelerated at 100 keV with a dose of 10^{12} ions/cm^2. We performed full cascade Stopping and Range of Ions in Matter (SRIM) Monte Carlo simulations [1, 171] to estimate the depth distribution of the created vacancies, predicting a distribution spanning the range

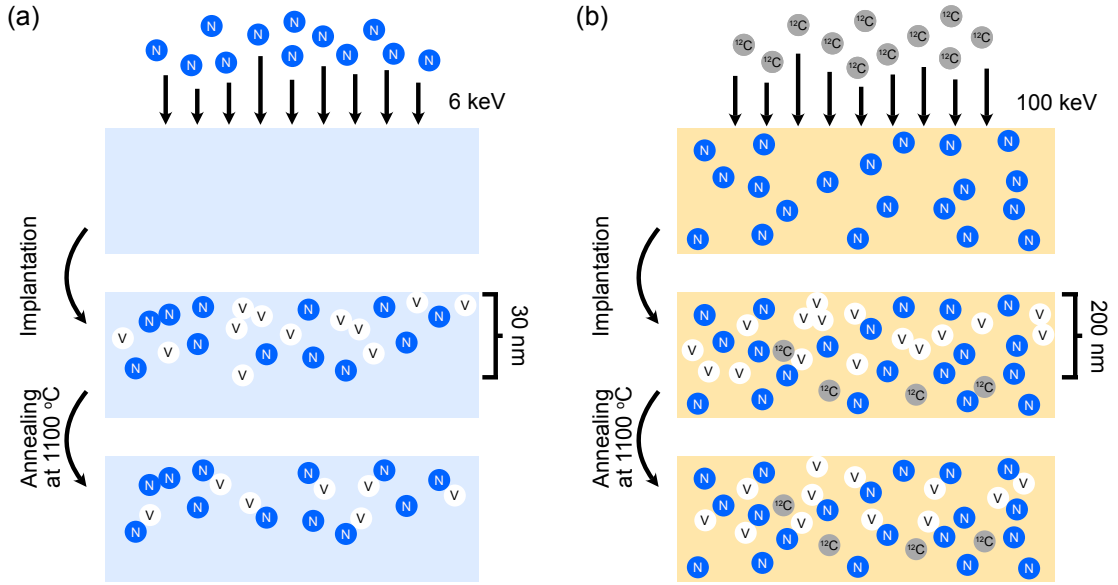

Figure 2.4: Schematic of two NV-diamond fabrication methods. (a) Method A implants $^{15}N^{+}$ species (blue) into an electronic-grade CVD diamond (pale blue). The energy of implantation determines the depth profile of the nitrogen dopant and subsequent vacancies (white) created. High-temperature annealing (1100 °C) is then used to mobilise the vacancies, allowing them to join with substitutional nitrogen forming NV centres, and anneal out paramagnetic defects, such as vacancy clusters resulting from the implantation. (b) Method B implants $^{12}C^{-}$ (grey) into a nitrogen-rich HPHT diamond substrate (yellow) to create vacancies near the surface. High-temperature annealing is used, as in Method A, to promote the formation of NV centres and anneal out damage arising from implantation.

0 - 200 nm with a peak vacancy density of 110 ppm at a depth of 130 nm, figure 2.5. The low yield of NV outside the implanted region and the high NV density within it following annealing ensures that the photoluminescence is dominated by NV centres within the implanted region, i.e. near the diamond surface. Following irradiation, the diamonds, which were received as 4.4 mm × 4.4 mm plates, were laser cut into four 2.2 mm × 2.2 mm samples for cost effectiveness. These samples are typically used for imaging static magnetic field arising from ferromagnetic samples or transport currents. Samples produced by this method are used extensively in chapter 5 to study low-temperature superconductivity in Nb, and also ferromagnetism in ultrathin materials in chapter 6. This method is illustrated in figure 2.4(b).

Regardless of the doping method used, all samples underwent similar high-temperature annealing process following implantation. The standard recipe used from this process oc-

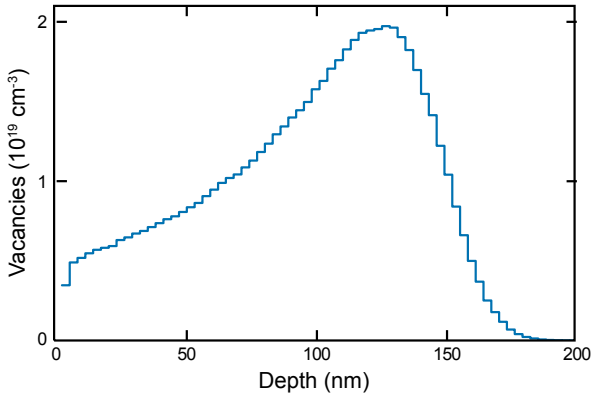

Figure 2.5: Stopping and Range of Ions in Matter (SRIM) simulations. Vacancy concentration as a function of depth for a 100 keV $^{12}C^{-}$ implant in diamond at a dose of 10^{12} ions/cm^2. We assumed a diamond density of 3.51 g cm^{-3} and a displacement energy of 50 eV. The peak vacancy concentration of $\sim 2 \times 10^{19}$ cm^{-3} corresponds to ~ 110 ppm.

curs under a vacuum of $\sim 10^{-5}$ Torr adhering to the following temperature ramp: 6 h at 400 °C, 6 h ramp to 800 °C, 6 h at 800 °C, 6 h ramp to 1100 °C, 2 h at 1100 °C, 2 h ramp to room temperature [24]. The samples were acid cleaned following annealing using the "Bristol boil" technique where the diamonds are added to a mixture of sulfuric acid (2 ml of $> 95\%$) and sodium nitrate (0.8 g) and brought to boil for $10 - 20$ min.

A combination of polished surfaces (produced by Method A or B as received without an overgrowth) and unpolished surfaces (Method A with a CVD overgrowth) were used depending on the application. For samples on which hundreds-of-micrometer scale devices were fabricated, such as the graphene field-effect transistors studied in chapter 4, polished diamond surfaces were used to avoid complications of fabricating around large diamond pyramid structures (> 100 nm in height) that can form during CVD growth [170]. For applications in which a target materials $1-10$ micrometers laterally could be deposited on the diamond surface, polished and unpolished surfaces were used given the often superior local flatness of as-grown CVD-diamond surfaces [170]. In the case of polished surfaces, polishing was done by DDK to a roughness of < 5 nm Ra [170].

2.3 Custom-built microscope for widefield imaging of NV ensembles

All of the measurements presented in this thesis were made using custom-built widefield microscopes. These systems, though relatively simple in design, require coordinated control of the illumination and photoluminescence collection of the NV diamond substrate, magnetic manipulation of the NV spin state via a microwave field, dc magnetic field to offset the NV spin state energy levels, and control/modulation of the device or system of interest at the diamond surface. In this section, the aspects common to all subsequent chapters are introduced, including the optics configuration, sample mounting, microwave circuitry, and dc magnetic field alignment. In chapter 5, which studies superconducting Nb within in a closed-cycle cryostat, the same basic elements presented here are used, but in a slightly different arrangement in order to interface with the cryostat. These details will be covered in that chapter.

2.3.1 Optics

The optical components of any NV diamond experiment must allow the initilisation and readout of the NV ensemble spin state via laser excitation and photoluminescence collection. For most applications, the laser excitation must be gated such that laser pulses of a controlled length can be used for spin-state pumping and readout to optimise sensitivity. In widefield imaging experiments, the excitation laser must provide sufficient laser power over a large field of view, at least tens of micrometres in diameter. The NV photoluminescence collected over the same area must be focused onto a camera for imaging. There are many approaches by which this can be achieved. Here, the methods used throughout this thesis are summarised. Descriptions of similar systems can be found in Refs. [2, 145, 146, 172].

Figure 2.6 shows the arrangement of optical components used to create a widefield microscope for NV-diamond imaging. This schematic is representative of all custom-built widefield microscopes used throughout this thesis. A 532 nm wavelength continuous wave solid-state laser (Laser Quantum Opus) is used to initilise and read out the NV spin state,

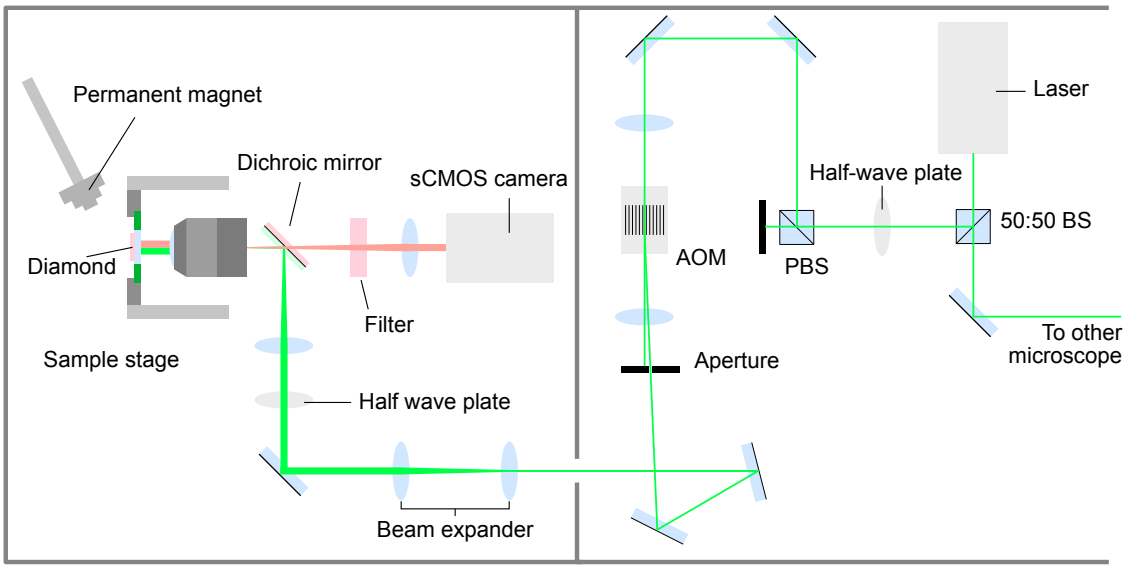

Figure 2.6: Optics schematic of our custom-built widefield NV diamond microscope. A 532 nm wavelength continuous-wave laser beam (green) is shared between two microscope systems by splitting with a 50 : 50 beam splitter. A half-wave plate and polarising beam splitter (PBS) are used to attenuate the laser power as required, but retain the power stability granted by operating the laser at high current. An acousto-optic modulator (AOM) is used to enact fast switching of the CW laser. A beam expander is used to tune beam waist and subsequent field-of-illumination from below 10 μm to more than 100 μm across. A half wave-plates rotates the linear polarisation of the laser to optimise pumping of target NV families are required. The beam is focused to the back of a microscope objective which provides widefield illumination of the sample. The subsequent NV photoluminescence (red) is collected through the objective, separated from the excitation laser by a dichroic mirror, and filtered before being focused onto an sCMOS camera for imaging. A permanent magnet is mounted above the sample stage to offset the NV spin resonance frequencies as desired. The system is housed in a laser-safe dark box (dark grey). See text for full description.

with an output power up to 2.0 W. These laser sources are typically shared between two widefield systems for cost effectiveness by splitting the laser output with a 50 : 50 beam splitter. A half-wave plate and polarising beam splitter (PBS) are used to attenuate the laser power used to image (typically hundreds of milliwatts) while retaining polarization of the laser and the power stability granted by higher operating laser power. The beam is focused into an acousto-optic modulator (AOM, AA Opto-Electronic MQ180-A0,25-VIS), after which an iris aperture is used to isolate the first-order diffraction maximum, allowing fast switching of the laser beam (extinction ratio of 10^{-3} with a 10 ns rise time). The beam is passed through a beam expander to tune beam waist, and hence the field of illumination, from $< 10\,\mu$m to $> 100\,\mu$m in diameter. A half-wave plate rotates the linear polarisation of the beam such that the pumping can be optimised for a given NV family, improving the optical spin state contrast [68], or balanced across the set of families to remove biasing in vector ODMR measurements [59, 170]. The expanded beam is focused into the back of an oil immersion microscope objective (Nikon CFI S Fluor 40×, NA = 1.30), which illuminates a large region of the diamond in parallel. The red NV photoluminescence emanating from the illuminated region is collected by the same microscope objective and separated from the excitation laser by a dichroic mirror. Stray light collected with the NV photoluminescence is filtered (wavelength $660-735$ nm) before the photoluminescence is focused with a tube lens ($f = 300$ mm) onto an sCMOS camera for imaging (Andor Neo, 5.5 megapixels). The entire system is assembled on an optical table and housed in a laser-safe dark box that separates the high power CW laser from the regularly accessed optics and sample stage, which only receive laser when the AOM is switched on.

The length of the applied laser pulse is determined in relation to the optical saturation of the NV centre. For a single NV centre illuminated by a 532 nm laser, optical saturation is achieved at an intensity of $10\,\text{mW}/\mu\text{m}^2$ [172]. For a single NV centre, that is, a diamond sample with no greater than one NV centre per optically resolvable volume, this requires a laser power of approximately 1 mW given the ~ 300 nm minimum laser spot size allowed by diffraction. Repumping of the NV spin state in this regime occurs within a few 100s of nanoseconds, as shown in figure 1.2(b). For our NV ensemble imaging, where the beam full-width-half-maximum is typically $60\,\mu$m, the laser power would need to be as large as 30 W to achieve optical saturation at the peak intensity. Given the obvious safety,

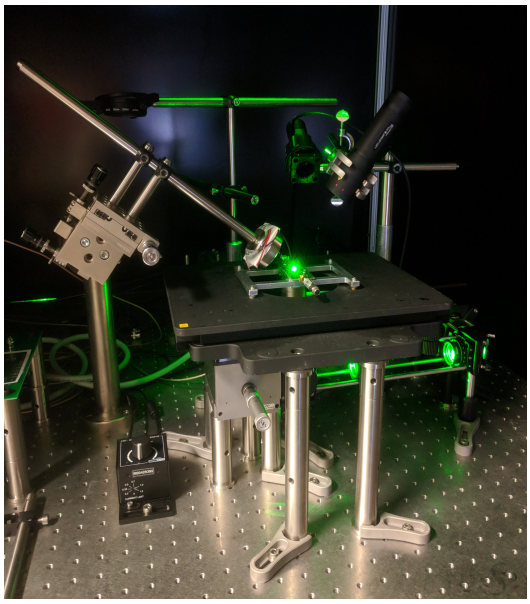

Figure 2.7: Widefield NV-diamond microscope. Photograph of the custom-built widefield microscope used for the work presented in chapters 3 and 4, housed within its laser-safe dark box. The diamond is mounted to a PCB which is secured to the sample stage. The permanent magnet stand is to the left of the sample stage. A torch is positioned above the sample stage to allow bright-field imaging.

financial, and practical challenges of using such a power, most widefield imaging applications operate well below saturation. For our systems we maintain 300 mW at the back of the microscope objective, giving a peak power intensity of 0.1 mW/μm^2, two orders of magnitude below saturation. Rumping at this laser intensity occurs on a timescale of 10s of microseconds. Peripheral regions within a 100 μm field of view remain under-pumped resulting in a reduced optical contrast and greater pixel-to-pixel noise than at the centre of the field of view.

A neodymium permanent magnet is mounted above the sample stage on a micrometer scanning stage allowing precise control over the dc magnetic field at the position of the sample. The magnetic field can be aligned with one family of NV centres within the imaging ensemble, tuning the $m_s = 0$ to $m_s = -1$ resonance frequency from close to zero field, 2.87 GHz, down to the GSLAC, ≈ 0 MHz, and upwards of 3 GHz which corresponds to a maximum field strength > 0.2 T. The magnet is shown mounted in this configuration for a moderate field strength at the sample (≈ 500 G) in figure 2.7. For vector ODMR

measurements, in which the spin resonances of all four NV families are measured, the magnet is mounted to auxiliary posts calibrated to separate the spin resonances by roughly equal frequency intervals to minimize fitting artefacts from overlapping resonances [1].

2.3.2 Microwave control and sample mounting

As outlined in section 1.3, the majority of NV sensing techniques require application of a pulsed resonant microwave field to manipulate NV spin states in conjunction with the pulsed laser which is used to initialise and read out the spin states. The typical dc magnetic field strengths applied for our widefield vector imaging require microwave frequencies between 2 GHz and 3 GHz, however, as outlined previously, some applications may require driving of NV spin resonances down to a few MHz, or above 3 GHz [51,52,173]. The microwave infrastructure must not only span this broad frequency range, but it must apply a microwave field of sufficient amplitude to give Rabi frequencies greater than the coherence decay rates of the NV ensemble. For our dense near-surface NV ensembles, this translates to Rabi frequencies on the order of MHz, which requires microwave magnetic field amplitude of 0.5 G at the NV. The microwave field must be fast-switching on this time scale to give fine control over the NV state vector rotations. And finally, for widefield imaging applications, we require that the applied microwave field is approximately uniform over our field of view to avoid imaging artefacts associated with non-uniform spin-state driving [1].

To satisfy the requirements outlined, our group utilises a microwave vector signal generator (Rohde & Schwarz SMBV100A) gated using the built-in IQ modulation (< 5 ns switching time), with output frequency range of 9 kHz to 3.2 GHz and power range of -145 dBm to $+18$ dBm. The output microwave signal is amplified by a 60 W amplifier (Amplifier Research 60S1G4A) which is fed to a custom-made printed circuit board (PCB) to which the diamond sample is mounted. Microwaves are delivered to the diamond by way of a custom-made glass coverslip upon which a microwave resonator is fabricated by photolithography. The resonators were a combination of Cr/Au ($\sim 10\,\text{nm}/1\,\mu\text{m}$) to promote adhesion to the glass and give sufficient conductivity to meet the required current densities. Resonators of various lateral sizes were used through this thesis, but most commonly a

1000 μm diameter resonator was used as it offers microwave field strengths sufficient for MHz scale Rabi oscillations with great uniformity at the centre of the resonator (a few percent over a 100 μm field of view). The resonator coverslips are glued to the PCBs and the resonators soldered to the PCB microwave striplines. The PBC circuit was terminated with a 50 Ω terminator.

Diamonds were mounted to the resonator coverslips by one of two methods. In the first method, diamonds were mounted in a small drop of low fluorescence immersion oil (Olympus), which gave adequate stability for measuring a single field of view for long period of acquisition (> 3 hours), but allowed the diamond to be translated relative to the microwave resonator should regions of interest be obscured by the resonator or suffer from microwave inhomogeneity or under-driving. In the second method, diamonds were secured to coverslips with a UV cured optical adhesive (Thorlabs). This was typically used for samples with electrical devices fabricated at their surface which required electrical contact by wire bonding (see chapters 4 and 5), and hence have a fixed region of interest from the outset. Pictures of two diamond samples mounted to resonator boards in these fashions are shown in figure 2.8(a) and (b). The interface of the PCB and the resonator coverslip is shown in figure 2.8(c).

2.3.3 Sequence control

The successful application of all of this infrastructure is contingent on the coordinated control of each element, such that orchestrated laser and microwave pulses can intialise, manipulate, and readout the NV spin state synchronous to the photoluminescence collection by the sCMOS camera. This coordination is enacted by a high speed programmable pulse generator (SpinCore PulseBlasterESR-PRO 500 MHz) dictated by a custom-made LabVIEW program. TTL pulses are sent from the PulseBlaster to the AOM, microwave signal generator, and sCMOS camera to coordinate the switching on/off of the laser, gating of the microwave field and setting of the microwave frequency/power, and the exposure of the sCMOS imaging chip.

Confocal microscopy experiments typically time-tag photon collection from a fast-acting photodiode, allowing photoluminescence to be integrated over only the relevant part

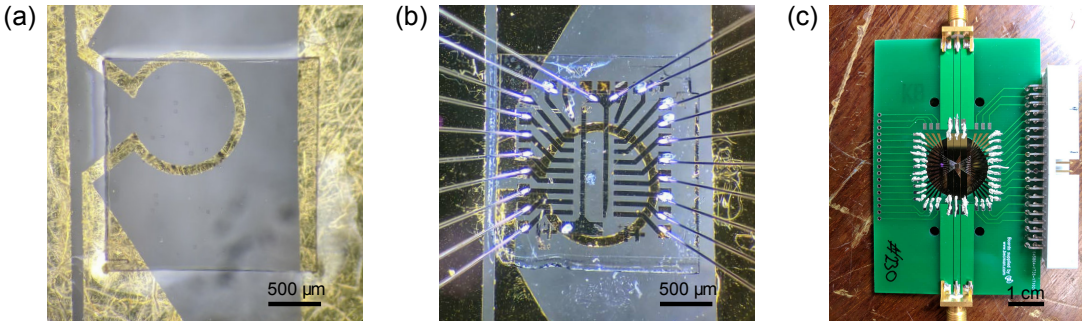

Figure 2.8: NV-diamond sample mounting. (a) CVD diamond substrate used in chapter 3 mounted on a microwave resonator coverslip in a small pillow of immersion oil (light sheen surrounding the diamond). The oil mount allows the diamond to be easily translated relative to the resonator. (b) CVD diamond with graphene field-effect transistors fabricated on its surface, mounted to the resonator coverslip by a UV cured glue. The mount is cured such that the region of interest lies within the resonator, and allows electrical contact to be made to the fabricated devices via Al wires. (c) Zoom out of the same sample shown in (b), showing the cover slip, which is glued to the PCB used to deliver microwaves to the coverslip, and secure the entire sample to the sample stage shown in figure 2.7. The resonator is soldered to the PCB, as are the source, drain, and gate contacts of the devices which can be interfaced with via the IDC connector (grey, right). Microwaves are delivered to the PCB via the SMA connectors (top and bottom), one of which is terminated with a 50 Ω terminator upon mounting to the sample stage.

of the measurement sequence improving the signal-to-noise ratio [174]. The photoluminescence acquisition by an sCMOS camera for widefield imaging, however, is limited by the camera's exposure times which is upwards of miliseconds depending of the precise acquisition parameters. This necessitates the repetition of a sequence under set conditions during a given camera exposure. For example, in an ODMR measurement, a single iteration of the ODMR pulse sequence may take 10 μs (dominated by the $\sim$ 10 μs laser readout/repumping pulse as compared to the $\sim$ 300 ns microwave pulse, delay times $\sim$ 1 μs), and hence, the sequence will be repeated 2000 times over a 20 ms camera exposure, before the microwave frequency is changed and the acquisition started over a new exposure. In principle, spin state photoluminescence contrast measured by widefield imaging could be improved by a factor $\sim$ 2 with specialised camera technologies, but these have other limitations [175].

2.4 Data Analysis: Fitting spectra

All data analysis presented in this thesis was performed using a custom-made MATLAB code. This code was written primarily by Dr. Jean-Philippe Tetienne, with additional input from Dr. David Broadway, myself, and other members of our research team. The broad purpose of the code was to restructure the photoluminescence data as received from the sCMOS camera via the LabVIEW program, reshaping it into a three-dimensional array where two dimensions correspond to the pixel array of the camera and the third dimension to the data of the measured sequence, e.g. photoluminescence counts for each frequency point in ODMR or evolution time in T_1 relaxometry. Fitting of the data was then implemented on a pixel-by-pixel basis, allowing images to be made from the fit parameters.

Prior to fitting, the photoluminescence data was rebinned as required to expedite fitting or improve the signal-to-noise ratio at the expense of spatial resolution in the case of short acquisitions. Each pixel of the 5.5 megapixel sCMOS camera corresponds spatially to $(108\,\mathrm{nm})^2$ of the imaged object, given the 60× magnification of the optical system (40× Nikon objective associated with a 300 mm imaging lens instead of the conventional 200 mm tube lens) and $(6.5\,\mu\mathrm{m})^2$ pixel area. The data can therefore undergo a 2×2 pixel rebinning without degrading the optical resolution ($\sim 300\,\mathrm{nm}$ laterally), or a 4×4 rebinning with a slight decrease in resolution. Prior to fitting at the individual pixel level, the data was binned over the entire field of view and fit based on input parameter guesses allowed to vary over a chosen range. The parameters fit to the full field-of-view spectrum were then used as input guesses to the pixel-by-pixel fitting, given the relatively small variation of most parameters across the field of view.

The fitting itself was achieved by a least squares method, minimising an error function of the difference between the photoluminescence data and fit function across the data set by varying fit parameters of the model. Our vector ODMR measurements, for example, would be fit by a sum of eight Lorentzians,

$$F(\mathrm{PL}_{\max}, f, f_i, \Delta f_i, C_i) = \mathrm{PL}_{\max}\left(1 - \sum_{i=1}^{8} \frac{C_i}{1 + ((f - f_i)/\Delta f_i)^2}\right), \tag{2.2}$$

where f_i, Δf_i, and C_i correspond to the frequency, linewidth, and fractional photoluminescence contrast of the ith resonance, and f is the scanned frequency variable. The fit function takes into account the maximum photoluminescence, $\mathrm{PL}_{\max}$, across the the spectrum, which corresponds to the off-resonance photoluminescence. A root mean square error function was used,

$$\varepsilon(\mathrm{PL}_{\max}, f_i, \Delta f_i, C_i) = \sqrt{\sum_{f_{\min}}^{f_{\max}} (F(\mathrm{PL}_{\max}, f, f_i, \Delta f_i, C_i) - \mathrm{PL}(f))^2}, \tag{2.3}$$

where $\mathrm{PL}(f)$ represents the photoluminescence data set as a function of sequenced microwave frequencies ($f_{\min} \leq f \leq f_{\max}$) for a given binned region. This same process was used to fit the data of alternate measurement sequences with an appropriate fit function, such as single or stretched exponential for T_1 and T_2 measurements, with fit parameters corresponding to the decay rate, decay contrast, and maximum photoluminescence as we will see in chapter 3 [170].

Fitting vector ODMR data using the outlined routine gives twenty-five parameters that can be used to form images of the field of view. To turn these fit parameters into a more relevant quantitative image, such a dc magnetic or electric field, we use the eight resonance frequency parameters and relate them to the NV spin Hamiltonian. For example, to calculate a dc magnetic field in Cartesian coordinates, $\mathbf{B} = (B_x, B_y, B_z)$, we first require knowledge of the NV-axis vector orientations relative to the field of view. This is typically determined from a reference measurement of a known magnetic field orientation such as the Ørsted field from a current carrying wire [60], and knowledge of the crystallographic orientations of the diamond faces. The NV-diamond sample used to study superconductivity in chapter 5, for example, has NV axes with unit vectors $\mathbf{u}_{\mathrm{NV}} = (\pm 1, \pm 1, 1)/\sqrt{3}$ in the laboratory frame (x, y, z). The total magnetic field, $\mathbf{B}_{\mathrm{tot}}$, is then inferred by minimising the root-mean-square error function,

$$\varepsilon(D, \mathbf{B}_{\mathrm{tot}}) = \sqrt{\frac{1}{8} \sum_{i=1}^{8} \left[f_i - f_i^{\mathrm{calc}}(D, \mathbf{B}_{\mathrm{tot}}) \right]^2}, \tag{2.4}$$

where $\{f_i^{\mathrm{calc}}(D, \mathbf{B}_{\mathrm{tot}})\}_{i=1\ldots8}$ are the calculated resonance frequencies obtained by numer-

ically computing the eigenvalues of the NV spin Hamiltonian for each NV orientation. Equation 1.1 is the complete ground-state NV spin Hamiltonian, however, in practice we take a simplified version, keeping only the terms relevant to the study at hand. For example, we ignore the Stark terms for electric field and strain in most of our magnetic imaging applications, and use the simplified Hamiltonian,

$$\mathcal{H}/h \;\; = DS_Z^2 + \gamma_{\mathrm{NV}} \mathbf{S} \cdot \mathbf{B}_{\mathrm{tot}} \;, \tag{2.5}$$

where $\mathbf{S} = (S_X, S_Y, S_Z)$ are the spin-1 operators, D is the temperature-dependent zero-field splitting, $\gamma_{\mathrm{NV}} = 28.035(3)\,\mathrm{GHz/T}$ is the isotropic gyromagnetic ratio, and XYZ is the reference frame specific to each NV orientation, Z being the symmetry axis of the defect [15,33] with unit vector $\mathbf{u}_{\mathrm{NV}}$ defined previously. The resulting total magnetic field contains both the applied bias field and the field from the sample of interest, $\mathbf{B}_{\mathrm{tot}} = \mathbf{B} + \mathbf{B}_{\mathrm{bias}}$. The bias field can then be subtracted if it is precisely known, as in chapters 5 and 6 where we apply a highly uniform field with a superconducting vector magnet, or removed via a plane subtraction, as in chapter 3 where the bias field from our permanent magnetic gives a slight gradient across the field of view. Note that the conversion from frequency to magnetic field is overdetermined given that projections along just three NV axes are required to span the three-dimensional vector space. The magnetic field can be reconstructed more approximately from the frequency difference between a given resonance pair, which gives the field projection along the corresponding NV axis, $B_{\mathrm{NV}} = (f_+ - f_-)/\gamma_{\mathrm{NV}}$. We can therefore use just three such projections to determine the vector magnetic field. In some cases the projection along a single axis suffices, such as in chapter 6 where the out-of-plane magnetisation M_z of a magnetic sample is determined from a single B_{NV} projection, foregoing the more involved Hamiltonian reconstruction.

The contrast and linewidth parameters, though not as commonly used for imaging, can provide insight into various inhomogeneities and non-magnetic processes within the measurement volume. For example, an NV ensemble in close proximity to a ferromagnetic material places a large dc magnetic field gradient across the ensemble giving a distribution of resonance frequencies on the order of the linewidth of a single NV. This effect results in a broadening of the resonance and a reduction of the maximum optical contrast [176].

Strong dc fields from such sources can remove the resonance of the nearest NVs from the measurement altogether, by shifting them beyond the parameter range or acquisition window, further reducing the optical contrast of the measured volume [176]. We will see examples of this in chapter 3 [170]. Reductions in contrast are also linked to changes to the NV charge stability and can be difficult to interpret without taking complementary measurements [30, 31]. Resonance linewidth and contrast are also affected by the local microwave power, which may be varied by the presence of the sample of interest as is the case of superconducting Nb in chapter 5 [1]. Typically variation in contrast and linewidth are similar across NV families and hence are plotted for a single representative resonance. However, caution should be applied when omitting fit parameters from NV family with the smallest axial magnetic field projection, as deviation from the other families may be due to an enhanced electric field sensitivity depending on the regime [10, 18].

Fitting artefacts are minimised by a number of good practices. Firstly, ensuring that a dc field of sufficient strength is applied to separate the NV spin resonances avoids complications arising from overlapped resonances [59, 170]. This is not always possible in the case where the measured phenomenon is contingent on low dc fields, as is the case from Arikosov vortices measured in superconducting Nb in chapter 5. In this case, magnetic field reconstruction is hampered by complex resonance lineshape close to zero-field [1, 177]. Similarly, driving the NV with a Rabi frequency upwards of 2 MHz during the ODMR π-pulse can broaden the resonance sufficiently to ignore the hyperfine structure, if it is not already obscured by a broad intrinsic linewidth. It is possible to fit the hyperfine structure with an augmented Lorentzian lineshape, but in our experience this limits the robustness of fitting. Finally, over-sampling critical regions of the spectrum (e.g. the resonance trough in ODMR, or short time-scale decay in T_1) rather than linearly spaced sampling can also improve the fitting robustness and expedite data acquisition.

2.5 Summary

This chapter, building on the fundamentals introduced in chapter 1, has discussed many of the practical concerns relating to the implementation of widefield NV imaging. The many materials challenges surrounding the formation of NV centers within a diamond

substrate for external sensing applications were discussed, before detailing the specific methods adopted throughout this thesis to address these challenges. After establishing this viable strategy for fabricating dense, near-surface NV ensembles, the infrastructure required to implement standard NV imaging experiments was surveyed, including optical, microwave, and magnetic field control. Finally, the data analysis strategy used to produce images and spectra throughout the thesis was summarised with a specific focus on ODMR measurements due to their prevalence in the coming chapters.

Have established both the physics underlying the NV centres in diamond and the implementation of widefield NV imaging experiments, we can now turn to the original research presented in this thesis. Chapter 3 demonstrates the capabilities of widefield NV imaging as they are applied to investigate a relatively simple system: thin metallic depositions on the diamond surface. This chapter exhibits the various types of images that can be extracted from widefield NV measurements, such as ODMR and T_1 relaxometry, and demonstrates their use in investigating an unanticipated effect of such depositions. Following this, chapters 4 and 5 apply these same techniques to more sophisticated systems, namely graphene field-effect transistors and superconducting Nb wires to further test the use of NV imaging to condensed matter systems and devices.

3

Magnetic noise from ultrathin abrasively deposited materials on diamond

The previous two chapters introduced a range of sensing techniques using NV centres in diamond and discussed their practical implementation for widefield imaging of systems extrinsic to the diamond host. Having established this foundation, we can now move to original research covered by this thesis. This chapter reports on the study of thin metallic depositions on the diamond surface as imaged by a near-surface NV ensemble. This project emerged from a collaboration with Dr. Torben Daeneke and Dr. Ali Zavabeti (RMIT University) in which we were touch printing atomically-thin metal oxides onto the surface of our NV-diamond substrates for magnetic characterisation [178,179]. While imaging the samples post-printing, we discovered ferromagnetic features in ODMR that were spatially correlated with extensive bands at which the NV spin-relaxation times were significantly reduced as measured by T_1 relaxometry. We determined that these features were due not to the touch-printed oxides as first thought, but to scratches left on the diamond surface by steel tweezers during cleaning and preparation of the diamond substrate.

This occurrence demonstrates the need for caution in applying NV imaging to two-dimensional and ultrathin samples. As the volume of target system is reduced, in this case approaching a monolayer, the presence of contaminants, even in trace quantities, may contribute a signal comparable in magnitude to that of the target material. Driven to better understand the role played by common contaminants in these NV imaging applications, we devised a set of experiments to study the effects of trace contamination at the diamond surface. The materials chosen for this study include inox steel, diamond, silicon, copper, gold, chromium, copper-beyllium alloy, and glass. These materials were chosen for their prevalence in our NV imaging experiments. For example, our diamonds are handled with steel tweezers throughout any cleaning and may be mounted to large silicon wafers to ease handling during extended fabrication. As shown in the previous chapter, our diamonds are mounted on glass cover-slips with chrome-gold microwave resonators throughout imaging. The graphene studied at length in the following chapter was commercially grown on a copper foil, which had to be etched away before transferring the graphene to a diamond surface. Finally, non-ferromagnetic copper-beryllium tools are used in favour of steel implements when working in proximity to the permanent magnets present near the microscope sample stage. The threat of contamination from all of these sources is possible in the routine handling and preparation of diamond samples for

imaging. These materials were deposited in a manner mimicking the case that inspired the study, by simply scratching a macroscopic block of the material across the diamond surface.

In the case of metallic depositions (inox steel, copper, chromium, gold, copper-beryllium), we observed the formation of ultrathin collections of nanoparticles, down to sub-nanometre thicknesses as measured by atomic force microscopy. These structures were spatially correlated with regions of significantly reduced T_1-relaxation times in the NV ensemble, by up to an order of magnitude as compared to regions under the pristine diamond surface. The precise cause of this reduction in the NV T_1 time is subject to speculation, the most likely cause being that it originates from spin or charge noise within the deposited material, that is, magnetic noise originating from fluctuating electron-spin species or the motion of free charge carriers respectively. Indirect effects are also possible such as the material affecting charge stability and magnetic environment of the sensing layer. The reduced T_1 times associated with the deposited material, regardless of their microscopic origin, demonstrate the need for caution to avoid contamination in any NV imaging application. This is particularly pertinent to studies of two-dimensional materials as these small metallic inclusions, despite being minuscule enough to be difficult to detect by independent characterisation, contribute a significant signal at the NV layer. This work therefore illustrates the excellent sensitivity of NV noise spectroscopy to ultrathin materials down to sub-nanometre regimes - a key step towards the study of two-dimensional electronic systems - and highlights the need to passivate the diamond surface for future sensing applications in ultrathin and two-dimensional materials. Additionally, for the purposes of this thesis, this chapter demonstrates the utility of multi-modal widefield NV imaging to interrogate an unknown sample at the diamond surface. This study was published under the title “Magnetic noise from ultrathin abrasively deposited materials on diamond” in *Physical Review Materials*, 2, 116002, 2018, Ref. [170].

3.1 Motivation

The application of NV sensing and imaging to condensed matter systems, especially ultrathin and two-dimensional materials, is a natural pursuit given the NV centre’s good

sensitivity to magnetic fields and short length scale interactions. NV imaging offers an advantage over bulk characterisation methods as the small volume of two-dimensional materials does not considerably reduce the target signal given the sharp fall off of the NV centre's magnetic dipole moment over nanometre length scales, the typical thickness of such systems. The motivation to image these systems is driven by the additional information provided by imaging that is inaccessible to electrical measurements or bulk characterisation. Ultrathin and two-dimensional materials are particularly appealing target materials given the unique consequences of low dimensionality for the electronic, magnetic, and transport properties of the material [99, 100, 180, 181].

The review presented in section 1.4.1 surveyed several applications of NV imaging to two-dimensional materials [14, 64, 65, 111, 114, 117]. At the commencement of this project, however, there were only a few such published applications, including NMR spectroscopy of hexagonal boron-nitride (h-BN) as measured by single NV centres, and widefield imaging of current densities in mono-layer graphene using dense near-surface ensembles [65, 117]. Theoretical proposals to use the NV as a noise probe to discriminate between different transport regimes and identify impurities within two-dimensional materials were also present, with similar applications proposed for one-dimensional systems [182, 183].

Despite the appeal of applying NV imaging techniques to two-dimensional and ultrathin materials, there exists several challenges to its practical implementation, particularly in the case that material is deposited directly on the diamond surface. For one, the properties of materials with such a large surface-area-to-volume ratio can be strongly altered by the interaction with the substrate, and hence, the relevance of any insight gained by NV measurements to the material in other settings can be called into question [184, 185]. Furthermore, as has been discussed at length in sections 1.3.1 and 2.2.3, near-surface NV centres are particularly sensitive to changes at the diamond surface, and so, the deposition of a target material may alter NV properties indirectly, giving rise to a signal that is not intrinsic to the material of interest. And finally, there exists a range of possible contaminants present in the standard preparation techniques used for NV quantum sensing, the effects of which have not been well described, particularly in the context of two-dimensional materials.

In this work, we take a straightforward approach to widefield NV imaging of systems

extrinsic to the diamond by using a dense near-surface NV ensemble that is maximally sensitive to the sample of interest, which is deposited directly on the diamond surface, figure 3.1(a). With this study, we investigate the extent to which NV imaging can discriminate between signals contributed by the sample of interest from those arising indirectly from changes to the diamond surface and sensing layer induced by the sample or transfer process or from contamination. To do this, we utilise a soft abrasion technique to deliberately deposit trace amounts of material onto diamond substrates, and characterise the resulting magnetic signals by measuring the near-surface NV layers. Initially, results are presented for the abrasive deposition of inox steel, which is shown to leave ferromagnetic nanoparticles on the diamond down to 20 nm in size, the magnetic fields of which are imaged by ODMR. Additionally, a thin coverage of the material, down to sub-nanometre thicknesses, is measured in the scratched regions, and found to be the source of broadband magnetic noise that quenches the NV-layer spin-lattice relaxation time, or T_1 time. Similar results are found from the deposition of other metallic materials, namely copper, chromium, and gold, whereas insulating materials, such as silicon, produce no such effect.

3.2 Materials and Methods

The NV measurements in these experiments were performed in ambient conditions using a home-built widefield microscope as described in section 2.3. The diamonds used were fabricated by method A outlined in section 2.2.4. Specifically, they are ⟨100⟩ oriented single crystal diamonds with surfaces as-grown by chemical vapour deposition [142], implanted with nitrogen ions at 4 keV and 6 keV, giving NV centres at mean depths of about 10 nm and 15 nm respectively [24]. In this configuration, the NV layer is sensitive to ferromagnetic materials at the diamond surface but also magnetic noise associated with those materials due to their close proximity. As always, the NV layer is sensitive to noise originating from defect states within the layer, such as substitutional nitrogen or vacancy complexes, however, the population and dynamics of these defect states may be altered by the presence of the sample, contamination, or other changes to the diamond surface [24]. These scenarios are illustrated in figure 3.1(b), where the interplay of material at the diamond surface with states in the NV layer can have a range of effects on the near-surface

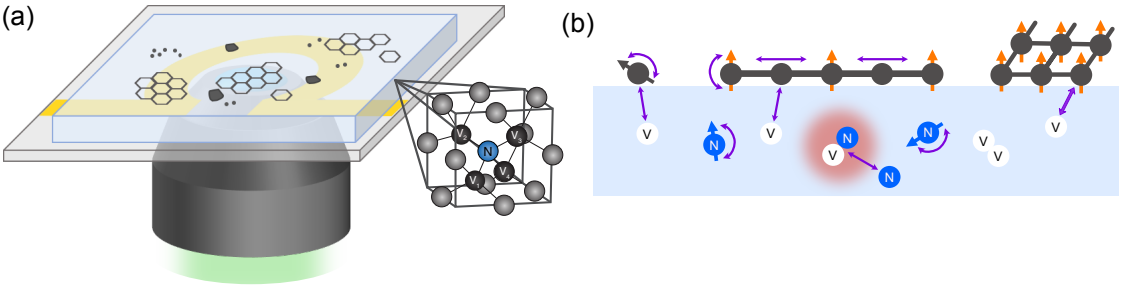

Figure 3.1: Near-surface NV imaging of ultrathin materials. (a) Schematic of a simple approach to widefield NV imaging of ultrathin and two-dimensional materials. The material of interest (honeycomb) is deposited directly on the surface of the diamond (pale blue) which contains a dense layer of near surface NV centres (unit cell). Contamination may be present at the diamond surface due to the preparation of the diamond substrate or transfer of the ultrathin material (grey particles). The diamond is mounted to a glass coverslip featuring a gold/chrome microwave resonator. (b) Illustration of potential interactions in near-surface NV imaging of nanoscale materials. Ferromagnetism may be detected in two-dimensional materials or nanoparticles (orange spins) via an ODMR measurement. Magnetic noise originating from spin fluctuations or charge motion in any deposited material can be detected via a T_1-relaxation measurement (purple arrows). Magnetic noise also arises from fluctuations of spin defects within the NV layer, such as substitutional nitrogen or charged vacancy complexes, the population and dynamics of which may be affected by the deposited material.

NV centres.

Prior to the soft abrasion of the target material, background measurements were taken of a chosen region of the diamond. For these as-grown diamond surfaces, growth pyramids served as convenient markers of the charaterised region, ensuring accurate comparison before and after the deposition (see appendix A.1.1). Photoluminescence and bright field images were taken under continuous-wave illumination by the 532 nm excitation laser and illumination by a light-emitting diode (LED) lamp positioned above the sample respectively. The background photoluminescence and bright field images for the region later scratched with inox steel tweezers are shown in figures 3.2(a) and (b). The images are relatively featureless, suggesting a pristine surface. Airy disks observed in the field of view are associated with dust on optical components far from the sample. Background ODMR and T_1 measurements were similarly featureless across the field of view (see appendix A.1.1).

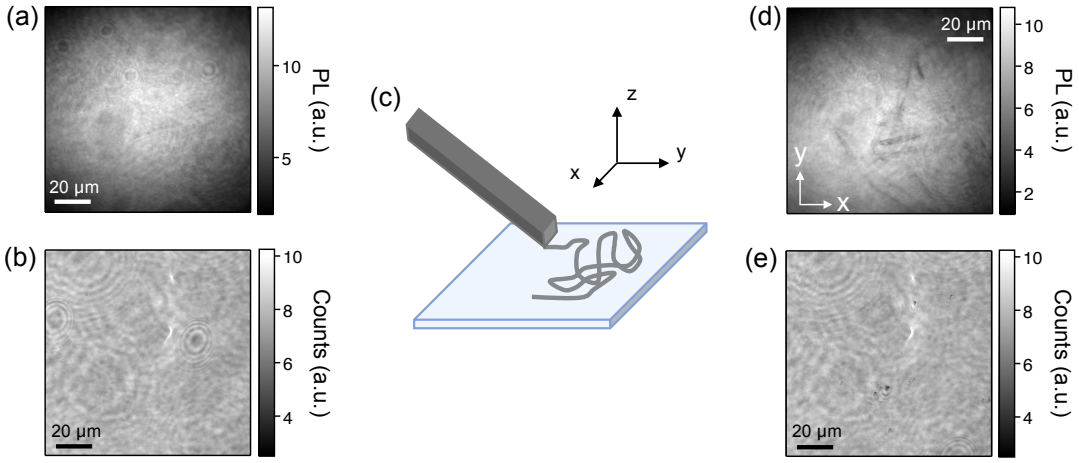

Figure 3.2: Abrasive deposition of inox steel. (a) Background NV photoluminescence (PL) image of a region later scratched with inox steel tweezer, taken under continuous wave illumination by a 532 nm excitation laser. The laser spot is approximately 100 μm in diameter. (b) Bright field micrograph of the same region shown in (a), taken under illumination of an LED lamp positioned above the sample. (c) Soft abrasion of the target materials was achieved by dragging the tip of a macroscopic block of the material across the diamond surface with moderate pressure. The xyz coordinate system used is-defined relative to the diamond surface. (d) PL micrograph of the same region shown in (a) following the soft abrasion of inox steel onto the diamond surface. The xy coordinate system used throughout the chapter is defined relative to the field of view. (e) Bright field image of the same region following the deposition.

3.3 Sample deposition and photoluminescence imaging

The abrasive deposition of all materials onto the diamond surface was achieved by manually dragging the tip of a macroscopic block of a given material across the fixed diamond surface with moderate pressure, depicted in figure 3.2(c). First, we explore the soft abrasion of inox steel onto the diamond surface, a particularly relevant study given its ubiquity in laboratory environments in many forms, such as tweezers which were used for the deposition in this instance (Dumont Inox 02). Figure 3.2(d) is a photoluminescence image of the previously characterised region following the deposition. The image shows quenching of the NV photoluminescence by up to 20% in streaked patterns, tens of micrometres in length across the field of view. A bright field micrograph of this same region, figure 3.2(e), provides a complimentary perspective. The micrograph shows dark shadows cast at locations where the photoluminescence quenching is greatest, suggesting the presence

of micron-scale particulates on the diamond surface. Comparing these images with those taken prior to the deposition, we can safely attribute these features to the deposited inox steel.

Quenching of photoluminescence under these larger particulates could be explained by a change in the boundary conditions for the laser reflected from the diamond surface [60]. These particulates, however, only correlate with a small portion of the quenched photoluminescence, and hence, quenching must be due to some other effect. These effects include Förster resonant energy transfer (FRET) effect from the NV layer to the deposited material [63, 64], a reduction in local laser intensity due to scattering from the sample, changes to the lifetime and angular distribution of the NV emission [62], or discharging of the NV centres (becoming charge neutral, NV^0 [19]) induced by the sample. Systematic control of the distance between the NV-layer and the deposited material would be required to determine the precise effect [60].

3.4 ODMR charcterisation

Having confirmed the presence of some material on the diamond surface following the soft abrasion of inox steel, we can move to characterise this material using NV spin measurements. A natural place to start is an ODMR measurement, which can detect ferromagnetic material via its static stray magnetic field. This ODMR measurement was taken with an external magnetic field applied by a permanent magnet such that the two electron-spin transition frequencies of each of the four NV-orientation families are resolved, as discussed in section 2.4 [65, 176]. The ODMR spectrum integrated over the entire field of view is shown in figure 3.3(a). Fitting the spectrum pixel-by-pixel we can create maps of the extracted parameters such as the resonance linewidth and optical contrast, figures 3.3(b) and (c) respectively. The extracted frequencies are used to calculate the static magnetic field in lab-frame coordinates and subtract the static field due to the permanent magnet. The B_x, B_y, and B_z magnetic field are shown in figure 3.3(d), (e), and (f) respectively (coordinate system defined in figure 3.2).

The ODMR parameters and reconstructed magnetic field maps indicate that there is ferromagnetic material present at the diamond surface. Features showing the largest

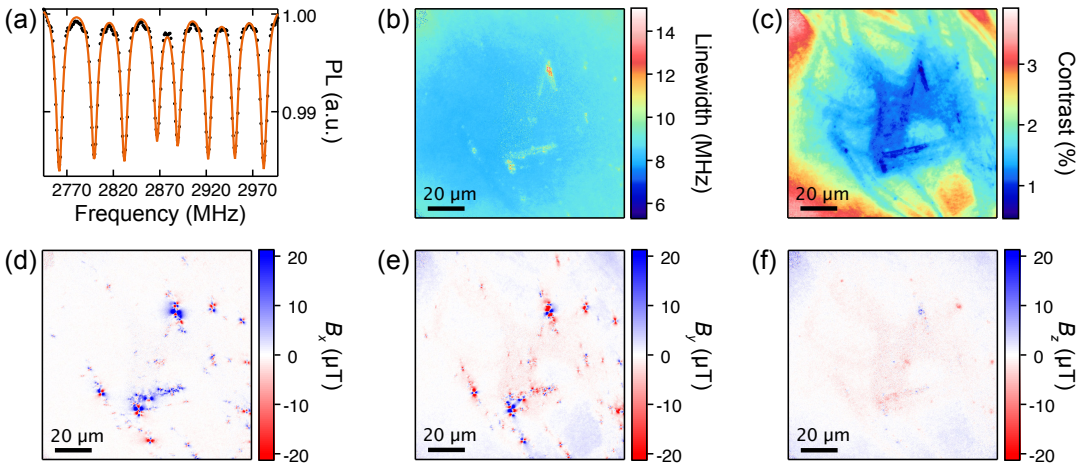

Figure 3.3: ODMR imaging of inox steel deposition. (a) ODMR spectrum integrated over the field of view presented in figure 3.2(d). The eight resonance lines correspond to the two spin transitions for each of the four NV orientations within the ensemble. The raw fluorescence data (points) is fit with a sum-of-eight-Lorentzian function (orange line) to extract the resonance frequencies, linewidths, and optical contrasts of the spectrum. (b) Resonance linewidth map across the full field of view, made by plotting the full width at half maximum (FWHM) of the lowest frequency resonance line. (c) Relative optical contrast map of the lowest frequency resonance line. (d) B_x, (e) B_y, and (f) B_z maps calculated from the fitted resonance frequencies. A plane subtraction has been taken to remove the magnetic field gradient originating from the permanent magnet used to offset the eight resonances. The colour scales are capped at $\pm 20\,\mu$T to highlight features at lesser field strengths. The largest fields measured are approximately $100\,\mu$T in magnitude. The direct frequency plots have been omitted as they are qualitatively similar to the B_x, B_y, and B_z maps.

field strengths are correlated with broader resonance lines and smaller optical contrasts. Curiously, the magnetic field amplitude in the z-direction is significantly smaller than that in the x and y directions. This observation has been explained by work from our group, led by Dr. Jean-Philippe Tetienne, published in Ref. [176]. The reduced z-field is an imaging artefact due to the close proximity of the sensing layer to the ferromagnetic material. The large fields seen by the closest NV centres shift their resonance frequencies beyond the bounds of the measurement and fitting routines. The signal is therefore dominated by those NVs in the same optically resolvable volume that experience smaller field strengths. This has the net effect of diminishing the measured z-field and altering the shape of the in-plane components. A large field gradient persists across the measurable NVs within the optically resolvable volume which broadens the resonance. Therefore, we see both reduced

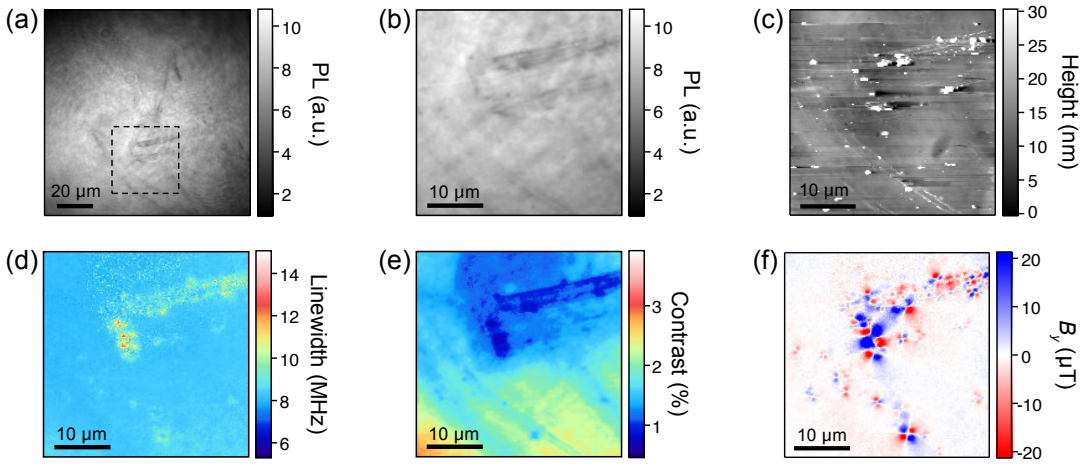

Figure 3.4: Spatially correlated ODMR and AFM imaging of inox steel. (a) Photoluminescence micrograph of the full field of view indicating the area to be compared with AFM topography scans. (b) Cropped photoluminescence micrograph of the region highlighted in (a). (c) AFM topography image of the region of interest. The colour scale is capped at 30 nm to emphasise smaller features. The largest particles near the centre of the image are greater than 500 nm in height. (d), (e), and (f) are cropped maps of the resonance linewidth, optical contrast, and B_y extracted from the ODMR measurement, of the same region highlighted in the photoluminescence image shown in (b).

optical contrast and broader resonance linewidths associated with large field strengths.

To better understand the features observed in ODMR we can compare the photoluminescence and ODMR images with an independent characterisation of the surface by atomic force microscopy (AFM, Asylum Research MFP-3D). Figure 3.4 shows photoluminescence, ODMR, and AFM topography images of a region within the previous field of view. Comparing the magnetic field and AFM topography images, it is clear that the magnetic dipole signatures are correlated with particles present at the diamond surface, with heights ranging from 20 nm to 500 nm. This observation is consistent with these features being due to ferromagnetic particles whose strong fields lead to broadening of the resonance linewidth and optical contrast seen in ODMR. Scattering of the excitation laser by the larger particles may be responsible for the reduced photoluminescence seen at their location. Energy-dispersive X-ray spectroscopy (EDXS) of larger particles from a similarly prepared sample confirm the presence of iron and oxygen, suggesting that the particles are iron oxide, likely Fe_2O_3 or Fe_3O_4 (see appendix A.1.2).

The ODMR contrast map, however, shows additional striped features across the

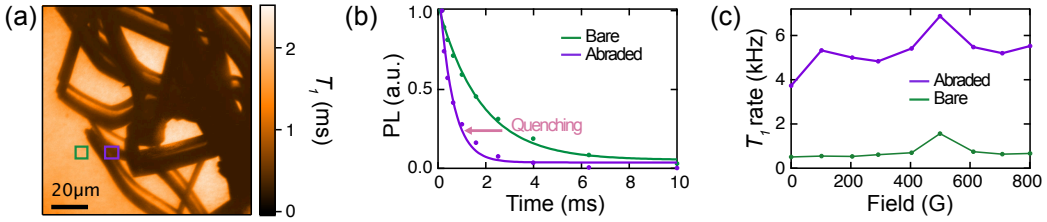

Figure 3.5: T_1-relaxation imaging of inox steel. (a) T_1-relaxation image showing significant quenching of the NV T_1-relaxation time under material residues left by abrasive deposition in the same region studied in figure 3.3. (b) Individual T_1-relaxation curves from the areas highlighted in (a). The relaxation time has been reduced from 1.79±0.36 ms in the untouched region (green) to 0.57±0.17 ms under the deposition (purple). The curves have been normalised as explained in the text. (c) T_1-relaxation rate ($1/T_1$) spectra of an untouched region (green) and a region under the material deposition (purple). The biasing field is applied along the NV axis of a single family, varying the $m_s = 0$ to $m_s = 1$ transition frequency from 2.87 GHz to 630 MHz across the range.

entire field of view that are not correlated with large ferromagnetic particles. The photoluminescence image shows similar features, though they are less pronounced as compared to the ODMR optical contrast image. The cropped AFM data shows that one such region is bounded by less than 10 nm tall ridges oriented along the direction of the abrasions, which do not show in the optical, photoluminescence, or magnetic micro-graphs. Given the transition of iron oxide from ferromagnetism to superparamagnetism at sizes less than 20 nm [186], imaging fluctuating magnetic fields is necessary to further characterise the system.

3.5 T_1-relaxation imaging

T_1 relaxometry [72] is a useful NV sensing technique that measures the decay of some prepared spin state back towards thermal equilibrium. As discussed in section 1.3.6, the T_1 decay rate is sensitive to magnetic noise fluctuating close to the spin transition frequency, 2.87 GHz at zero bias field. Consequently, T_1 relaxometry has been used to detect magnetic noise from proximal electron spin species, many of which fluctuate at gigahertz frequencies [79–84].

The application of T_1 relaxometry to widefield imaging uses a simple all-optical pulse sequence with initialisation and readout laser pulses separated by some free evolution time.

The sCMOS camera measures a decay in photoluminescence across the field of view as the evolution time increases and the state relaxes from the pumped bright state, $m_s = 0$, to a thermal mixture of all spin sub-levels, $m_s = 0, \pm 1$. This photoluminescence signal is normalised by that from an intercalated sequence that includes a microwave π-pulse before the readout laser pulse to isolate the spin-dependent photoluminescence decay from common mode variations. Here, all T_1-relaxometry imaging was performed at zero-field, i.e. with the $m_s = 0$ to $m_s = \pm 1$ spin-transition frequencies at 2.87 GHz, unless otherwise stated. The sensitivity is enhanced in this regime as the optical contrasts of all NV families contribute to the same measurement.

The normalised T_1-relaxation curves are fit with a single exponential function to extract the T_1-decay times, allowing us to map the fit parameters across the field of view as for ODMR, namely the maximum photoluminescence, optical spin contrast, and the characteristic decay time, T_1. The first two parameters are qualitatively similar to the direct photoluminescence and ODMR optical contrast, and are therefore not presented here. The fit parameters were determined by minimising a least square error function as described for the ODMR sequence in section 2.4. Alternate fit functions were considered including stretched exponentials with the exponent power left as a free parameter, however, the fitting was found to be less robust and lacking physical justification for its variation across the field of view. Therefore, for consistency, so called single exponentials were used to fit all T_1 data.

To further analyse the inox steel deposition studied in figure 3.3, we made a T_1-relaxation measurement of the same region. Figure 3.5(a) shows a map of the T_1 fit parameter extracted from this measurement. Here, we see a significant reduction of the T_1 decay time in broad streaks which match the shapes seen in the optical contrast maps extracted from the ODMR measurement, though they are more pronounced and extensive here. Examples of the relaxation curves used to compose the T_1 map are given in figure 3.5(b), which shows curves binned over two small areas, one adjacent to and the other beneath the abrasion. These regions have T_1-relaxation times of 1.79 ± 0.36 ms and 0.57 ± 0.17 ms respectively, the former matching the background T_1 time measured in the region prior to the deposition (see appendix A.1.1). Therefore, we can calculate the noise contribution of the abraded material using these two areas, by calculating the increase to

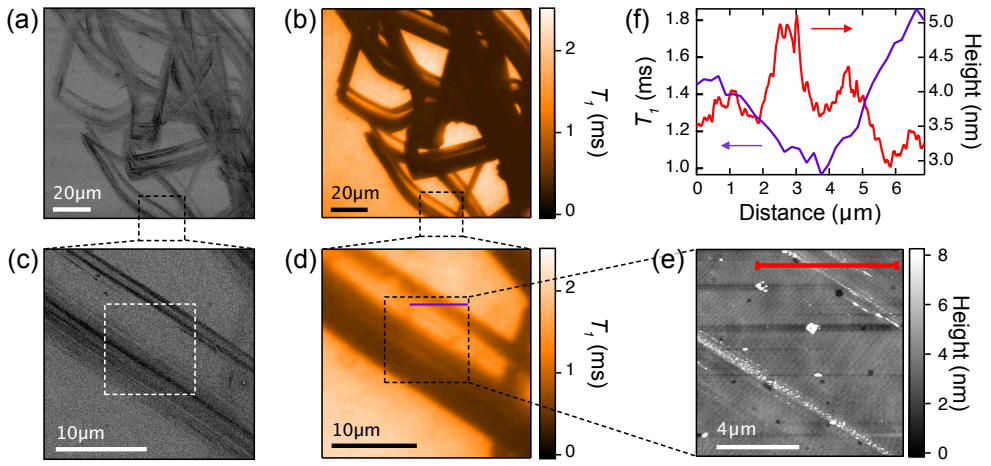

Figure 3.6: Spatially correlated SEM, T_1-relaxation, and AFM imaging of inox steel. (a) SEM and (b) NV T_1-relaxation images showing significant quenching of T_1-relaxation time under material residues left by abrasive deposition. (c) and (d) show zoomed SEM and T_1-relaxation images, respectively, of the highlighted regions. (e) AFM topography of the region highlighted in (c) and (d). The z-scale is capped at 8 nm to emphasise the smaller features. The tallest particles within the aggregate are approximately 20 nm in height. (f) AFM (red) and T_1 (purple) taken along the lines shown in (d) and (e). Approximately 1 nm step heights are seen across the edge of parallel bands, which define the quenched T_1 region. The less than 1 μm separation of the bands is close to the resolution limit of the T_1 imaging.

the relaxation rate, $\Delta\Gamma = (1/T_1)_{\text{abraded}} - (1/T_1)_{\text{bare}} \approx 1.8\,\text{kHz}$.

T_1-relaxation measurements can be used to perform noise spectroscopy by tuning the NV spin transition frequency, which sets the spectral sensitivity of T_1 decay, by varying the applied bias field [24,47,187]. Here we align the magnetic field with a single NV family and track the $m_s = 0$ to $m_s = -1$ transition over an applied field range of 0 G to 800 G, shifting the transition frequency from 2.87 GHz to 630 MHz. Figure 3.5(c) compares T_1-rate spectra of two regions, one under and the other beside the abraded region, similar but not identical to those compared previously. Across this range, there is an approximately constant offset of 4.5 kHz between the spectra of the bare diamond and the abraded region, suggesting that the abrasive deposition adds a broadband source of magnetic noise to the sample. The enhanced relaxation rate around 512 G in both spectra is due to a cross-relaxation resonance with unpaired electron spins intrinsic to the diamond [24, 187].

To compare the insight gained from T_1-relaxation imaging with that of independent

charaterisation techniques, we turn again to AFM topography imaging and also scanning electron microscopy (SEM). SEM is particularly useful here given its high spatial resolution and capacity to show good contrast for thin materials with poor optical absorption. Figures 3.6(a) and (b) show SEM and T_1 images of the full region of interest. The SEM image shows the same broad pattern seen in the T_1 image, however, it reveals more texture within the abraded region as compared to the T_1 maps. This difference is emphasised by comparing a higher-resolution SEM image with a zoom-in of the T_1 map shown in figures 3.6(c) and (d). Here we see two parallel bands running diagonally across the images, a more narrow band at the top and a more broad band at the bottom of the frame. The optical-diffraction-limited T_1 map shows relatively flat quenching under the abraded regions, whereas the SEM image shows large variations in contrast and clear streaking along the abrasions. The topography within this region, as mapped by AFM in figure 3.6(e), shows some of the same structures seen in SEM. For the band running across the top half of the image, spatially correlated line profiles of the T_1 and AFM images, figure 3.6(f), show an approximately 1.0 nm step height at the edge of quenched T_1 band. The dark streak seen running through the lower band in the SEM image is revealed to be a collection of nanoparticles, 5 nm to 10 nm in height. However, for this band there is no clear step height measured at the boundary of quenched T_1, suggesting a sparse deposition below the noise floor of the AFM is responsible for the quenching here despite the near-uniform T_1 reduction in this region.

3.6 Comparison of abrasively deposited materials

To better understand the cause of the T_1 reduction associated with abrasively deposited inox steel, we deposited a range of alternate materials on similar NV diamond samples and imaged the depositions using T_1 relaxometry and AFM. These materials include silicon, copper, chromium, copper-beryllium alloy, and gold, all chosen for their prevalence in our NV experiments as outlined previously. The abrasive deposition of a given material and the subsequent T_1-relaxation and AFM imaging were repeated as before, but replacing the inox steel tweezers with macroscopic blocks of the relevant material. A sharp piece of silicon cleaved from a larger wafer was used for the silicon deposition. The deposited

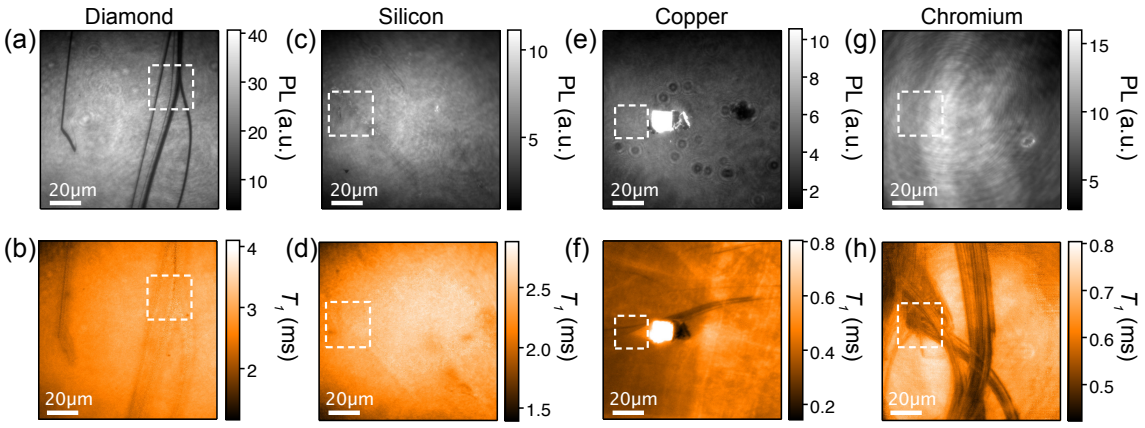

Figure 3.7: Alternate abrasive depositions. (a) Photoluminescence and (b) T_1-relaxation-time image of a region scratched with a diamond scribe. (c) and (d) show the same image types for a region featuring abrasively deposited silicon. (e) and (f), and (g) and (h) show the same for copper and chromium depositions respectively. The regions chosen for the correlated AFM imaging presented in figure 3.8 are highlighted (white boxes).

gold and chromium were sourced from pellets typically used in e-beam evaporation, with a purity greater than 99.95%. The copper used was an off-cut from a larger copper sheet whose purity is unknown, and the copper-beryllium alloy was sourced from a non-magnetic laboratory screwdriver of unknown purity. Additionally, a diamond scribe was scratched across the diamond surface as a control experiment to investigate the effect of possible structural changes due to the abrasion process. Background images of the T_1-relaxation time were taken prior to deposition, such that subsequent features could be attributed to the deposited material as before. All bulk materials were cleaned using acetone and isopropyl alcohol prior to making contact with the diamond surface to remove any common organics from the surface. Note that ODMR measurements were taken of these supplementary depositions, however, none showed any ferromagnetic features and hence are not presented here.

Figure 3.7 shows photoluminescence and T_1-relaxation images of regions scratched with the diamond scribe, silicon wafer, copper, and chromium, over a 100 μm field of view. The region scratched with the diamond scribe shows long streaks where the photoluminescence is reduced, figure 3.7(a), to a greater extent than was observed for the inox steel deposition. These streaks are somewhat visible in the T_1 image, figure 3.7(b), but do

not show a clear or consistent associated change in T_1. Similarly, the silicon wafer region shows a faint band of quenched photoluminescence running diagonally across the image, figure 3.7(c), but no significant change in T_1, figure 3.7(d). The copper region was centred around a diamond growth pyramid, visible as a bright square in photoluminescence, figure 3.7(e), and had pre-existing T_1 features where the left hand side of the image has a slightly shorter relaxation time than the right, figure 3.7(f). This feature remained after the copper deposition, which did not directly affect photoluminescence, figure 3.7(e), but quenched T_1, figure 3.7(f). The large triangular feature seen to the right hand side of the pyramid is a large chunk of metallic copper (greater than $1\,\mu$m in height), which appears bright in photoluminescence and strongly quenches T_1. Finally, the chromium deposited region shows no discernible photoluminescence quenching at this scale, figure 3.7(d), but does show significant T_1 quenching, figure 3.7(h).

As for the case of inox steel, we compared our NV imaging with AFM to better understand the NV observations. Here we performed AFM imaging within the highlighted regions of the large-field-of-view images in figure 3.7. Figure 3.8 compares photoluminescence, T_1-relaxometry, and AFM images of these four additional materials. A zoomed-in photoluminescence image of the diamond scribe scratch, figure 3.7(a), more clearly shows the dramatic reduction of NV photoluminescence under the abrasions. The T_1 map shows that the scratch is distinguishable in the T_1 signal due to an increased pixel-to-pixel noise rather than a clear reduction in T_1-relaxation time, figure 3.8(b). AFM topography images show that the abrasion has, predictably, chipped the diamond surface by up to 10 nm for the strongly quenched regions, with more shallow 2 nm cavities running parallel to the deeper trench, figure 3.8(c) and (d). Given the initial NV depth profile of $0-20$ nm, strong photoluminescence quenching from the 10 nm-deep cavity is explained by the removal of some NV centres and reduced charge stability of those remaining which are now closer to the surface (see section 1.2.1 [19, 23]). The unaffected T_1-relaxation time under these cavities is commensurate with studies of dense NV ensembles, where the T_1-relaxation time is limited by the noise within the NV layer rather than surface noise (see section 2.2.1 [24]). Therefore we can conclude that the enhanced magnetic noise observed under the inox steel depositions does not arise from mechanical damage to the diamond surface.

The zoomed-in NV images of the silicon region shows quenching of the NV pho-

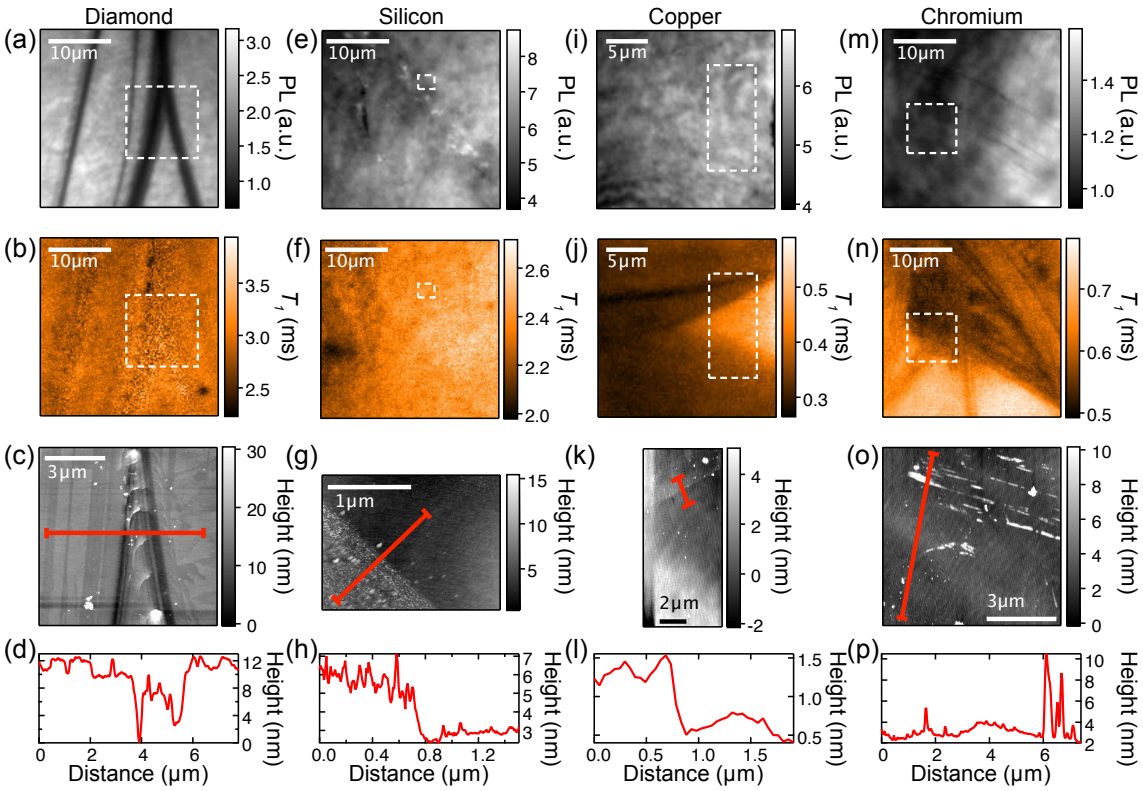

Figure 3.8: Spatially correlated AFM and T_1 imaging of alternate depositions. (a), (b), (c), and (d) PL, T_1-relaxometry, AFM topography images, and AFM height profile of a region abraded with the diamond scribe. The location of the AFM images region is indicated in the PL and T_1 images (white), and the AFM profile location is shown in the AFM image (red). (e) - (h), (i) - (l), and (m) - (p) As previously stated but for regions of abrasively deposited silicon, copper, and chromium respectively.

toluminescence by up to 15%, figure 3.8(e), but again no clear T_1 reduction associated with the deposited material, figure 3.8(f). This is despite an approximately 3 nm-thick coverage of material on the diamond surface as measured by AFM at the edge of the quenched photoluminescence band, figure 3.8(g) and (h). The brighter points observed within the band are due to larger silicon particles (greater than 1 μm), demonstrating a non-trivial relationship between presence of bulk material at the diamond surface and photoluminescence.

The results for copper and chromium, however, bear resemblance to those of inox steel. The copper deposition, despite not resulting in a photoluminescence quenching, figure 3.8(i), does reduce the T_1-relaxation time under the deposition, figure 3.8(j). AFM

imaging, figures 3.8(k) and (l), shows a 1 nm step height from the bare diamond to the copper deposition that is associated with T_1 quenching from 0.4 ms to 0.3 ms; an increase to the NV relaxation rate of $\Delta\Gamma \approx 3$ kHz. No discernible step height was measured at the edge of the pronounced band of quenched T_1 running across the centre of the figure 3.7(f). Chromium, on the other hand, shows some streaks of quenched photoluminescence that run parallel to a large T_1 feature, figures 3.8(m) and (n). AFM imaging of the same region shows that these photoluminescence features are associated with metallic-looking topography features 10 - 20 nm in height, figures 3.8(o) and (p). The AFM imaging here detected no clear step at the edge of the T_1-quenched regions despite the 0.5 kHz increase to the relaxation rate in the abraded region. Again, this suggests that a sparse coverage of material, close to the noise floor of the AFM (approximately 0.5 nm), is responsible for the enhanced noise.

Finally, to demonstrate prevalence and reproducibility of this phenomenon we abrasively deposited copper-beryllium alloy and gold, and repeated the depositions of copper and inox steel onto further diamond samples. These samples were only analysed by NV imaging, omitting complementary but time-consuming AFM. The photoluminescence and T_1 images of regions scratched with copper-beryllium, gold, copper, and inox steel are shown in figures 3.9. None of the depositions show particularly strong photoluminescence quenching, except that of inox steel, which is more pronounced than the inox steel deposition shown previously. The bright splodges seen in photoluminescence image of the copper-beryllium scratches, figure 3.9(a), are due to large chunks of alloy sitting on the surface (greater than 1 μm thick), while the dark lines running horizontally across the field of view were pre-existing defects in the sample. All depositions, regardless of their impact on photoluminescence, result in significant and extensive quenching of the NV-layer T_1-relaxation time. The total added noise for each deposition is 0.6 kHz, 0.7 kHz, 2.0 kHz, and 5.0 kHz for the copper-beryllium, gold, copper, and inox steel respectively. The added noise was calculated by comparing the T_1 times under and beside the abraded regions for the copper-beryllium, copper, and inox steel deposition, whereas the gold deposition was compared to a background measurement, as the T_1 decreased across the entire field of view after the scratch in this instance, due to the blunt nature of the gold pellet used. The result for gold is particularly interesting given the absence of paramagnetic gold species

which would be obvious agents of the enhanced T_1 decay. The effect in this case may be a more subtle influence mediated by defects within the diamond.

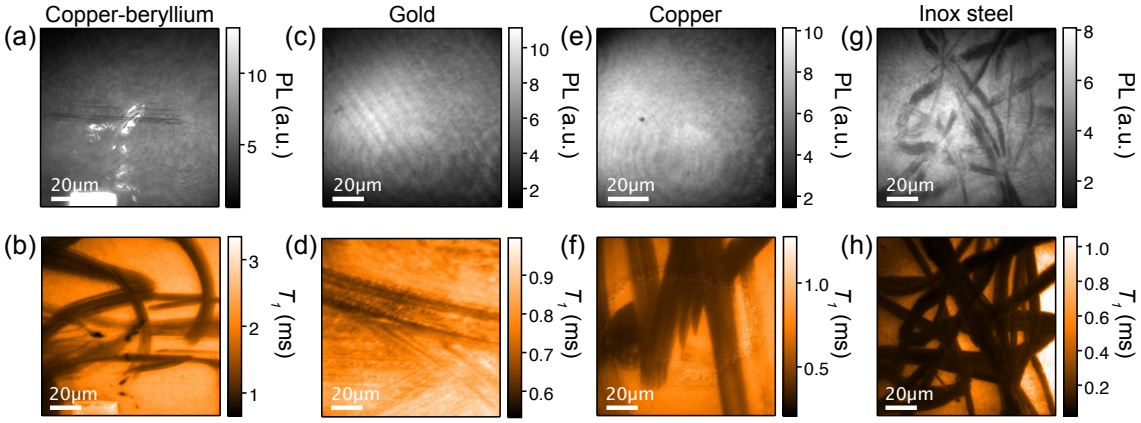

Figure 3.9: Additional depositions. (a) Photoluminescence and (b) T_1-relaxation-time images of additional copper-beryllium alloy deposition. The bright rectangle at the bottom of the photoluminescence image is a diamond growth pyramid. (c) and (d) show the same images for the gold deposition on a polished diamond surface. Polishing marks are seen as parallel lines running diagonally through the photoluminescence image. (e) and (f), and (g) and (h) show the same image types for the repeated copper and inox steel depositions. For (h), the colour scale is capped at 1.05 ms to emphasise contrast in the left hand side of the image. The T_1 time is up to 2 ms long in the right hand side of the image.

3.7 Discussion of T_1-quenching mechanism

The data presented so far has demonstrated that the abrasive deposition of five metallic materials, inox steel, copper, chromium, copper-beryllium alloy, and gold, all quench the NV layer T_1-relaxation time, whereas two semi-conducting materials, diamond and silicon, give no such effect. Glass deposited from a coverslip was also studied and found to produce no effect. We now move to discuss the potential mechanisms by which the NV T_1 time could be quenched by abrasive depositions of metallic materials. As mentioned in section 1.3.6, the T_1-relaxation time of solid state spin qubits is sensitive to both phonon activity and magnetic noise at the qubit transition frequency [188]. Here, we exclude the possibility of phonon-mediated quenching given the negligible impact that such depositions could have on the thermal vibrations of the diamond, and look at the magnetic contributions in terms

of spin noise and charge noise.

Magnetic noise arising from fast-fluctuating spin species, so called spin noise, has been observed to quench the T_1-relaxation times of nearby NV centres [79–82, 84, 89, 130, 150]. Our study of the inox steel deposition could therefore be explained by a large coverage of superparamagnetic nanoparticles on the diamond surface, likely iron oxide particles below some threshold size. These findings are commensurate with previous studies of Fe_2O_3 and Fe_3O_4 nanoparticles at room temperature [83,189]. Our AFM topography scans identified many particles below the reported threshold size at which Fe_3O_4 transitions from ferromagnetic to superparamagnetic, approximately 20 nm at room temperature [186]. The difficulty in measuring a clear step height at the edge of the reduced-T_1 regions suggests that a more sparse distribution of nanoparticles may be responsible for the T_1 reduction. These nanoparticles would be hard to detect with AFM at sizes smaller than the diamond roughness, a few nanometers in this case, but could still cause the near-uniform T_1 quenching provided there were sufficiently many per optically resolvable spot. This explanation is equally applicable to copper and chromium depositions, which both have paramagnetic forms that could explain the apparent magnetic noise [190–193].

The metallic nature of the bulk materials whose abrasive depositions quench T_1-relaxation times warrants a discussion of the role played by their conductivity. As mentioned in section 1.4.1, NV T_1-relaxation sensing has been used to detect charge noise, specifically Johnson-Nyquist noise arising from metallic films; an effect that scales with the conductivity of the deposited metals [112, 113]. These experiments, however, studied metallic films at a minimum thickness of 60 nm, due to reduced conductivity at thicknesses less than the electron mean free path [113, 194, 195]. To demonstrate that quenching due to Johnson-Nyquist noise is negligible in our system for this reason, we entertain the idea that abrasive deposition results in a 1 nm-thick continuous metallic film, and use the model developed in Ref. [113] to calculate the subsequent T_1 quenching. The enhanced relaxation rate due to Johnson-Nyquist noise is calculated as

$$\Gamma_{\text{metal}} = \gamma^2 \frac{\mu_0^2 k_B T \sigma}{8\pi} \left(\frac{1}{d} - \frac{1}{d + t_{\text{film}}} \right), \tag{3.1}$$

where γ is the electron gyromagnetic ratio, μ_0 is the vacuum permeability, T is temper-

ature, σ is the metal conductivity, d is the separation between the sensing layer and the metallic film, which has thickness t_{film}. Calculating the expected noise for a film thickness of 1 nm with the conductivity of bulk copper, $\sigma = 6.0 \times 10^7\,\Omega^{-1}\text{m}^{-1}$, gives a noise $\Gamma_{\text{metal}} = 2.0\,\text{kHz}$. However, once the reduced conductivity at film thicknesses less than the mean free path is taken into account, which, conservatively, reduces conductivity by an order or magnitude at a 5 nm film thickness [195], the calculated noise is well below that observed for even the lowest conductivity metal studied. Additionally, this model does not account for the lateral confinement of our particulate deposition, which will further reduce the conductivity [113]. For this reason, we exclude the possibility of Johnson-Nyquist noise causing the enhanced T_1-relaxation rates observed in our samples.

A final possible explanation for the observed T_1 quenching is that it occurs by an indirect effect, where the deposited material alters the dynamics and filling of existing charge traps at the diamond surface and within the NV layer. The effects of such defects on T_1 times have been studied previously. Reduced T_1-relaxation times due to fluctuating low-density surface states have been observed in single-NV samples [150]. In dense near-surface NV ensembles, similar to those used in this work, a strong dependence of T_1 times on the specific diamond surface treatments has been noted [24]. Recently, apparent reductions in T_1-relaxation times have been linked to ionisation of NV^- to NV^0 by electron tunneling to nearby defects [30,31,196]. For the dense NV ensembles used in this study, charge trap densities within the sensing layer can be as high as one per $(\text{nm})^2$, corresponding to ten charge traps created for each implanted nitrogen [22]. The addition of surface donors, in the form of metallic nanoparticles, at a similar density could substantially change the filling and dynamics of these states, and the electron tunneling between them and proximal NV centres. The low area density of donors needed to achieve this would also explain why a perfect correlation of sample topography and T_1 quenching is not seen, as the density required to quench T_1 relaxation may be far below AFM noise floor. Imaging unpaired electron spins by double electron-electron resonance measurements is suggestive of such an indirect effect on defects states of the diamond (see appendix A.1.3).

3.8 Summary

In this work, we have applied multi-modal NV imaging to nanoscale systems arising from the abrasive deposition of bulk materials onto the diamond surface. These systems were analysed using photoluminescence, ODMR, and T_1 imaging techniques, finding significant quenching of the NV layer T_1-relaxation time under depositions of the metallic materials (inox steel, copper, chromium, copper-beryllium, and gold). Complementary AFM imaging of the diamond surface indicates that this quenching was associated with sub-nanometer thick collections of nanoparticles of the deposited material, though precise correlation with the T_1 imaging was not clear in all cases. Explanations for this effect have been discussed, including direct spin noise and charge noise arising from the sample, which in general, cannot be separated from indirect effects that alter the population and dynamics of defects intrinsic to the diamond.

The project demonstrates the great sensitivity of NV imaging to small sample volumes at the diamond surface - a key step towards studying two-dimensional and ultrathin materials. The static magnetic fields from ferromagnetic nanoparticles were comfortably imaged, as were the significant reduction to the T_1-relaxation time induced by sub-nanometre thick collection of nanoparticles. However, some difficulty was encountered in identifying the precise origin of the observed T_1 reduction. This highlights a key problem for NV sensing of ultrathin and nanoscale systems, namely, the need to passivate the diamond surface such that intrinsic sample properties are not conflated with induced changes to the sensing environment. Progress has been made in this area by reducing the number of additional defects in the sensing layer [22], however, further solutions may involve targeted surface functionalisation [197] or the addition of a capping layer to fix the interface chemistry close to the sensing layer. Using NV ensembles at a greater depth in the diamond will also mitigate this issue by reducing interactions between the target sample and defects within the sensing layer, and diminishing sensitivity to surface states that may also be altered by the material. This solution is only appropriate in the case that the target signal is long reaching as compared to short range noise contributions. In chapter 6 we will see both an insulating oxide layer and deeper NV ensemble utilised for imaging two-dimensional ferromagnetic materials.

4

Imaging graphene field-effect transistors on diamond

An especially interesting application of NV microscopy is to image transport phenomena in working electrical devices. The ability to spatially resolve transport within a device gives us information that is not directly or unambiguously available to standard characterisation techniques, for example, bulk electrical/resistance measurements. The previous chapter demonstrated the good sensitivity of near-surface NV ensembles to both static and fluctuating magnetic fields associated with thin depositions and minute sample volumes at the diamond surface. In this chapter, we use this good sensitivity to detect the static Ørsted field arising from charge transport in electrical devices fabricated on the diamond surface. As discussed in section 1.4.1, in the case of two-dimensional and thin transport devices, we can use this measurement to reconstruct the current density in the device by inverting the Biot-Savart law. The details of this process will be introduced here in section 4.4. This capability will also be utilised in chapter 5, where we map superconducting transport in niobium wires.

Prior to this work, there were only two published applications of current-density mapping by NV-diamond microscopy since the technique was established in 2015, when it was used to study an integrated circuit, a simple test system [198]. The first application, published by our group at The University of Melbourne, imaged current densities in simple graphene wires fabricated on the surface of a diamond by measuring the near-surface NV ensemble [65]. The second, published by ETH Zurich, mapped current densities in carbon nanotubes by scanning a single-NV nanodiamond [110]. Both of these applications used ODMR measurements to detect the Ørsted field associated with transport in each device via the Zeeman effect on the NV ground-state spin levels. These important milestones demonstrated the capability of NV microscopy in this space, however, to push towards studying exotic transport phenomena, we must look to more sophisticated devices that allow us to vary the conditions of transport within the device, for example, by changing the level of doping in the conductive channel. A field-effect transistor allow us to do precisely that, giving us control over both the injected source-drain current via an applied source-drain potential and the doping of the conductive channel via an applied gate potential. At the commencement of this project, the compatibility of NV imaging with operational gated devices was largely unexplored.

In this project, we investigate this compatibility by fabricating graphene field-effect

transistors (GFETs) directly on the diamond surface and characterising them via NV microscopy. The current density within the gated graphene channel is reconstructed under both mostly n-type and p-type doping, however, we observe that the precise level of doping is affected by our measurements. We establish that this problem is in part due to a photo-assisted doping effect arising from our excitation laser which shines directly on the device. Additionally, we find a surprisingly large modulation of the electric field at the diamond surface under large applied gate potentials, seen in NV photoluminescence and NV electrometry measurements, likely due to an accumulation of charge at the diamond-oxide interface. These observations suggest a complex electrostatic response of the oxide-graphene-diamond structure, and inspire refined device designs and approaches to NV microscopy for future projects.

4.1 Motivation

The ability to spatially map charge transport is relevant to a range of emerging materials and applications which rely on highly non-uniform transport properties. Topological insulators hold promise for a new generation of low-energy electronics by virtue of their protected conductive edge modes [199, 200]. Superconducting single-photon detectors, an already widely adopted technology, rely on local disruption of superconducting transport by incident photons to register a detection. Non-uniform transport phenomena are also relevant to the physics of strongly interacting quantum systems, for example, hydrodynamic transport in quantum critical fluids such as viscous flow of Dirac fluids in graphene [111, 201, 202]. In each of these cases, signatures of these phenomena are accessible to bulk electrical characterisation, however, the ability to spatially resolve transport phenomena gives us an extra characterisation tool that may lend insight overlooked by existing techniques. For example, despite the widespread use superconducting bolometers, the precise dynamics of the quenching superconductivity are not well understood and are additionally complicated by the already non-uniform transport in these device geometries [203,204]. We will demonstrate the capability of NV imaging towards this goal in chapter 5, but for now we turn specifically to transport in graphene.

Graphene is a both convenient and interesting platform on which to test our trans-

port mapping capabilities. The popularity of graphene research over the past sixteen years lends some practical advantages to working with graphene devices. There are many well-established fabrication and measurement techniques for graphene-based devices, and demand is such that the raw materials can be purchased commercially (e.g. Graphenea and Graphene Supermarket). In addition to these practical benefits, graphene is host to a range of exotic phenomena to which we can apply our imaging. As mentioned above, the various hydrodynamic transport regimes of graphene, though detectable by electrical measurement [201], have clear hallmarks in the spatial distribution of their current. These include parabolic versus square-top current density profiles for viscous and non-viscous regimes of transport across narrow channels [111, 202, 205]. Charge injection through narrow constrictions should also be detectable by NV microscopy via the magnetic signature associated with charge backflow in the viscous-flow regime [205]. Other spatially inhomogeneous transport phenomena that could potentially be imaged with NV microscopy include electron-hole puddling [206], and gate controlled steering of carriers [207]. Recently, the discovery of superconducting phases in twisted-bilayer graphene opens up the possibility of studying superconducting transport in graphene systems [180, 181], however, this requires both precise control over the doping and temperature of the twisted-bilayer graphene, a capability we look to integrate in chapter 5.

Although there are several techniques that can be used to locally probe transport, such as scanning SQUIDs, scanning single-electron transistors, and thermography [208, 209], NV microscopy offers several advantages. These include the ability to quantitatively map the Ørsted fields and produce corresponding quantitative current density maps, and its experimental flexibility that we discussed in chapter 1. In addition to static field detection, NV microscopy's sensitivity to fluctuating fields is similarly useful here. NV spin-relaxation time measurements have been used to probe and map the local conductivity of thin metallic films via the fluctuation fields associated with Johnson-Nyquist noise [112, 113], revealing information on the motion of carriers within the material. These same measurements can be used to study low-dimensional systems where magnetic noise profiles give insight into local electronic correlations [114, 182, 183]. Both scanning and widefield approaches to NV microscopy are useful here to probe nano- to meso-scale transport phenomena [111, 202], but again we focus on the widefield approach for reasons discussed

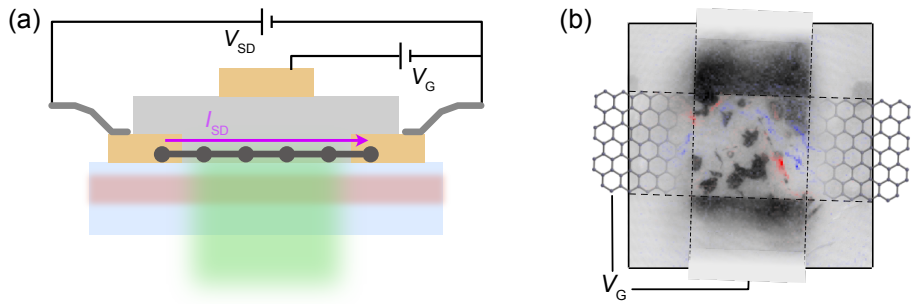

Figure 4.1: Concept for NV imaging of GFETs. (a) Schematic of a top-gated GFET on an NV-diamond substrate. The devices comprises a graphene ribbon (black), metallic source-drain and top-gate contacts (yellow), a gate oxide (grey), fabricated on top of a diamond (blue) with a near-surface NV layer (red). Current is injected into the graphene ribbon, I_{SD}, by application of a source-drain potential, V_{SD}, and the graphene is doped by application of a top-gate potential, V_G. (b) Illustration of the phenomena imaged in this work including deviations in current density through the gated-graphene channel under different doping conditions (red/blue) and interface charge accumulation as imaged by NV fluorescence measurements (grey).

in chapter 1.

Widefield imaging of electrical devices using NV ensembles generally requires the devices to be fabricated directly on the NV-diamond substrate, while many interesting transport phenomena highlighted so far require precise control over doping in the conductive channel. This can be achieved in a field-effect transistor (FET) device, employing either a top gate [111, 114, 210], back gate [202], an in-plane gate [57, 211], or an electrolytic gate [212]. Recently, graphene-based devices have been fabricated successfully on NV diamond substrates [65, 111, 114], but the compatibility of operational gated devices with widefield NV microscopy remains largely unexplored, with questions of whether the operating conditions required for NV microscopy may affect the operation and integrity of the FET, or whether the fabrication/operation of the FET may affect the ability to perform NV sensing.

In this work, we fabricate several top-gated graphene field-effect transistors (GFETs) on an NV-diamond substrate, and characterise device phenomena via widefield imaging of the near-surface NV ensemble. Current is injected into the graphene ribbons, I_{SD}, by application of a source-drain potential, V_{SD}, and the doping of the ribbon is tunable via the applied top gate potential, V_G, allowing charge transport to be probed in different doping

regimes and for the effect of the gate to be studied. The device schematic is shown in figure 4.1(a). Firstly, the devices are characterised by electrical measurements and the influence of the laser used to excite the NV layer is assessed. Secondly, the current density within the graphene ribbon is reconstructed under n-type and p-type doping by measuring the associated Ørsted field via optical readout of the NV electron-spin resonances. Thirdly, an effect is observed by which the NV-layer photoluminescence (PL) is modulated by the applied gate potential in regions proximal to the gated device, but extending up to $20\,\mu$m away from the graphene ribbon. Direct measurement of the electric field by the NV ensemble electron-spin resonances demonstrate that this effect is due to an enhanced electric field surrounding the graphene ribbon which diminishes the NV^-/NV^0 charge state ratio. These findings are illustrated in figure 4.1(b). Finally, we discuss possible solutions to overcome the challenges identified in this study to facilitate further investigation of transport phenomena in graphene and other two-dimensional materials.

4.2 Fabrication of GFETs

The graphene field-effect transistors (GFETs) studied in this work all consisted of monolayer polycrystalline graphene ribbons, Cr/Au source drain contacts, and an 80-nm-thick Al_2O_3 gate oxide with a Cr/Au top gate contact. A set of 10 GFETs was fabricated on each of two separate NV-diamond substrates, labeled as diamond #200 and diamond #230. The diamond themselves were electronic-grade single-crystal diamonds produced by method A outlined in chapter 2, implanted with 6 keV $^{15}N^+$ at a fluence of 10^{13} ions/cm^2, giving a near-surface NV ensemble with a mean depth of $10-20$ nm, similar to many of the samples studied in chapter 3. The GFET fabrication on each diamond was identical except for two slight differences. On diamond #200 the graphene ribbons were $50\,\mu\text{m} \times 500\,\mu$m, with the source-drain contacts evaporated on top of the graphene. On diamond #230 the ribbons were $20\,\mu\text{m} \times 500\,\mu$m, and the graphene was transferred on top of already existing contacts. The latter process resulted in minimal tearing of the graphene, either due to the transfer itself (same process but highly variable) or due to it reducing the number of fabrication steps endured by the graphene once on the diamond. Unfortunately, the NV properties of diamond #230 were compromised during fabrication (ODMR contrast

0.6% on diamond #230 versus 1.8% for #200 and with a factor 5 lower photoluminescence count rate) and hence most of the data presented is of devices from diamond #200.

The general fabrication process used to make GFETs on diamond is illustrated in figure 4.2. Our GFETs were made using mono-layer polycrystalline graphene grown on copper foil by chemical vapour deposition (CVD), sourced commercially from Graphenea. The graphene was isolated from the copper foil and transferred onto our NV-diamond substrates using a standard wet chemical technique [213], figure 4.2(a). Prior to transfer, the graphene was spin-coated with a PMMA A4 (950) protective layer. The copper foil was etched by floating the copper-graphene-PMMA film on a 0.5% wt. $Fe(NO_3)_3$ solution for 24 hours. The sample was put through multiple deionised water (DI) rinses, a dilute RCA2 (34%HCl:H_2O_2:DI 1:1:5) cleaning step, and a final rinsing step, by lifting the film with a clean silicon wafer to transfer between solutions. The clean graphene-PMMA film was then transferred onto our NV-diamond substrates by lifting the film out of the final DI rinse with the diamonds, which were mounted to their own silicon wafer, and left to dry for 48 hours. A photograph of the graphene-PMMA film drying over one of our diamonds is shown in figure 4.2(e).

Once dry, the transferred graphene was selectively etched into ribbons 20 μm (diamond #230) or 50 μm (diamond #200) wide and metallic source-drain contacts and bonding pads were formed, figure 4.2(b). This was achieved with photolithography using SU8 (negative-tone photoresist) on a protective PMMA layer to create a removable hard mask for etching in an oxygen plasma asher (750 W, 10 sccm O_2 in Ar). The source-drain contacts and bonding pads were then patterned by photolithography using TI35E photoresist, followed by thermal electron-beam evaporation and liftoff of a 10-nm-thick chrome layer, to promote adhesion to the diamond, followed by a more conductive 70-nm-thick gold layer. An SEM image of diamond #230 after completing these fabrications steps is shown in figure 4.2(f).

The Al_2O_3 top-gate oxides were grown at the Melbourne Centre of Nanofabrication by atomic layer deposition (ALD) using TMA and water precursors at 200°C. Nucleation issues on the graphene were mitigated by increasing the water residence time with a double pulse within the first 50 cycles [214]. This deposition resulted in 80-nm-thick Al_2O_3 across the entire diamond, figure 4.2(c). The metallic top-gate was fabricated by

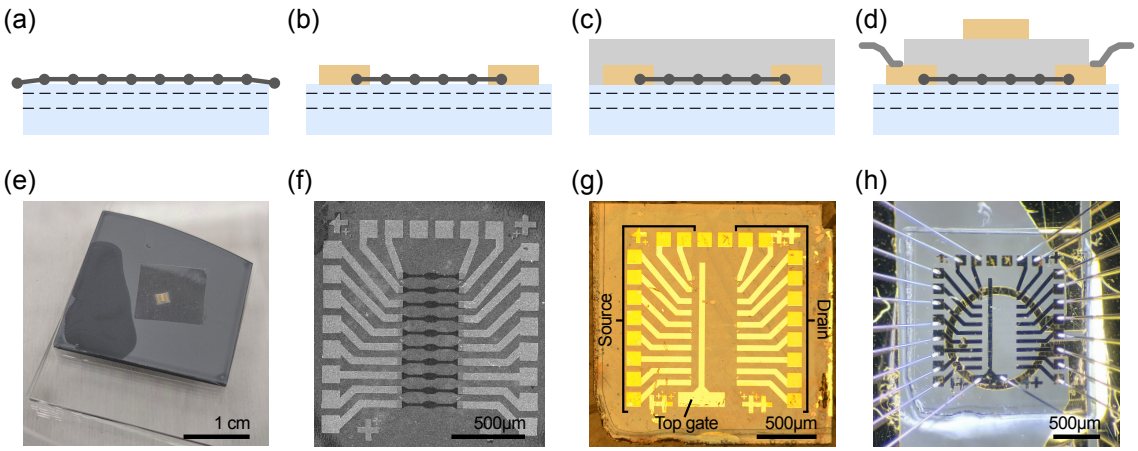

Figure 4.2: Fabrication of GFETs on diamond. (a) Mono-layer polycrystalline graphene was transferred to NV diamond substrates using a standard wet chemical technique. (b) Graphene ribbons and Cr/Au source-drain contacts were patterned using photolithography. (c) Atomic-layer deposition was used to deposit 80 nm of Al_2O_3 across the sample. (d) A Cr/Au top-gate was fabricated on top of the diamond using photolithography and electron-beam evaporation as for the source drain contacts. The oxide was selectively etched over the source-drain bonding pad and electrically contacted with Al wires. (e) Photograph of graphene-PMMA film drying over an NV-diamond substrate mounted to a silicon wafer. (f) SEM image of diamond with patterned graphene ribbons and Cr/Au source drain contacts. (g) Photograph of devices after fabricating the metallic top-gate and etching the oxide over the source-drain bonding pads. (h) Photograph of the wire-bonded device on a microwave resonator coverslip and ready for NV imaging.

photolightography and electron-beam evaporation as for the source-drain contacts (Cr/Au 10 nm/70 nm). The source-drain-contact bonding pads were exposed by etching the oxide in a 8% NH_4OH solution at 50°C for 25 min, through a photolithographic mask. The photo of diamond #230 taken after these steps, figure 4.2(g), shows a slight discolouration of the source-drain bonding pads as compared to the source-drain contacts due to the removed oxide. Finally, the diamonds were removed from the silicon substrates used to ease handling throughout fabrication and glued to resonator coverslips and PCBs. After wire bonding to the top-gate and source-drain bonding pads with Al wires, the samples were ready to image, figures 4.2(d) and (h).

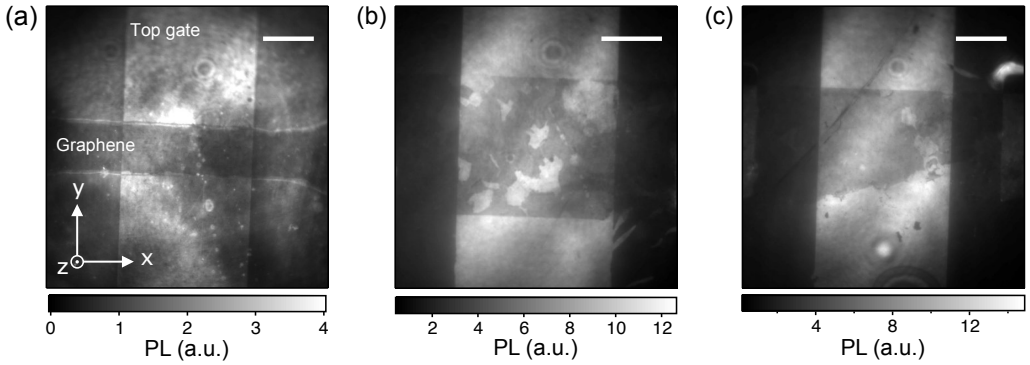

Figure 4.3: Photoluminescence images of three GFET devices. (a) Device 5 on diamond #230. (b) Device 2 on diamond #200. (c) Device 3 on diamond #200. The graphene ribbons are visible via a FRET effect with the NV layer which reduces the photoluminescence, while the top gate is visible due to an enhanced photoluminescence from a standing wave formed with the reflected laser. All scale bars are 20 μm.

4.3 Photoluminescence and electrical characterisation

After fabrication, the devices were imaged by collecting the NV-layer photoluminescence under continuous wave illumination as outlined in chapter 2. One benefit of using a near-surface NV ensemble for this project is that it allows us to directly image the graphene via a Förster resonant energy transfer (FRET) effect, which non-radiatively dissipates excitations in the NV-layer via the graphene, and therefore reduces the NV photoluminescence under the graphene [64, 65]. Figure 4.3 shows photoluminescence images of three devices where the graphene ribbons are visible due to the FRET effect. The metallic top gate appears bright in these images due to NV layer residing at a maximum of the standing wave formed with the reflected excitation laser [60]. The oxide thickness was chosen deliberately to facilitate this to enhance the photoluminescence count rate under the gate. The photoluminescence images show that the thinner graphene ribbons on diamond #230, figure 4.3(a), are in better condition than those on diamond #200 which were torn at some point during fabrication, figure 4.3(b) and (c). Despite this, the devices on diamond #200 are fully functioning and are the focus of the following work given the superior photoluminescence count rate and optical spin contrast of the NV layer in diamond #200.

To electrically characterise the GFET devices, we measured both their source-drain resistance and doping level throughout their lifetime using a source-measurement unit

(Keithley SMU 2450). The source-drain resistances varied between 6 kΩ and 13 kΩ for the 50 μm wide devices on diamond #200 (100 μm between source to drain contacts), and between 16 kΩ and 91 kΩ for the 20 μm wide devices on diamond #230 (400 μm between source to drain contacts). We attribute this spread to different doping in each channel at zero applied gate potential, and varying degrees of tearing in each graphene ribbon. Plots of the source-drain current, I_{SD}, as a function of the applied source-drain potential, V_{SD}, for three devices on diamond #200 are shown in figure 4.4(a), indicating good ohmic behaviour. The doping of each device was determined by measuring transport curves for each device, in this case, by tracking the source-drain current under a fixed source-drain potential while varying the applied gate potential, V_G. A conductivity minimum, which indicates the charge neutrality point and transition from majority p-type to n-type doping in the gated-graphene channel, was observed in most devices. Figure 4.4(b) shows transport curves of devices 1, 2, and 3 on diamond #200, taken at $V_{SD} = 100$ mV under CW laser illumination, indicating conductivity minima at $V_G \approx -11$ V.

Repeated electrical characterisation of the devices throughout their lifetimes revealed variations in their transport curves and resistance measurements. The conductivity minima were found to shift significantly depending on the measurement conditions and the history of the device, specifically, the applied gate potential and illumination conditions prior to the measurement. This effect is studied thoroughly in appendix A.2.1. We attribute this to a photon-assisted charge transfer between the graphene and oxide, similar to the optical-doping seen with other gate dielectrics and substrates [215–217]. In addition to the photodoping effect, we observe hysteresis in our transport curve measurements, even when measuring in the dark. The hysteresis is likely due to screening of the electric field associated with the gate potential by an accumulation of trapped charge at both the graphene-oxide interface and within the oxide bulk. This has been demonstrated to cause similar hysteresis in graphene devices on SiO_2 [218, 219], and may be associated with the density of growth-related defects in the graphene itself [220]. The presence of the laser is likely to exacerbate this situation by creating additional trapped mobile charges within the oxide [221]. Despite the variation of conductivity minima, the photodoping and hysterisis are sufficiently stable and reproducible under fixed illumination and gate potentials conditions in an individual device to maintain doping of a given type (i.e. n-type or

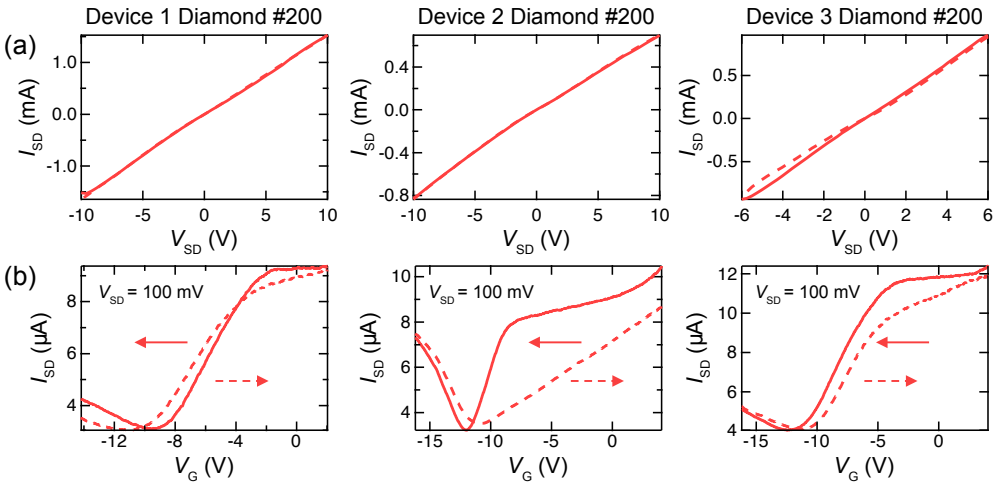

Figure 4.4: Electrical characterisation of GFETs. (a) I_{SD} versus V_{SD} measurements of three devices from diamond #200. Averaging linear fits of the increasing and decreasing sweeps gives resistances of 6.38 kΩ, 13.21 kΩ, and 6.49 kΩ for devices 1, 2, and 3 respectively. Solid (dashed) lines indicate increasing (decreasing) V_{SD} sweeps. (b) Transport curves for the same three devices showing neutrality points at $V_G \approx -11$ V, measured with a small source-drain current, $I_{SD} = 100$ mV under CW laser illumination. Solid (dashed) lines indicate decreasing (increasing) V_G sweeps. The device current was left to equilibrate at the initial point of each sweep prior to sweeping the gate potential.

p-type) over the time frame required for current-density imaging.

4.4 Current density reconstruction: Biot-Savart Inversion

Before presenting the current density imaging of our GFET devices, we pause to explain the method used to transform an ODMR measurement of static magnetic field, which we saw implemented in chapter 3, into the current density maps presented here and in chapter 5. This method has been utilised in previous work from our group [60, 65]. For a more detailed discussion of this process see the recent publication by Broadway et al. [16] which compares the benefits of various approaches to the reconstruction of current densities and magnetisation of ferromagnetic materials from static field images.

The ODMR measurement, which is the basis of the current density reconstruction, is taken in much the same way as outlined in chapter 2 and demonstrated in chapter 3. A bias field is used to split the eight spin-transition frequencies of the four NV-family orientations such that they are individually resolvable, giving spectra qualitatively similar to that

shown in figure 3.3(a). Photoluminescence is accumulated over a microwave frequency range incorporating these resonances, and the resulting ODMR spectrum is fit pixel-by-pixel, extracting the frequency, linewdith and contrast parameters for each resonance. The resonance frequencies are then used to reconstruct the magnetic field projection along each NV-family axis by relation to the NV spin-Hamiltonian, and converted to Cartesian lab-frame coordinates using a previous calibration measurement [145, 222]. Rather than subtracting the background field associated with the biasing permanent magnet as in chapter 3, here we took secondary ODMR images without an injected source-drain current which was then subtracted from the current-on measurement to control for any magnetic or electric field features not associated with the carrier transport in the GFET, leaving a map of the isolated Ørsted field.

After imaging the Ørsted field due to charge transport in some nearby device, we can reconstruct the responsible current density distribution under certain assumptions. To this aim, we look to the Biot-Savart law which describes the relationship between a current density distribution and the resulting magnetic field. The Biot-Savart law relates these quantities via a real-space integral,

$$\mathbf{B}(\mathbf{r}) = \frac{\mu_0}{4\pi} \int d^3\mathbf{r}' \frac{\mathbf{J}(\mathbf{r}') \times (\mathbf{r} - \mathbf{r}')}{|\mathbf{r} - \mathbf{r}'|^3}, \tag{4.1}$$

where $\mathbf{B}(\mathbf{r})$ is the magnetic field due to a current density, $\mathbf{J}(\mathbf{r})$, and μ_0 is the vacuum permeability. Equation 4.1 is in general difficult to solve for the current density, however, provided that the current density is restricted to a plane, i.e. $\mathbf{J}(\mathbf{r}) = (J_x(x, y), J_y(x, y), 0)$ the problem can be solved easily in Fourier space. By taking a two-dimensional Fourier transform of equation 4.1 in the case of a planar current distribution and invoking current-density continuity, $\nabla \cdot \mathbf{J} = 0$, we arrive at a straightforward relation of the Fourier space magnetic field and planar current densities. For instance, using the out-of-plane field component, B_z, we get

$$j_x = \frac{\alpha k_y}{ik} b_z, \tag{4.2}$$

$$j_y = -\frac{\alpha k_x}{ik} b_z. \tag{4.3}$$

Here, the Fourier-space current density and magnetic field vectors are given by $\mathbf{j} = (j_x, j_y)$ and $\mathbf{b} = (b_x, b_y, b_z)$ respectively, and k_x and k_y are the Fourier-space vector components with $k = \sqrt{k_x^2 + k_y^2}$ and $\alpha = 2e^{kz}/\mu_0$ (propagation from current plane to NV layer, separated by a distance z). Calculating the current density from a measurement of the magnetic field can therefore be achieved by taking a Fourier transform of the B_z image produced from an ODMR measurement, computing the in-plane Fourier space current densities via equations 4.2 and 4.3, and recovering the real-space current densities via an inverse Fourier transform. Note that it is possible to reconstruct the current density from expressions analogous to equations 4.2 and 4.3 that are dependent on the b_x and b_y components instead of both being derived from the b_z component. This can be advantageous in that it minimises artefacts associated with the Fourier transform [16], however, here we favour reconstruction from b_z because the in-plane field measured from our GFETs was found to be anomalously small, similar to the anomaly reported in Ref. [60], albeit to a lesser degree in the present case.

One consequence of reconstructing the field from z-component of the magnetic field is the need to deal with the slowly vanishing nature of the z-component far from the conductive wire. Computing the Fourier transform of B_z with a remnant field at the edge of the image gives rise to artefacts in Fourier space, and hence affects the computed current density. There are various strategies to deal with this issue. Here we artificially pad out our B_z images in the y-direction beyond our field of view and linearly extrapolate the remnant field in this region to minimise these truncation artefacts in the Fourier transform [16, 60].

4.5 Transport mapping under doping

Now that we have established the method by which current densities can be reconstructed from ODMR imaging of their associated Ørsted field, we can move to current mapping in our GFETs under different doping conditions. For this measurement, we will look at device 2 on diamond #200. To create a suitably large Ørsted field for our ODMR measurements, i.e. one that gives at least kilohertz shifts for the NV-spin resonances, a large source-drain need to be applied. For these current mapping experiments, we maintain a constant total

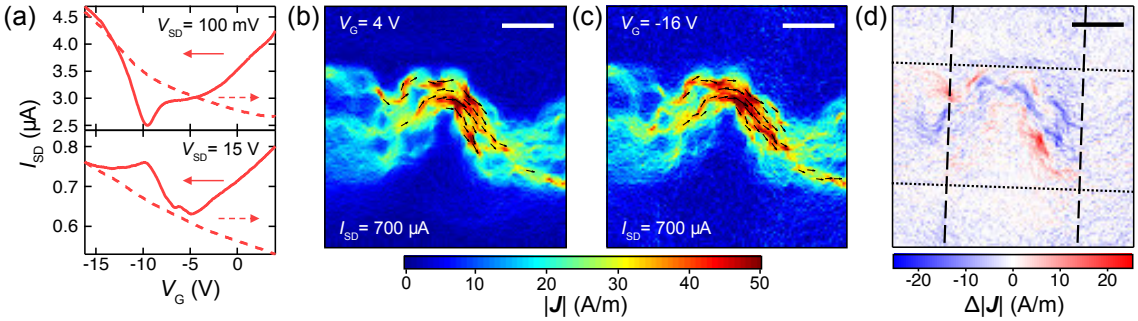

Figure 4.5: Current density mapping under n-type and p-type doping. (a) Transport curves of device 2 on diamond #200 just prior to current density mapping taken with $V_{SD} = 100\,\text{mV}$ (upper) and $V_{SD} = 15\,\text{V}$ (lower), the latter of which is representative of that used during acquisition to give $I_{SD} = 700\,\mu\text{A}$. The device current was left to equilibrate at the initial point of each sweep under laser illumination before the gate potential was swept with the laser on to best capture the effects of photodoping and interfacial charge accumulation. Arrows denote the sweep direction. (b) Current density map under mostly n-type doping, $V_G = 4\,\text{V}$. (c) Current density map under mostly p-type doping, $V_G = -16\,\text{V}$. Each map was made with a constant injected current, $I_{SD} = 700\,\mu\text{A}$, throughout the measurement. Vector arrows are shown for pixels with a current density $> 30\,\text{A/m}$. (d) Difference in norm current density map between the current densities under $V_G = 4\,\text{V}$ and $V_G = -16\,\text{V}$. The dashed and dotted lines mark the edges of the gate and graphene respectively. All scale bars are $20\,\mu\text{m}$.

injected current $I_{SD} = 700\,\mu\text{A}$ throughout the hour-long ODMR measurement, which is facilitated by varying the source-drain potential about $V_{SD} \approx 15\,\text{V}$ to compensate for changes in the device resistance.

Electrical characterisation of the chosen device indicated that we could reliably dope the graphene channel to n-type or p-type throughout a current imaging ODMR measurement, figure 4.4(b). However, to confirm this we need to re-characterise our device at the higher source-drain potential required from this measurement. Figure 4.5(a) shows two transport curves for device 2 taken with $V_{SD} = 100\,\text{mV}$ (upper) and $V_{SD} = 15\,\text{V}$ (lower) under CW laser illumination just prior to current mapping. For the decreasing gate potential sweeps, conductivity minima are observed at $V_G = -9\,\text{V}$ when $V_{SD} = 100\,\text{mV}$, and $V_G = -5\,\text{V}$ when $V_{SD} = 15\,\text{V}$. The shift in the conductivity minimum and altered shape of the transport curve at higher source-drain potentials are due to V_G being referenced to the drain contact and V_G being of comparable magnitude to V_{SD}. For the increasing V_G sweeps, we observe conductivity minima at $V_G \approx 4\,\text{V}$ and $V_G > 4\,\text{V}$

for the lower and higher V_{SD} cases respectively, where the end-of-range is set to mitigate leakage current through the oxide. The stark difference between transport curves measured with different sweep directions is due a photodoping effect in the graphene channel. The difference in the $V_{SD} = 100\,\text{mV}$ transport curve from that shown in figure 4.4(b) is due to the degradation of the device due to interceding measurements at sustained high gate potentials. Both of these effects are studied in appendix A.2.1 but are omitted here for brevity. Accounting for the gate-potential-dependent photodoping, we conclude that fixed gate potentials of $V_G = 4\,\text{V}$ and $V_G = -16\,\text{V}$ give n-type and p-type doping of the graphene ribbon respectively, and can be maintained under subsequent laser pulsing, and hence move to acquire current density maps under each of these conditions.

The reconstructed current density maps of the GFET under n-type and p-type doping, figures 4.5(b) and (c) respectively, show broadly similar current distributions. In both images the current density increases under the top gate as charge carriers are restricted to narrow passages due to the tears in the graphene identified in figure 4.3(b). We note that in these devices, unlike in Ref. [60], there was little apparent current leakage into the diamond, and hence, we neglect this point in the subsequent discussion. Taking a subtraction of the norm current density at each pixel between the two doping conditions, however, reveals clear differences in the current distributions, figure 4.5(d). In principle, doping-dependent current distributions could arise from a number of effects including inhomogeneous doping of the graphene channel, gate-controlled steering of carriers [207], and gate-induced changes to charge defects which have different consequences to the scattering of electrons and holes [223–227]. Unfortunately, in this case the observed variation between doping conditions is mostly the result of degradation of the graphene ribbon during the measurement which is visible in photoluminescence imaging. Figure 4.6(a) is a photoluminescence image taken prior to the $V_G = 4\,\text{V}$ (mostly n-type) measurement, which was the first of the two doping conditions measured. Comparing this image to one taken after the $V_G = -16\,\text{V}$ (mostly p-type) map, which was the second measurement performed, we observed some regions where the reduced photoluminescence associated with the graphene ribbon has vanished, figure 4.6(b). Specifically, a subtraction of these two photoluminescence images highlights two regions, marked as 1 and 2 in figure 4.4(c), where the FRET effect has vanished following the p-type current mapping. Photoluminescence

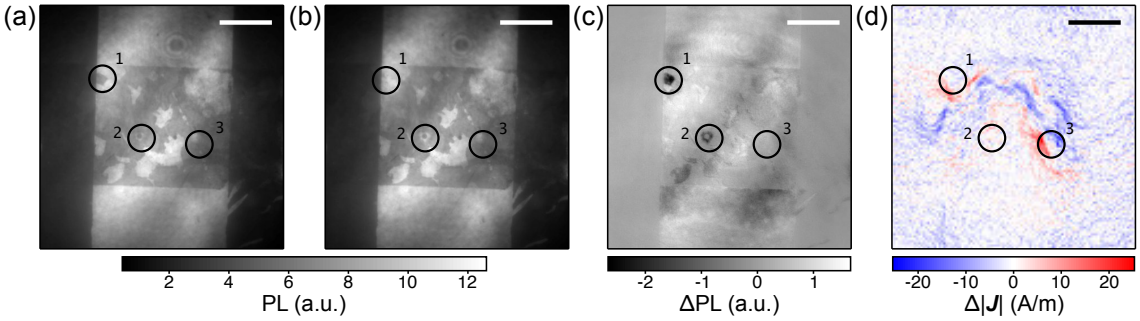

Figure 4.6: Photoluminescence imaging of graphene degradation. Photoluminescence images of the current-density-mapped GFET device at $V_G = 0\,V$ taken: (a) before mapping at $I_{SD} = 700\,\mu A$ and $V_G = 4\,V$; and (b) after mapping at $I_{SD} = 700\,\mu A$ and $V_G = -16\,V$. (c) Subtraction of photoluminescence images in (a) and (b). (c) Difference in norm current densities under doping conditions $V_G = 4\,V$ and $V_G = -16\,V$ for comparison with the subtracted photoluminescence map. All scale bars are $20\,\mu m$.

imaging between the two measurements indicate that these changes occurred during the $V_G = -16\,V$ measurement. The fringes visible across the device in the subtraction are due to a slight shift in the optics between measurements.

Comparing the photoluminescence-difference image to the current-density-difference image, figure 4.6(d), shows that there is a significant current deviations close to tear 1, while tear 2 does not seem to have a significant impact on the current density. Interestingly, the region showing the most distinct change in current distribution, marked 3, shows no local change in photoluminescence at our imaging resolution. This could still be due to tearing downstream from the deviation, or a tear that is difficult to image at our resolution as the deviation occurs near an already narrow constriction (a few microns). To further investigate these non-trivial variations in current density, repeated imaging of the device under varied doping conditions is necessary. Unfortunately, such interrogation is precluded by the gradual deterioration of our devices throughout measurement, which prevents us from precisely replicating measurement conditions. Such degradation was observed following sustained high source-drain currents ($I_{SD} > 500\,\mu A$) and at high gate potentials ($|V_G| > 8\,V$), conditions necessary to map current densities in different carrier-type regimes. Additional observation of this degradation as related to the photodoping effect are covered in appendix A.2.1. These issues motivate the design of a new generation of graphene devices in which the graphene channel is better isolated from the diamond-

oxide interfaces, for example, by encapsulation in hexagonal boron-nitride.

4.6 Gate-dependent photoluminescence

During our current density mapping experiment we noticed an unexpected effect at the large gate potentials required to dope the graphene channel to p-type. At these large negative gate-potentials we observed that the total photoluminescence of the near-surface NV ensemble was reduced significantly. To investigate this effect, we devised a measurement to track the NV photoluminescence under CW laser illumination while varying the gate potential. Each applied potential was left to settle for a short amount of time, $\sim 1\,\mathrm{s}$, before recording the associated photoluminescence to ignore fast transients associated with oxide charging. The photoluminescence at a given gate potential was averaged over approximately 100 exposures each 20 ms in length to average out temporal fluctuations in the excitation laser intensity, before applying a new potential and repeating the process. A small source-drain potential, $V_{\mathrm{SD}} = 100\,\mathrm{mV}$, was applied to track the device conductivity throughout the measurement.

Here we investigate the gate-potential-dependent photoluminescence at device 2 on diamond #200. The gate potential is swept across from 4 V to −16 V and back, after being left to equilibrate at $V_{\mathrm{G}} = 4\,\mathrm{V}$ under laser illumination. The charge-neutrality point can be seen in the transport curve measured during this sweep at approximately −12 V, figure 4.7(a). Comparing photoluminescence snapshots from the endpoints of the sweep, we see a clear quenching of the NV photoluminescence about the device at the lower gate potential, figure 4.7(b). To map this effect, we look at the photoluminescence averaged across a 2 V window at either end of the sweep, PL_- and PL_+, and plot the normalised difference between these quantities (ΔPL norm. $= 1 - \mathrm{PL}_-/\mathrm{PL}_+$) across for field of view, figure 4.7(c). The normalised photoluminescence difference image shows that photoluminescence is quenched only beneath the metallic top gate in regions next to but not directly under the graphene ribbon. Area normalised curves of the photoluminescence as a function of gate potential show that for these regions the photoluminescence is constant above $V_{\mathrm{G}} = -8\,\mathrm{V}$, and then declines by up to 25 % as V_{G} approaches −16 V. Surprisingly, this effect extends laterally from the graphene ribbon by up to $20\,\mu\mathrm{m}$, figure 4.7(e). We note

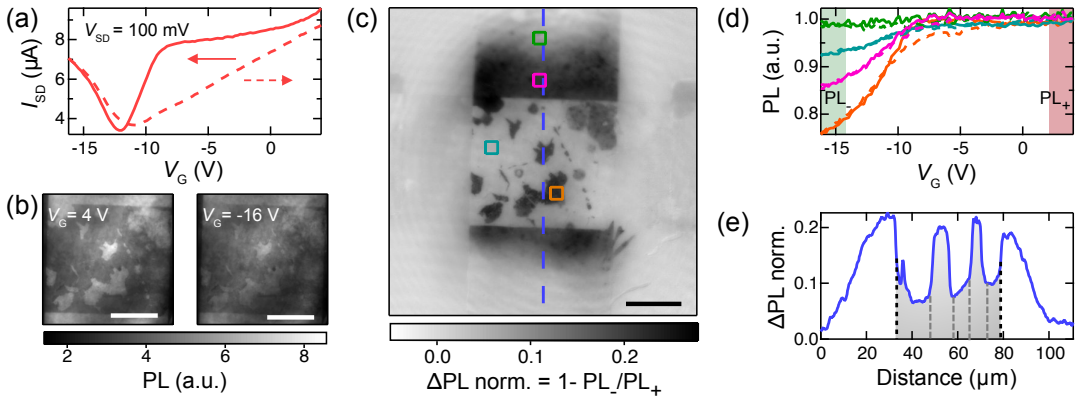

Figure 4.7: Gate-potential-dependent photoluminescence. (a) Transport curve of device 2 on diamond #200 measure in parallel to the photoluminescenec measurement. The sweep moves from high to low gate potentials (solid) and then reverses (dashed). (b) Photoluminescence snapshots the gated region of the device at th extrema of the measurement, $V_G = 4\,V$ and $V_G = -16\,V$. (c) Normalised photoluminescence difference map across the device. The difference is taken between photoluminescence accumulated between $V_G = 2\,V$ to $4\,V$ (PL_+) and between $V_G = -16\,V$ to $-14\,V$ (PL_-) and normalised by the former, i.e. (ΔPL norm. $= 1 - PL_-/PL_+$). The photoluminescence is averaged across both sweep directions. A settling time of 0.5 s with 5 camera cycles per data point was used for this sweep to minimise fringe artefacts from drifting optics. The coloured squares and dashed line indicate the areas and profile studies in (d) and (e) respectively. (d) Photoluminescence curves of four regions surrounding the GFET, specifically, a tear in the gated graphene region (orange), pristine gated graphene (blue), and two regions under the gate at 5 μm (pink) and 20 μm (green) from the graphene ribbon edge. Solid (dashed) lines shows photoluminescence measurements as the gate potential decreases (increases). Each sweep is normalised to the value at $V_G = 4\,V$ to aid comparison. A settling time of 2 s with 50 camera cycles per data point was used for this sweep. (e) Profile of the normalised photoluminescence difference across the graphene ribbon parallel to the gate. The edges of the graphene ribbon (tears) are indicated by the black (grey) dashed lines. All scale bars are 20 μm.

that the magnitude of this photoluminescence quenching increases throughout the lifetime of the device, particularly following sustained measurement at large gate and source-drain potentials (see appendix A.2.1).

As discussed in sections 1.2.1 and 1.3.1, there are a number of phenomena that can alter the photoluminescence of near-surface NV centres. A likely explanation in our case is that a large electric field is present at the diamond-oxide interface which alters the NV^-/NV^0 charge-state ratio via the associated band bending within the diamond, as in the case of various chemical terminations to the diamond surface [18–20]. Such an effect has been observed previously in experiments applying a gate electric field directly to NV centres, but not due to the gating of a proximal device [56–58]. Here, we suggest that large negative gate potentials populate/depopulate charge defects at the diamond surface, which could be defects associated with the diamond-oxide interface, oxide bulk, or known acceptor layer at the diamond surface [26]. At some threshold population shift, associated with the $V_G = -8\,V$ onset of photoluminescence quenching seen in figure 4.7(d), the resultant band bending in the diamond is significant enough to alter the NV^-/NV^0 charge state ratio in the NV layer and hence reduce the photoluminescence. The comparative abundance of charge carriers in the graphene is expected to screen this effect, and therefore we only observe photoluminescence quenching close to the gated device, but not directly under the graphene ribbon. The large spatial extent of the effect is likely due to a diffusion of charge outwards from the device, over length-scales not incompatible with previous observations in diamond [228]. We note that the charge-state stability and dynamics under illumination and in the dark may also be altered by the gate potential through the local charge environment within the diamond [25, 31].

4.7 Electric field imaging

To test the outlined hypothesis, we attempted to quantitatively image the electric field via an ODMR measurement and compare with our gate-dependent-photoluminescence images. As discussed in section 1.2.3, electric fields can be measured quantitatively via the Stark effect acting on the NV ground state spin levels [15]. To achieve this, we performed an ODMR measurement similar to that made for the Ørsted field imaging, but

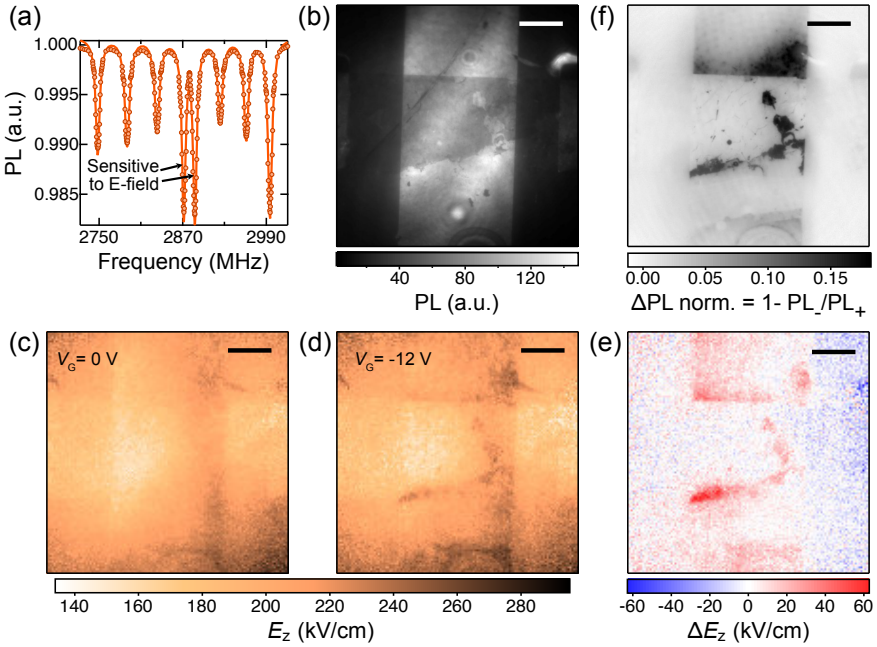

Figure 4.8: Electric-field imaging. (a) ODMR spectrum optimised for electric field sensing by minimising the biasing magnetic field projection along one NV-family orientation and enhancing their optical contrast. (b) Photoluminescence image of the device 3 on diamond #200, taken under CW illumination. (c) and (d) are electric field images at applied gate potentials $V_G = 0\,V$, and $V_G = -12\,V$ respectively. The map was extracted from the electric-field-sensitive resonances, presuming the field lay only in the z-direction for simplicity. A small source-drain potential was applied for each measurement $V_{SD} = 100\,mV$ to track the conductivity of the device. (e) Map of the difference in electric fields measured at $V_G = -12\,V$ and $V_G = 0\,V$. (f) Normalised photoluminescence difference between the photoluminescence across $V_G = -1$ to $+1\,V$ and $V_G = -13$ to $-11\,V$, normalised by the former value, as in figure 4.7 but with shifted accumulation bands to mirror the electric-field-imaging conditions. The data was taken using a $0.5\,s$ settling time and 5 camera accumulations per gate potential value. All scale bars are $20\,\mu m$.

now with the biasing magnetic field oriented to minimise the magnetic field projection along one NV-family axis, thereby enhancing its electric-field sensitivity, but still allowing each individual resonance to be resolved [10, 18]. The optical contrast of these transitions was selectively enhanced by rotating the linear polarisation of the excitation laser to further improve sensitivity [68]. The ODMR spectrum optimised for electric-field imaging of our GFETs is shown in figure 4.8(a). In fitting the extracted resonance frequencies to a Hamiltonian model to quantify the electric field, we opted for a simplified model where we consider only electric field components in the z-direction to make the fitting more robust. The z-component should be the dominant contribution for a space-charge layer at the diamond-oxide interface, expect for at the edge of the layer where fast vanishing in-plane terms may persist.

Here we study device 3 on diamond #200, pictured in raw photoluminescence in figure 4.8(b). We performed ODMR-based electric-field imaging under two gate conditions, the first with no applied potential, $V_G = 0\,V$, and the second a potential over the threshold where we start to observe photoluminescence quenching, $V_G = -12\,V$. Images of the electric field in the z-direction across the field of view are shown in figures 4.8(c) and (d) for each of these conditions. In both measurements, the electric field is up to $40\,kV/cm$ less in the NV layer under the graphene ribbon than directly under the oxide. This may be partially due to the graphene modifying space-charge distribution at the diamond surface, and hence decreasing the band bending, or it may be an artefact arising from FRET effect where the graphene quenches the photoluminescence of NV centres closer to the surface, therefore biasing the ODMR measurement in favour of deeper NVs which see a lower electric field. Both measurements also show an enhanced electric field to the right-hand side of the metallic top-gate which is likely due to strain associated with the gate fabrication that is ascribed to electric field by our fitting [229].

The electric field image at $V_G = -12\,V$, shows a clear increase in the field strength at the edges and within tears of the graphene ribbon beneath the top gate. These features are highlighted by taking a subtraction of the two maps, figure 4.7(e), which show the electric field is enhanced by up to $60\,kV/cm$ in these regions, while regions beneath the graphene are unaffected. Having isolated electric field contributions due to gating the device, we can now compare this map to a normalised-photoluminescence-difference map of the same

device, figure 4.7(f). Here we repeated the measurement outlined in section 4.6 on this device, changing the PL_+ and PL_- bands to photoluminesecence accumulated across gate potentials $V_G = -1\,V$ to $V_G = 1\,V$, and $V_G = -13\,V$ to $V_G = -11\,V$, respectively, to mirror the electric field imaging conditions. Comparing these two images, we see a strong spatial correlation between the enhanced electric field and reduced photoluminescence at high gate potential. Quantitatively, we conclude that a $20 - 60\,kV/cm$ increase in the electric field is associated with a $10 - 20\%$ photoluminescence reduction, both similar in magnitude to surface-termination-mediated band bending measured in the literature [18]. Interestingly, the photoluminescence imaging provides a much better-resolved image of the effect. This is likely due to the fact that we collect photoluminescence from both NV^- and NV^0 in this measurement whereas ODMR-based imaging accounts only for NV^-, therefore compounding low signal with the already limited spin-sensitivity to electric fields discussed in section 1.2.3. The fact that ODMR measures only the NV^- charge state means that ODMR-based imaging may under-represent the electric field strength across the NV layer, as the spin-insensitive NV^0 sees a greater field strength by virtue of being closer to the diamond surface. Purely photoluminescence based imaging of electric field may be interesting to pursue in future for applications in which a quantitative measurement can be forfeited.

The above comparison validates our hypothesis that the photoluminescence quenching is electric-field mediated. Although an accumulation of charge at the diamond-oxide interface or within the oxide bulk is the most likely explanation, another possibility is that the electric field is a residual component of the field applied by the gate to dope the graphene channel. To confirm that this is not the case, a finite element method simulation of the purely dielectric response of the system was performed. The simulation indicates that the electric field at $|V_G| = 16\,V$ should be less than $10\,kV/cm$ at the NV layer for distances larger than $5\,\mu m$ from the graphene edge, and thus cannot account for the observations (see appendix A.2.2). The electric field arising due to an accumulation of charge at the diamond-oxide interface or within the oxide bulk, is therefore the mostly likely explanation for the observed electric field and associated photoluminescence quenching, and may also be related to the hysteresis and photodoping effects seen in our electrical characterisation. Explaining the large spatial distribution of this effect, which extends up

to 20 μm from the gated device, is more complicated. Although the exact mechanism is unclear, this accumulation may result from charge diffusion either through the oxide or the diamond itself, mediated by photo-excitation from the laser [228].

4.8 Summary

This work has demonstrated the capabilities of NV imaging to study phenomena associated with working electrical devices, in this case, graphene field-effect transistors. We have demonstrated the use of direct photoluminescence imaging, where a FRET effect between the graphene ribbon and our near-surface NV ensemble provided a simple way to identify tears within the ribbons. ODMR-based current density imaging was demonstrated under different doping regimes, n-type and p-type, where we were able to resolve clear deviations of the current path between these conditions. Although most of these variations were due to degradation in our graphene channel throughout the measurement, the efficacy of the technique is clear and can be readily applied to future devices [1,111,202]. In chapter 5 we will see one such application of current-density mapping, studying superconducting transport in niobium wires where we vary the temperature of the device rather than the doping. Despite preventing a more detailed study of doping-dependent transport phenomena in our GFETs, we used this as an opportunity to study the degradation with NV measurements. By studying the NV photoluminescence as a function of applied gate-potential and corroborating ODMR-based electrometry, we were able to identify a significant electric field present at the NV layer under large gate-potentials. This electric field is likely due to an accumulation of charge at the diamond-oxide interface or within the oxide bulk under large applied potentials, and may be related to hysteresis and photodoping observed in the electrical characterisation of our devices.

This work highlights the invasiveness of NV microscopy in the case of GFETs fabricated directly on an NV-diamond substrate. Namely, we found that control over the average doping in the graphene layer is strongly affected by a gate potential dependent photodoping effect, while degradation in the device from measuring at high gate potentials over the time scales required for NV imaging limits the ability to probe a single device in numerous scenarios. Additionally, we see evidence of a complex electrostatic response

at the oxide-graphene and diamond-oxide interfaces that is not limited to ALD Al_2O_3 dielectric [215–217], which raises the possibility of uncontrolled spatially-dependent doping variations. For future applications of NV microscopy where precise and reliable control over the doping is required, these effects must be mitigated. One possible solution is to decouple the GFET from the diamond by capping the diamond with a metal-oxide bilayer before fabricating the GFET. The extra metallic layer would prevent laser radiation from reaching the GFET [230], drastically reduce any charge transfer effect at the diamond surface by providing an electron reservoir, and could even serve as a bottom gate for the GFET. A downside of this solution is that the graphene layer can no longer be visualised optically through the FRET effect. If fact, we did fabricate such a device where a broad metallic strip was deposited directly on the diamond surface followed by an insulating oxide layer. The metallic layer was used as both a laser shield and the gate contact for graphene ribbons, which were deposited on top of the oxide with metallic source-drain contacts. These devices were in general more robust to imaging at larger current densities and gate potentials, with less variation in their charge-neutrality points following measurement. Direct comparisons to the devices presented in this chapter were precluded due to oxide being compromised during the final fabrications steps, which had its own implications for the gate performance. Further enhancements can made by encapsulating the graphene ribbon in hexagonal boron nitride (hBN), which allows the hBN to be used as a gate dielectric and gives higher-quality graphene. Progress was made towards hBN-encapsulated devices in collaboration with Dr. Nikolai Dontschuk, using a polycarbonate stamp technique, however, this avenue was abandoned following publication of detailed studies of electron phonon instabilities and viscous flow in graphene in such devices [111, 114, 202].

One remaining issue arises from the large source-drain current densities required for NV magnetometry, which may have contributed to the deterioration of our devices here. This requirement is particularly problematic in application to topological insulators, where the limited densities of highly localised current distributions may push the sensitivity limits of NV imaging. The demand for high source-drain currents can be relaxed by improving the sensitivity of the NV-sensing layer. In the present work, we aimed for a mean graphene-NV distance of only $10 - 20\,\mathrm{nm}$ to foster a sizable FRET effect to

facilitate photoluminescence imaging. This requirement has a direct impact on sensitivity by limiting the maximum number of NV centres without compromising the NV spin coherence [24]. However, in principle thicker NV layers (e.g. 200 nm) can be employed without deteriorating the spatial resolution which would remain limited by diffraction ($\approx$ 300 nm) [176]. For instance, the optimised NV-layer in Ref. [132] would provide a ten-fold improvement in magnetic sensitivity. This realisation is the motivation behind method B of NV-diamond fabrication presented in section 2.2.4, which will be used in the remaining chapters, as compared to the method A samples used in this project. With a further increase in collected photoluminescence signal due to the extra metallic layer, NV measurements with source-drain currents in the μA range can be envisaged. Implementing these solutions may allow for minimally-invasive wide-field NV microscopy of GFETs and other electrical devices based on two-dimensional materials.

5

Laser modulation of superconductivity in a cryogenic widefield nitrogen-vacancy microscope

In this thesis we have applied NV-diamond imaging to a range of systems. We used the magnetic field sensitivity of NV centres to study both static and fluctuating magnetic fields associated with minute volumes of metals deposited on the diamond surface. In the previous chapter, we applied this same static magnetic field sensitivity to image current densities within working electrical devices fabricated on the diamond surface. Both of these experiments were carried out using the widefield diamond microscope introduced in section 2.3, at room temperature under ambient conditions. In this chapter, we develop and characterise a widefield NV diamond microscope system in a cryogenic environment, adding another crucial handle to our NV imaging experiments: temperature. The ability to vary temperature in our experiments opens up a range of low-temperature phenomena that were previously inaccessible, and also allows us to track changes in samples over a broad temperature range. Low-temperature phenomena that we can study using cryo-NV imaging include exotic transport phenomena such as superconducting transport and quenching dynamics, and conductive edge modes in topological insulators, as discussed in the previous chapter [181, 199, 200, 203, 204]. As for systems that would benefit from study over a broad temperature range, the broadband magnetic noise associated with metallic nanoparticles studied in chapter 3 is a good example. Here, we were not able to identify the precise origin of the noise in each case, leaving some ambiguity as to whether it arose from the deposited sample or was mediated by defects in the diamond. Having control over the temperature in this case could have helped confirm our speculations by observing changes in the noise signal at characteristic temperatures, for example, as nanoparticles transition from super-paramagnetic to ferromagnetic state. Such a capability is essential to the study of two-dimensional magnetic materials, an application explored in chapter 6, many of which have Curie temperatures below 100 K [14, 99–101].

NV imaging has only recently been extended to cryogenic conditions, but already a number of impressive applications have emerged, many of which were reviewed in section 1.4.1. However, a question remains as to how viable the technique is for imaging temperature-critical phenomena below 10 K given the laser illumination requirements inherent to the technique, particularly in a widefield configuration. Here we attempt to answer this question by studying a low-critical-temperature sample in a cryogenic widefield system with a base temperature close to the critical temperature. Specifically, we

realise a widefield NV-diamond microscope with a base temperature of 4 K and use it to image Abrikosov vortices and superconducting transport in niobium wires which have a critical temperature of approximately 9 K. We observe the disappearance of the Abrikosov vortices as we increase the laser power used to image, and observe clustering about local hot spots as the laser power is decreased. These observations indicate that there is significant heating of the niobium due to the laser, with powers as low as 1 mW (4 orders of magnitude below the NV saturation) being sufficient to locally quench superconductivity in the film. This significant local heating is confirmed by resistance measurements of the niobium wires, although we find that electrical measurements can under represent the extent of local heating depending on the device geometry. Finally, we study the impact of these local temperature gradients on superconducting transport currents, finding that the current path is correlated with the temperature profile. Despite these observations, we are able to successfully image mesoscale superconductivity phenomena over a 100-μm-wide field of view with submicrometer spatial resolution. We demonstrate that under sufficiency low laser power conditions imaging is minimally invasive to low critical-temperature systems, and offer suggestion to further mitigate unwanted heating from the necessary excitation laser. This work established cryogenic widefield NV-diamond microscopy as an appealing platform for spatially-resolved investigations of a range of low temperature systems from topological insulators to van der Waals ferromagnets.

5.1 Motivation

The NV centre in diamond is most famous for its anomalously good quantum properties at room temperature, which permit high-sensitivity imaging in ambient conditions with applications to biological and condensed matter systems [36, 86]. Though capacity for ambient room temperature operation makes many NV experiments very accessible, requiring little infrastructure to perform, the properties of the NV centre are preserved across a broad range of conditions, including down to cryogenic temperatures. This temperature flexibility means that NV sensing and imaging can be used to interrogate low-temperature physics accessible only below some critical temperature, but also gives us an extra handle by which we can investigate phenomena already accessible at room tempera-

ture. Low-temperature phenomena are of increasing interest to the NV community, which recently has studied transport phenomena, magnetism in low-dimensional systems, and superconductivity at cryogenic temperatures. Applications to transport include probing Johnson noise from metallic films across a broad temperature range using T_1 relaxometry, and in graphene, electron-phonon instabilities and mapping of various hydrodynamic flow regimes as discussed in the previous chapter [111, 112, 114, 202]. Ferromagnetism in two-dimensional materials is an emerging application that has been studied by both scanning and widefield NV experiments [14, 101]. Superconductivity is perhaps the most prevalent low-temperature physics studied by NV microscopy given the broad range of critical temperatures and the typically large magnetic fields associated with superconducting phenomena [102, 103]. Previous NV-microscopy studies of superconductivity have mainly focused on high-T_c superconductors, probing the Meissner effect with ensembles of NV centres [104–108], and achieving nanoscale imaging of microstructures and Abrikosov vortices using scanning single NV experiments [13, 95, 231]. Vortices in a high-T_c superconductor have also been imaged using widefield imaging of NV ensembles [109].

Despite the growing popularity of low-temperature applications, the viability of applying NV microscopy to more temperature-sensitive systems, such as superconductors with a $T_c \lesssim 10\,\mathrm{K}$ or electronic systems in the ballistic regime, remains to be seen. Indeed, at low temperatures the "non-invasiveness" of NV imaging becomes questionable given the appreciable laser intensity impinging on the sample (up to $\sim 1\,\mathrm{mW}/\mu\mathrm{m}^2$, corresponding to saturation of the NV optical cycling) and microwave power (milliwatts to watts) necessary to initialise, manipulate, and read out the NV spin state. Application of these fields can cause undesirable heating of the sample of interest and hence potentially affect the imaged phenomenon. Widefield imaging, despite its many appealing qualities, is particularly challenging in this respect owing to the significant total laser power required to image a large area in parallel, up to hundreds of milliwatts for a field of view $100\,\mu\mathrm{m}$ across. Such powers are much larger than the typical cooling power provided by a helium bath of closed-cycle cryostats at a base temperature of $4\,\mathrm{K}$, the state-of-the-art systems used for low-temperature NV-imaging experiments, and hence casts serious doubt over our ability to image phenomena with critical-temperatures in this regime.

In this work, we assess the impact of these essential NV-microscopy components

by imaging superconducting niobium (Nb) devices in a closed-cycle cryostat with a base temperature ($\approx 4\,\mathrm{K}$) close to the critical temperature of Nb ($T_c \approx 9\,\mathrm{K}$). We successfully image a range of superconducting phenomena, including Abrikosov vortices [232] and supercurrent densities, across a 100-μm-wide field of view. By varying the imaging laser power, we are able to assess the local heating caused by the laser via its impact on the imaged phenomena, for example, the local nucleation and suppression of vortices. Electrical resistance measurements are used to quantify heating along the conduction path through the device, and are found to underestimate the degree of heating as compared to local imaging, depending on the precise geometry. Transport currents are imaged within the device in both fully superconducting and normal states, and we observe a non-uniform spatial distribution of the supercurrents associated with the temperature profile seeded by the laser. Through this work, we are able to identify a minimally-invasive laser-power regime for which imaging with sample temperature approaching 4 K is possible, a finding relevant to future low-temperature NV-imaging experiments in both widefield and confocal configurations. Strategies to further mitigate heating from the illumination laser are discussed. Under these minimally-invasive conditions, the widefield NV microscope demonstrated here is an appealing tool for condensed matter studies, which may enable real-space investigations of a range of phenomena such as transport in topological insulators or in low-dimensional electronic systems, magnetisation dynamics in van der Waals ferromagnets and heterostructures, and superconductivity in two-dimensional materials.

5.2 A cryogenic widefield NV-diamond microscope

The cryogenic widefield NV microscope is not dissimilar to the system described in section 2.3, used in the previous two chapters. The fundamental optics remain the same, using a 532 nm CW laser (Laser Quantum Ventus 1 W, coupled to a single-mode fibre) with pulsing enabled by a fibre-coupled acousto-optic modulator (AAOpto MQ180-G9-Fio), rather than the free space alternatives used previously. A 60 mm lens at the output of the fibre is used to adjust the collimation of the laser beam which controls the laser spot size at the sample. The key difference with the cryogenic system is that the sample and some of the optical components are housed in a closed-cycle cryostat (Attocube attoDRY1000),

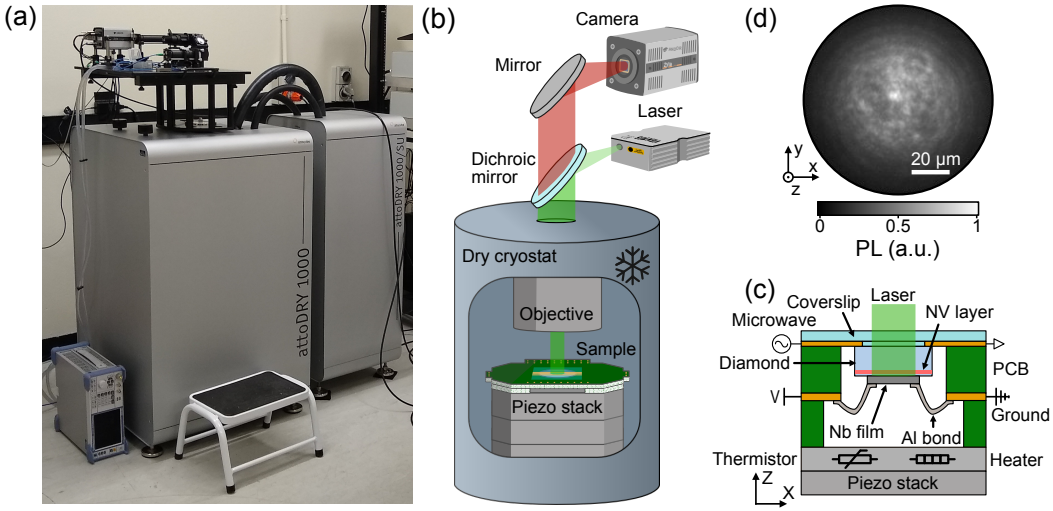

Figure 5.1: A cryogenic widefield nitrogen-vacancy microscope. (a) Photograph of the attoDRY1000 cryostat with an optical breadboard mounted on top. (b) Schematic of the cryogenic widefield NV microscope (see description in text). (c) Schematic of the sample mount (see description in text). (d) NV-photoluminescence image showing illumination over a 100 μm field of view, taken under CW laser illumination at $P_{\text{laser}} = 1.0\,\text{mW}$. Coordinate system used for all subsequent measurements is defined.

pictured in figure 5.1(a). The cold plate of the cryostat is thermally coupled to the sample-holding optical column via a He exchange gas, the pressure of which tunes the base temperature at the sample down to 4.0 K. In these experiments, we use an exchange gas pressure such that $T_{\text{base}} = 4.3\,\text{K}$. The cryostat features a superconducting vector magnet (Cryomagnetics) capable of applying up to 1 T along an arbitrary axis at the sample, $\mathbf{B}_{\text{app.}}$. A dichroic mirror is used to reflect the excitation laser into the optical column through a small window, where it is focused to the back of a low-temperature high-numerical-aperture microscope objective (Attocube LT-APO/VISIR/0.82) located just above the sample. The NV photoluminescence is collected along the same optical path, which includes two 250 mm lenses in the column in a $4f$ configuration to increase the field of view. The photoluminescence passes out of the optical column and is separated from the excitation laser by the dichroic mirror, after which it is filtered through a 731/137 nm band pass filter (the photoluminescence does not change significantly at these low temperatures [233]) and focused by a 300 mm tube lens onto a water cooled sCMOS camera (Andor Zyla 5.5-W USB3) for imaging, as before.

The diamonds used in these experiments were fabricated by method B, outlined in section 2.2.4. Briefly, these are nitrogen-rich type Ib membranes (50 μm thick with [N] $\sim$ 100 ppm), irradiated with carbon atoms at 100 keV and a fluence of $10^{12}\,\mathrm{cm}^{-2}$ to create the vacancies (peak vacancy density $\sim$ 110 ppm at a depth of $\sim$ 130 nm), giving an NV imaging layer extending 200 nm below the diamond surface [132]. As discussed in section 4.8, this method improves our sensitivity due to the enhanced photoluminescence count rate from the thicker ensemble, which we can afford here without sacrificing spatial resolution as the standoff to the deepest NV centres is still less than the diffraction limit. These NV diamonds are mounted to microwave-resonator coverslips as before, which are mounted to custom-designed PCBs. These PCBs are mounted to the cryostat sample stage within the optical column, which is equipped with a resistive heater and a calibrated thermistor (Lakeshore Cernox CX-1050-CU-HT-1.4L), and tri-axial piezo drives for positioning. A temperature controller (Lakeshore 335 Temperature Controller) was used to vary and regulate the near-sample temperature via the thermistor and heater that are both thermally attached to the top Ti plate of the piezo stack. Imaging of the near surface NV-layer occurs through the cover slip and bulk of the diamond, which is mounted upside down, with the NV layer and sample of interest on the underside of the diamond, as shown in figure 5.1(c). Electrical contact to the sample of interest, if necessary, is made via the PCB, as with the microwave circuitry. This microwave infrastructure is similar to that used previously, comprising a signal generator (Rohde & Schwarz SMB100A), switch (Mini-Circuits ZASWA-2-50DR+), and 50 W amplifier (Mini-Circuits HPA-50W-63), while electrical control of the sample are enacted by a source-measurement unit (Keithley SMU 2450).

A typical photoluminescence image taken with this system is shown in figure 5.1(d). Here we see a Gaussian beam giving reasonable illumination across a 100 μm field of view at a total laser power $P_{\mathrm{laser}} = 1.0\,\mathrm{mW}$, measured just before the dichroic mirror. The optical resolution of our system is calculated to be $\approx 0.4\,\mu$m, given the objective numerical aperture of 0.82 and target photoluminescence wavelengths of $650 - 800\,\mathrm{nm}$. In practice, the smallest observed resolvable features are down to 0.7 μm, likely limited by optical aberrations, especially due to imaging through the 150-μm-thick coverslip, and the 50-μm-thick diamond (see appendix A.3.1). We note that turning on the laser at

this power when the cryostat is at the base temperature, the thermistor measures a small temperature change, $\Delta T_{\text{sensor}} = 0.05\,\text{K}$, indicative of the global heating near the diamond sample. To probe the local heating at the point of illumination, we need to image a temperature sensitive sample.

5.3 Fabrication and characterisation of Nb wires

Our target material for this study is Nb, chosen for being one of the highest critical-temperature single-element superconductors, with $T_c \approx 9\,\text{K}$. Nb is a type-II conventional superconductor with critical fields $B_{c1} \ll 1\,\text{G}$ and $B_{c2} \approx 0.4\,\text{T}$ [234]. For these experiments, the magnetic field strength applied by our superconducting vector magnet is always between these two critical fields, $B_{c1} < B_{\text{app.}} < B_{c2}$, as we cannot ensure a field lower than B_{c1} due to residual magnetisation of components within the cryostat. In this regime we expect to see the permeation of the superconductor by quantised flux lines and the associated Abrikosov vortices, but do not expect any magnetic-field-induced quenching of superconductivity.

Four 200 nm-thick Nb devices were fabricated directly on the diamond surface by e-beam thermal evaporation of 99.95% pure Nb through a invar shadow mask. The films feature two square bonding pads (500 μm) connected by a narrow channel (500 μm $\times$40 μm). These devices were fabricated by Dr. Nikolai Dontschuk using facilities in the School of Physics cleanroom at the University of Melbourne. To achieve superconducting Nb, care was taken in preparing the high vacuum of our Thermionics e-beam evaporator. Namely, Nb pellets in a Fabmate crucible were first heated to evaporating temperatures with the sample shutter closed for 10 min. Then Ti was evaporated, again with the sample shutter closed, to bring the chamber vacuum below 10^{-7} mbar via a sublimation effect. Finally the Nb was heated to evaporation temperature and the shutter was opened with an evaporation rate of 6 - 8 Å/s and chamber pressure below 2×10^{-5} mbar throughout the evaporation. Care was taken to ensure sufficient Nb was present in the crucible to avoid damage from the high Nb evaporation temperatures, as visible crucible burning damage correlated with poor quality superconductivity (i.e., low T_c). After deposition of the Nb devices, the diamond was glued to the resonator coverslip and electrically contacted with

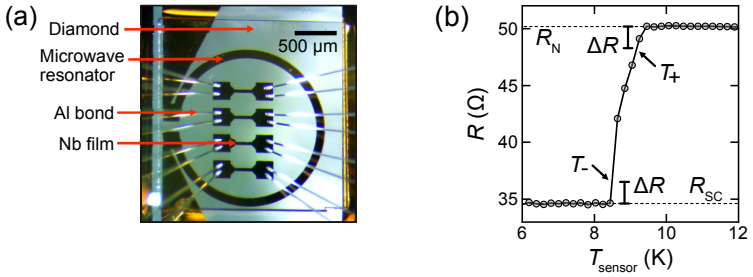

Figure 5.2: Superconducting Nb wires. (a) Photograph of four 200-nm-thick Nb wires fabricated on an NV-diamond, electrically contacted with Al wire bonds. The diamond is mounted to a cover slip with a microwave resonator visible beneath the diamond. (b) R versus T_{sensor} measurement for a single Nb film. The resistance drops from the normal state resistance, R_{N}, to the superconducting resistance, R_{SC}, and is characterised by temperatures T_+ and T_- which differ from R_{N} and R_{SC} by $\Delta R = 0.05 \times (R_{\text{N}} - R_{\text{SC}})$ respectively.

Al wire bonds. The Nb devices are pictured in figure 5.2(a).

Prior to imaging, the devices were characterised electrically to identify their critical temperatures and characterise their transitions to superconductivity. The resistance across each device (R) was measured as a function of the temperature read by the thermistor on the sample holder, T_{sensor}, which is a good representation of the temperature at the sample in this case. The R and T_{sensor} values for a given temperature set by the controller were taken 2 s after the controller was set. We found this was sufficiently long for the values to have settled given the temperature increments of 0.2 K used for this, and all subsequent R versus T_{sensor} measurements. Each of the four Nb devices showed a superconducting transition at a critical temperature $T_c \approx 9\,\text{K}$. Figure 5.2(b) shows this data for one of the Nb devices, where R decreases from the normal-state resistance, $R_{\text{N}} = 50.2\,\Omega$, to the superconducting-state resistance, $R_{\text{SC}} = 34.6\,\Omega$, which corresponds to the resistance of the non-superconducting leads. R_{SC} was similar for all four devices, but R_{N} varied by up to a factor of two, in correlation with the value of T_c. We further characterise this transition by two temperatures points, T_+ and T_-, which correspond to T_{sensor} at resistances $R_{\text{N}} - \Delta R$ and $R_{\text{SC}} + \Delta R$ respectively, where ΔR is a chosen threshold. Given the temperature uniformity of this present characterisation, T_+ and T_- indicate non-uniform Nb quality giving slightly different critical temperatures across the film. As we introduce non-uniform heating due to our excitation laser, however, T_+ and T_- will be

indicative of the coolest and hottest points along the conduction path through the Nb device, and hence provide an avenue by which we can infer spatial information from resistance measurements. Throughout this work we use $\Delta R = 0.05 \times (R_{\mathrm{N}} - R_{\mathrm{SC}})$, to get the most localised information possible while staying above the noise of the electrical measurements. All of the measurements presented from here onward are of the device with the highest critical temperature, the same device characterised in figure 5.2(b). From these resistance measurements we calculated the effective coherence length and magnetic penetration depth of this device at base temperature, $T_{\mathrm{base}} = 4.3\,\mathrm{K}$, to be $\xi(T_{\mathrm{base}}) \approx 6\,\mathrm{nm}$ and $\lambda(T_{\mathrm{base}}) \approx 300\,\mathrm{nm}$ respectively (see appendix A.3.2).

5.4 Imaging superconducting vortices

Now that we have confirmed that the superconducting state is accessible for these devices in our cryostat, we can move to ODMR-based imaging of Abrikosov vortices. In type-II conventional superconductors, Abrikosov vortices arise when a magnetic field is incident on the superconductor with a magnitude $B_{c1} < B_{\mathrm{app.}} < B_{c2}$. In this regime, flux tubes penetrate the superconductor and are surrounded by a supercurrent vortex. The penetrating flux lines are quantised by the magnetic flux quantum, $\Phi_0 = 2.068 \times 10^{-15}\,\mathrm{Wb}$, and therefore, their areal density is dictated by only the incident magnetic field strength, as the flux through the superconductor is conserved across the superconducting transition. The expected number of flux tubes, N, in a given area, A, subjected to uniform magnetic field, $\mathbf{B}_0$, is therefore calculated as $N\,\Phi_0 = \mathbf{B}_0 \cdot \mathbf{A}$. We can use this equation to determine an appropriate biasing field to image this phenomenon and resolve individual flux lines. Considering comfortable benchmark for our optical-resolution-limited imaging of one vortex per $(5\,\mu\mathrm{m})^2$, the corresponding magnetic field is approximately 1 G in the z direction. This constraint presents a challenge to our ODMR imaging technique. Until now, we have relied on biasing field up to hundreds of Gauss such that all eight resonance lines of our NV ensemble could be resolved. Here, we require an alternate approach to accommodate the necessarily low bias field strength for vortex imaging, and comparably low laser powers to minimise heating of the sample.

To manage these limitations, we use continuous wave (CW) ODMR measurement

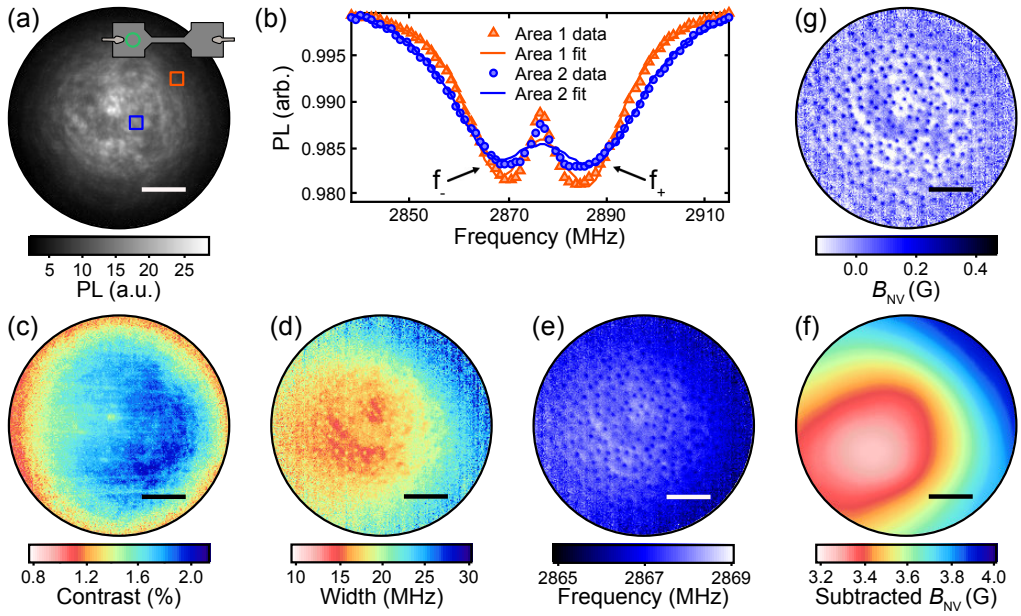

Figure 5.3: Low-field-ODMR imaging of vortices. (a) Photoluminescence image of a region within the large bonding pad of the Nb device (inset). (b) Low-field CW ODMR spectra from two areas highlighted in (a), at higher (blue, circles) and lower (orange, triangles) local laser intensity. The solid lines are the sum-of-two-Lorentzian fits to each data set, which do not accurately capture the narrow central feature. (c) Contrast, (d) width (FWHM), and (e) frequency fit parameters plotted across the field of view. These parameters are from the lower-frequency resonance (f_-), which are qualitatively similar to those from the higher-frequency resonance (f_+). (f) B_{NV} contour subtracted from the field calculated by the frequency splitting, $B_{\mathrm{NV}} = (f_+ - f_-)/(2\gamma_e)$, to remove artefacts associated with our simplified fitting model and inhomogeneous laser illumination across the field of view. The contour is fit to Gaussian features varying over 20 pixels or greater in the raw B_{NV} map, capturing the slow variation seen in the frequency plots. (g) Map of the average magnetic field projected along all four NV axes, B_{NV}, after subtracting the smooth background contour. All scale bars are 20 μm.

sequence with an altered fitting scheme suitable for low-field ODMR spectra. This sequence differs from those used in chapter 3 and 4 by virtue of the microwave field and laser being on continuously in parallel, as briefly discussed in section 1.3.2. Firstly, we demonstrate this approach to ODMR by imaging vortices within the large bonding pad of the Nb device under no applied field from our superconducting magnet. Figure 5.3(a) is a photoluminescence image of this region. The CW ODMR spectra acquired are plotted in figure 5.3(b) for two regions within the field of view, subjected to different local laser intensities. The ODMR spectra show two broad resonances corresponding to the $m_s = 0$ to $m_s = -1$ and $m_s = 0$ to $m_s = +1$ resonance of each NV family collapsed into just two lines at low field. We refer to these two resonance frequencies as f_- and f_+. The line shape of the resonances in this regime is non-trivial due the inhomogeneous environments (charge and spin) and symmetry axes across the ensemble. In particular, the narrow feature separating the two resonances has been explained by Mittiga et al. [177], as arising from random distributions of both local electric field (caused by charge fluctuations in nearby defects) and local magnetic field (spin fluctuations). While in principle it is possible to use the model from Ref. [177] to fit our data and extract the mean value of the magnetic field, we found the convergence of the fit to be very sensitive to the initial guess, and so were not able to obtain consistent fits across the entire field of view, which encompasses more than $10,000$ spectra, each with slightly different illumination and microwave broadening conditions in addition to local field variations. Instead, we fit our data with simple sum-of-two-Lorentzians fit function with independent frequencies, amplitudes, and widths, a slight modification of the function described by equation 2.2. These fits are the solid lines in figure 5.3(b), and while they do not accurately capture the narrow central feature, which may lead to systematic errors in the estimation of the magnetic field, this method was the most robust and allowed us to resolve small magnetic features such as vortices.

Figure 5.3(c), (d), and (e) are plots of the contrast, width, and frequency extracted from the fit across the field of view for one resonance. Each parameter shows long-range variations correlated with the laser intensity which we attribute to fitting errors stemming from our simplified fitting model. For instance, fits to the two spectra in figure 5.3(c) give resonance frequencies $f_- = 2867.8\,\mathrm{MHz}$ and $f_+ = 2886.4\,\mathrm{MHz}$ for Area 1, against

$f_- = 2866.8\,\text{MHz}$ and $f_+ = 2888.0\,\text{MHz}$ for Area 2, however, as evident in the spectra, this difference is really due to a change in width caused mainly by a difference in laser intensity between the two areas, rather than a change of the resonance frequency due to a magnetic field. To calculate the magnetic field from the fit frequencies, we used the approximate formula $B_{\text{NV}} = (f_+ - f_-)/(2\gamma_e)$ [8], however, the resulting map is plagued with unphysical variations seen in the direct frequency plots. These long-range variations are removed from magnetic field image by applying a smoothing filter to the image, which fits features in the raw B_{NV} map that vary over more than 20 pixels and subtracts them, leaving only the short range features (i.e. the vortices). The B_{NV} contour subtracted from the fit data is shown in figure 5.3(g), leaving the relatively clean image of vortices shown in figure 5.3(h). Note that B_{NV} here corresponds to the average projection of the magnetic field along the four different NV axes, since the individual NV families are not resolvable at low field. For a field pointing in the z direction (i.e. normal to the diamond surface, which is the case at the centre of the vortices), the projection is identical for all four NV families in our $\langle 100 \rangle$-oriented diamond, related by $B_{\text{NV}} = B_z/\sqrt{3}$. All vortex images to come are produced by this method and scaled to B_z.

Now that we have established a robust method for imaging superconducting vortices, we can investigate how these vortices change as we vary the conditions of imaging. The image presented in figure 5.3 was taken at zero applied field strength. Despite this, we observe a considerable number of vortices within the field of view. To investigate this further, we image the same region repeatedly while varying the magnetic field applied by our superconducting vector magnet, $\mathbf{B}_{\text{app.}}$, so that we can compare the imaged number of vortices to theoretical expectation, $N\,\Phi_0 = \mathbf{B}_0 \cdot \mathbf{A}$.

Figures 5.4(a) to (e) show B_z images produced from ODMR measurements with $\mathbf{B}_{\text{app.}}$ between $2.0\,\text{G}$ to $-4.0\,\text{G}$ in the z direction. The number of vortices within the field of view changes considerably over this range, and is asymmetric about $B_{\text{app.}} = 0\,\text{G}$. Counting the number of vortices within a fixed area of each image, $(33.81\,\mu\text{m})^2$, we can plot this as a function of the applied field and compare with theory. Figure 5.4(f) shows a linear relation between number of vortices and the applied field, with an effective zero field at $B_{\text{app.}} = -1.4054\,\text{G}$. Accounting for this offset in field strength, $B_0 = B_{\text{app.}} + 1.4054\,\text{G}$, our data compares well with theory, though these is a slight divergence, likely due an

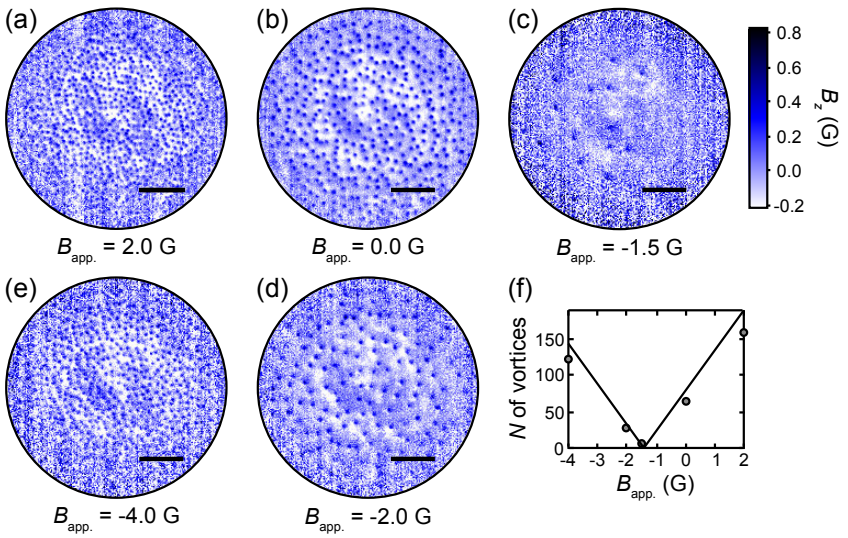

Figure 5.4: Vortex imaging varying the applied field. B_z maps imaged at base temperature, with $P_{\text{laser}} = 0.5\,\text{mW}$, and $\mathbf{B}_{\text{app.}}$ in the z direction with magnitudes: (a) 2.0 G, (b) 0.0 G, (c) -1.5 G. (d) -2.0 G, and (e) -4.0 G. The system was degaussed prior to this imaging series to minimise contributions from magnetic components within the cryostat. All scale bars are 20 μm. (f) Number of vortices, N, within a $(33.81\,\mu\text{m})^2$ area, counted from the previous images, as a function of $B_{\text{app.}}$. The solid line shows $N\,\Phi_0 = (B_{\text{app.}} + 1.4054\,\text{G}) \times A$.

uncalibrated magnification (approximately 10%) from a non-ideal optics setup. Note that the size and magnitude of individual vortex fields deviates from theory expectations, likely due to our simplified fitting model (see appendix A.3.3).

5.5 Laser heating of Abrikosov vortices

The advantage of studying a system with a critical temperature close to the base temperature of our cryostat is that we can investigate the effect that imaging has on low-temperature phenomena, such as superconducting Abrikosov vortices. The previous vortex images were all taken at the base temperature of the cryostat, $T_{\text{sensor}} = 4.3\,\text{K}$, using a very low laser power, $P_{\text{laser}} = 0.5\,\text{mW}$ to mitigate any effects that our imaging may have on the device. Here, we gradually increase the power of our excitation laser and observe the impact that this has on the imaged vortices. The following images were all taken under zero applied field, which we saw corresponds to $\mathbf{B}_0 \approx 1.5\,\text{G}$ in the z direction due to

remnant magnetisation within the cryostat. The sample was cooled to base temperature under this field in the dark prior to imaging.

Figure 5.5 shows the B_z images of vortices in the same region imaged previously, at laser powers ranging from 0.5 mW to 4.0 mW. At $P_{\text{laser}} = 0.5\,\text{mW}$, figure 5.5(a), the B_z image shows vortices distributed evenly across the field of view as before. Increasing the laser power to $P_{\text{laser}} = 1.0\,\text{mW}$, figure 5.5(b), we see the vortices disappear from small pockets near the centre of the image, while those towards the periphery are unchanged. At $P_{\text{laser}} = 2.0\,\text{mW}$ and 4.0 mW, figures 5.5(c) and (d) respectively, we see a large disc at the centre of each image where the vortices are entirely absent, with a radius proportional to the laser power. Comparing the B_z images to maps of the ODMR contrast extracted from the same measurement, figures 5.5(e) to (h), we see that the regions where vortices are suppressed are correlated with regions of reduced ODMR contrast. Supplemental measurements confirm that this contrast reduction is due to a decreased microwave-field strength in these regions, rather than being related to the optical cycling of the NV ensemble (see appendix A.3.4).

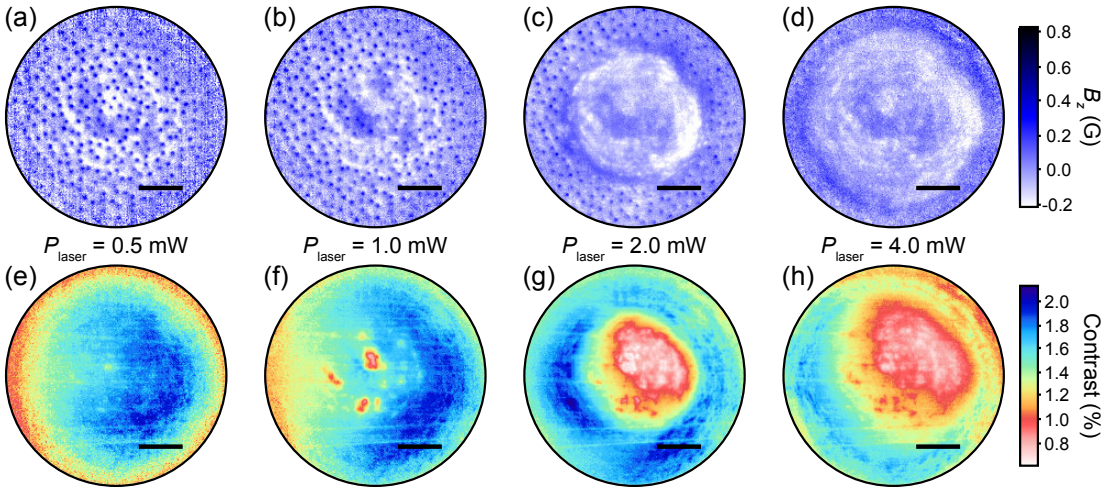

Figure 5.5: Laser heating of Abrikosov vortices. (a), (b), (c), and (d) are B_z images of vortices measured by ODMR at $P_{\text{laser}} = 0.5\,\text{mW}$, 1.0 mW, 2.0 mW, and 4.0 mW respectively, in the same region imaged previously. The sample was cooled to base temperature ($T_{\text{sensor}} = 4.3\,\text{K}$) with the laser off, at a field $B_0 = 1.5\,\text{G}$, and imaged at the same field. (e), (f), (g), and (h) are maps of the optical contrast of a single resonance line extracted from the same ODMR measurements. The reduced contrast near sites of vortex suppression indicates local reduction in the microwave field strength (see appendix A.3.4).

These observations are explained by local heating of the Nb film due to the imaging laser. Prior to the laser being turned on, our device is uniformly at the base temperature of our cryostat. When the laser is turned on for ODMR imaging, the laser spot seeds an inhomogeneous temperature profile at the device. For low laser powers, $P_{\text{laser}} \leq 0.5\,\text{mW}$, the local heating is not substantial enough to affect the vortices. At $P_{\text{laser}} = 1.0\,\text{mW}$, regions exposed to the highest laser intensity are heated upwards of 5 K ($T > T_c$), causing a transition to the normal state and suppression of vortices. Increasing P_{laser} further causes these pockets to merge and form a normal-state disc centred in the field of view. This heating is represented schematically in figure 5.6(a). The local hot spots where superconductivity is quenched first are highlighted in figure 5.6(b), which is simply a photoluminescence image put through the same smooth routing used for the magnetic field maps. The observed reduction in ODMR contrast associated with the region of normal-state Nb is due to it having a lower reflectivity to the microwave field, which attenuates the microwave field strength at the NV layer in this geometry [108].

With this understanding, we can now probe the dynamics of vortex formation. Starting from a laser power that gives a large normal state region ($P_{\text{laser}} = 4.0\,\text{mW}$), we reduce the laser power to one at which the entire Nb film is in the superconducting state ($P_{\text{laser}} = 0.5\,\text{mW}$) and observe the resulting vortex configuration. The timescale over which the laser power is reduced strongly affects the final vortex arrangement. If the reduction is done quickly, by switching the laser off and then turning it back on at the new power after T_{sensor} has stabilised, we see the vortices re-nucleate in the centre of the image but are heavily clustered, figure 5.6(d). If the laser power is reduced more gradually, over $\sim 5\,\text{s}$, the vortices still cluster but to a lesser extent, figure 5.6(e). We see a similar clustering if the entire system is heated above T_c via the heater on the sample stack, and then cooled back to base temperature with the laser turned on, figure 5.6(f). Note that we can recover a uniform vortex arrangement by heating the cryostat above T_c and cooling back down in the absence of laser, figure 5.6(g).

This clustering arises from the inhomogeneous temperature profile seeded by our laser. As the laser power is reduced, regions seeing less laser power transition to the superconducting state first and the vortices re-nucleate. However, as the local temperature is close to T_c in these regions, the vortices are weakly pinned and free to move along the

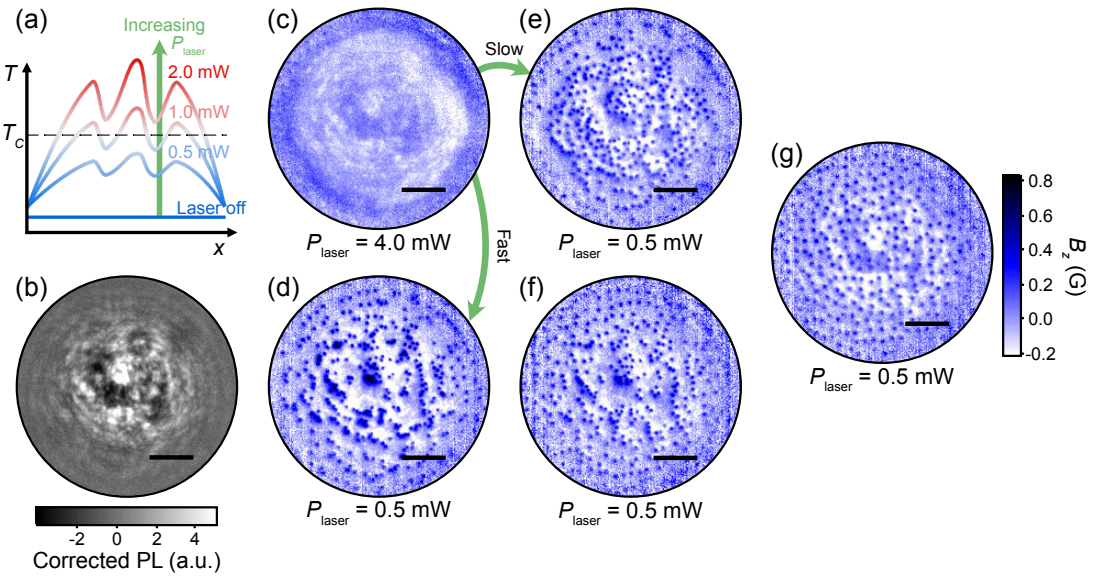

Figure 5.6: Vortex heating and cooling dynamics. (a) Illustration of the local temperature profile across the imaged Nb film due to the excitation laser at various powers, as described in the text. (b) Smoothed photoluminescence image highlighting local hotspots in the Nb film due to the speckled laser beam. Broader variations have been subtracted via the same smoothing algorithm used for the B_z plots. (c) B_z image at $P_{\text{laser}} = 4.0\,\text{mW}$ giving a large normal state region at the centre of the image. (d) B_z image taken at $P_{\text{laser}} = 0.5\,\text{mW}$ after switching the $P_{\text{laser}} = 4.0\,\text{mW}$ beam off, letting T_{sensor} stabilise to base temperature, and then imaging. (e) B_z image taken at $P_{\text{laser}} = 0.5\,\text{mW}$ after gradually reducing from $P_{\text{laser}} = 4.0\,\text{mW}$ over $\sim 5\,\text{seconds}$. (f) and (g) are B_z images at $P_{\text{laser}} = 0.5\,\text{mW}$ after heating the cryostat such that $T_{\text{sensor}} > T_c$ and cooling to base temperature in the presence and absence of laser respectively. All scale bars are $20\,\mu\text{m}$ and all vortex images are taken with $B_0 = 1.5\,\text{G}$.

local temperature gradient [235]. The vortices therefore migrate towards local hot spots until the vortices become pinned when their local temperature is sufficiently far below T_c. The dynamics of the laser power reduction, i.e. switching versus gradual reduction, affect the cooling rates and hence the extent of migration before the vortices become pinned. This phenomenon was studied in detail by our collaborators Sebastian Wolf and Dr. Stephan Rachel, and the results of their simulations can be found in the supplemental information of Ref. [1]. Recently, thermal gradients arising from focused laser beams have been used to pattern vortex fields at the single vortex level [236], while ensembles of vortices have been manipulated by nano-patterned current profiles [237], temperature patterning [238], and local magnetic fields [239]. Widefield NV imaging may therefore be a suitable platform to

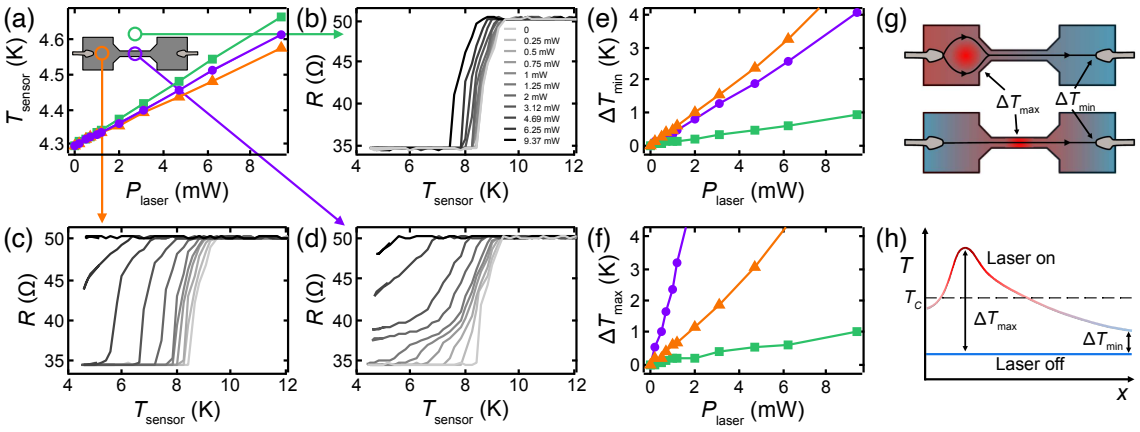

Figure 5.7: Quantifying laser heating with electrical measurements. (a) T_{sensor} versus P_{laser} for the three locations of the laser spot identified on the inset diagram: 200 μm from the Nb film (green), on the narrow Nb channel (purple), and on the centre of the Nb bonding pad (orange). The heater is off for this measurement. (b), (c), and (d) are R versus T_{sensor} for the Nb film at $P_{\text{laser}} = 0$ mW to 9.37 mW (light to dark) with the laser spot located in the three respective locations. The resistance was measured with a 10 μA current under fixed laser conditions as the heater varies T_{sensor}. (e) and (f) show ΔT_{min} and ΔT_{max} respectively, as a function of P_{laser} for the laser spot locations identified in (a). ΔT_{min} and ΔT_{max} are the magnitude of the shift in T_+ and T_- respectively from their values when the laser is off. (g) Schematic of the heating across the device when the laser focused on the bonding pad (upper) and the narrow channel (lower). The location of ΔT_{min} and ΔT_{max} are indicated in each case. (h) Illustrative plot of the temperature profile along the conduction path with the laser on (red) and off (blue), showing the locations of ΔT_{min} and ΔT_{max}.

image these experiments conveniently over 100 μm fields of view.

5.6 Electrical characterisaion of laser heating

The vortex images presented demonstrate the invasiveness of widefield NV microscopy in this configuration, where the sample of interest is directly exposed to the laser. Imaging the Nb film with $P_{\text{laser}} = 2.0$ mW gave a normal-state region nearly the size of the laser spot ($\sim 60\,\mu$m), indicating heating in this region upwards of 5 K given the base temperature of 4.3 K with $T_c \approx 9$ K for the Nb film. This modest laser power corresponds to a peak intensity of 40 W/cm^2, which is 4 orders of magnitude lower than the laser intensity needed to saturate the optical cycling of the NV, often employed in single-NV experiments [240]. Despite the significant heating of the Nb film, the temperature measured by the sensor

on the sample stack remains close to base temperature during these measurements, with $T_{\text{sensor}} < 4.4\,\text{K}$ at $P_{\text{laser}} = 2\,\text{mW}$. Tracking the T_{sensor} as we vary P_{laser} gives a linear response, with a gradient that depends on the location of the laser beam, figure 5.7(a). The sensor is heated more efficiently as a greater portion of the laser in incident on the transparent diamond rather than the opaque Nb. In any case, T_{sensor} remains below 4.7 K for P_{laser} up to 10 mW, implying strong temperature gradients across the sample, which may be overlooked if local indicators are not available.

NV imaging gives us a very local picture of the laser heating, while T_{sensor} gives a more global picture of the heating in the cryostat near the sample. To probe the laser heating on a more intermediate scale, laterally across the entire device, we turn to resistance measurements which are sensitive to the temperature along the entire conduction path across the Nb film. Here, we measure the device resistance, R, as a function of T_{sensor} (controlled by the heater) and P_{laser}, when the laser spot is focused at various locations around the device. We look specifically to T_+ and T_- as defined in figure 5.2(b) to give us a more local insight into the heating. When the laser is focused 200 μm from the Nb film, the R versus T_{sensor} curves shift symmetrically to lower T_{sensor} values as P_{laser} increases, indicating a global heating of the Nb device, figure 5.7(b). When the laser spot is focused on the Nb bonding pad, the curves shift again, but the shape is severely distorted, as T_- moves to lower T_{sensor} values at a faster rate than T_+ as P_{laser} increases, figure 5.7(c). This scenario is exacerbated when the laser is focused on the narrow channel, where the full width of the current path is encompassed by the laser spot, figure 5.7(d).

The temperature changes in the device can be quantified semi-locally by looking at the shift in T_+ and T_- under given laser conditions from their value when the laser is off and there are no temperature gradients across the sample. Specifically, we identify the shift in T_+ as being indicative of the minimum temperature change along the conduction path, ΔT_{min}, whereas the shift in T_- indicates the maximum temperature change, ΔT_{max}. Figures 5.7(e) and (f) plot ΔT_{min} and ΔT_{max} respectively for the three laser locations studied. When the laser is focused on the narrow channel, the current must pass through the maximally heated part of the device. In this case, we find a maximum temperature increase of $> 2\,\text{K/mW}$, sufficient to completely quench the superconductivity of the illuminated 40-μm-wide strip at $P_{\text{laser}} = 2\,\text{mW}$. This observation is consistent with our vortex

imaging where we saw $P_{\text{laser}} = 2.0\,\text{mW}$ give a normal-state disc centred on the laser spot $\sim 50\,\mu\text{m}$ in diameter. The minimum temperature increase of $\sim 0.5\,\text{K/mW}$ suggests that the whole Nb device experiences significant heating even 1 mm away from the laser spot. This may indicate a relatively poor thermal conductivity of our implanted diamond substrate, and/or a poor thermal contact with the Nb film. When the laser is focused on the bonding pad, the current is able to avoid the hottest part of the device directly under the laser spot and so ΔT_{max} is closer to the minimum heating along the current path (again $\sim 0.5\,\text{K/mW}$) as compared to the previous case. The temperature and subsequent current paths across the device are illustrated for both of these cases in figure 5.7(g), and the temperature profile along the conduction path in the bonding pad case is represented in figure 5.7(h). The heating of the Nb film is reduced but still measurable with the laser spot to the side of the device ($\sim 0.2\,\text{mm}$ away), $\sim 0.1\,\text{K/mW}$, with similar behaviours of ΔT_{min} and ΔT_{max} indicating no significant temperature gradient across the device. The heating inferred from the resistance measurements here is just a factor of 3 larger than that measured by the sensor.

Here it's important to emphasise that ΔT_{max} describes the maximum temperature change along the current path and not the maximum change across the entire Nb film, which occurs at the centre of the laser spot. The divergence between these two quantities is dependent of the device and laser geometry. For example, when the laser spot ($\sim 60\,\mu\text{m}$) is positioned on the narrow channel ($40\,\mu\text{m}$ wide), the maximum heating inferred from the resistance measurements ($> 2\,\text{K/mW}$) is much closer to that inferred from our vortex imaging (up to 5 K locally at $P_{\text{laser}} = 1.0\,\text{mW}$). However, when the laser is positioned on the bonding pad, the heating inferred from resistance measurements ($\sim 0.5\,\text{K/mW}$) drastically underestimates the heating inferred from our ODMR images. Care should therefore be taken in quantifying local heating in NV imaging experiments from resistance-based measurement, as these will always be dependent of the sample and laser geometry.

Our study so far has only considered the impact of the excitation laser as assessed by ODMR imaging and resistance measurements. Another source of heating that may affect the sample of interest is the microwave infrastructure, which is essential to most NV experiments. The precise microwave power required varies greatly depending on the measurement (e.g. dynamical decoupling sequences versus ODMR), the mode of delivery

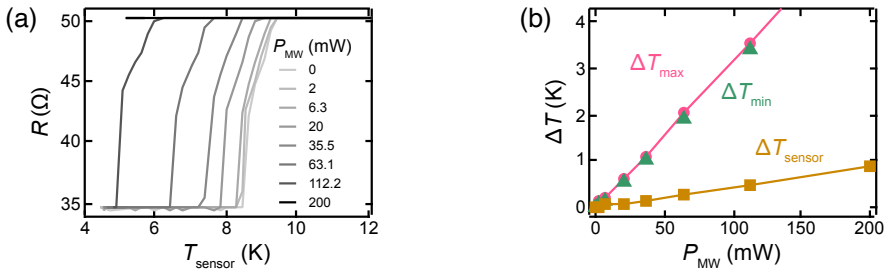

Figure 5.8: Quantifying microwave heating with electrical measurements. (a) R versus T_{sensor} curves for P_{MW} ranging from 0 mW to 200 mW (light to dark). The measurements were taken with the laser off. (b) Temperature changes as a function of P_{MW}. The temperature changes across the device are taken from resistance measurements in (a), quantified by ΔT_{max} (pink) and ΔT_{min} (green) defined previously. The temperature change measured by the thermistor (~ 2 mm below the Nb sample) is the difference between the reading at a given P_{MW} and the reading when the microwave field is off with no additional heating, ΔT_{sensor} (gold).

(e.g. resonator or strip line), and the microwave-source-sample configuration. Here, we assess heating of the Nb device due to our microwave resonator by measuring the device resistance as we vary cryostat temperature under a range of microwave field powers, P_{MW}, with the laser off. Figure 5.8(a) shows the R versus T_{sensor} curves for the device for $P_{\text{MW}} = 0$ mW to 200 mW. As P_{MW} increases we see the transition to superconductivity shift to lower T_{sensor} in a symmetric fashion, not dissimilar to that seen for laser heating when the spot is positioned away from the Nb film. The preserved shape of the transition is highlighted by the closely matching dependence of ΔT_{max} and ΔT_{min} on P_{MW} (~ 32 mK/mW) shown in figure 5.8(b), indicating minimal temperature gradients across the sample. The temperature change measured by the thermistor, ΔT_{sensor}, over the same P_{MW} range without heating the cryostat is comparably small (~ 5 mK/mW), indicating a significant temperature gradient between resonator-sample plane and the thermistor, which are separated by > 2 mm. All ODMR-based imaging presented in this chapter uses $P_{\text{MW}} = 2$ mW, and hence, the microwave heating of the Nb film is negligible as compared to the laser heating in these measurements.

5.7 Imaging superconducting transport

Resistance measurements allow us to semi-locally quantify temperature gradients across the device caused by the laser and infer their impact on the current path. NV imaging, however, lends us the ability to image local current distributions within devices directly by measuring their associated Ørsted field, as we saw in chapter 4. Applying this technique to superconducting transport is particularly interesting given the relevance of non-uniform supercurrents and quenching dynamics to widely employed single-photon and single-electron detectors [203, 204]. Here, we aim to map the current density passing through the narrow channel of our Nb device under three different laser powers to determine the effect this local heating has on the imaged current distribution. To do this, we make vector ODMR measurements of the NV ensemble under a biasing field, $\mathbf{B}_{\text{app.}} = (47.5, 97.4, 19.1)\,\text{G}$, such that we can resolve each of the eight NV transitions independently. Note that at this field strength $B_{\text{app.}} < B_{c2}$, however, the Abrikosov vortices present are at a density that cannot be resolved by our diffraction-limited imaging. After fitting the resulting ODMR spectra and calculating the local magnetic field via the NV spin Hamiltonian, we subtract the biasing field applied by our vector magnet to extract the Ørsted field from the Nb device, $\mathbf{B} = (B_x, B_y, B_z)$. The two-dimensional current density within the channel $\mathbf{J} = (J_x, J_y)$, is then reconstructed from the Ørsted field by inverting the Biot-Savart law, as discussed in section 4.4. Note that here we show current densities reconstructed from the B_z field, as in chapter 4, due to the recurring issue from in-plane magnetic field reconstruction which undervalues the reconstructed current in certain cases. The full details of this vector ODMR measurement and current reconstruction are given in appendix A.3.7.

The Ørsted field was measured near the middle of the narrow channel under three different laser powers, $P_{\text{laser}} = 0.25\,\text{mW}$, $0.5\,\text{mW}$, and $1.0\,\text{mW}$, each with a constant total current, $I = 20\,\text{mA}$. This total current is significantly larger than that used for the resistance measurements of the device ($I = 10\,\mu\text{A}$) and has consequences for the transition to superconductivity. At $P_{\text{laser}} = 0.25\,\text{mW}$ and $0.5\,\text{mW}$, $R = 34.6\,\Omega$ for the duration of measurement (approximately 1 hour), indicating fully superconducting current pathways across the device. At $P_{\text{laser}} = 1.0\,\text{mW}$, $R = 50.2\,\Omega$ throughout the measurement, indicating a fully normal-state current pathway. We did not observe any intermediate resistances due

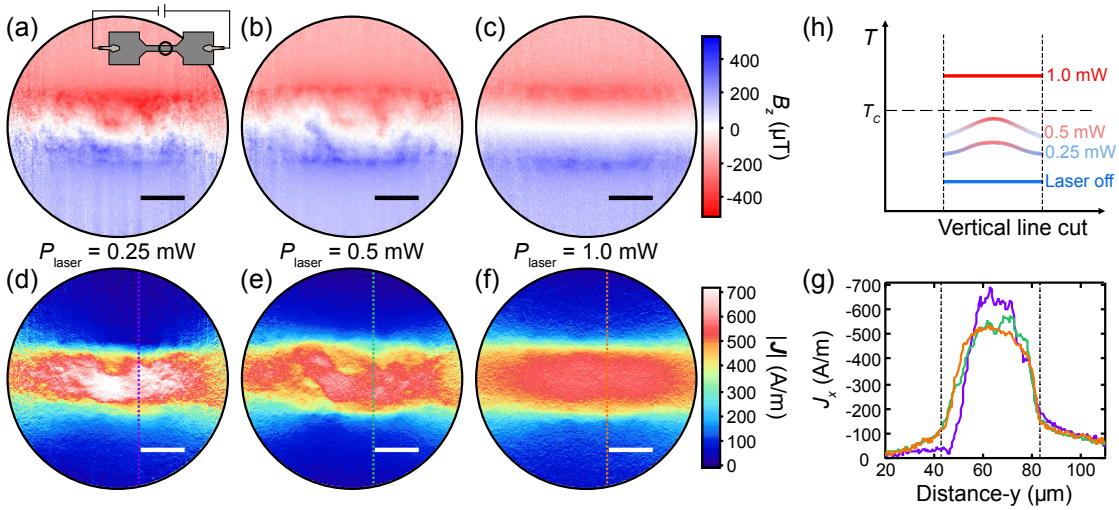

Figure 5.9: Laser heating of superconducting transport. (a), (b), and (c) are images of the z component of the Ørsted field from a 20 mA current passing through the narrow Nb channel, imaged at $P_{\text{laser}} = 0.25\,\text{mW}$, 0.5 mW, and 1.0 mW respectively. (d), (e), and (f) the corresponding current density maps reconstructed from the B_z images (see appendix A.3.7 for details). $R = 34.6\,\Omega$ at $P_{\text{laser}} = 0.25\,\text{mW}$ and 0.5 mW, indicating fully superconducting current paths, whereas $R = 50.2\,\Omega$ at $P_{\text{laser}} = 1.0\,\text{mW}$, indicating an entirely normal state Nb film. All scale bars are 20 μm. (g) Profiles of the x component of the current density, J_x, across the same section of the Nb channel for $P_{\text{laser}} = 0.25\,\text{mW}$ (purple), 0.5 mW (green), and 1.0 mW (orange). The profile locations are shown in the current density images. The edge of the Nb channel was identified from the ODMR contrast (see appendix A.3.6). (h) Illustration of the temperature profile across the Nb channel at each laser power studied. At $P_{\text{laser}} = 0.25$ and 0.5 mW the laser heats the channel reducing the critical current density as T approaches T_c. At $P_{\text{laser}} = 1.0\,\text{mW}$, Joule heating from the normal state Nb dominates and gives a near-uniform temperature profile.

to cascade Joule heating at these large currents, which sharpens the transition from normal to superconducting states (see appendix A.3.5). Figures 5.9(a), (b), and (c) show the B_z fields measured by ODMR with $P_{\text{laser}} = 0.25\,\text{mW}$, 0.5 mW, and 1.0 mW respectively, and figures 5.9(d), (e) and (f) show their corresponding current density magnitudes, $|\mathbf{J}|$. At $P_{\text{laser}} = 0.25\,\text{mW}$ and 0.5 mW, when the Nb device is fully superconducting, we see a highly non-uniform current density distribution that shifts considerably along the length of the channel. We observe a maximum local current density of $\sim 700\,\text{A/m}$ at $P_{\text{laser}} = 0.25\,\text{mW}$, figure 5.9(d), which also shows a more narrow current distribution that at $P_{\text{laser}} = 0.5\,\text{mW}$, figure 5.9(e). At $P_{\text{laser}} = 1.0\,\text{mW}$, when the entire Nb device is in the normal state, the

current distribution is uniform along the length of the channel with a reduction in the current at the edges, figure 5.9(f). The current density appear to taper towards the edge of the image due a reconstruction issue associated with noise in the B_z field (see appendix A.3.7 where we show that $|\mathbf{J}|$ reconstructed from B_y does not show this tapering effect). Note that imaging with $P_{\text{laser}} = 0.5\,\text{mW}$ but using the heater to raise the temperature above T_c ($T_{\text{sensor}} = 12\,\text{K}$) gave results identical to the case where $P_{\text{laser}} = 1.0\,\text{mW}$. Line profiles of the x-component current density, J_x, across the channel highlight its laser-power-dependent spread, figure 5.9(g). The non-uniform current density is most confined at the lowest laser power, broader but still asymmetric at $P_{\text{laser}} = 0.5\,\text{mW}$, before broadening further to give a symmetric distribution across the channel in the normal-state case at $P_{\text{laser}} = 1.0\,\text{mW}$.

The non-uniform current density through the superconducting state Nb channel is a direct consequence of the temperature profile imprinted by our laser spot. As the local temperature increases, the superconducting gap, and hence the critical current density, J_c, is reduced. The measured current density is therefore larger where the local temperature is lower. Increasing the total laser power reduces J_c across the channel, and the current density distribution broadens to maintain the same total current. Joule heating dominates laser heating when the Nb device is in the normal state and therefore the temperature is expected to be uniform across the channel. The temperature profile across the channel is illustrated for each of these cases in figure 5.9(h). We note that $|\mathbf{J}|$ imaged under fixed laser conditions retains a consistent shape as the field of view is translated along the Nb channel, indicating that the non-uniformity observed arises from the excitation laser rather than local variations in the Nb (see appendix A.3.7). We also observed an interesting magnetic response of the Nb channel to the application of current, namely a magnetic texture visible after the current is applied to the region (see appendix A.3.6).

5.8 Summary

In this work we have successfully implemented NV imaging in a cryogenic environment with temperatures down to 4 K, a considerable extension to the capabilities explored in chapter 3 and 4. We demonstrated submicrometer spatial resolution over a 100 μm field of

view, five times larger than a previous demonstration of widefield NV imaging at cryogenic temperatures, which reported a field of view of 20 μm [109]. This new capability is ideal for spatially-resolved investigations of mesoscopic phenomena in a variety of materials and devices, and also enables imaging of several samples in parallel. For instance, atomically thin samples of van der Waals materials prepared by mechanical exfoliation typically come in the form of multiple micrometre-sized flakes with different properties (thickness, shape), and so widefield imaging of such samples would allow simultaneous studies of many of them, greatly speeding up the characterisation process. This capability could be particularly useful to investigate, for example, the magnetic properties of ferromagnetic van der Waals materials and heterostructures. Indeed, such an application is the final topic of study in this thesis and is presented briefly in chapter 6.

Our test system for this study, superconducting Nb wires fabricated directly on the diamond surface, allowed us to image low-temperature phenomena in a system close to its critical temperature, $T_c \approx 9\,\mathrm{K}$. Specifically, we achieved ODMR-based imaging of Abrikosov vortices and superconducting transport in the device across a range of conditions and assessed their impact on the imaged phenomena. Here we found a key limitation of NV microscopy for low temperature measurements, where the laser required to optically interrogate the NV centres can lead to significant heating of the sample under study. Using the Nb superconducting film as a local temperature probe, we found that even modest illumination powers (2 mW, corresponding to peak intensity of 40 $\mathrm{W/cm^2}$) can locally quench the superconductivity of the film, implying a local temperature rise greater than 5 K (from a base temperature of 4.3 K to above T_c). This local heating is overlooked by the thermistor located 2 mm below the sample which reads below 5 K under these conditions, close to the base temperature of the cryostat. Resistance measurements of the Nb device also underestimated the degree of local heating depending on the precise sample geometry.

This work thus demonstrates the need for caution in NV sensing experiments at low temperatures, and the need to define minimally-invasive imaging parameters. In our experiments, a total power of 0.5 mW (peak intensity of 10 $\mathrm{W/cm^2}$) was sufficiently low to keep the Nb devices fully superconducting, allowing an array of frozen superconducting vortices to be imaged. Supercurrents imaged at this same power, despite being in a fully superconducting state, were still affected by the local laser heating. The acceptable

illumination conditions therefore depend on both the sample and phenomenon studied, and the precise experimental setup. Especially delicate samples will require strategies to mitigate laser-induced heating such as the introduction of a thin high-reflectance metallic film between the diamond and sample of interest, the use of better thermal conductors between the sample and cooling elements of the cryostat, or an optimised illumination geometry to reduce the required laser power such as total internal reflection [85, 129, 230]. These precautions may be necessary even in single-NV experiments which can have similar laser power densities at the point of imaging despite using less total power. Such measures would also overcome a key limitation in using NV imaging to study non-uniform temperature systems, namely that the laser heating is inextricably linked to the field of view. Using a metallic laser shield and introducing a second heating laser that is incident on the sample only, would allow more detailed studies of vortex dynamics in local temperature gradients, and quenching dynamics of non-uniform supercurrents relevant to superconducting detectors [203, 204].

In chapter 6, we implement such a strategy to reduce sample heating from our imaging laser in order to study ferromagnetic van der Waals materials at low temperatures. Our NV diamond substrates are re-designed to include a thin metallic laser shield and an insulating oxide layer following the insight from this work. The ferromagnetic flakes are then deposited on to the oxide surface instead of the diamond directly as in this project. A useful follow up to this project would be to repeat this suite of measurements for a Nb device fabricated on such a diamond sample. This study would allow us to quantify any remnant heating in the new configuration and be confident of the precise impact out imaging has on samples moving forward. Such steps will unlock the potential of NV microscopy for a broader range of low temperature condensed matter phenomena including topological insulators, van der Waals heterostructures, and exotic transport phenomena.

6

Application of widefield nitrogen-vacancy imaging to the characterisation of ultrathin ferromagnetic materials

So far in this thesis, we have utilised a widefield approach to magnetic imaging with NV centres in diamond to study a range of systems. Each of these studies, in addition to having its own interesting physics to investigate, has highlighted various shortfalls of this approach to NV imaging, and thus helped us refine our methodology in subsequent applications. For example, the study of thin depositions of metallic nanoparticles presented in chapter 3, motivated the use of a deeper NV ensemble that is less susceptible to noise from surface or interface defects. Similarly, the study of graphene field-effect transistors presented in chapter 4, despite successfully imaging charge transport through the graphene channel under different doping conditions, revealed susceptibility of the device to the excitation laser used for imaging, which altered the doping. Modulation of the NV photoluminescence on application of large gate potentials highlighted the need to insulate our sensing layer for the electrostatics of the target device. Chapter 5 extended the imaging capability to low temperature, by incorporating a closed-cycle cryostat in our apparatus. We characterised the inadvertent heating due to the excitation laser by imaging superconductivity phenomena, which again motivated the isolation of our target system from the laser, and importantly, gave us an upper bound on such heating moving forward.

In this chapter, we implement these refinements by re-designing our NV-diamond substrate and apply this new design to characterise ultrathin, free-standing magnetic materials. Specifically, we include a reflective metallic layer and insulating oxide layer at the diamond surface. The samples of interest are deposited on top of the oxide layer where they are shielded from the imaging laser which is incident on the underside of the diamond and reflected by the metallic layer. This strongly attenuates the laser power seen by the sample of interest, and therefore the local heating seen in the previous chapter, allowing us to more accurately characterise the temperature-related properties of these magnetic materials. Here we summarise two applications of this new design, the first to a layered ferromagnetic material, VI_3, and the second to a non-layered ferromagnetic material, magnetite. In the first instance, we use our cryogenic widefield NV microscope to quantitatively reconstruct the magnetisation of a number of VI_3 flakes of varying thicknesses, and compare this relation with ab initio calculations. Varying the temperature and magnetic field conditions between imaging allows us to determine the Curie temper-

atures, and coercive and nucleation fields of the flakes. In the second case, we use mostly room-temperature NV microscopy and correlated atomic-force microscopy to characterise a threshold size below which magnetite flakes no longer exhibit ferromagnetism, even down to cryogenic temperatures. These applications demonstrate the current capabilities of our research group, which in future will be used to characterise novel magnetic materials and heterostructures, and exotic transport phenomena.

6.1 Motivation

Ferromagnetism in two-dimensional and ultrathin materials is an emerging field of study. The persistence of ferromagnetism and antiferromagnetism down to atomic-scale thicknesses was is an intriguing problem given the dominance of thermal excitations in the two-dimensional limit, as described by the Mermin-Wagner theorem [241]. In 2017, the field took a new turn with the discovery of two free-standing van der Waals materials, $Cr_2Ge_2Te_6$ and CrI_3, that exhibit intrinsic ferromagnetism down to bilayer and monolayer limits respectively [99, 100]. Since this discovery, ferromagnetism has been observed in a range of other ultrathin materials including Fe_3GeTe_2, $CrCl_3$, and $CrBr_3$ [174, 242–244]. The now broad range of experimentally realisable ferromagnetic and antiferromagnetic materials has created opportunities to make exotic van der Waals heterostructures which may find application in spintronics and novel technologies [245].

The expanding catalogue of two-dimensional and ultrathin magnetic materials necessitates a robust and efficient technique by which their magnetic properties can be characterised. Characterisation until now has been achieved using optical techniques [246], such as the magneto-optical-Kerr-effect (MOKE) microscopy and magnetic circular dichroism (MCD) [99,100,247], and electrical measurements, such as anomalous Hall effect [243] and electron tunneling measurements [248,249]. While these techniques have their advantages, they both rely on experimental parameters to transform their measured quantity into a quantification of the sample magnetisation, such as device geometry in the case of electrical measurements, or calibrated polarisation rotation for MOKE and MCD. Recently, NV microscopy has emerged as an alternate charaterisation technique that overcomes this limitation. Scanning single-NV experiment have been used to measure the stray mag-

netic field from CrI_3 down to the monolayer, and in turn, quantitatively map the local magnetisation of the sample [14]. The advantage here is that transforming the measured stray magnetic field into a local magnetisation is achieved via the NV spin Hamiltonian (section 1.2.3) which depends only on well-known physical constants, such as NV-electron gyromagnetic ratio, rather than parameters specific to the experiment as in the standard techniques discussed [14, 16, 101]. This ability to directly quantify local magnetisation across a sample permits quality comparison with ab initio calculations which will foster a better understanding of these systems.

In this chapter we utilise our refined approach to widefield NV microscopy to study two different ultrathin magnetic materials, VI_3, a layered van der Waals material, and magnetite, a non-layered material. The widefield configuration, despite being diffraction limited, allows us to study multiple sample flakes over a broad field of view in parallel, an endeavor that would be time consuming for the sub-diffraction-limit, scanning single-NV microscopy presented in Ref. [14]. This demonstration establishes widefield NV microscopy as a valuable technique for future characterisation of two-dimensional magnetic materials which may lend new insight into nanoscale phases [250]. Our previously demonstrated capabilities of injecting current and gating samples of interest in parallel to our imaging open up future opportunities to study the interplay of current and magnetism in a sample, spintronics, and gate-tunable magnetism [242, 244, 251, 252].

6.2 Characterisation of a van der Waals ferromagnet: VI_3

Layered van der Waals materials were the first observed, and are perhaps the best studied, free-standing two-dimensional ferromagnetic materials [99, 100, 250]. This is due largely to the relative ease with which they can be exfoliated from bulk samples down to atomic-scale thicknesses, which is a consequence of their weak interlayer bonding. Here we study a particular van der Waals ferromagnetic material, VI_3, to demonstrate the capability of our refined NV imaging approach. Note that this project is primarily the work of Dr. Jean-Philippe Tetienne and Dr. David Broadway, but is reported here briefly to exhibit our refined approach to widefield NV imaging that was informed by the work of this thesis. The material here was fabricated by Prof. Lan Wang and his team at RMIT. For

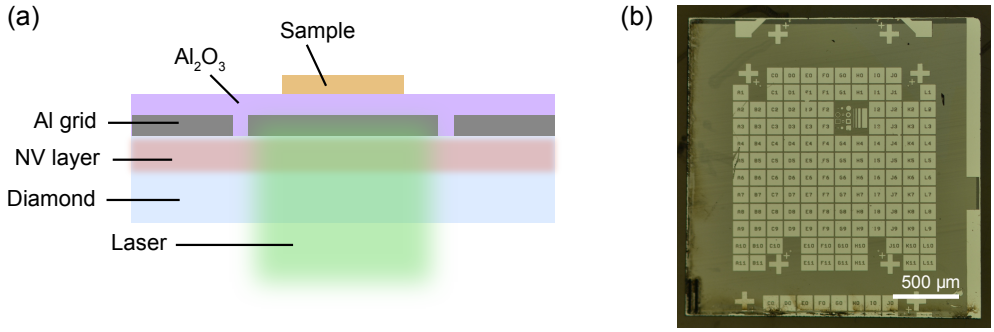

Figure 6.1: Refined design of NV diamond imaging substrate. (a) Schematic of our refined NV-diamond substrate for widefield magnetic imaging at low temperatures. (b) Photograph of such a sample. The metallic laser shield included markers, allowing us to reliably catalogue samples deposited on the oxide surface and spatially correlate corroborating measurements. The oxide coats the entire substrate surface and is not visible.

full details and findings of the project, see Ref. [101].

Key to this and future applications, is our redesigned NV-diamond substrate for widefield imaging. This new design relies on the same NV-diamond materials used in the previous chapter, that is, diamonds fabricated by method B as outlined in section 2.2. However, here we include two additional fabrication steps: the first, patterning a reflective metallic layer on the diamond surface; the second, depositing an insulating oxide layer across the entire diamond. The metallic layer shields the sample of interest from the excitation laser while the oxide layer isolates the sample from the metallic layer, as shown in figure 6.1(a). These innovations were implemented in direct response to the work presented in the preceding chapters. Specifically, the inclusion of a reflective metallic layer was informed by the work presented in chapter 5, where we saw direct exposure of the sample to the excitation laser causes significant heating that can be devastating to low-temperature applications. This refinement should also benefit future studies of electrical devices by avoiding photodoping effects similar to those observed in our GFETs in chapter 4. The intervening oxide layer ensures any such device is isolated from the metallic layer, and further mitigates heating due to the laser. Finally, the standoff afforded by the deeper NV ensemble and the intervening oxide layer avoid any ambiguities in signal that

we observed with our metallic nanoparticle depositions in chapter 3, limiting ourselves to studying longer-range magnetic signals. The metallic layer here is an 80-nm-thick Al grid deposited by electron-beam thermal evaporation and patterned using the same photolithographic steps used elsewhere in this thesis, detailed in section 4.2 for example. The 80-nm-thick oxide layer (Al_2O_3) was deposited by atomic layer deposition, using a process similar to that described in section 4.2. A photograph of one such diamond substrate is shown in figure 6.1(b). Note that the added 160 nm standoff between the NV layer and sample does not degrade our spatial resolution as the standoff is still below the diffraction limit.

Ultrathin VI_3 flakes were isolated by mechanical exfoliation of a bulk VI_3 crystal and deposited onto a SiO_2/Si substrate. Here, the number of layers in each flake was determined by optical imaging where the contrast varies significantly with the number of layers due to an engineered interference effect with the substrate, as seen in figure 6.2(a). The optical contrast was previously calibrated with AFM measurements. The flakes were then encapsulated in hexagonal boron nitride (hBN) to prevent their degradation in air, and stamped onto the oxide of our refined NV-diamond substrate which was then loaded into the cryostat system for imaging. All of the imaging presented here is at the cryostat base temperature, $T_{\text{base}} = 4.0\,\text{K}$. To image the stray field associated with the transferred VI_3 flakes, we performed an ODMR measurement by applying a bias field along a single NV axis, $B_{\text{bias}} = 5\,\text{mT}$, and mapping the two resonance frequencies of that NV family across the 100 μm field of view. The magnetic field projection along this NV axis is then calculated from the difference between these fit frequencies, $\Delta f = 2\gamma_{\text{NV}}(B_{\text{NV}}^{\text{bias}} + B_{\text{NV}})$, foregoing the more elaborate Hamiltonian fitting used for vector-ODMR measurements presented previously. Subtracting the known bias field, we extract an image of the stray field of the deposited flakes as projected along this NV family axis, B_{NV}, shown in figure 6.2(b). Here we image with a laser power of 50 mW, a factor 50 larger than the less-invasive power identified in chapter 5. This is in part due to the Curie temperature of ultrathin VI_3 (approximately 50 K) being much higher than the critical temperature of Nb (approximately 9 K), but is also permitted by our redesigned NV-diamond substrate greatly mitigate and delocalises heating due to the laser. Indeed, we notice $T_{\text{sensor}} \approx 5\,\text{K}$ under these conditions, which suggests at least a 75% reduction in the global heating from

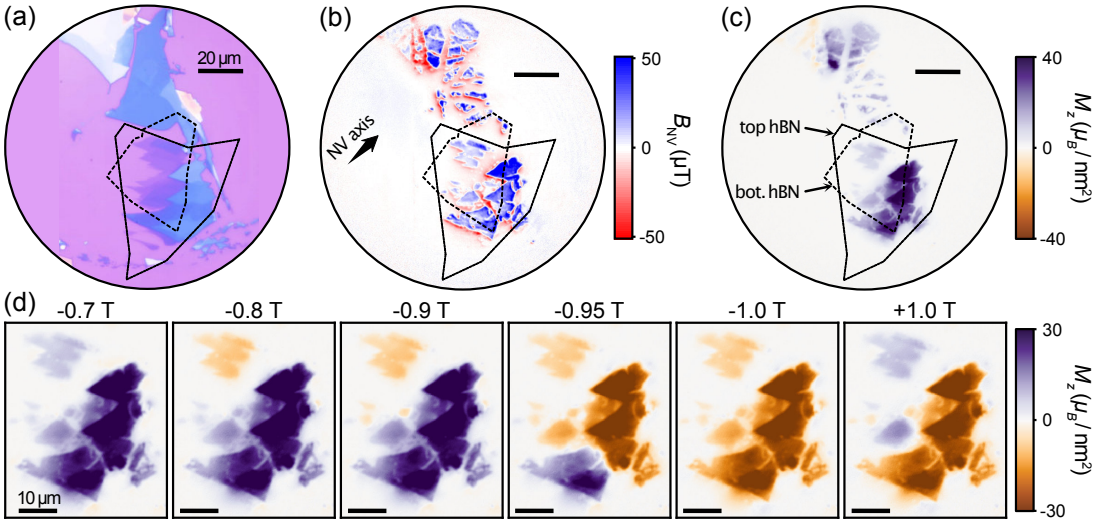

Figure 6.2: Stray field imaging and magnetisation reconstruction of VI_3. (a) Photograph of VI_3 flakes desposited on a SiO_2/Si substrate. The optical contrast varies significantly with number of VI_3 layers, by design of the substrate, allowing us to determine the thickness of the flakes with a calibrating AFM measurement. (b) B_{NV} image of the flakes after encapsulation in hBN and transfer to the refined NV-diamond substrate. The map is produced from an ODMR image with the sample at 5 K in our cryogenic system, under a small bias field applied along a single NV-family axis (labeled). (c) M_z map reconstructed from the B_{NV} image. The location of the top and bottom hBN layers used to encapsulate the VI_3 flakes are indicated. (d) M_z map of a collection of VI_3 flakes imaged under the same ODMR conditions after applying labeled magnetic field in the z direction before imaging. The coercive field of each flake was identified from these images.

the laser in this case. Note that a strong bias field of 1 T in the z direction was applied prior to imaging to magnetise the deposited flakes.

While a map of the stray field associated deposited ferromagnetic flakes is useful, we can go a step further and turn this map into a quantitative image of the sample magnetization. Here we use a Fourier-transform method, analogous to that used for current reconstruction presented in section 4.4, to recover the real-space areal magnetisation [14, 86]. For the details of the reconstruction used in this work, see the supplemental information to Ref. [101], and see Ref. [16] for a comparative analysis of the various approaches to this reconstruction. Figure 6.2(c) is a map of the magnetisation in the z direction, M_z, reconstructed from the B_{NV} image. Interestingly, the magnetisation patterns match those seen in the optical image taken before transfer for the region covered by the top layer of hBN. The magnetisation in regions outside of this layer has receded into small islands distinct to

the large flakes seen before transfer, which indicates degradation of the un-encapsulated VI_3. The bottom layer of hBN seems to not affect the magnetisation observed under the top layer. By analysing maximum magnetisation of a flake with a given layer number, we determined the areal magnetisation of $1.9(2)\,\mu_B/\mathrm{nm}^2$ per atomic layer, corresponding to $0.4\,\mu_B$ per formula unit (f.u.). This value is significantly lower than that observed in bulk VI_3, approximately $1.0\,\mu_B$/f.u., and that predicted by ab initio calculation, $2.0\,\mu_B$/f.u.. This discrepancy could be due to degradation of the flakes during their brief exposure to an oxygen environment between deposition and loading into the cryostat, or may be indicative of a mixture of ferromagnetic and antiferromagnetic interlayer coupling on a sub-micrometer scale [101]. Regardless, the ability to map sample magnetisation across a range of flakes of varying thickness in parallel, across a range of magnetic fields and temperatures, allows us to easily investigate layer-dependence of the Curie temperature (approximately 50 K for all flakes), cooercive fields (between 0.5 T and 1 T at 5 K), and domain-wall depinning fields (between 0.1 T and 0.4 T) in the material. Illustrative data for the coercive field study is shown in figure 6.2(d), where the sample is studied by repeated ODMR imaging at same bias field, but varying the large field applied in the z direction between images.

6.3 Characterisation of an ultrathin non-layered ferromagnetic material: Magnetite

The previous section demonstrated the capabilities of our cryogenic widefield microscope with a refined NV-diamond design, towards the characterisation of ultrathin magnetic materials. The materials studied there, VI_3, was a layered van der Waals ferromagnet, which is the most well-studied type of free-standing magnetic materials at atomic-scale thicknesses given the relative ease of exfoliation. Interest in ultrathin magnetic materials, however, is not limited to van der Waals materials, with a few studies of thin non-layered ferromagnetic materials emerging in the past couple years [253]. Here we report on such a study, towards the magnetic characterisation of ultrathin flakes of magnetite, formed by a spatially-confined direct synthesis. This project is in collaboration with Prof. Vipul Bansal, Aviraj Ingle, and their team at RMIT University, who developed the process for

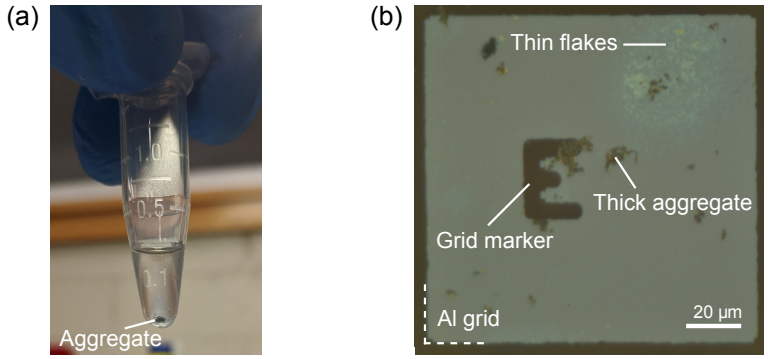

Figure 6.3: Drop-cast deposition of synthesised magnetite flakes. (a) Photograph of the exfoliated magnetite suspension in isopropyl alcohol. Sample was deposited from the top portion of the solution to avoid the thick aggregate seen at the bottom. (b) Photograph of a single grid region of our NV-diamond substrate after drop casting the magnetite. Thick aggregates are visible across grid, and a region of thinner flakes that appear faint blue.

reliably isolating atomically-thin flakes of magnetite. This work is part of a manuscript in preparation and so we omit the details of the sample synthesis, focusing only on our magnetic characterisation using our refined NV-diamond imaging technique.

The sample was received as a suspension of magnetite flakes in isopropyl alcohol that was drop cast onto several of our refined NV-diamond substrates by Aviraj Ingle. A photograph of one such suspension is shown in figure 6.3(a). Numerous depositions were made at various dilutions of the stock suspension to ensure a reasonable coverage of the substrate with magnetite, giving several isolated flakes per 100 μm field of view. Figure 6.3(b) is a photograph of one grid-marker region following the deposition showing a mixture of thick aggregates, which appear as a dark masses, and thinner flakes visible as pale blue spots. A disadvantage of drop-casting directly onto our diamond substrates is that, unlike for calibrated SiO_2/Si substrates, we do not observe strong layer-dependent optical contrast and so must rely of AFM topography scans to determine flake thicknesses following deposition. The suspensions were drop cast onto SiO_2/Si and NV-diamonds substrates simultaneously, so that we could infer a reasonable coverage of our diamond samples with ultrathin flakes from optical images of the SiO_2/Si substrates.

To image the stray field associated with the deposited magnetite flakes, we performed an ODMR measurement similar to that described in the previous section, i.e. with a bias

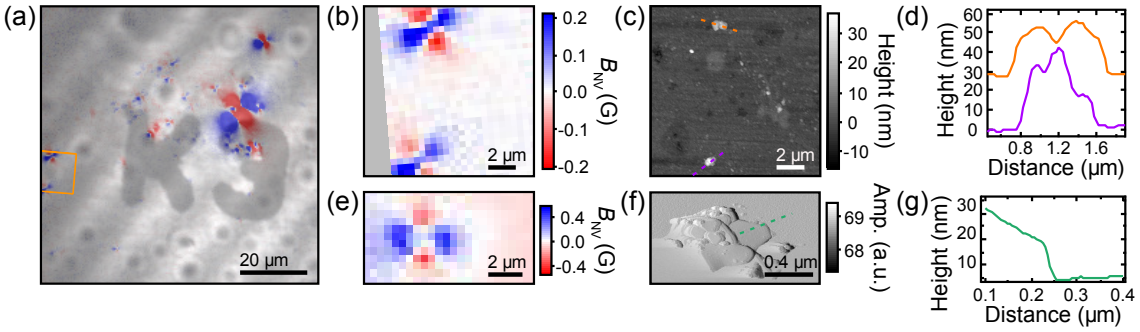

Figure 6.4: Stray field imaging and AFM of ultrathin magnetite. (a) Overlaid B_{NV} and photoluminescence images across a 100 μm field of view around marker "K3" in our metallic grid. (b) Cropped B_{NV} image of the region highlighted in (a), showing two lobed magnetic features associated with the deposition. The greyed region lies outside the field of view of the magnetic image. (c) AFM topography image of the same region as in (b) showing two flakes spatially correlated with the magnetic features. (d) AFM height profiles of the two flakes highlighted in (c), showing heights of 20 nm (orange) and 40 nm (purple). The profiles are offset vertically for clarity. (e) Cropped magnetic image of a magnetite deposition on a different NV-diamond substrate. (f) AFM amplitude image acquired at the centre of the magnetic feature shown in (e). The amplitude image is presented to highlight the layered appearance of the material. (g) AFM height profile from the region highlighted in (f). A 20 nm step is present from the edge of the thinnest part of the material to the diamond surface.

field applied along a singe NV-family axis. Initially, this was done at room-temperature under ambient conditions given the high Curie temperature of magnetite and other iron oxides [186]. A typical B_{NV} produced from these measurements is shown in figure 6.4(a), where the NV fluorescence image has been overlaid to show the location of the grid marker used to spatially correlate AFM images. A number of magnetic features can be seen within the 100 μm field of view, not dissimilar to those seen in chapter 3, with maximum field strengths varying from 0.02 G to 2.5 G between features. Comparing a cropped region of the magnetic field image, figure 6.4(b), with an AFM topography image of the same area, figure 6.4(c), we find that the two magnetic features correlate with the location of two particles on the substrate. Line profiles through each of these particles, figure 6.4(d), show that they are 20 nm and 40 nm in height and extend over approximately 1 μm laterally. This aspect ratio is indicative of a platelet-like shape, strong evidence that the material imaged here is indeed the thin magnetite synthesized and studied in the manuscript. Further evidence is given in figures 6.4(e) and (f), which are spatially correlated B_{NV} and

AFM images respectively, of a separate deposition. Here the AFM image shows a terraced structure, suggesting that the feature is a stack of individual flakes. A line profile reveals a minimum step of 20 nm across the feature, figure 6.4(g).

The measured magnetic field images are consistent with numerical simulations of plates similar in size to those imaged, taking a spontaneous magnetization corresponding to bulk magnetite, $M_s = 200\,\mathrm{kA/m}$ (using the same methods as in Ref. [176]). The large magnetic field amplitudes and gradients prevented us from extracting precise quantitative information from the NV measurements, as the simulations become strongly dependent on the unknown details of the sample geometry in this regime [176]. These fields also inhibit our ability to quantitatively reconstruct the magnetisation of individual flakes, as we were able to with VI_3, given that the Fourier reconstruction is very sensitive to measured field [16]. This presents a challenge to imaging ultrathin magnetic materials synthesized by this method given the often limited lateral dimensions of such flakes as compared to those produced by mechanical exfoliation.

ODMR-based magnetic imaging with accompanying AFM topography was repeated on several depositions over different diamond substrates. Across all samples, we observed the maximum magnetic field from individual magnetic features varying from 0.1 G to 2.5 G. AFM measurements of these same features showed platelet-like particles from 20 nm to 800 nm in height, typically 1 μm laterally. No clear correlation was found between the maximum field strength and the flake height. Furthermore, no platelet thinner than about 20 nm showing clear magnetic signal was found, despite simulations predicting that a monolayer of ferromagnetic magnetite should produce a measurable signal [176]. This may indicate that either the ultrathin magnetite flakes present in the suspension did not adhere to the diamond substrate, or that they are not ferromagnetic. These same samples were imaged in our cryostat system down to 4 K, which did not reveal any additional magnetic features.

6.4 Summary

This chapter has demonstrated that by implementing refinements to our imaging methodology, informed by work presented in the previous few chapters, we have established a

robust and efficient imaging system to characterise ultrathin magnetic materials. Our widefield approach to imaging allows us to characterise multiple individual flakes of the target material in parallel with diffraction-limited resolution. In the case of VI_3, a layered van der Waals material, we were able to image the magnetisation of flakes and determine its dependence on the number of layers present. This allowed us to make a quantitative comparison with ab initio calculations, which in this case revealed a significant discrepancy requiring further investigation. By imaging across a broad range of temperatures and magnetic field conditions, we were able to determine the Curie temperatures, coercive and depinning fields of individual flakes. In the case of magnetite, a non-layered magnetic material, we identified a threshold thickness of 20 nm below which we did not observe any ferromagnetism in the deposited flakes. This study highlighted some difficulties in imaging bottom-up synthesised ultrathin materials, where the often limited lateral dimensions and stochastic deposition hamper our reconstruction of the flake magnetisation. These difficulties could be overcome in future experiments, for example, by first drop casting onto a SiO_2/Si substrate to easily characterise the deposited material, and then transferring it onto our imaging substrates as in the case for VI_3. Combining this magnetic characterisation with our previously demonstrated capabilities in current injection and electrostatic gating opens up future studies of current and gate-dependent magnetic phenomena, and spintronics [242, 244, 251, 252].

Conclusion

This thesis has reported on a number of applications of widefield imaging using ensembles of NV centres in diamond in the realm of condensed matter physics. The pattern for each of these applications has been to implement some initial experimental design, interrogate the target system via NV imaging and corroborating measurements, and to also study the interaction/impact of our imaging technique with/on the sample of interest. Each of these projects, in addition to lending novel insights into their target systems, have motivated a number of refinements to our NV imaging technique to mitigate interactions between the sample and the sensing ensemble, which either hinders our ability to image or affects the imaged phenomenon. At the conclusion of this work, we have developed a robust and minimally-invasive approach to widefield imaging with NV ensembles in diamond, ready for future applications to delicate condensed matter systems.

One of the key challenges as we move to study more sophisticated and delicate systems is an increasing reliance on collaborators to synthesize interesting samples, and, most significantly, the constraints that our imaging technique imposes on their established fabrications protocol. For studies of passive samples, such as ultrathin ferromagnetic materials, the substrate requirements and post-deposition fabrication are minimal, and so direct transfer onto our refined NV-diamond substrates is a suitable approach. However, if we consider studying sophisticated devices, such as topological insulator which require many well-controlled fabrication steps and subsequent electrical characterisation, the added constraint of fabricating on an NV-diamond substrate is a potential deal breaker. An inelegant but effective solution to minimise the constraint placed on collaborators is to allow them to fabricate and characterise samples on their substrate of choice, after which we simply rest one of our refined NV-diamond substrates across the sample, imag-

ing from above. This approach is currently being explored by our research team, to study photovoltaics and magnetic materials. If it proves to be suitably reliable, this approach combines the flexibility of scanning-based NV experiments with the many benefits of the widefield imaging, expanding the range of future applications.

Bibliography

[1] S. E. Lillie, D. A. Broadway, N. Dontschuk, S. C. Scholten, B. C. Johnson, S. Wolf, S. Rachel, L. C. L. Hollenberg, and J.-P. Tetienne, "Laser Modulation of Superconductivity in a Cryogenic Wide-field Nitrogen-Vacancy Microscope," *Nano Letters*, vol. 20, no. 3, pp. 1855–1861, 2020.

[2] D. A. Simpson, J.-P. Tetienne, J. M. McCoey, K. Ganesan, L. T. Hall, S. Petrou, R. E. Scholten, and L. C. L. Hollenberg, "Magneto-optical imaging of thin magnetic films using spins in diamond," *Scientific Reports*, vol. 6, no. 1, p. 22797, 2016.

[3] C. L. Degen, F. Reinhard, and P. Cappellaro, "Quantum sensing," *Reviews of Modern Physics*, vol. 89, no. 3, p. 035002, 2017.

[4] M. Buchner, K. Höfler, B. Henne, V. Ney, and A. Ney, "Tutorial: Basic principles, limits of detection, and pitfalls of highly sensitive SQUID magnetometry for nanomagnetism and spintronics," *Journal of Applied Physics*, vol. 124, no. 16, p. 161101, 2018.

[5] D. Vasyukov, Y. Anahory, L. Embon, D. Halbertal, J. Cuppens, L. Neeman, A. Finkler, Y. Segev, Y. Myasoedov, M. L. Rappaport, M. E. Huber, and E. Zeldov, "A scanning superconducting quantum interference device with single electron spin sensitivity," *Nature Nanotechnology*, vol. 8, no. 9, pp. 639–644, 2013.

[6] A. M. Tyryshkin, S. Tojo, J. J. L. Morton, H. Riemann, N. V. Abrosimov, P. Becker, H.-J. Pohl, T. Schenkel, M. L. W. Thewalt, K. M. Itoh, and S. a. Lyon, "Electron spin coherence exceeding seconds in high-purity silicon," *Nature Materials*, vol. 11, no. 2, pp. 143–147, 2012.

[7] G. Balasubramanian, P. Neumann, D. Twitchen, M. Markham, R. Kolesov, N. Mizuochi, J. Isoya, J. Achard, J. Beck, J. Tissler, V. Jacques, P. R. Hemmer,

F. Jelezko, and J. Wrachtrup, "Ultralong spin coherence time in isotopically engineered diamond," *Nature Materials*, vol. 8, no. 5, pp. 383–387, 2009.

[8] L. Rondin, J.-P. Tetienne, T. Hingant, J.-F. Roch, P. Maletinsky, and V. Jacques, "Magnetometry with nitrogen-vacancy defects in diamond," *Reports on Progress in Physics*, vol. 77, no. 5, p. 056503, 2014.

[9] D. M. Toyli, D. J. Christle, A. Alkauskas, B. B. Buckley, C. G. Van de Walle, and D. D. Awschalom, "Measurement and Control of Single Nitrogen-Vacancy Center Spins above 600 K," *Physical Review X*, vol. 2, no. 3, p. 031001, 2012.

[10] F. Dolde, H. Fedder, M. W. Doherty, T. Nöbauer, F. Rempp, G. Balasubramanian, T. Wolf, F. Reinhard, L. C. L. Hollenberg, F. Jelezko, and J. Wrachtrup, "Electric-field sensing using single diamond spins," *Nature Physics*, vol. 7, no. 6, pp. 459–463, 2011.

[11] S. Hsieh, P. Bhattacharyya, C. Zu, T. Mittiga, T. J. Smart, F. Machado, B. Kobrin, T. O. Höhn, N. Z. Rui, M. Kamrani, S. Chatterjee, S. Choi, M. Zaletel, V. V. Struzhkin, J. E. Moore, V. I. Levitas, R. Jeanloz, and N. Y. Yao, "Imaging stress and magnetism at high pressures using a nanoscale quantum sensor," *Science*, vol. 366, no. 6471, pp. 1349–1354, 2019.

[12] P. Neumann, I. Jakobi, F. Dolde, C. Burk, R. Reuter, G. Waldherr, J. Honert, T. Wolf, A. Brunner, J. H. Shim, D. Suter, H. Sumiya, J. Isoya, and J. Wrachtrup, "High-Precision Nanoscale Temperature Sensing Using Single Defects in Diamond," *Nano Letters*, vol. 13, no. 6, pp. 2738–2742, 2013.

[13] L. Thiel, D. Rohner, M. Ganzhorn, P. Appel, E. Neu, B. Müller, R. Kleiner, D. Koelle, and P. Maletinsky, "Quantitative nanoscale vortex imaging using a cryogenic quantum magnetometer," *Nature Nanotechnology*, vol. 11, no. 8, pp. 677–681, 2016.

[14] L. Thiel, Z. Wang, M. A. Tschudin, D. Rohner, I. Gutiérrez-Lezama, N. Ubrig, M. Gibertini, E. Giannini, A. F. Morpurgo, and P. Maletinsky, "Probing magnetism in 2D materials at the nanoscale with single-spin microscopy," *Science*, vol. 364, no. 6444, pp. 973–976, 2019.

[15] M. W. Doherty, N. B. Manson, P. Delaney, F. Jelezko, J. Wrachtrup, and L. C. Hollenberg, "The nitrogen-vacancy colour centre in diamond," *Physics Reports*, vol. 528,

no. 1, pp. 1–45, 2013.

[16] D. Broadway, S. Lillie, S. Scholten, D. Rohner, N. Dontschuk, P. Maletinsky, J.-P. Tetienne, and L. Hollenberg, "Improved Current Density and Magnetization Reconstruction Through Vector Magnetic Field Measurements," *Physical Review Applied*, vol. 14, no. 2, p. 024076, 2020.

[17] L. Rondin, G. Dantelle, A. Slablab, F. Grosshans, F. Treussart, P. Bergonzo, S. Perruchas, T. Gacoin, M. Chaigneau, H.-C. Chang, V. Jacques, and J.-F. Roch, "Surface-induced charge state conversion of nitrogen-vacancy defects in nanodiamonds," *Physical Review B*, vol. 82, no. 11, p. 115449, 2010.

[18] D. A. Broadway, N. Dontschuk, A. Tsai, S. E. Lillie, C. T.-K. Lew, J. C. McCallum, B. C. Johnson, M. W. Doherty, A. Stacey, L. C. L. Hollenberg, and J.-P. Tetienne, "Spatial mapping of band bending in semiconductor devices using in situ quantum sensors," *Nature Electronics*, vol. 1, no. 9, pp. 502–507, 2018.

[19] M. V. Hauf, B. Grotz, B. Naydenov, M. Dankerl, S. Pezzagna, J. Meijer, F. Jelezko, J. Wrachtrup, M. Stutzmann, F. Reinhard, and J. A. Garrido, "Chemical control of the charge state of nitrogen-vacancy centers in diamond," *Physical Review B*, vol. 83, no. 8, p. 081304, 2011.

[20] S. Cui and E. L. Hu, "Increased negatively charged nitrogen-vacancy centers in fluorinated diamond," *Applied Physics Letters*, vol. 103, no. 5, p. 051603, 2013.

[21] F. Fávaro De Oliveira, S. A. Momenzadeh, Y. Wang, M. Konuma, M. Markham, A. M. Edmonds, A. Denisenko, and J. Wrachtrup, "Effect of low-damage inductively coupled plasma on shallow nitrogen-vacancy centers in diamond," *Applied Physics Letters*, vol. 107, no. 7, 2015.

[22] F. Fávaro de Oliveira, D. Antonov, Y. Wang, P. Neumann, S. A. Momenzadeh, T. Häußermann, A. Pasquarelli, A. Denisenko, and J. Wrachtrup, "Tailoring spin defects in diamond by lattice charging," *Nature Communications*, vol. 8, no. 1, p. 15409, 2017.

[23] H. Yamano, S. Kawai, K. Kato, T. Kageura, M. Inaba, T. Okada, I. Higashimata, M. Haruyama, T. Tanii, K. Yamada, S. Onoda, W. Kada, O. Hanaizumi, T. Teraji, J. Isoya, and H. Kawarada, "Charge state stabilization of shallow nitrogen vacancy

centers in diamond by oxygen surface modification," *Japanese Journal of Applied Physics*, vol. 56, no. 4S, p. 04CK08, 2017.

[24] J.-P. Tetienne, R. W. de Gille, D. A. Broadway, T. Teraji, S. E. Lillie, J. M. McCoey, N. Dontschuk, L. T. Hall, A. Stacey, D. A. Simpson, and L. C. L. Hollenberg, "Spin properties of dense near-surface ensembles of nitrogen-vacancy centers in diamond," *Physical Review B*, vol. 97, no. 8, p. 085402, 2018.

[25] S. Dhomkar, H. Jayakumar, P. R. Zangara, and C. A. Meriles, "Charge Dynamics in near-Surface, Variable-Density Ensembles of Nitrogen-Vacancy Centers in Diamond," *Nano Letters*, vol. 18, no. 6, pp. 4046–4052, 2018.

[26] A. Stacey, N. Dontschuk, J.-P. Chou, D. A. Broadway, A. K. Schenk, M. J. Sear, J.-P. Tetienne, A. Hoffman, S. Prawer, C. I. Pakes, A. Tadich, N. P. de Leon, A. Gali, and L. C. L. Hollenberg, "Evidence for Primal sp2 Defects at the Diamond Surface: Candidates for Electron Trapping and Noise Sources," *Advanced Materials Interfaces*, vol. 6, no. 3, p. 1801449, 2019.

[27] G. Waldherr, J. Beck, M. Steiner, P. Neumann, A. Gali, T. Frauenheim, F. Jelezko, and J. Wrachtrup, "Dark States of Single Nitrogen-Vacancy Centers in Diamond Unraveled by Single Shot NMR," *Physical Review Letters*, vol. 106, no. 15, p. 157601, 2011.

[28] K. Beha, A. Batalov, N. B. Manson, R. Bratschitsch, and A. Leitenstorfer, "Optimum Photoluminescence Excitation and Recharging Cycle of Single Nitrogen-Vacancy Centers in Ultrapure Diamond," *Physical Review Letters*, vol. 109, no. 9, p. 097404, 2012.

[29] K. Y. Han, D. Wildanger, E. Rittweger, J. Meijer, S. Pezzagna, S. W. Hell, and C. Eggeling, "Dark state photophysics of nitrogen-vacancy centres in diamond," *New Journal of Physics*, vol. 14, no. 12, p. 123002, 2012.

[30] N. B. Manson, M. Hedges, M. S. J. Barson, R. Ahlefeldt, M. W. Doherty, H. Abe, T. Ohshima, and M. J. Sellars, "NV- - N + pair centre in 1b diamond," *New Journal of Physics*, vol. 20, no. 11, p. 113037, 2018.

[31] D. Bluvstein, Z. Zhang, and A. C. B. Jayich, "Identifying and Mitigating Charge Instabilities in Shallow Diamond Nitrogen-Vacancy Centers," *Physical Review Letters*, vol. 122, no. 7, p. 076101, 2019.

[32] M. W. Doherty, N. B. Manson, P. Delaney, and L. C. L. Hollenberg, "The negatively charged nitrogen-vacancy centre in diamond: the electronic solution," *New Journal of Physics*, vol. 13, no. 2, p. 025019, 2011.

[33] M. W. Doherty, F. Dolde, H. Fedder, F. Jelezko, J. Wrachtrup, N. B. Manson, and L. C. L. Hollenberg, "Theory of the ground-state spin of the NV- center in diamond," *Physical Review B*, vol. 85, no. 20, p. 205203, 2012.

[34] A. Batalov, C. Zierl, T. Gaebel, P. Neumann, I.-Y. Chan, G. Balasubramanian, P. R. Hemmer, F. Jelezko, and J. Wrachtrup, "Temporal Coherence of Photons Emitted by Single Nitrogen-Vacancy Defect Centers in Diamond Using Optical Rabi-Oscillations," *Physical Review Letters*, vol. 100, no. 7, p. 077401, 2008.

[35] L. Robledo, H. Bernien, T. V. D. Sar, and R. Hanson, "Spin dynamics in the optical cycle of single nitrogen-vacancy centres in diamond," *New Journal of Physics*, vol. 13, no. 2, p. 025013, 2011.

[36] R. Schirhagl, K. Chang, M. Loretz, and C. L. Degen, "Nitrogen-Vacancy Centers in Diamond: Nanoscale Sensors for Physics and Biology," *Annual Review of Physical Chemistry*, vol. 65, no. 1, pp. 83–105, 2014.

[37] E. Van Oort and M. Glasbeek, "Electric-field-induced modulation of spin echoes of N-V centers in diamond," *Chemical Physics Letters*, vol. 168, no. 6, pp. 529–532, 1990.

[38] F. Dolde, M. W. Doherty, J. Michl, I. Jakobi, B. Naydenov, S. Pezzagna, J. Meijer, P. Neumann, F. Jelezko, N. B. Manson, and J. Wrachtrup, "Nanoscale Detection of a Single Fundamental Charge in Ambient Conditions Using the NV- Center in Diamond," *Physical Review Letters*, vol. 112, no. 9, p. 097603, 2014.

[39] G. D. Fuchs, V. V. Dobrovitski, R. Hanson, A. Batra, C. D. Weis, T. Schenkel, and D. D. Awschalom, "Excited-State Spectroscopy Using Single Spin Manipulation in Diamond," *Physical Review Letters*, vol. 101, no. 11, p. 117601, 2008.

[40] G. D. Fuchs, V. V. Dobrovitski, D. M. Toyli, F. J. Heremans, C. D. Weis, T. Schenkel, and D. D. Awschalom, "Excited-state spin coherence of a single nitrogen-vacancy centre in diamond," *Nature Physics*, vol. 6, no. 9, pp. 668–672, 2010.

[41] F. Jelezko, T. Gaebel, I. Popa, A. Gruber, and J. Wrachtrup, "Observation of Coherent Oscillations in a Single Electron Spin," *Physical Review Letters*, vol. 92, no. 7,

p. 076401, 2004.

[42] R. Hanson, O. Gywat, and D. D. Awschalom, "Room-temperature manipulation and decoherence of a single spin in diamond," *Physical Review B*, vol. 74, no. 16, p. 161203, 2006.

[43] A. Barfuss, J. Teissier, E. Neu, A. Nunnenkamp, and P. Maletinsky, "Strong mechanical driving of a single electron spin," *Nature Physics*, vol. 11, no. 10, pp. 820–824, 2015.

[44] A. Batalov, C. Zierl, T. Gaebel, P. Neumann, I.-Y. Chan, G. Balasubramanian, P. R. Hemmer, F. Jelezko, and J. Wrachtrup, "Temporal Coherence of Photons Emitted by Single Nitrogen-Vacancy Defect Centers in Diamond Using Optical Rabi-Oscillations," *Physical Review Letters*, vol. 100, no. 7, p. 077401, 2008.

[45] J. R. Rabeau, P. Reichart, G. Tamanyan, D. N. Jamieson, S. Prawer, F. Jelezko, T. Gaebel, I. Popa, M. Domhan, and J. Wrachtrup, "Implantation of labelled single nitrogen vacancy centers in diamond using N15," *Applied Physics Letters*, vol. 88, no. 2, p. 023113, 2006.

[46] V. Jacques, P. Neumann, J. Beck, M. Markham, D. Twitchen, J. Meijer, F. Kaiser, G. Balasubramanian, F. Jelezko, and J. Wrachtrup, "Dynamic Polarization of Single Nuclear Spins by Optical Pumping of Nitrogen-Vacancy Color Centers in Diamond at Room Temperature," *Physical Review Letters*, vol. 102, no. 5, p. 057403, 2009.

[47] J. D. A. Wood, D. A. Broadway, L. T. Hall, A. Stacey, D. A. Simpson, J.-P. Tetienne, and L. C. L. Hollenberg, "Wide-band nanoscale magnetic resonance spectroscopy using quantum relaxation of a single spin in diamond," *Physical Review B*, vol. 94, no. 15, p. 155402, 2016.

[48] D. A. Broadway, J. D. A. Wood, L. T. Hall, A. Stacey, M. Markham, D. A. Simpson, J.-P. Tetienne, and L. C. L. Hollenberg, "Anticrossing Spin Dynamics of Diamond Nitrogen-Vacancy Centers and All-Optical Low-Frequency Magnetometry," *Physical Review Applied*, vol. 6, no. 6, p. 064001, 2016.

[49] M. Auzinsh, A. Berzins, D. Budker, L. Busaite, R. Ferber, F. Gahbauer, R. Lazda, A. Wickenbrock, and H. Zheng, "Hyperfine level structure in nitrogen-vacancy centers near the ground-state level anticrossing," *Physical Review B*, vol. 100, no. 7, p. 075204, 2019.

[50] J. D. A. Wood, J.-P. Tetienne, D. A. Broadway, L. T. Hall, D. A. Simpson, A. Stacey, and L. C. L. Hollenberg, "Microwave-free nuclear magnetic resonance at molecular scales," *Nature Communications*, vol. 8, no. 1, p. 15950, 2017.

[51] S. E. Lillie, D. A. Broadway, J. D. A. Wood, D. A. Simpson, A. Stacey, J.-P. Tetienne, and L. C. L. Hollenberg, "Environmentally Mediated Coherent Control of a Spin Qubit in Diamond," *Physical Review Letters*, vol. 118, no. 16, p. 167204, 2017.

[52] D. A. Broadway, J.-P. Tetienne, A. Stacey, J. D. A. Wood, D. A. Simpson, L. T. Hall, and L. C. L. Hollenberg, "Quantum probe hyperpolarisation of molecular nuclear spins," *Nature Communications*, vol. 9, no. 1, p. 1246, 2018.

[53] D. A. Broadway, S. E. Lillie, N. Dontschuk, A. Stacey, L. T. Hall, J.-P. Tetienne, and L. C. L. Hollenberg, "High precision single qubit tuning via thermo-magnetic field control," *Applied Physics Letters*, vol. 112, no. 103103, 2018.

[54] N. Xu, Y. Tian, B. Chen, J. Geng, X. He, Y. Wang, and J. Du, "Dynamically Polarizing Spin Register of N-VCenters in Diamond Using Chopped Laser Pulses," *Physical Review Applied*, vol. 12, no. 2, p. 024055, 2019.

[55] D. J. McCloskey, N. Dontschuk, D. A. Broadway, A. Nadarajah, A. Stacey, J.-P. Tetienne, L. C. L. Hollenberg, S. Prawer, and D. A. Simpson, "Enhanced Widefield Quantum Sensing with Nitrogen-Vacancy Ensembles Using Diamond Nanopillar Arrays," *ACS Applied Materials & Interfaces*, vol. 12, no. 11, pp. 13421–13427, 2020.

[56] B. Grotz, M. V. Hauf, M. Dankerl, B. Naydenov, S. Pezzagna, J. Meijer, F. Jelezko, J. Wrachtrup, M. Stutzmann, F. Reinhard, and J. A. Garrido, "Charge state manipulation of qubits in diamond," *Nature Communications*, vol. 3, no. 1, p. 729, 2012.

[57] M. V. Hauf, P. Simon, N. Aslam, M. Pfender, P. Neumann, S. Pezzagna, J. Meijer, J. Wrachtrup, M. Stutzmann, F. Reinhard, and J. A. Garrido, "Addressing Single Nitrogen-Vacancy Centers in Diamond with Transparent in-Plane Gate Structures," *Nano Letters*, vol. 14, no. 5, pp. 2359–2364, 2014.

[58] M. Pfender, N. Aslam, P. Simon, D. Antonov, G. Thiering, S. Burk, F. Fávaro de Oliveira, A. Denisenko, H. Fedder, J. Meijer, J. A. Garrido, A. Gali, T. Teraji, J. Isoya, M. W. Doherty, A. Alkauskas, A. Gallo, A. Grüneis, P. Neumann, and

J. Wrachtrup, "Protecting a Diamond Quantum Memory by Charge State Control," *Nano Letters*, vol. 17, no. 10, pp. 5931–5937, 2017.

[59] S. E. Lillie, N. Dontschuk, D. A. Broadway, D. L. Creedon, L. C. Hollenberg, and J.-P. Tetienne, "Imaging Graphene Field-Effect Transistors on Diamond Using Nitrogen-Vacancy Microscopy," *Physical Review Applied*, vol. 12, no. 2, p. 024018, 2019.

[60] J.-P. Tetienne, N. Dontschuk, D. A. Broadway, S. E. Lillie, T. Teraji, D. A. Simpson, A. Stacey, and L. C. L. Hollenberg, "Apparent delocalization of the current density in metallic wires observed with diamond nitrogen-vacancy magnetometry," *Physical Review B*, vol. 99, no. 1, p. 014436, 2019.

[61] W. L. Barnes, "Fluorescence near interfaces: The role of photonic mode density," *Journal of Modern Optics*, vol. 45, no. 4, pp. 661–699, 1998.

[62] B. C. Buchler, T. Kalkbrenner, C. Hettich, and V. Sandoghdar, "Measuring the Quantum Efficiency of the Optical Emission of Single Radiating Dipoles Using a Scanning Mirror," *Physical Review Letters*, vol. 95, no. 6, p. 063003, 2005.

[63] J. Tisler, R. Reuter, A. Lämmle, F. Jelezko, G. Balasubramanian, P. R. Hemmer, F. Reinhard, and J. Wrachtrup, "Highly Efficient FRET from a Single Nitrogen-Vacancy Center in Nanodiamonds to a Single Organic Molecule," *ACS Nano*, vol. 5, no. 10, pp. 7893–7898, 2011.

[64] J. Tisler, T. Oeckinghaus, R. J. Stöhr, R. Kolesov, R. Reuter, F. Reinhard, and J. Wrachtrup, "Single Defect Center Scanning Near-Field Optical Microscopy on Graphene," *Nano Letters*, vol. 13, no. 7, pp. 3152–3156, 2013.

[65] J.-P. Tetienne, N. Dontschuk, D. A. Broadway, A. Stacey, D. A. Simpson, and L. C. L. Hollenberg, "Quantum imaging of current flow in graphene," *Science Advances*, vol. 3, no. 4, p. e1602429, 2017.

[66] A. Gruber, A. Dräbenstedt, C. Tietz, L. Fleury, J. Wrachtrup, and C. von Borczyskowski, "Scanning Confocal Optical Microscopy and Magnetic Resonance on Single Defect Centers," *Science*, vol. 276, no. 5321, pp. 2012–2014, 1997.

[67] G. D. Fuchs, V. V. Dobrovitski, D. M. Toyli, F. J. Heremans, and D. D. Awschalom, "Gigahertz Dynamics of a Strongly Driven Single Quantum Spin," *Science*, vol. 326, no. 5959, pp. 1520–1522, 2009.

[68] T. P. M. Alegre, C. Santori, G. Medeiros-Ribeiro, and R. G. Beausoleil, "Polarization-selective excitation of nitrogen vacancy centers in diamond," *Physical Review B*, vol. 76, no. 16, p. 165205, 2007.

[69] J. Herrmann, M. A. Appleton, K. Sasaki, Y. Monnai, T. Teraji, K. M. Itoh, and E. Abe, "Polarization- and frequency-tunable microwave circuit for selective excitation of nitrogen-vacancy spins in diamond," *Applied Physics Letters*, vol. 109, no. 18, p. 183111, 2016.

[70] L. P. McGuinness, L. T. Hall, A. Stacey, D. A. Simpson, C. D. Hill, J. H. Cole, K. Ganesan, B. C. Gibson, S. Prawer, P. Mulvaney, F. Jelezko, J. Wrachtrup, R. E. Scholten, and L. C. L. Hollenberg, "Ambient nanoscale sensing with single spins using quantum decoherence," *New Journal of Physics*, vol. 15, no. 7, p. 073042, 2013.

[71] M. S. Grinolds, M. Warner, K. De Greve, Y. Dovzhenko, L. Thiel, R. L. Walsworth, S. Hong, P. Maletinsky, and A. Yacoby, "Subnanometre resolution in three-dimensional magnetic resonance imaging of individual dark spins," *Nature Nanotechnology*, vol. 9, no. 4, pp. 279–284, 2014.

[72] J. H. Cole and L. C. L. Hollenberg, "Scanning quantum decoherence microscopy," *Nanotechnology*, vol. 20, no. 49, p. 495401, 2009.

[73] L. T. Hall, J. H. Cole, C. D. Hill, and L. C. L. Hollenberg, "Sensing of Fluctuating Nanoscale Magnetic Fields Using Nitrogen-Vacancy Centers in Diamond," *Physical Review Letters*, vol. 103, no. 22, p. 220802, 2009.

[74] L. T. Hall, C. D. Hill, J. H. Cole, and L. C. L. Hollenberg, "Ultrasensitive diamond magnetometry using optimal dynamic decoupling," *Physical Review B*, vol. 82, no. 4, p. 045208, 2010.

[75] J. R. Maze, P. L. Stanwix, J. S. Hodges, S. Hong, J. M. Taylor, P. Cappellaro, L. Jiang, M. V. G. Dutt, E. Togan, A. S. Zibrov, A. Yacoby, R. L. Walsworth, and M. D. Lukin, "Nanoscale magnetic sensing with an individual electronic spin in diamond," *Nature*, vol. 455, no. 7213, pp. 644–647, 2008.

[76] J. E. Lang, T. Madhavan, J.-P. Tetienne, D. A. Broadway, L. T. Hall, T. Teraji, T. S. Monteiro, A. Stacey, and L. C. L. Hollenberg, "Nonvanishing effect of detuning errors

in dynamical-decoupling-based quantum sensing experiments," *Physical Review A*, vol. 99, no. 1, p. 012110, 2019.

[77] N. Zhao, S.-W. Ho, and R.-B. Liu, "Decoherence and dynamical decoupling control of nitrogen vacancy center electron spins in nuclear spin baths," *Physical Review B*, vol. 85, no. 11, p. 115303, 2012.

[78] T. Staudacher, F. Shi, S. Pezzagna, J. Meijer, J. Du, C. A. Meriles, F. Reinhard, and J. Wrachtrup, "Nuclear Magnetic Resonance Spectroscopy on a (5-Nanometer) 3 Sample Volume," *Science*, vol. 339, no. 6119, pp. 561–563, 2013.

[79] S. Steinert, F. Ziem, L. T. Hall, A. Zappe, M. Schweikert, N. Götz, A. Aird, G. Balasubramanian, L. Hollenberg, and J. Wrachtrup, "Magnetic spin imaging under ambient conditions with sub-cellular resolution," *Nature Communications*, vol. 4, no. 1, p. 1607, 2013.

[80] A. Ermakova, G. Pramanik, J.-M. Cai, G. Algara-Siller, U. Kaiser, T. Weil, Y.-K. Tzeng, H. C. Chang, L. P. McGuinness, M. B. Plenio, B. Naydenov, and F. Jelezko, "Detection of a Few Metallo-Protein Molecules Using Color Centers in Nanodiamonds," *Nano Letters*, vol. 13, no. 7, pp. 3305–3309, 2013.

[81] S. Kaufmann, D. A. Simpson, L. T. Hall, V. Perunicic, P. Senn, S. Steinert, L. P. McGuinness, B. C. Johnson, T. Ohshima, F. Caruso, J. Wrachtrup, R. E. Scholten, P. Mulvaney, and L. Hollenberg, "Detection of atomic spin labels in a lipid bilayer using a single-spin nanodiamond probe," *Proceedings of the National Academy of Sciences*, vol. 110, no. 27, pp. 10894–10898, 2013.

[82] A. O. Sushkov, N. Chisholm, I. Lovchinsky, M. Kubo, P. K. Lo, S. D. Bennett, D. Hunger, A. Akimov, R. L. Walsworth, H. Park, and M. D. Lukin, "All-Optical Sensing of a Single-Molecule Electron Spin," *Nano Letters*, vol. 14, no. 11, pp. 6443–6448, 2014.

[83] J.-P. Tetienne, A. Lombard, D. A. Simpson, C. Ritchie, J. Lu, P. Mulvaney, and L. C. L. Hollenberg, "Scanning Nanospin Ensemble Microscope for Nanoscale Magnetic and Thermal Imaging," *Nano Letters*, vol. 16, no. 1, pp. 326–333, 2016.

[84] D. A. Simpson, R. G. Ryan, L. T. Hall, E. Panchenko, S. C. Drew, S. Petrou, P. S. Donnelly, P. Mulvaney, and L. C. L. Hollenberg, "Electron paramagnetic resonance

microscopy using spins in diamond under ambient conditions," *Nature Communications*, vol. 8, no. 1, p. 458, 2017.

[85] J. M. McCoey, M. Matsuoka, R. W. Gille, L. T. Hall, J. A. Shaw, J. Tetienne, D. Kisailus, L. C. L. Hollenberg, and D. A. Simpson, "Quantum Magnetic Imaging of Iron Biomineralization in Teeth of the Chiton Acanthopleura hirtosa," *Small Methods*, vol. 4, no. 3, p. 1900754, 2020.

[86] F. Casola, T. van der Sar, and A. Yacoby, "Probing condensed matter physics with magnetometry based on nitrogen-vacancy centres in diamond," *Nature Reviews Materials*, vol. 3, no. 1, p. 17088, 2018.

[87] G. Balasubramanian, I. Y. Chan, R. Kolesov, M. Al-Hmoud, J. Tisler, C. Shin, C. Kim, A. Wojcik, P. R. Hemmer, A. Krueger, T. Hanke, A. Leitenstorfer, R. Bratschitsch, F. Jelezko, and J. Wrachtrup, "Nanoscale imaging magnetometry with diamond spins under ambient conditions," *Nature*, vol. 455, no. 7213, pp. 648–651, 2008.

[88] J.-P. Tetienne, T. Hingant, J. V. Kim, L. H. Diez, J. P. Adam, K. Garcia, J. F. Roch, S. Rohart, A. Thiaville, D. Ravelosona, and V. Jacques, "Nanoscale imaging and control of domain-wall hopping with a nitrogen-vacancy center microscope," *Science*, vol. 344, no. 6190, pp. 1366–1369, 2014.

[89] J.-P. Tetienne, T. Hingant, L. Rondin, S. Rohart, A. Thiaville, J.-F. Roch, and V. Jacques, "Quantitative stray field imaging of a magnetic vortex core," *Physical Review B*, vol. 88, no. 21, p. 214408, 2013.

[90] I. Gross, W. Akhtar, V. Garcia, L. J. Martínez, S. Chouaieb, K. Garcia, C. Carrétéro, A. Barthélémy, P. Appel, P. Maletinsky, J.-V. Kim, J. Y. Chauleau, N. Jaouen, M. Viret, M. Bibes, S. Fusil, and V. Jacques, "Real-space imaging of non-collinear antiferromagnetic order with a single-spin magnetometer," *Nature*, vol. 549, no. 7671, pp. 252–256, 2017.

[91] I. Gross, W. Akhtar, A. Hrabec, J. Sampaio, L. J. Martínez, S. Chouaieb, B. J. Shields, P. Maletinsky, A. Thiaville, S. Rohart, and V. Jacques, "Skyrmion morphology in ultrathin magnetic films," *Physical Review Materials*, vol. 2, no. 2, p. 024406, 2018.

[92] Y. Dovzhenko, F. Casola, S. Schlotter, T. X. Zhou, F. Büttner, R. L. Walsworth, G. S. D. Beach, and A. Yacoby, "Magnetostatic twists in room-temperature skyrmions explored by nitrogen-vacancy center spin texture reconstruction," *Nature Communications*, vol. 9, no. 1, p. 2712, 2018.

[93] W. Akhtar, A. Hrabec, S. Chouaieb, A. Haykal, I. Gross, M. Belmeguenai, M. Gabor, B. Shields, P. Maletinsky, A. Thiaville, S. Rohart, and V. Jacques, "Current-Induced Nucleation and Dynamics of Skyrmions in a Co-based Heusler Alloy," *Physical Review Applied*, vol. 11, no. 3, p. 034066, 2019.

[94] P. Maletinsky, S. Hong, M. S. Grinolds, B. Hausmann, M. D. Lukin, R. L. Walsworth, M. Loncar, and A. Yacoby, "A robust scanning diamond sensor for nanoscale imaging with single nitrogen-vacancy centres," *Nature Nanotechnology*, vol. 7, no. 5, pp. 320–324, 2012.

[95] M. Pelliccione, A. Jenkins, P. Ovartchaiyapong, C. Reetz, E. Emmanouilidou, N. Ni, and A. C. Bleszynski Jayich, "Scanned probe imaging of nanoscale magnetism at cryogenic temperatures with a single-spin quantum sensor," *Nature Nanotechnology*, vol. 11, no. 8, pp. 700–705, 2016.

[96] T. van der Sar, F. Casola, R. Walsworth, and A. Yacoby, "Nanometre-scale probing of spin waves using single electron spins," *Nature Communications*, vol. 6, no. 1, p. 7886, 2015.

[97] P. Andrich, C. F. de las Casas, X. Liu, H. L. Bretscher, J. R. Berman, F. J. Heremans, P. F. Nealey, and D. D. Awschalom, "Long-range spin wave mediated control of defect qubits in nanodiamonds," *npj Quantum Information*, vol. 3, no. 1, p. 28, 2017.

[98] D. R. Glenn, R. R. Fu, P. Kehayias, D. Le Sage, E. A. Lima, B. P. Weiss, and R. L. Walsworth, "Micrometer-scale magnetic imaging of geological samples using a quantum diamond microscope," *Geochemistry, Geophysics, Geosystems*, vol. 18, no. 8, pp. 3254–3267, 2017.

[99] C. Gong, L. Li, Z. Li, H. Ji, A. Stern, Y. Xia, T. Cao, W. Bao, C. Wang, Y. Wang, Z. Q. Qiu, R. J. Cava, S. G. Louie, J. Xia, and X. Zhang, "Discovery of intrinsic ferromagnetism in two-dimensional van der Waals crystals," *Nature*, vol. 546, no. 7657, pp. 265–269, 2017.

[100] B. Huang, G. Clark, E. Navarro-Moratalla, D. R. Klein, R. Cheng, K. L. Seyler, D. Zhong, E. Schmidgall, M. A. McGuire, D. H. Cobden, W. Yao, D. Xiao, P. Jarillo-Herrero, and X. Xu, "Layer-dependent ferromagnetism in a van der Waals crystal down to the monolayer limit," *Nature*, vol. 546, no. 7657, pp. 270–273, 2017.

[101] D. A. Broadway, S. C. Scholten, C. Tan, N. Dontschuk, S. E. Lillie, B. C. Johnson, G. Zheng, Z. Wang, A. R. Oganov, S. Tian, C. Li, H. Lei, L. Wang, L. C. L. Hollenberg, and J.-P. Tetienne, "Imaging Domain Reversal in an Ultrathin Van der Waals Ferromagnet," *Advanced Materials*, vol. 32, no. 39, p. 2003314, 2020.

[102] V. M. Acosta, L. S. Bouchard, D. Budker, R. Folman, T. Lenz, P. Maletinsky, D. Rohner, Y. Schlussel, and L. Thiel, "Color Centers in Diamond as Novel Probes of Superconductivity," *Journal of Superconductivity and Novel Magnetism*, vol. 32, no. 1, pp. 85–95, 2019.

[103] L.-S. Bouchard, V. M. Acosta, E. Bauch, and D. Budker, "Detection of the Meissner effect with a diamond magnetometer," *New Journal of Physics*, vol. 13, no. 2, p. 025017, 2011.

[104] A. Waxman, Y. Schlussel, D. Groswasser, V. M. Acosta, L.-S. Bouchard, D. Budker, and R. Folman, "Diamond magnetometry of superconducting thin films," *Physical Review B*, vol. 89, no. 5, p. 054509, 2014.

[105] N. Alfasi, S. Masis, O. Shtempluck, V. Kochetok, and E. Buks, "Diamond magnetometry of Meissner currents in a superconducting film," *AIP Advances*, vol. 6, no. 7, p. 075311, 2016.

[106] N. M. Nusran, K. R. Joshi, K. Cho, M. A. Tanatar, W. R. Meier, S. L. Bud'ko, P. C. Canfield, Y. Liu, T. A. Lograsso, and R. Prozorov, "Spatially-resolved study of the Meissner effect in superconductors using NV-centers-in-diamond optical magnetometry," *New Journal of Physics*, vol. 20, no. 4, p. 043010, 2018.

[107] K. Joshi, N. Nusran, M. Tanatar, K. Cho, W. Meier, S. Bud'ko, P. Canfield, and R. Prozorov, "Measuring the Lower Critical Field of Superconductors Using Nitrogen-Vacancy Centers in Diamond Optical Magnetometry," *Physical Review Applied*, vol. 11, no. 1, p. 014035, 2019.

[108] Y. Xu, Y. Yu, Y. Y. Hui, Y. Su, J. Cheng, H.-C. Chang, Y. Zhang, Y. R. Shen, and C. Tian, "Mapping Dynamical Magnetic Responses of Ultrathin Micron-Size

Superconducting Films Using Nitrogen-Vacancy Centers in Diamond," *Nano Letters*, vol. 19, no. 8, pp. 5697–5702, 2019.

[109] Y. Schlussel, T. Lenz, D. Rohner, Y. Bar-Haim, L. Bougas, D. Groswasser, M. Kieschnick, E. Rozenberg, L. Thiel, A. Waxman, J. Meijer, P. Maletinsky, D. Budker, and R. Folman, "Wide-Field Imaging of Superconductor Vortices with Electron Spins in Diamond," *Physical Review Applied*, vol. 10, no. 3, p. 034032, 2018.

[110] K. Chang, A. Eichler, J. Rhensius, L. Lorenzelli, and C. L. Degen, "Nanoscale Imaging of Current Density with a Single-Spin Magnetometer," *Nano Letters*, vol. 17, no. 4, pp. 2367–2373, 2017.

[111] M. J. H. Ku, T. X. Zhou, Q. Li, Y. J. Shin, J. K. Shi, C. Burch, L. E. Anderson, A. T. Pierce, Y. Xie, A. Hamo, U. Vool, H. Zhang, F. Casola, T. Taniguchi, K. Watanabe, M. M. Fogler, P. Kim, A. Yacoby, and R. L. Walsworth, "Imaging viscous flow of the Dirac fluid in graphene," *Nature*, vol. 583, no. 7817, pp. 537–541, 2020.

[112] S. Kolkowitz, A. Safira, A. A. High, R. C. Devlin, S. Choi, Q. P. Unterreithmeier, D. Patterson, A. S. Zibrov, V. E. Manucharyan, H. Park, and M. D. Lukin, "Probing Johnson noise and ballistic transport in normal metals with a single-spin qubit," *Science*, vol. 347, no. 6226, pp. 1129–1132, 2015.

[113] A. Ariyaratne, D. Bluvstein, B. A. Myers, and A. C. B. Jayich, "Nanoscale electrical conductivity imaging using a nitrogen-vacancy center in diamond," *Nature Communications*, vol. 9, no. 1, p. 2406, 2018.

[114] T. I. Andersen, B. L. Dwyer, J. D. Sanchez-Yamagishi, J. F. Rodriguez-Nieva, K. Agarwal, K. Watanabe, T. Taniguchi, E. A. Demler, P. Kim, H. Park, and M. D. Lukin, "Electron-phonon instability in graphene revealed by global and local noise probes," *Science*, vol. 364, no. 6436, pp. 154–157, 2019.

[115] M. S. Grinolds, S. Hong, P. Maletinsky, L. Luan, M. D. Lukin, R. L. Walsworth, and A. Yacoby, "Nanoscale magnetic imaging of a single electron spin under ambient conditions," *Nature Physics*, vol. 9, no. 4, pp. 215–219, 2013.

[116] H. J. Mamin, M. Kim, M. H. Sherwood, C. T. Rettner, K. Ohno, D. D. Awschalom, and D. Rugar, "Nanoscale Nuclear Magnetic Resonance with a Nitrogen-Vacancy Spin Sensor," *Science*, vol. 339, no. 6119, pp. 557–560, 2013.

[117] I. Lovchinsky, J. D. Sanchez-Yamagishi, E. K. Urbach, S. Choi, S. Fang, T. I. Andersen, K. Watanabe, T. Taniguchi, A. Bylinskii, E. Kaxiras, P. Kim, H. Park, and M. D. Lukin, "Magnetic resonance spectroscopy of an atomically thin material using a single-spin qubit," *Science*, vol. 355, no. 6324, pp. 503–507, 2017.

[118] S. J. DeVience, L. M. Pham, I. Lovchinsky, A. O. Sushkov, N. Bar-Gill, C. Belthangady, F. Casola, M. Corbett, H. Zhang, M. Lukin, H. Park, A. Yacoby, and R. L. Walsworth, "Nanoscale NMR spectroscopy and imaging of multiple nuclear species," *Nature Nanotechnology*, vol. 10, no. 2, pp. 129–134, 2015.

[119] F. Ziem, M. Garsi, H. Fedder, and J. Wrachtrup, "Quantitative nanoscale MRI with a wide field of view," *Scientific Reports*, vol. 9, no. 1, p. 12166, 2019.

[120] S. Schmitt, T. Gefen, F. M. Stürner, T. Unden, G. Wolff, C. Müller, J. Scheuer, B. Naydenov, M. Markham, S. Pezzagna, J. Meijer, I. Schwarz, M. Plenio, A. Retzker, L. P. McGuinness, and F. Jelezko, "Submillihertz magnetic spectroscopy performed with a nanoscale quantum sensor," *Science*, vol. 356, no. 6340, pp. 832–837, 2017.

[121] J. M. Boss, K. S. Cujia, J. Zopes, and C. L. Degen, "Quantum sensing with arbitrary frequency resolution," *Science*, vol. 356, no. 6340, pp. 837–840, 2017.

[122] D. R. Glenn, D. B. Bucher, J. Lee, M. D. Lukin, H. Park, and R. L. Walsworth, "High-resolution magnetic resonance spectroscopy using a solid-state spin sensor," *Nature*, vol. 555, no. 7696, pp. 351–354, 2018.

[123] M. H. Abobeih, J. Randall, C. E. Bradley, H. P. Bartling, M. A. Bakker, M. J. Degen, M. Markham, D. J. Twitchen, and T. H. Taminiau, "Atomic-scale imaging of a 27-nuclear-spin cluster using a quantum sensor," *Nature*, vol. 576, no. 7787, pp. 411–415, 2019.

[124] V. S. Perunicic, C. D. Hill, L. T. Hall, and L. Hollenberg, "A quantum spin-probe molecular microscope," *Nature Communications*, vol. 7, no. 1, p. 12667, 2016.

[125] D. B. Bucher, D. P. L. Aude Craik, M. P. Backlund, M. J. Turner, O. Ben Dor, D. R. Glenn, and R. L. Walsworth, "Quantum diamond spectrometer for nanoscale NMR and ESR spectroscopy," *Nature Protocols*, vol. 14, no. 9, pp. 2707–2747, 2019.

[126] L. P. McGuinness, Y. Yan, A. Stacey, D. A. Simpson, L. T. Hall, D. Maclaurin, S. Prawer, P. Mulvaney, J. Wrachtrup, F. Caruso, R. E. Scholten, and L. C. L.

Hollenberg, "Quantum measurement and orientation tracking of fluorescent nanodiamonds inside living cells," *Nature Nanotechnology*, vol. 6, no. 6, pp. 358–363, 2011.

[127] G. Kucsko, P. C. Maurer, N. Y. Yao, M. Kubo, H. J. Noh, P. K. Lo, H. Park, and M. D. Lukin, "Nanometre-scale thermometry in a living cell," *Nature*, vol. 500, no. 7460, pp. 54–58, 2013.

[128] D. A. Simpson, E. Morrisroe, J. M. McCoey, A. H. Lombard, D. C. Mendis, F. Treussart, L. T. Hall, S. Petrou, and L. C. L. Hollenberg, "Non-Neurotoxic Nanodiamond Probes for Intraneuronal Temperature Mapping," *ACS Nano*, vol. 11, no. 12, pp. 12077–12086, 2017.

[129] D. Le Sage, K. Arai, D. R. Glenn, S. J. DeVience, L. M. Pham, L. Rahn-Lee, M. D. Lukin, A. Yacoby, A. Komeili, and R. L. Walsworth, "Optical magnetic imaging of living cells," *Nature*, vol. 496, no. 7446, pp. 486–489, 2013.

[130] M. Pelliccione, B. A. Myers, L. M. A. Pascal, A. Das, and A. C. Bleszynski Jayich, "Two-Dimensional Nanoscale Imaging of Gadolinium Spins via Scanning Probe Relaxometry with a Single Spin in Diamond," *Physical Review Applied*, vol. 2, no. 5, p. 054014, 2014.

[131] P. Wang, S. Chen, M. Guo, S. Peng, M. Wang, M. Chen, W. Ma, R. Zhang, J. Su, X. Rong, F. Shi, T. Xu, and J. Du, "Nanoscale magnetic imaging of ferritins in a single cell," *Science Advances*, vol. 5, no. 4, p. eaau8038, 2019.

[132] E. E. Kleinsasser, M. M. Stanfield, J. K. Q. Banks, Z. Zhu, W.-D. Li, V. M. Acosta, H. Watanabe, K. M. Itoh, and K.-M. C. Fu, "High density nitrogen-vacancy sensing surface created via He+ ion implantation of 12C diamond," *Applied Physics Letters*, vol. 108, no. 20, p. 202401, 2016.

[133] A. Stacey, T. J. Karle, L. P. McGuinness, B. C. Gibson, K. Ganesan, S. TomljenovicâĂŘHanic, A. D. Greentree, A. Hoffman, R. G. Beausoleil, and S. Prawer, "Depletion of nitrogen-vacancy color centers in diamond via hydrogen passivation," *Applied Physics Letters*, vol. 100, no. 7, p. 071902, 2012.

[134] M. N. R. Ashfold, J. P. Goss, B. L. Green, P. W. May, M. E. Newton, and C. V. Peaker, "Nitrogen in Diamond," *Chemical Reviews*, vol. 120, no. 12, pp. 5745–5794, 2020.

[135] L. Chen, X. Miao, H. Ma, L. Guo, Z. Wang, Z. Yang, C. Fang, and X. Jia, "Synthesis and characterization of diamonds with different nitrogen concentrations under high pressure and high temperature conditions," *CrystEngComm*, vol. 20, no. 44, pp. 7164–7169, 2018.

[136] H. Zheng, J. Xu, G. Z. Iwata, T. Lenz, J. Michl, B. Yavkin, K. Nakamura, H. Sumiya, T. Ohshima, J. Isoya, J. Wrachtrup, A. Wickenbrock, and D. Budker, "Zero-Field Magnetometry Based on Nitrogen-Vacancy Ensembles in Diamond," *Physical Review Applied*, vol. 11, no. 6, p. 064068, 2019.

[137] K. Ohno, F. Joseph Heremans, L. C. Bassett, B. A. Myers, D. M. Toyli, A. C. Bleszynski Jayich, C. J. Palmstrøm, and D. D. Awschalom, "Engineering shallow spins in diamond with nitrogen delta-doping," *Applied Physics Letters*, vol. 101, no. 8, p. 082413, 2012.

[138] C. A. McLellan, B. A. Myers, S. Kraemer, K. Ohno, D. D. Awschalom, and A. C. Bleszynski Jayich, "Patterned Formation of Highly Coherent Nitrogen-Vacancy Centers Using a Focused Electron Irradiation Technique," *Nano Letters*, vol. 16, no. 4, pp. 2450–2454, 2016.

[139] J. M. Smith, S. A. Meynell, A. C. Bleszynski Jayich, and J. Meijer, "Colour centre generation in diamond for quantum technologies," *Nanophotonics*, vol. 8, no. 11, pp. 1889–1906, 2019.

[140] N. Mizuochi, P. Neumann, F. Rempp, J. Beck, V. Jacques, P. Siyushev, K. Nakamura, D. J. Twitchen, H. Watanabe, S. Yamasaki, F. Jelezko, and J. Wrachtrup, "Coherence of single spins coupled to a nuclear spin bath of varying density," *Physical Review B*, vol. 80, no. 4, p. 041201, 2009.

[141] K. Ohashi, T. Rosskopf, H. Watanabe, M. Loretz, Y. Tao, R. Hauert, S. Tomizawa, T. Ishikawa, J. Ishi-Hayase, S. Shikata, C. L. Degen, and K. M. Itoh, "Negatively Charged Nitrogen-Vacancy Centers in a 5 nm Thin 12C Diamond Film," *Nano Letters*, vol. 13, no. 10, pp. 4733–4738, 2013.

[142] T. Teraji, "High-quality and high-purity homoepitaxial diamond (100) film growth under high oxygen concentration condition," *Journal of Applied Physics*, vol. 118, no. 11, p. 115304, 2015.

[143] H. Ishiwata, M. Nakajima, K. Tahara, H. Ozawa, T. Iwasaki, and M. Hatano, "Perfectly aligned shallow ensemble nitrogen-vacancy centers in (111) diamond," *Applied Physics Letters*, vol. 111, no. 4, 2017.

[144] S. Chouaieb, L. Martínez, W. Akhtar, I. Robert-Philip, A. Dréau, O. Brinza, J. Achard, A. Tallaire, and V. Jacques, "Optimizing synthetic diamond samples for quantum sensing technologies by tuning the growth temperature," *Diamond and Related Materials*, vol. 96, pp. 85–89, 2019.

[145] S. Steinert, F. Dolde, P. Neumann, A. Aird, B. Naydenov, G. Balasubramanian, F. Jelezko, and J. Wrachtrup, "High sensitivity magnetic imaging using an array of spins in diamond," *Review of Scientific Instruments*, vol. 81, no. 4, p. 043705, 2010.

[146] L. M. Pham, D. Le Sage, P. L. Stanwix, T. K. Yeung, D. Glenn, A. Trifonov, P. Cappellaro, P. R. Hemmer, M. D. Lukin, H. Park, A. Yacoby, and R. L. Walsworth, "Magnetic field imaging with nitrogen-vacancy ensembles," *New Journal of Physics*, vol. 13, no. 4, p. 045021, 2011.

[147] L. M. Pham, S. J. DeVience, F. Casola, I. Lovchinsky, A. O. Sushkov, E. Bersin, J. Lee, E. Urbach, P. Cappellaro, H. Park, A. Yacoby, M. Lukin, and R. L. Walsworth, "NMR technique for determining the depth of shallow nitrogen-vacancy centers in diamond," *Physical Review B*, vol. 93, no. 4, p. 045425, 2016.

[148] K. Ito, H. Saito, K. Sasaki, H. Watanabe, T. Teraji, K. M. Itoh, and E. Abe, "Nitrogen-vacancy centers created by N+ ion implantation through screening SiO2 layers on diamond," *Applied Physics Letters*, vol. 110, no. 21, p. 213105, 2017.

[149] B. Naydenov, F. Reinhard, A. Lämmle, V. Richter, R. Kalish, U. F. S. D'Haenens-Johansson, M. Newton, F. Jelezko, and J. Wrachtrup, "Increasing the coherence time of single electron spins in diamond by high temperature annealing," *Applied Physics Letters*, vol. 97, no. 24, p. 242511, 2010.

[150] T. Rosskopf, A. Dussaux, K. Ohashi, M. Loretz, R. Schirhagl, H. Watanabe, S. Shikata, K. M. Itoh, and C. L. Degen, "Investigation of Surface Magnetic Noise by Shallow Spins in Diamond," *Physical Review Letters*, vol. 112, no. 14, p. 147602, 2014.

[151] B. A. Myers, A. Das, M. C. Dartiailh, K. Ohno, D. D. Awschalom, and A. C. Bleszynski Jayich, "Probing Surface Noise with Depth-Calibrated Spins in Diamond," *Phys-*

ical Review Letters, vol. 113, no. 2, p. 027602, 2014.

[152] M. Kim, H. J. Mamin, M. H. Sherwood, K. Ohno, D. D. Awschalom, and D. Rugar, "Decoherence of Near-Surface Nitrogen-Vacancy Centers Due to Electric Field Noise," *Physical Review Letters*, vol. 115, no. 8, p. 087602, 2015.

[153] P. Jamonneau, M. Lesik, J. P. Tetienne, I. Alvizu, L. Mayer, A. Dréau, S. Kosen, J.-F. Roch, S. Pezzagna, J. Meijer, T. Teraji, Y. Kubo, P. Bertet, J. R. Maze, and V. Jacques, "Competition between electric field and magnetic field noise in the decoherence of a single spin in diamond," *Physical Review B*, vol. 93, no. 2, p. 024305, 2016.

[154] T. H. Taminiau, J. Cramer, T. van der Sar, V. V. Dobrovitski, and R. Hanson, "Universal control and error correction in multi-qubit spin registers in diamond," *Nature Nanotechnology*, vol. 9, no. 3, pp. 171–176, 2014.

[155] K. S. Cujia, J. M. Boss, K. Herb, J. Zopes, and C. L. Degen, "Tracking the precession of single nuclear spins by weak measurements," *Nature*, vol. 571, no. 7764, pp. 230–233, 2019.

[156] S. Pezzagna, B. Naydenov, F. Jelezko, J. Wrachtrup, and J. Meijer, "Creation efficiency of nitrogen-vacancy centres in diamond," *New Journal of Physics*, vol. 12, no. 6, p. 065017, 2010.

[157] Z. Huang, W. D. Li, C. Santori, V. M. Acosta, A. Faraon, T. Ishikawa, W. Wu, D. Winston, R. S. Williams, and R. G. Beausoleil, "Diamond nitrogen-vacancy centers created by scanning focused helium ion beam and annealing," *Applied Physics Letters*, vol. 103, no. 8, 2013.

[158] K. Ohno, F. Joseph Heremans, C. F. de las Casas, B. A. Myers, B. J. Alemán, A. C. Bleszynski Jayich, and D. D. Awschalom, "Three-dimensional localization of spins in diamond using 12C implantation," *Applied Physics Letters*, vol. 105, no. 5, p. 052406, 2014.

[159] V. M. Acosta, E. Bauch, M. P. Ledbetter, C. Santori, K.-M. C. Fu, P. E. Barclay, R. G. Beausoleil, H. Linget, J. F. Roch, F. Treussart, S. Chemerisov, W. Gawlik, and D. Budker, "Diamonds with a high density of nitrogen-vacancy centers for magnetometry applications," *Physical Review B*, vol. 80, no. 11, p. 115202, 2009.

[160] J. Botsoa, T. Sauvage, M.-P. Adam, P. Desgardin, E. Leoni, B. Courtois, F. Treussart, and M.-F. Barthe, "Optimal conditions for NV- center formation in type-1b diamond studied using photoluminescence and positron annihilation spectroscopies," *Physical Review B*, vol. 84, no. 12, p. 125209, 2011.

[161] Y.-C. Chen, P. S. Salter, S. Knauer, L. Weng, A. C. Frangeskou, C. J. Stephen, S. N. Ishmael, P. R. Dolan, S. Johnson, B. L. Green, G. W. Morley, M. E. Newton, J. G. Rarity, M. J. Booth, and J. M. Smith, "Laser writing of coherent colour centres in diamond," *Nature Photonics*, vol. 11, no. 2, pp. 77–80, 2017.

[162] T. R. Eichhorn, C. A. McLellan, and A. C. Bleszynski Jayich, "Optimizing the formation of depth-confined nitrogen vacancy center spin ensembles in diamond for quantum sensing," *Physical Review Materials*, vol. 3, no. 11, p. 113802, 2019.

[163] G. Davies, S. C. Lawson, A. T. Collins, A. Mainwood, and S. J. Sharp, "Vacancy-related centers in diamond," *Physical Review B*, vol. 46, no. 20, pp. 13157–13170, 1992.

[164] T. Yamamoto, T. Umeda, K. Watanabe, S. Onoda, M. L. Markham, D. J. Twitchen, B. Naydenov, L. P. McGuinness, T. Teraji, S. Koizumi, F. Dolde, H. Fedder, J. Honert, J. Wrachtrup, T. Ohshima, F. Jelezko, and J. Isoya, "Extending spin coherence times of diamond qubits by high-temperature annealing," *Physical Review B*, vol. 88, no. 7, p. 075206, 2013.

[165] M. T. Edmonds, L. H. Willems van Beveren, O. Klochan, J. Cervenka, K. Ganesan, S. Prawer, L. Ley, A. R. Hamilton, and C. I. Pakes, "Spin-Orbit Interaction in a Two-Dimensional Hole Gas at the Surface of Hydrogenated Diamond," *Nano Letters*, vol. 15, no. 1, pp. 16–20, 2015.

[166] K.-M. C. Fu, C. Santori, P. E. Barclay, and R. G. Beausoleil, "Conversion of neutral nitrogen-vacancy centers to negatively charged nitrogen-vacancy centers through selective oxidation," *Applied Physics Letters*, vol. 96, no. 12, p. 121907, 2010.

[167] M. Kim, H. J. Mamin, M. H. Sherwood, C. T. Rettner, J. Frommer, and D. Rugar, "Effect of oxygen plasma and thermal oxidation on shallow nitrogen-vacancy centers in diamond," *Applied Physics Letters*, vol. 105, no. 4, p. 042406, 2014.

[168] I. Lovchinsky, A. O. Sushkov, E. Urbach, N. P. de Leon, S. Choi, K. De Greve, R. Evans, R. Gertner, E. Bersin, C. Muller, L. McGuinness, F. Jelezko, R. L.

Walsworth, H. Park, and M. D. Lukin, "Nuclear magnetic resonance detection and spectroscopy of single proteins using quantum logic," *Science*, vol. 351, no. 6275, pp. 836–841, 2016.

[169] C. Osterkamp, J. Lang, J. Scharpf, C. Müller, L. P. McGuinness, T. Diemant, R. J. Behm, B. Naydenov, and F. Jelezko, "Stabilizing shallow color centers in diamond created by nitrogen delta-doping using SF6 plasma treatment," *Applied Physics Letters*, vol. 106, no. 11, p. 113109, 2015.

[170] S. E. Lillie, D. A. Broadway, N. Dontschuk, A. Zavabeti, D. A. Simpson, T. Teraji, T. Daeneke, L. C. L. Hollenberg, and J.-P. Tetienne, "Magnetic noise from ultra-thin abrasively deposited materials on diamond," *Physical Review Materials*, vol. 2, no. 11, p. 116002, 2018.

[171] J. F. Ziegler, M. Ziegler, and J. Biersack, "SRIM - The stopping and range of ions in matter (2010)," *Nuclear Instruments and Methods in Physics Research Section B: Beam Interactions with Materials and Atoms*, vol. 268, no. 11-12, pp. 1818–1823, 2010.

[172] E. V. Levine, M. J. Turner, P. Kehayias, C. A. Hart, N. Langellier, R. Trubko, D. R. Glenn, R. R. Fu, and R. L. Walsworth, "Principles and techniques of the quantum diamond microscope," *Nanophotonics*, vol. 8, no. 11, pp. 1945–1973, 2019.

[173] V. Stepanov, F. H. Cho, C. Abeywardana, and S. Takahashi, "High-frequency and high-field optically detected magnetic resonance of nitrogen-vacancy centers in diamond," *Applied Physics Letters*, vol. 106, no. 6, p. 063111, 2015.

[174] W. Chen, Z. Sun, Z. Wang, L. Gu, X. Xu, S. Wu, and C. Gao, "Direct observation of van der Waals stacking-dependent interlayer magnetism," *Science*, vol. 366, no. 6468, pp. 983–987, 2019.

[175] A. M. Wojciechowski, M. Karadas, A. Huck, C. Osterkamp, S. Jankuhn, J. Meijer, F. Jelezko, and U. L. Andersen, "Contributed Review: Camera-limits for wide-field magnetic resonance imaging with a nitrogen-vacancy spin sensor," *Review of Scientific Instruments*, vol. 89, no. 3, p. 031501, 2018.

[176] J.-P. Tetienne, D. Broadway, S. Lillie, N. Dontschuk, T. Teraji, L. Hall, A. Stacey, D. Simpson, and L. Hollenberg, "Proximity-Induced Artefacts in Magnetic Imaging

with Nitrogen-Vacancy Ensembles in Diamond," *Sensors*, vol. 18, no. 4, p. 1290, 2018.

[177] T. Mittiga, S. Hsieh, C. Zu, B. Kobrin, F. Machado, P. Bhattacharyya, N. Z. Rui, A. Jarmola, S. Choi, D. Budker, and N. Y. Yao, "Imaging the Local Charge Environment of Nitrogen-Vacancy Centers in Diamond," *Physical Review Letters*, vol. 121, no. 24, p. 246402, 2018.

[178] T. Daeneke, P. Atkin, R. Orrell-Trigg, A. Zavabeti, T. Ahmed, S. Walia, M. Liu, Y. Tachibana, M. Javaid, A. D. Greentree, S. P. Russo, R. B. Kaner, and K. Kalantar-Zadeh, "Wafer-Scale Synthesis of Semiconducting SnO Monolayers from Interfacial Oxide Layers of Metallic Liquid Tin," *ACS Nano*, vol. 11, no. 11, pp. 10974–10983, 2017.

[179] A. Zavabeti, J. Z. Ou, B. J. Carey, N. Syed, R. Orrell-Trigg, E. L. H. Mayes, C. Xu, O. Kavehei, A. P. O'Mullane, R. B. Kaner, K. Kalantar-zadeh, and T. Daeneke, "A liquid metal reaction environment for the room-temperature synthesis of atomically thin metal oxides," *Science*, vol. 358, no. 6361, pp. 332–335, 2017.

[180] Y. Cao, V. Fatemi, A. Demir, S. Fang, S. L. Tomarken, J. Y. Luo, J. D. Sanchez-Yamagishi, K. Watanabe, T. Taniguchi, E. Kaxiras, R. C. Ashoori, and P. Jarillo-Herrero, "Correlated insulator behaviour at half-filling in magic-angle graphene superlattices," *Nature*, vol. 556, no. 7699, pp. 80–84, 2018.

[181] Y. Cao, V. Fatemi, S. Fang, K. Watanabe, T. Taniguchi, E. Kaxiras, and P. Jarillo-Herrero, "Unconventional superconductivity in magic-angle graphene superlattices," *Nature*, vol. 556, no. 7699, pp. 43–50, 2018.

[182] K. Agarwal, R. Schmidt, B. Halperin, V. Oganesyan, G. Zaránd, M. D. Lukin, and E. Demler, "Magnetic noise spectroscopy as a probe of local electronic correlations in two-dimensional systems," *Physical Review B*, vol. 95, no. 15, p. 155107, 2017.

[183] J. F. Rodriguez-Nieva, K. Agarwal, T. Giamarchi, B. I. Halperin, M. D. Lukin, and E. Demler, "Probing one-dimensional systems via noise magnetometry with single spin qubits," *Physical Review B*, vol. 98, no. 19, p. 195433, 2018.

[184] P. Dev and T. L. Reinecke, "Substrate effects: Disappearance of adsorbate-induced magnetism in graphene," *Physical Review B*, vol. 89, no. 3, p. 035404, 2014.

[185] S. Lippert, L. M. Schneider, D. Renaud, K. N. Kang, O. Ajayi, J. Kuhnert, M.-u. Halbich, O. M. Abdulmunem, X. Lin, K. Hassoon, S. Edalati-Boostan, Y. D. Kim, W. Heimbrodt, E.-H. Yang, J. C. Hone, and A. Rahimi-Iman, "Influence of the substrate material on the optical properties of tungsten diselenide monolayers," *2D Materials*, vol. 4, no. 2, p. 025045, 2017.

[186] Q. Li, C. W. Kartikowati, S. Horie, T. Ogi, T. Iwaki, and K. Okuyama, "Correlation between particle size/domain structure and magnetic properties of highly crystalline Fe3O4 nanoparticles," *Scientific Reports*, vol. 7, no. 1, p. 9894, 2017.

[187] L. T. Hall, P. Kehayias, D. A. Simpson, A. Jarmola, A. Stacey, D. Budker, and L. C. L. Hollenberg, "Detection of nanoscale electron spin resonance spectra demonstrated using nitrogen-vacancy centre probes in diamond," *Nature Communications*, vol. 7, no. 1, p. 10211, 2016.

[188] A. Jarmola, V. M. Acosta, K. Jensen, S. Chemerisov, and D. Budker, "Temperature- and Magnetic-Field-Dependent Longitudinal Spin Relaxation in Nitrogen-Vacancy Ensembles in Diamond," *Physical Review Letters*, vol. 108, no. 19, p. 197601, 2012.

[189] D. Schmid-Lorch, T. Häberle, F. Reinhard, A. Zappe, M. Slota, L. Bogani, A. Finkler, and J. Wrachtrup, "Relaxometry and Dephasing Imaging of Superparamagnetic Magnetite Nanoparticles Using a Single Qubit," *Nano Letters*, vol. 15, no. 8, pp. 4942–4947, 2015.

[190] S. Schultz and C. Latham, "Observation of Electron Spin Resonance in Copper," *Physical Review Letters*, vol. 15, no. 4, pp. 148–151, 1965.

[191] K. Kindo, M. Honda, T. Kôhashi, and M. Date, "Electron Spin Resonance in Cupric Oxide," *Journal of the Physical Society of Japan*, vol. 59, no. 7, pp. 2332–2335, 1990.

[192] D. Gao, J. Zhang, J. Zhu, J. Qi, Z. Zhang, W. Sui, H. Shi, and D. Xue, "Vacancy-Mediated Magnetism in Pure Copper Oxide Nanoparticles," *Nanoscale Research Letters*, vol. 5, no. 4, pp. 769–772, 2010.

[193] M. Bañobre-López, C. Vázquez-Vázquez, J. Rivas, and M. A. López-Quintela, "Magnetic properties of chromium (III) oxide nanoparticles," *Nanotechnology*, vol. 14, no. 2, pp. 318–322, 2003.

[194] W. Zhang, S. Brongersma, O. Richard, B. Brijs, R. Palmans, L. Froyen, and K. Maex, "Influence of the electron mean free path on the resistivity of thin metal

films," *Microelectronic Engineering*, vol. 76, no. 1-4, pp. 146–152, 2004.

[195] F. Lacy, "Developing a theoretical relationship between electrical resistivity, temperature, and film thickness for conductors," *Nanoscale Research Letters*, vol. 6, no. 1, p. 636, 2011.

[196] R. Giri, F. Gorrini, C. Dorigoni, C. E. Avalos, M. Cazzanelli, S. Tambalo, and A. Bifone, "Coupled charge and spin dynamics in high-density ensembles of nitrogen-vacancy centers in diamond," *Physical Review B*, vol. 98, no. 4, p. 045401, 2018.

[197] R. G. Ryan, A. Stacey, K. M. O'Donnell, T. Ohshima, B. C. Johnson, L. C. L. Hollenberg, P. Mulvaney, and D. A. Simpson, "Impact of Surface Functionalization on the Quantum Coherence of Nitrogen-Vacancy Centers in Nanodiamonds," *ACS Applied Materials & Interfaces*, vol. 10, no. 15, pp. 13143–13149, 2018.

[198] A. Nowodzinski, M. Chipaux, L. Toraille, V. Jacques, J.-F. Roch, and T. Debuisschert, "Nitrogen-Vacancy centers in diamond for current imaging at the redistributive layer level of Integrated Circuits," *Microelectronics Reliability*, vol. 55, no. 9-10, pp. 1549–1553, 2015.

[199] L. Kou, Y. Ma, Z. Sun, T. Heine, and C. Chen, "Two-Dimensional Topological Insulators: Progress and Prospects," *The Journal of Physical Chemistry Letters*, vol. 8, no. 8, pp. 1905–1919, 2017.

[200] S. Rachel, "Interacting topological insulators: a review," *Reports on Progress in Physics*, vol. 81, no. 11, p. 116501, 2018.

[201] D. A. Bandurin, I. Torre, R. K. Kumar, M. Ben Shalom, A. Tomadin, A. Principi, G. H. Auton, E. Khestanova, K. S. Novoselov, I. V. Grigorieva, L. A. Ponomarenko, A. K. Geim, and M. Polini, "Negative local resistance caused by viscous electron backflow in graphene," *Science*, vol. 351, no. 6277, pp. 1055–1058, 2016.

[202] A. Jenkins, S. Baumann, H. Zhou, S. A. Meynell, D. Yang, K. Watanabe, T. Taniguchi, A. Lucas, A. F. Young, and A. C. B. Jayich, "Imaging the breakdown of ohmic transport in graphene," *arXiv*, pp. 1–14, 2020.

[203] L. N. Bulaevskii, M. J. Graf, and V. G. Kogan, "Vortex-assisted photon counts and their magnetic field dependence in single-photon superconducting detectors," *Physical Review B*, vol. 85, no. 1, p. 014505, 2012.

[204] O. A. Adami, D. Cerbu, D. Cabosart, M. Motta, J. Cuppens, W. A. Ortiz, V. V. Moshchalkov, B. Hackens, R. Delamare, J. Van De Vondel, and A. V. Silhanek, "Current crowding effects in superconducting corner-shaped Al microstrips," *Applied Physics Letters*, vol. 102, no. 5, pp. 1–5, 2013.

[205] K. A. Guerrero-Becerra, F. M. D. Pellegrino, and M. Polini, "Magnetic hallmarks of viscous electron flow in graphene," *Physical Review B*, vol. 99, no. 4, p. 041407, 2019.

[206] J. Martin, N. Akerman, G. Ulbricht, T. Lohmann, J. H. Smet, K. von Klitzing, and A. Yacoby, "Observation of electron-hole puddles in graphene using a scanning single-electron transistor," *Nature Physics*, vol. 4, no. 2, pp. 144–148, 2008.

[207] J. R. Williams, T. Low, M. S. Lundstrom, and C. M. Marcus, "Gate-controlled guiding of electrons in graphene," *Nature Nanotechnology*, vol. 6, no. 4, pp. 222–225, 2011.

[208] J. A. Sulpizio, L. Ella, A. Rozen, J. Birkbeck, D. J. Perello, D. Dutta, M. Ben-Shalom, T. Taniguchi, K. Watanabe, T. Holder, R. Queiroz, A. Principi, A. Stern, T. Scaffidi, A. K. Geim, and S. Ilani, "Visualizing Poiseuille flow of hydrodynamic electrons," *Nature*, vol. 576, no. 7785, pp. 75–79, 2019.

[209] H. Nakajima, T. Morimoto, Y. Okigawa, T. Yamada, Y. Ikuta, K. Kawahara, H. Ago, and T. Okazaki, "Imaging of local structures affecting electrical transport properties of large graphene sheets by lock-in thermography," *Science Advances*, vol. 5, no. 2, p. eaau3407, 2019.

[210] I. Meric, M. Y. Han, A. F. Young, B. Ozyilmaz, P. Kim, and K. L. Shepard, "Current saturation in zero-bandgap, top-gated graphene field-effect transistors," *Nature Nanotechnology*, vol. 3, no. 11, pp. 654–659, 2008.

[211] B. Hähnlein, B. Händel, J. Pezoldt, H. Töpfer, R. Granzner, and F. Schwierz, "Side-gate graphene field-effect transistors with high transconductance," *Applied Physics Letters*, vol. 101, no. 9, p. 093504, 2012.

[212] Y. Ohno, K. Maehashi, Y. Yamashiro, and K. Matsumoto, "Electrolyte-Gated Graphene Field-Effect Transistors for Detecting pH and Protein Adsorption," *Nano Letters*, vol. 9, no. 9, pp. 3318–3322, 2009.

[213] X. Liang, B. a. Sperling, I. Calizo, G. Cheng, C. A. Hacker, Q. Zhang, Y. Obeng, K. Yan, H. Peng, Q. Li, X. Zhu, H. Yuan, A. R. Hight Walker, Z. Liu, L.-m. Peng, and C. a. Richter, "Toward Clean and Crackless Transfer of Graphene," *ACS Nano*, vol. 5, no. 11, pp. 9144–9153, 2011.

[214] A. I. Aria, K. Nakanishi, L. Xiao, P. Braeuninger-Weimer, A. A. Sagade, J. A. Alexander-Webber, and S. Hofmann, "Parameter Space of Atomic Layer Deposition of Ultrathin Oxides on Graphene," *ACS Applied Materials & Interfaces*, vol. 8, no. 44, pp. 30564–30575, 2016.

[215] Y. D. Kim, M.-H. Bae, J.-T. Seo, Y. S. Kim, H. Kim, J. H. Lee, J. R. Ahn, S. W. Lee, S.-H. Chun, and Y. D. Park, "Focused-Laser-Enabled p-n Junctions in Graphene Field-Effect Transistors," *ACS Nano*, vol. 7, no. 7, pp. 5850–5857, 2013.

[216] A. Tiberj, M. Rubio-Roy, M. Paillet, J. R. Huntzinger, P. Landois, M. Mikolasek, S. Contreras, J. L. Sauvajol, E. Dujardin, and A. A. Zahab, "Reversible optical doping of graphene," *Scientific Reports*, vol. 3, no. 1, p. 2355, 2013.

[217] L. Ju, J. Velasco, E. Huang, S. Kahn, C. Nosiglia, H.-Z. Tsai, W. Yang, T. Taniguchi, K. Watanabe, Y. Zhang, G. Zhang, M. Crommie, A. Zettl, and F. Wang, "Photoinduced doping in heterostructures of graphene and boron nitride," *Nature Nanotechnology*, vol. 9, no. 5, pp. 348–352, 2014.

[218] Y. G. Lee, C. G. Kang, U. J. Jung, J. J. Kim, H. J. Hwang, H.-J. Chung, S. Seo, R. Choi, and B. H. Lee, "Fast transient charging at the graphene/SiO2 interface causing hysteretic device characteristics," *Applied Physics Letters*, vol. 98, no. 18, p. 183508, 2011.

[219] D.-c. Mao, S.-q. Wang, S.-a. Peng, D.-y. Zhang, J.-y. Shi, X.-n. Huang, M. Asif, and Z. Jin, "The two timescales in the charge trapping mechanism for the hysteresis behavior in graphene field effect transistors," *Journal of Materials Science: Materials in Electronics*, vol. 27, no. 9, pp. 9847–9852, 2016.

[220] B. Krishna Bharadwaj, H. Chandrasekar, D. Nath, R. Pratap, and S. Raghavan, "Intrinsic limits of channel transport hysteresis in graphene-SiO2 interface and its dependence on graphene defect density," *Journal of Physics D: Applied Physics*, vol. 49, no. 26, p. 265301, 2016.

[221] T.-J. Ha, "Visible-light-induced instability in amorphous metal-oxide based TFTs for transparent electronics," *AIP Advances*, vol. 4, no. 10, p. 107136, 2014.

[222] M. Chipaux, A. Tallaire, J. Achard, S. Pezzagna, J. Meijer, V. Jacques, J.-F. Roch, and T. Debuisschert, "Magnetic imaging with an ensemble of nitrogen-vacancy centers in diamond," *The European Physical Journal D*, vol. 69, no. 7, p. 166, 2015.

[223] S. Adam, E. H. Hwang, V. M. Galitski, and S. Das Sarma, "A self-consistent theory for graphene transport," *Proceedings of the National Academy of Sciences*, vol. 104, no. 47, pp. 18392–18397, 2007.

[224] E. H. Hwang, S. Adam, and S. D. Sarma, "Carrier Transport in Two-Dimensional Graphene Layers," *Physical Review Letters*, vol. 98, no. 18, p. 186806, 2007.

[225] T. O. Wehling, S. Yuan, A. I. Lichtenstein, A. K. Geim, and M. I. Katsnelson, "Resonant Scattering by Realistic Impurities in Graphene," *Physical Review Letters*, vol. 105, no. 5, p. 056802, 2010.

[226] I. Silvestre, E. A. de Morais, A. O. Melo, L. C. Campos, A.-M. B. Goncalves, A. R. Cadore, A. S. Ferlauto, H. Chacham, M. S. C. Mazzoni, and R. G. Lacerda, "Asymmetric Effect of Oxygen Adsorption on Electron and Hole Mobilities in Bilayer Graphene: Long- and Short-Range Scattering Mechanisms," *ACS Nano*, vol. 7, no. 8, pp. 6597–6604, 2013.

[227] K.-K. Bai, Y.-C. Wei, J.-B. Qiao, S.-Y. Li, L.-J. Yin, W. Yan, J.-C. Nie, and L. He, "Detecting giant electron-hole asymmetry in a graphene monolayer generated by strain and charged-defect scattering via Landau level spectroscopy," *Physical Review B*, vol. 92, no. 12, p. 121405, 2015.

[228] H. Jayakumar, J. Henshaw, S. Dhomkar, D. Pagliero, A. Laraoui, N. B. Manson, R. Albu, M. W. Doherty, and C. A. Meriles, "Optical patterning of trapped charge in nitrogen-doped diamond," *Nature Communications*, vol. 7, no. 1, p. 12660, 2016.

[229] D. A. Broadway, B. C. Johnson, M. S. J. Barson, S. E. Lillie, N. Dontschuk, D. J. McCloskey, A. Tsai, T. Teraji, D. A. Simpson, A. Stacey, J. C. McCallum, J. E. Bradby, M. W. Doherty, L. C. L. Hollenberg, and J.-P. Tetienne, "Microscopic Imaging of the Stress Tensor in Diamond Using in Situ Quantum Sensors," *Nano Letters*, vol. 19, no. 7, pp. 4543–4550, 2019.

[230] J. F. Barry, M. J. Turner, J. M. Schloss, D. R. Glenn, Y. Song, M. D. Lukin, H. Park, and R. L. Walsworth, "Optical magnetic detection of single-neuron action potentials using quantum defects in diamond," *Proceedings of the National Academy of Sciences*, vol. 113, no. 49, pp. 14133–14138, 2016.

[231] D. Rohner, L. Thiel, B. Müller, M. Kasperczyk, R. Kleiner, D. Koelle, and P. Maletinsky, "Real-Space Probing of the Local Magnetic Response of Thin-Film Superconductors Using Single Spin Magnetometry," *Sensors*, vol. 18, no. 11, p. 3790, 2018.

[232] A. Abrikosov, "The magnetic properties of superconducting alloys," *Journal of Physics and Chemistry of Solids*, vol. 2, no. 3, pp. 199–208, 1957.

[233] X. D. Chen, C. H. Dong, F. W. Sun, C. L. Zou, J. M. Cui, Z. F. Han, and G. C. Guo, "Temperature dependent energy level shifts of nitrogen-vacancy centers in diamond," *Applied Physics Letters*, vol. 99, no. 16, pp. 1–4, 2011.

[234] S. Casalbuoni, E. Knabbe, J. Kötzler, L. Lilje, L. von Sawilski, P. Schmüser, and B. Steffen, "Surface superconductivity in niobium for superconducting RF cavities," *Nuclear Instruments and Methods in Physics Research Section A: Accelerators, Spectrometers, Detectors and Associated Equipment*, vol. 538, no. 1-3, pp. 45–64, 2005.

[235] V. L. Vadimov, D. Y. Vodolazov, S. V. Mironov, and A. S. Mel'nikov, "Photoinduced Local Nonequilibrium States in Superconductors: Hot Spot Model," *JETP Letters*, vol. 108, no. 4, pp. 270–278, 2018.

[236] I. S. Veshchunov, W. Magrini, S. V. Mironov, A. G. Godin, J.-B. Trebbia, A. I. Buzdin, P. Tamarat, and B. Lounis, "Optical manipulation of single flux quanta," *Nature Communications*, vol. 7, no. 1, p. 12801, 2016.

[237] Y. Kalcheim, E. Katzir, F. Zeides, N. Katz, Y. Paltiel, and O. Millo, "Dynamic Control of the Vortex Pinning Potential in a Superconductor Using Current Injection through Nanoscale Patterns," *Nano Letters*, vol. 17, no. 5, pp. 2934–2939, 2017.

[238] J. González, M. Joya, and J. Barba-Ortega, "Vortex state in thermally-induced pinning patterns in superconducting film," *Physics Letters A*, vol. 382, no. 42-43, pp. 3103–3108, 2018.

[239] H. Polshyn, T. Naibert, and R. Budakian, "Manipulating Multivortex States in Superconducting Structures," *Nano Letters*, vol. 19, no. 8, pp. 5476–5482, 2019.

[240] N. B. Manson, J. P. Harrison, and M. J. Sellars, "Nitrogen-vacancy center in diamond: Model of the electronic structure and associated dynamics," *Physical Review B*, vol. 74, no. 10, p. 104303, 2006.

[241] N. D. Mermin and H. Wagner, "Absence of Ferromagnetism or Antiferromagnetism in One- or Two-Dimensional Isotropic Heisenberg Models," *Physical Review Letters*, vol. 17, no. 22, pp. 1133–1136, 1966.

[242] Y. Deng, Y. Yu, Y. Song, J. Zhang, N. Z. Wang, Z. Sun, Y. Yi, Y. Z. Wu, S. Wu, J. Zhu, J. Wang, X. H. Chen, and Y. Zhang, "Gate-tunable room-temperature ferromagnetism in two-dimensional Fe3GeTe2," *Nature*, vol. 563, no. 7729, pp. 94–99, 2018.

[243] C. Tan, J. Lee, S.-G. Jung, T. Park, S. Albarakati, J. Partridge, M. R. Field, D. G. McCulloch, L. Wang, and C. Lee, "Hard magnetic properties in nanoflake van der Waals Fe3GeTe2," *Nature Communications*, vol. 9, no. 1, p. 1554, 2018.

[244] X. Wang, J. Tang, X. Xia, C. He, J. Zhang, Y. Liu, C. Wan, C. Fang, C. Guo, W. Yang, Y. Guang, X. Zhang, H. Xu, J. Wei, M. Liao, X. Lu, J. Feng, X. Li, Y. Peng, H. Wei, R. Yang, D. Shi, X. Zhang, Z. Han, Z. Zhang, G. Zhang, G. Yu, and X. Han, "Current-driven magnetization switching in a van der Waals ferromagnet Fe 3 GeTe 2," *Science Advances*, vol. 5, no. 8, p. eaaw8904, 2019.

[245] B. Shabbir, M. Nadeem, Z. Dai, M. S. Fuhrer, Q.-K. Xue, X. Wang, and Q. Bao, "Long range intrinsic ferromagnetism in two dimensional materials and dissipationless future technologies," *Applied Physics Reviews*, vol. 5, no. 4, p. 041105, 2018.

[246] K. F. Mak, J. Shan, and D. C. Ralph, "Probing and controlling magnetic states in 2D layered magnetic materials," *Nature Reviews Physics*, vol. 1, no. 11, pp. 646–661, 2019.

[247] J. Seo, D. Y. Kim, E. S. An, K. Kim, G.-Y. Kim, S.-y. Hwang, D. W. Kim, B. G. Jang, H. Kim, G. Eom, S. Y. Seo, R. Stania, M. Muntwiler, J. Lee, K. Watanabe, T. Taniguchi, Y. J. Jo, J. Lee, B. I. Min, M. H. Jo, H. W. Yeom, S.-y. Choi, J. H. Shim, and J. S. Kim, "Nearly room temperature ferromagnetism in a magnetic metal-rich van der Waals metal," *Science Advances*, vol. 6, no. 3, p. eaay8912, 2020.

[248] D. R. Klein, D. MacNeill, J. L. Lado, D. Soriano, E. Navarro-Moratalla, K. Watanabe, T. Taniguchi, S. Manni, P. Canfield, J. Fernández-Rossier, and P. Jarillo-

Herrero, "Probing magnetism in 2D van der Waals crystalline insulators via electron tunneling," *Science*, vol. 360, no. 6394, pp. 1218–1222, 2018.

[249] D. R. Klein, D. MacNeill, Q. Song, D. T. Larson, S. Fang, M. Xu, R. A. Ribeiro, P. C. Canfield, E. Kaxiras, R. Comin, and P. Jarillo-Herrero, "Enhancement of interlayer exchange in an ultrathin two-dimensional magnet," *Nature Physics*, vol. 15, no. 12, pp. 1255–1260, 2019.

[250] K. S. Burch, D. Mandrus, and J.-G. Park, "Magnetism in two-dimensional van der Waals materials," *Nature*, vol. 563, no. 7729, pp. 47–52, 2018.

[251] Ø. Johansen, V. Risinggård, A. Sudbø, J. Linder, and A. Brataas, "Current Control of Magnetism in Two-Dimensional Fe3GeTe2," *Physical Review Letters*, vol. 122, no. 21, p. 217203, 2019.

[252] D. Zhong, K. L. Seyler, X. Linpeng, R. Cheng, N. Sivadas, B. Huang, E. Schmidgall, T. Taniguchi, K. Watanabe, M. A. McGuire, W. Yao, D. Xiao, K.-M. C. Fu, and X. Xu, "Van der Waals engineering of ferromagnetic semiconductor heterostructures for spin and valleytronics," *Science Advances*, vol. 3, no. 5, p. e1603113, 2017.

[253] A. Puthirath Balan, S. Radhakrishnan, C. F. Woellner, S. K. Sinha, L. Deng, C. D. L. Reyes, B. M. Rao, M. Paulose, R. Neupane, A. Apte, V. Kochat, R. Vajtai, A. R. Harutyunyan, C.-W. Chu, G. Costin, D. S. Galvao, A. A. Martí, P. A. van Aken, O. K. Varghese, C. S. Tiwary, A. Malie Madom Ramaswamy Iyer, and P. M. Ajayan, "Exfoliation of a non-van der Waals material from iron ore hematite," *Nature Nanotechnology*, vol. 13, no. 7, pp. 602–609, 2018.

[254] B. Grotz, J. Beck, P. Neumann, B. Naydenov, R. Reuter, F. Reinhard, F. Jelezko, J. Wrachtrup, D. Schweinfurth, B. Sarkar, and P. Hemmer, "Sensing external spins with nitrogen-vacancy diamond," *New Journal of Physics*, vol. 13, no. 5, p. 055004, 2011.

[255] H. J. Mamin, M. H. Sherwood, and D. Rugar, "Detecting external electron spins using nitrogen-vacancy centers," *Physical Review B*, vol. 86, no. 19, p. 195422, 2012.

[256] N. W. Ashcroft and N. D. Mermin, *Solid state physics*. Holt, Rinehart and Winston, 1976.

[257] G. Carneiro and E. H. Brandt, "Vortex lines in films: Fields and interactions," *Physical Review B*, vol. 61, no. 9, pp. 6370–6376, 2000.

[258] M. W. Doherty, V. M. Acosta, A. Jarmola, M. S. J. Barson, N. B. Manson, D. Budker, and L. C. L. Hollenberg, "Temperature shifts of the resonances of the NV- center in diamond," *Physical Review B*, vol. 90, no. 4, p. 041201, 2014.

[259] G. Stan, S. B. Field, and J. M. Martinis, "Critical Field for Complete Vortex Expulsion from Narrow Superconducting Strips," *Physical Review Letters*, vol. 92, no. 9, p. 097003, 2004.

[260] E. A. Lima and B. P. Weiss, "Obtaining vector magnetic field maps from single-component measurements of geological samples," *Journal of Geophysical Research*, vol. 114, no. B6, p. B06102, 2009.

[261] J. Barzola-Quiquia, M. Stiller, P. D. Esquinazi, A. Molle, R. Wunderlich, S. Pezzagna, J. Meijer, W. Kossack, and S. Buga, "Unconventional Magnetization below 25 K in Nitrogen-doped Diamond provides hints for the existence of Superconductivity and Superparamagnetism," *Scientific Reports*, vol. 9, no. 1, p. 8743, 2019.

A

Appendices

A.1 Chapter 3

A.1.1 Background characterisation

Prior to the abrasive deposition of the materials studied in this work, background measurements were taken for all areas of interest. All ensemble NV diamonds used in this work were cleaned using the Bristol boil technique outlined in section 2.2.4, prior to background characterisation and subsequent abrasive deposition. Figures 3.2(a) and (b) showed the photoluminescence and bright field images of the inox steel target area prior to the deposition. This area was chosen due to its close proximity to two identifiable diamond growth pyramids, visible in figure A.1(a), which were used to ensure the same region was studied before and after the deposition. The background static field and T_1-relaxation time images for the region later scratched with inox steel are shown in figures A.1(b) and (c). The background images are featureless, showing none of the ferromagnetic signatures or bands of reduced T_1 observed after the deposition. The slight modulation of the background T_1 time across the field of view is correlated with the laser spot which was slightly off-centre in this case. We attribute this apparent reduction in T_1 to an imperfect NV-spin initialisation under the weaker illumination. This highlights potential issues in interpreting T_1 imaging features associated with changes in photoluminescence. Fortunately, much of the T_1 imaging presented in the study shows features uncorrelated with the photoluminescence imaging, so we can be confident in the findings presented. Similar background measurements were taken for all regions presented in this study. We note that features associated with each abrasive deposition were removed by Bristol boiling the diamond samples.

A.1.2 EDXS of inox steel deposition

One of the outstanding challenges in working with atomically-thin samples on a rough diamond surface is characterising the deposited materials independent of the NV measurements. Raman spectroscopy was attempted on similar samples to those presented in the main text, however, their small contribution to the total sensing volume and the background fluorescence of the NV layer make this a particularly difficult measurement. Energy-dispersive X-ray spectroscopy (EDXS) is a useful technique for characterising such

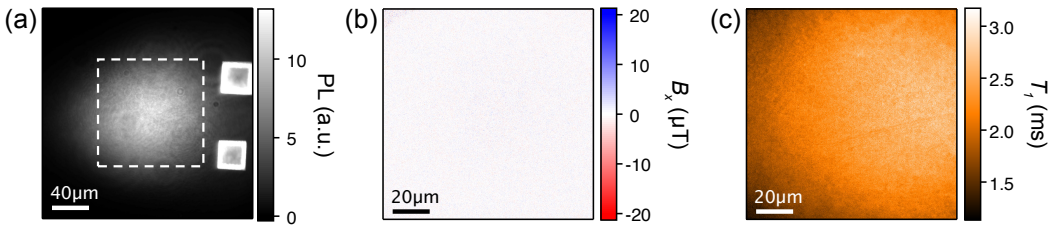

Figure A.1: Background characterisation of inox steel region. (a) PL image of the extended area surrounding the region studied for the inox steel deposition (white box). The bright diamond pyramids were used to reliably align the image, allowing comparison between images taken before and after deposition. (b) Background static field map, B_x, of the region of interest. (c) Background T_1-relaxation time map showing a slight modulation correlated with the laser illumination of the otherwise clean region.

samples as it combines high-resolution SEM imaging, which typically shows contrast between bare substrates and monolayer coverage, with spectroscopy that can identify the atomic composition of larger particles (greater than 100 nm). Here we present results for an inox steel deposition on diamond, prepared similarly to those presented in the main text.

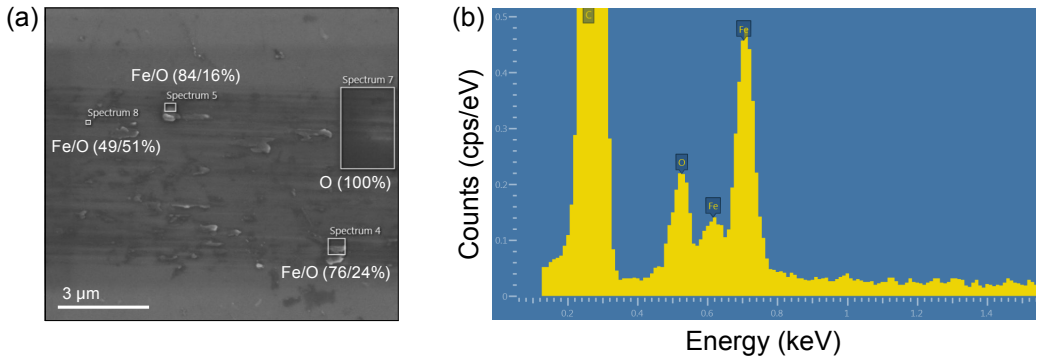

Figure A.2: EDXS of inox steel deposition. (a) SEM image of a inox steel deposited region (dark streak), annotated with results from EDXS giving relative atomic abundances, excluding the dominant contribution of carbon from the diamond substrate. (b) Representative EDXS spectra of one of the large particles deposited within the streak.

Figure A.2(a) shows an SEM image of the deposited region, showing features similar to those seen in the SEM imaging of the sample presented in the main text. A streaky band, approximately 5 μm wide, is seen with larger particles embedded in it. The EDXS spectra of these particles show the presence of Fe and O in abundances commensurate

with Fe_2O_3 and Fe_3O_4. A representative spectrum of these particles is shown in figure A.2(b), where the large peak at low energy is due to carbon. It is important to note that spectrum 7 in figure A.2(a), acquired from a region of the streak free of large particles, shows only the presence of oxygen, likely due to the surface termination of the diamond, again suggesting a sparse coverage of material from the abrasive deposition.

A.1.3 Double electron-electron resonance imaging

Double electron-electron resonance (DEER) is a standard technique in NV sensing used to detect electron spin species [254, 255]. Target species within some frequency range are driven synchronously with a spin-echo sequence driving one NV family, resulting in a detectable phase variance upon repetition. Figure A.3(a) shows the DEER spectrum integrated across the entire inox steel deposited region (identical to the region shown in figures 3.3 and 3.5), taken at a bias field strength of 437 G. Here we fit the frequency of the free-electron peak (centre), with a fixed relative shift of the substitutional nitrogen (P1) peak, given by the transverse hyperfine coupling parameters with the ^{14}N nucleus [47], and produce maps of the contrast, figures A.3(b) and (c), and linewidths, figures A.3(d) and (e), of each peak.

The optical contrast of both the free-electron peak and the central P1 centre peak, figures A.3(b) and (c), closely resembles the optical contrast map of the NV ODMR measurement, which suggests a more complex interaction between the NV layer and its environment. Comparing the widths of the two peaks across the field of view, both are broadened at the sites of ferromagnetism, as for the NV ODMR lines, but the free-electron peak is narrowed under the abraded region. The reduced contrast and width of the free-electron peak suggest a reduced visibility of these species to the DEER sequence under the abraded regions, which may result from a reduction in their own T_1-relaxation times or changes to their population. This again suggests an effect from the deposited material on the NV environment.

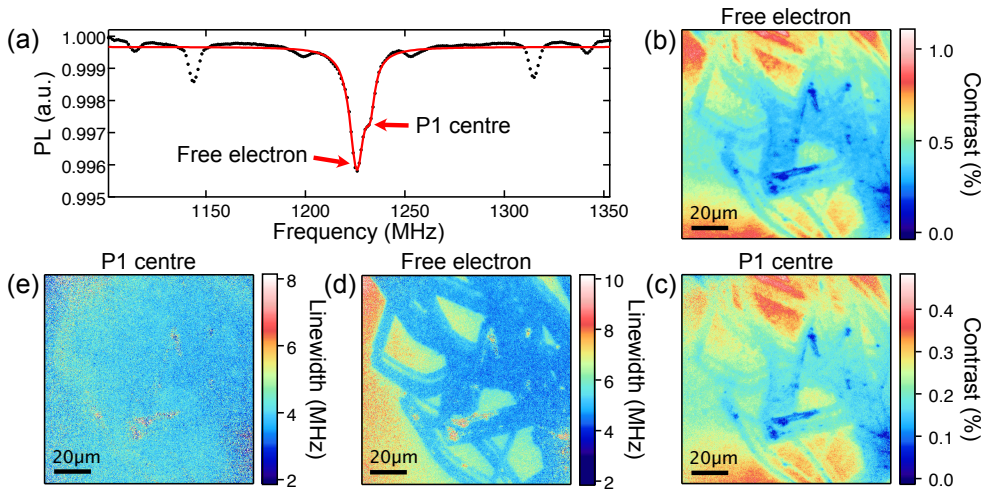

Figure A.3: DEER imaging of inox steel deposition. (a) DEER spectrum centred around the free-electron peak at 437 G. The large central peak is associated with free-electron spins. The shoulder and five outer peaks are associated with the electron spin of substitutional nitrogen (P1) centres intrinsic to the diamond. (b) and (c) DEER spectrum peak contrast for the central free-electron, and P1 shoulder peaks respectively. (d) and (e) Linewidth maps of the free-electron and central P1 peaks respectively.

A.2 Chapter 4

A.2.1 Electrical characterisation and photodoping

In addition to the initial electrical characterisation of each device shown in section 4.3, devices were monitored throughout their lifetime to track changes in their electrical behaviour. We found that sustained current-density or electric-field mapping of devices, which require a prolonged exposure to some combination of laser, gate potential, and source-drain current, resulted in significant changes to their transport curves. For example, figure A.4(a) shows the conductivity minimum of device 3 on diamond #200 shifting drastically between electric field measurements, and an associated increase in the hysteresis. In conjunction with this effect, we observed growth in the magnitude and spread of the gate-dependent quenching of the NV photoluminescence, figure A.4(b). Importantly, we note that the onset of this photoluminescence quenching occurs consistently at a threshold gate potential, $V_G = -8\,V$. Having established the link between the gate-dependent photoluminescence and the electric field in the NV layer, this indicates a greater accumulation

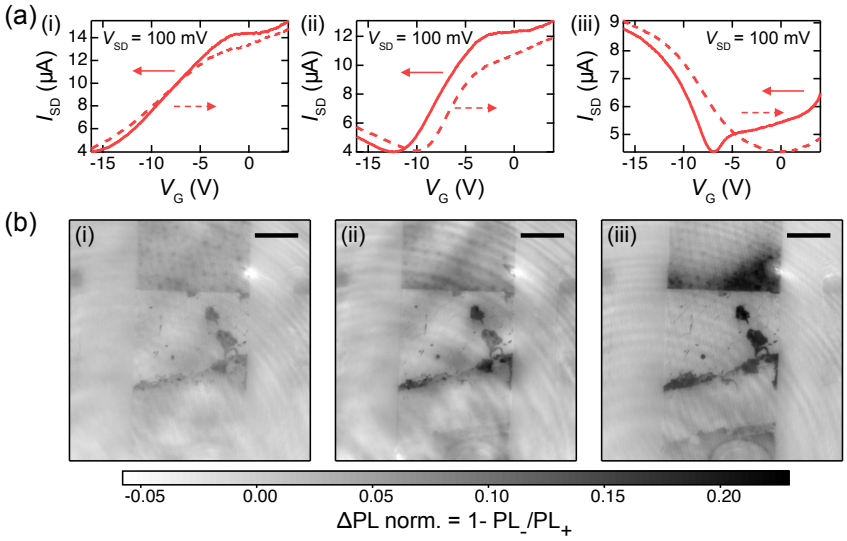

Figure A.4: Evolution of transport curves and gate-dependent photoluminescence. (a) Transport curves for device 3 on diamond #200: (i) prior to any sustained measurements; (ii) after electric field mapping at $V_G = 0\,V$ and $V_G = -8\,V$; and (iii) after electric field mapping at $V_G = -12\,V$. All measurements were taken under CW laser illumination with $V_{SD} = 100\,mV$. (b) (i)-(iii) Normalised photoluminescence difference maps of device 3 on diamond #200 taken immediately after the measurements in (a). The plotted value is the difference between the integrated photoluminescence at high gate potential, $V_G = 2\,V$ to $4\,V$ (PL_+) and the photoluminescence at low gate potential, $V_G = -16\,V$ to $-14\,V$ (PL_-), normalised by the former value. The photoluminescence is averaged across both sweep directions. A settling time of 2.0 s with 50 camera cycles per data point was used for this sweep. All scale bars are $20\,\mu m$.

and diffusion of charge at the diamond-oxide interface throughout the device's lifetime, which may also be responsible for evolution seen in the electrical measurements.

The measurements in figure A.4 demonstrate the enhanced variability in the electrical properties of our devices after being measured for sustained periods at high gate-potentials. While characterising our devices between these degrading measurements, we noticed that any given transport curve was dependent on the gate and illumination conditions immediately prior to the measurement. An explanation for this is that there is some photo-assisted charge transfer between the graphene and oxide, similar to the optical-doping seen with other gate dielectrics and substrates [215–217], which has some dependence on the applied gate potential at the time of illumination. To test this, a single device was exposed to CW laser illumination under a fixed gate potential, which we

call the photodoping potential (V_G^{PD}), and left to equilibrate over a 6 min time period, while a small source-drain potential, $V_{SD} = 100\,mV$, was applied to measure the current through the device. The laser was then turned off and a transport curve was measured, sweeping the gate potential between $-10\,V$ and $+10\,V$ while measuring the source-drain current to identify the conductivity minimum (V_G^{min}). The measurement was repeated for each photodoping gate potential, reversing the sweep direction, which was seen to systematically shift the location of the minima. We attribute this to the presence of stray light incident on the sample altering the photodoping during the sweep. The sample was photo-doped at $V_G^{PD} = 0\,V$ between each measurement, such that subsequent photodoping proceeded from similar initial conditions.

Figure A.5(a) shows conductivity minima of device 3 on diamond #200 for V_G^{PD} between $-10\,V$ and $10\,V$. Photodoping at $V_G^{PD} = 0\,V$ gives an n-type doped graphene channel with conductivity minimum at $V_G^{min} \approx -5\,V$. The minimum shifts to higher gate potentials as V_G^{PD} is increased, giving a p-type device for $V_G^{PD} \geq 8\,V$. At negative V_G^{PD}, we identify a strong threshold at $V_G^{PD} = -6\,V$ where conductivity minimum shifts to positive gate-potentials, $V_G^{min} > 10\,V$, a regime we are unable to measure due to large leakage currents through the gate oxide. We note that this threshold closely corresponds to the onset of the photoluminescence quenching effect, and hence suggest that both phenomena may be due an accumulation of holes within the oxide and at the diamond-oxide and graphene-oxide interfaces. The full photodoped transport curves measured with increasing gate potentials illustrate this effect, figure A.5(b), where the conductivity minima are beyond the range of the sweep for photodoping $V_G^{PD} \leq -8\,V$.

To investigate the time scales over which this photodoping occurs, we took time traces of the source-drain current while varying the applied gate potential and illumination conditions. Figure A.5(c) shows three 6-min-long time traces of the device. The time evolution of I_{SD} at $V_G = 0\,V$ (green curve) demonstrates the necessity of the laser in the photodoping effect, which initiates a decrease in conductivity of the device over a minutes-long time scale from some initially pinned value. The gate potential dependence is evident in the time trace when the gate potential is set from $V_G = 0\,V$ to $10\,V$ (purple curve) and $-10\,V$ (orange curve) under CW laser illumination, after having equilibrated under laser illumination at $V_G^{PD} = 0\,V$. As the new gate potential is set there is a large change in

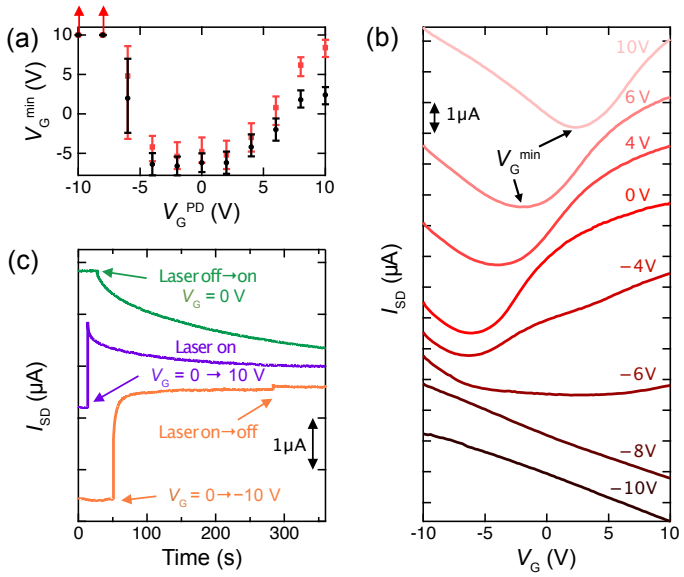

Figure A.5: Photo-doping of device 3 on diamond #200. (a) Gate potential at the conductivity minimum, V_G^{min}, as a function of the gate potential applied during photodoping, V_G^{PD}. V_G^{min} are given as measured from increasing (black) and decreasing (red) V_G transport curve sweeps. The error bars show the transport-curve width at $+0.1\,\mu$A from the conductivity minimum. (b) Transport curves measured in the dark following photodoping at the labeled gate potential, V_G^{PD}. These curves were all measured with increasing gate potential sweeps, with minima corresponding to the black data set shown in (a). The curves are offset for clarity. The minimum I_{SD} for each measurement are 2.69, 3.10, 3.22, 3.01, 3.78, 4.49, 3.79, and 4.39 μA in descending order of the photodoping gate potentials. (c) Time traces of I_{SD} showing the effect of photodoping parameters. $V_G = 0\,$V for the entirety of the green curve, and the laser is turned on at the indicated time point, leading to a bi-exponential decay in the device current. The CW laser is on initially for the purple (orange) curves, and the gate potential is switched from $V_G = 0\,$V to $+10\,$V ($-10\,$V). The laser is turned off in the orange time trace at approximately 280 s. The curves are offset for clarity while minimum current in each time trace is 3.20, 3.39, and 2.81 μA for the green, purple and orange curves respectively.

conductivity as the system jumps to a doping level commensurate with the transport curve measured at $V_G^{PD} = 0\,V$. The current then evolves slowly due to the conductivity minimum shifting to higher gate potentials under the new bias, therefore reducing (increasing) the I_{SD} in the $V_G = 10\,V$ ($-10\,V$) case. The time evolution of I_{SD} is best fit by a bi-exponential with a fast and slow component acting on time scales of 10 s and 100 s respectively, the exact values of which are sensitive to the initial conditions of the photodoping. We also observe a jump in the conductivity of the device when the laser is turned off after the device has equilibrated under CW illumination (seen at 280 s, orange curve), suggesting a gate-dielectric dynamic faster than our time-resolution (0.08 s), however, the system equilibrates to a similar doping level as reached under illumination. For this reason, we conclude that the doping achieved by a set gate potential under CW laser illumination is maintained when the illumination is then pulsed as required for NV measurements such as ODMR. Time-traces of the device source-drain current throughout ODMR measurements also endorse this.

A.2.2 Electric field simulations

To calculate the expected electric field from the top gate within the NV layer such that it can be compared to electric field measured in figure 4.8, a finite element method (FEM) simulation was performed using COMSOL. The device geometry was replicated with a 50 μm wide metallic top gate separated from a graphene ribbon by 80 nm of Al_2O_3, all hosted on top of a 50 μm thick diamond substrate. The electric field distribution was calculated in a shell surrounding the device, using a high-density mesh in the region of interest between the metallic planes and beneath the graphene plane across the NV layer.

Figure A.6(a) shows a map of the electric field beneath the top gate at the edge of the graphene ribbon, i.e. in the yz-plane through the centre of one of our devices. The simulated electric field shows a high field strength between the parallel plates of the capacitor ($-2\,MV/cm$ in the centre of oxide), which is screened from the diamond by the graphene plate. Appreciable field strengths only exist within the NV layer at the edge of the graphene ribbon under the top gate, where the magnitude reaches $-0.9\,MV/cm$ in the z-direction. However, this field reverses in sign within 300 nm from the edge, as shown by

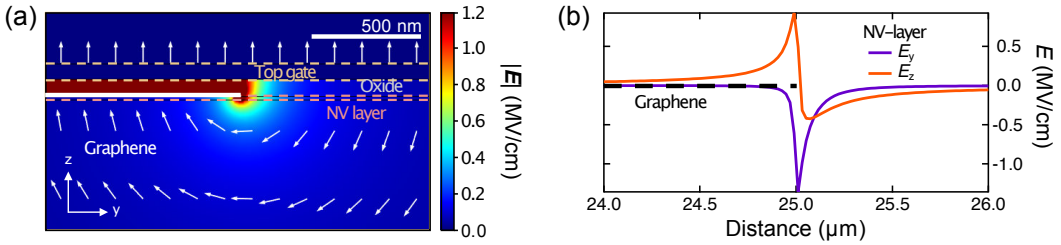

Figure A.6: COMSOL simulation of top gate electric field. (a) Simulated electric field magnitude plot for $V_G = 16\,V$ within a plane running perpendicular to the graphene ribbon edge, in the middle of the top gate (i.e. corresponding to a vertical line cut of the images shown in the main text). The graphene extends from the left-hand-side to the middle of the plot, whereas the top gate, oxide, and diamond cover the full region. The arrows show the projection of the electric field in the plane. The aspect ratio is 1 : 1, and the colour scale has been capped at 1.2 MV/cm to highlight features at lower field magnitudes. (b) Electric field components in the y and z directions in the NV layer (15 nm below the diamond surface) at $V_G = 16\,V$ across the width of the image shown in (a). The graphene ribbon edge lies at 25 μm.

the profiles plotted in figure A.6(b). The y-component of the field reaches $-1.2\,MV/cm$ at the graphene edge, but is laterally confined to 200 nm. Given our optical-resolution-limited imaging, these features are difficult to resolve and hence we conclude that the NV-layer measurements should not be sensitive to electric field from the gate directly. The enhanced electric field measured in the main text, which correlates strongly with the gate-potential-dependent photoluminescence, therefore likely results from a change in the surface charge distribution at the diamond-oxide interface.

A.3 Chapter 5

A.3.1 Optical resolution of the cryogenic widefield NV microscope

As mentioned in section 5.2, despite the $\approx 0.4\,\mu m$ calculated optical diffraction limit of our cryogenic widefield NV-diamond microscope, in practice, the smallest resolvable features are only down to 0.7 μm in size. Figure A.7(a) shows such a feature in a map of the shift in ODMR resonance frequency due to stress features found in a bare region of the diamond imaged for this project. A Lorentzian fit of the smallest observable feature gives a 0.7 μm FWHM, figure A.7(b).

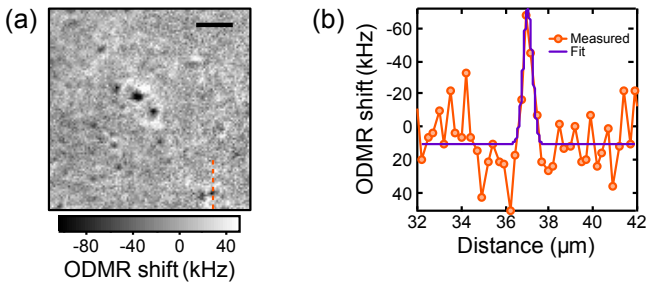

Figure A.7: Optical resolution of the cryogenic widefield NV-diamond microscope. (a) ODMR-frequency-shift map (i.e. frequency fit to a single NV-spin resonance with a mean value subtraction) of a stress feature on the bare diamond surface, away from the Nb film. The scale bar is 5 μm. (b) ODMR-shift profile across the small feature seen in (a) (orange), and Lorentzian fit (purple) showing a FWHM of 0.7 μm.

A.3.2 Nb calculation

In the main text, resistance measurements of the device were used primarily to determine whether the film was in the normal or superconducting states. Here we extend our analysis of the resistance versus temperature measurements to extract key parameters of the Nb film including the coherence length and magnetic penetration depth. From the difference in normal and superconducting state resistances, $R_{\mathrm{N}} - R_{\mathrm{SC}} \approx 15\,\Omega$, we estimate the resistivity of the Nb film, $\rho \approx 6 \times 10^{-7}\,\Omega\,\mathrm{m}$ where we took the dimensions of the Nb strip to be 200/40/0.2 (length/width/thickness in μm). Knowing the product of resistivity and mean free path for Nb, $\rho l = 3.75 \times 10^{-16}\,\Omega\,\mathrm{m}^2$ [256], we deduce the mean free path for our Nb film, $l \approx 0.6\,\mathrm{nm}$. For pure Nb, the coherence length is $\xi_0 = 38\,\mathrm{nm}$, hence our sample lies in the dirty limit, $l \ll \xi_0$. We can therefore use the dirty limit approximations to estimate the effective coherence length at zero temperature, $\xi(0) = 0.85\sqrt{\xi_0 l} \approx 4\,\mathrm{nm}$, and the magnetic penetration depth at zero temperature, $\lambda(0) = 0.62\lambda_L\sqrt{\xi_0/l} \approx 200\,\mathrm{nm}$ using the London penetration depth for pure Nb, $\lambda_L = 39\,\mathrm{nm}$. These quantities can be calculated at finite temperatures using $\xi(T) = \xi(0)/\sqrt{1 - T/T_c}$ and $\lambda(T) = \lambda(0)/\sqrt{1 - T/T_c}$. At the base temperature of our cryostat, $T_{\mathrm{base}} = 4.3\,\mathrm{K}$, this gives $\xi(T_{\mathrm{base}}) \approx 6\,\mathrm{nm}$ and $\lambda(T_{\mathrm{base}}) \approx 300\,\mathrm{nm}$, however, these parameters may be significantly larger when imaged due to local laser heating, to the point where the superconductivity is quenched as demonstrated in figure 5.5 of the main text.

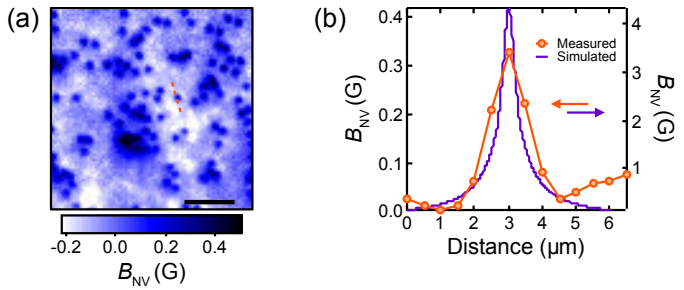

Figure A.8: Measured and simulated vortex field distribution. (a) B_{NV} image of vortices taken at $P_{\mathrm{laser}} = 0.5\,\mathrm{mW}$ with $B_0 = 1.5\,\mathrm{G}$. The isolated vortex compared with simulation is highlighted (orange dashed line). The scale bar is $10\,\mu\mathrm{m}$. (b) B_{NV} profiles across a single vortex as taken from (a) (orange, left axis), and simulated as described in the text (purple, right axis).

A.3.3 Vortex size

In the main text, ODMR-based imaging of vortices focused on their properties over our $100\,\mu\mathrm{m}$ field of view, such as their number density and behavior in non-uniform temperature environments. Here, we look at the structure of individual vortices and compare our observations with theory. Figure A.8(a) is a zoomed-in B_{NV} image that highlights features of individual vortices. Taking a line profile through a single isolated vortex, figure A.8(b), reveals the maximum B_{NV} for a single vortex is approximately $0.3\,\mathrm{G}$, with a FWHM of $1.4\,\mu\mathrm{m}$, comfortably above the resolution limit of our microscope. To compare this result with theory, we calculated the expected vortex field distribution following Carneiro, et al., Ref. [257]. We consider a straight vortex in a $200\,\mathrm{nm}$ thick film with an isotropic London response, with London penetration depth $\lambda = 400\,\mathrm{nm}$, and superconducting coherence length $\xi = 8\,\mathrm{nm}$, at temperature $T/T_c = 0.75$, as inferred from figures 5.2 and 5.5. The NV response is accounted for by considering this field at a distance $130\,\mathrm{nm}$ below the film, which corresponds to the mean NV depth, as discussed in section 2.2.4. The field as seen by the NV is taken as the average projection of this field along each NV axis, which we compare directly to the measured distribution in figure A.8(b). The simulated vortex field has a FWHM of $600\,\mathrm{nm}$, less than half the width measured, and a peak field strength of $4\,\mathrm{G}$, an order of magnitude above our measured value. This discrepancy in size is likely due to disorder within the film, which will alter the straightness of the vortex within the

film, and hence its apparent size. Local disorder would also explain the variation in vortex sizes seen across our field of view. The peak field discrepancy is partially explained by the observed broadening, but is likely dominated by our simplified fitting model, which neglects residual splitting of the NV spin-resonance lines, and hence reduces the apparent B_{NV} [18, 229].

A.3.4 Correlation of ODMR contrast and Rabi measurements

In figure 5.5, we saw local reductions in ODMR contrast correlated with regions where vortices were suppressed at larger imaging laser powers. These were attributed to a reduction in the local microwave field strength due to the differing microwave reflectivity of normal-state and superconducting Nb. However, as discussed at length in chapter 3, there are a number of effect that can reduce optical contrast of NV centres including laser intensity, large magnetic field gradients, and interaction between NV centres and nearby defects or materials [31, 170, 176]. To validate our interpretation, we made Rabi and ODMR measurements of the same region at base temperature with $P_{\mathrm{laser}} = 1.0\,\mathrm{mW}$. Here the Rabi measurement gives us direct insight into the local microwave field strength, as this dictates the Rabi cycling rate (see section 1.3.3), which we can then compare to the ODMR contrast data. Figure A.9(a) is an ODMR contrast map taken under these conditions in an area within the Nb bonding pad, showing several pockets of reduced contrast, similar to those seen in figure 5.5(f). Rabi curves from these pockets show slower Rabi oscillations as compared to neighbouring regions with greater ODMR contrast, figure A.9(b). Note that these measurements are done in a high-damping regime because of the low microwave power used to mimic the CW ODMR measurements, hence only the initial decay is observed. This slower Rabi evolution means that, for a given microwave field pulse duration, these regions give greater photoluminescence than those correlated with higher ODMR contrast, giving up to 0.2% more photoluminescence for an interaction time of 0.15 ms. Quantitative comparisons with ODMR contrast measurements are non-trivial given the pulsed nature of the Rabi measurement versus the CW ODMR measurement, however, this result demonstrates that locally reduced microwave fields at least partially explain the reduction in ODMR contrast. We note that the laser heating in each mea-

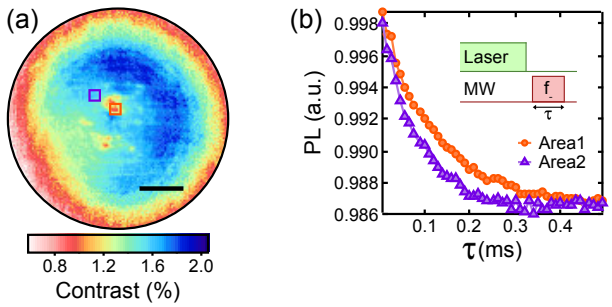

Figure A.9: Correlation of ODMR contrast and Rabi measurements. (a) ODMR contrast map of the lower frequency resonance line (f_-) taken within the Nb bonding pad at $P_{\text{laser}} = 1.0\,\text{mW}$. The scale bar is $20\,\mu\text{m}$. (b) Rabi curves integrated over two areas marked in (a), one that showed lower (orange) and the other higher ODMR contrast (purple). The Rabi evolution rate is greater for the area with higher ODMR contrast. The Rabi measurement is a pulsed sequence, using a long laser pulse for initilisation and readout of the NV spin state, and a resonant microwave pulse of varying duration, τ, (inset). $P_{\text{laser}} = 1.0\,\text{mW}$ and $P_{\text{MW}} = 2.0\,\text{mW}$ for both measurements.

surement should be comparable given that a 1 s initialising laser pulse was used prior to camera exposure (0.5 s), which has a minimum laser duty cycle 0.2 for the microwave pulse durations explored in the Rabi measurement.

A.3.5 Electrical charaterisation at large currents

In section 5.7, we demonstrated current-density mapping in the narrow channel of the Nb device. To achieve an Ørsted field suitably large for our ODMR-based imaging, we applied a DC current of $I = 20\,\text{mA}$, which is significantly larger than that used previously to characterise the superconducting transition with resistance measurements ($I = 10\,\mu\text{A}$). This large current will affect the transition due the interdependence of critical current densities and critical temperature, and additional Joule heating from the non-superconducting portion of the circuit within the cryostat. To characterise this effect, we recorded the device resistance as a function of the cryostat temperature, as in section 5.6, at increasing currents and laser powers, with the laser centred on the narrow Nb channel.

Without laser illumination, figure A.10(a), the threshold T_- is lowered to 7.4 K when $I = 20\,\text{mA}$, a 1 K drop from the $I = 10\,\mu\text{A}$ case, owing to a decrease in T_c which is dependent on current. The change in T_+ as the current increases is larger, giving a sharp transition at $I = 20\,\text{mA}$ mainly due to Joule heating at this large current: when

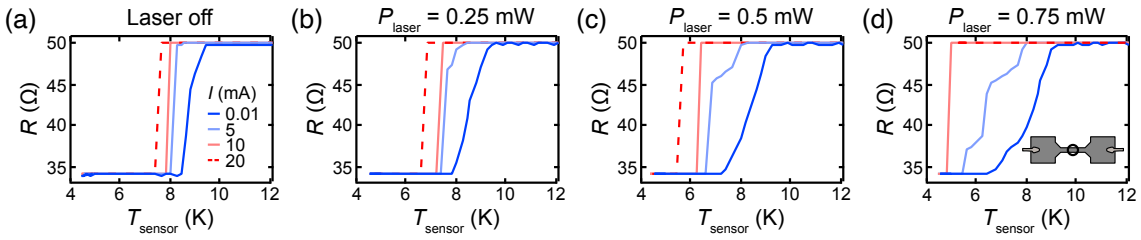

Figure A.10: Electrical characterisation at large currents. R versus T_{sensor} recorded with current values ranging from $I = 0.01\,\text{mA}$ to $20\,\text{mA}$, at laser powers: (a) $P_{\text{laser}} = 0\,\text{mW}$, (b) $0.25\,\text{mW}$, (c) $0.5\,\text{mW}$, and (d) $0.75\,\text{mW}$. The laser is centred on the narrow channel of the Nb device (inset).

a small section of the Nb wire turns normal with a resistance of, e.g., $R = 1\,\Omega$, there is a dissipated power $RI^2 = 0.4\,\text{mW}$ in this section which will raise the temperature of the neighbouring sections, eventually quenching the superconductivity of the entire device. At $P_{\text{laser}} = 0.25\,\text{mW}$ and $0.5\,\text{mW}$, figures A.10(b) and (c), with $I = 20\,\text{mA}$ T_- becomes $6.6\,\text{K}$ and $5.4\,\text{K}$ respectively, indicating local temperature increases caused by the laser of $0.8\,\text{K}$ and $2.0\,\text{K}$. Thus, at the base temperature (i.e. in the absence of active heating from the resistive heater, as during our ODMR measurements), the reduced temperatures ($t = T/T_c$) in this region under these laser and current conditions are $t = 0.70$ and $t = 0.86$ for $P_{\text{laser}} = 0.25\,\text{mW}$ and $0.5\,\text{mW}$ respectively, assuming $T_c = 7.4\text{K}$ at $I = 20\,\text{mA}$. At $P_{\text{laser}} = 0.75\,\text{mW}$, figure A.10(d), the device is no longer superconducting at the base temperature with $I = 20\,\text{mA}$, an observation that is commensurate with our current-density imaging at $P_{\text{laser}} = 1.0\,\text{mW}$.

A.3.6 Vector ODMR analysis for current reconstruction

Our approach to reconstructing current densities from ODMR measurements was detailed in the previous chapter, in section 4.4. The same technique was used for the current density mapping through the narrow Nb channel presented in figure 5.9, however, the analysis in this case is more complicated. In the following two sections, we present the complete analysis of the vector ODMR measurement and subsequent current reconstruction, where the precise method of reconstruction has significant consequences for the final image. We show this analysis for the case where $I = 20\,\text{mA}$ and $P_{\text{laser}} = 0.5\,\text{mW}$ presented in figure 5.9. A photoluminescence image of this region is shown in figure A.11(a), where the edges

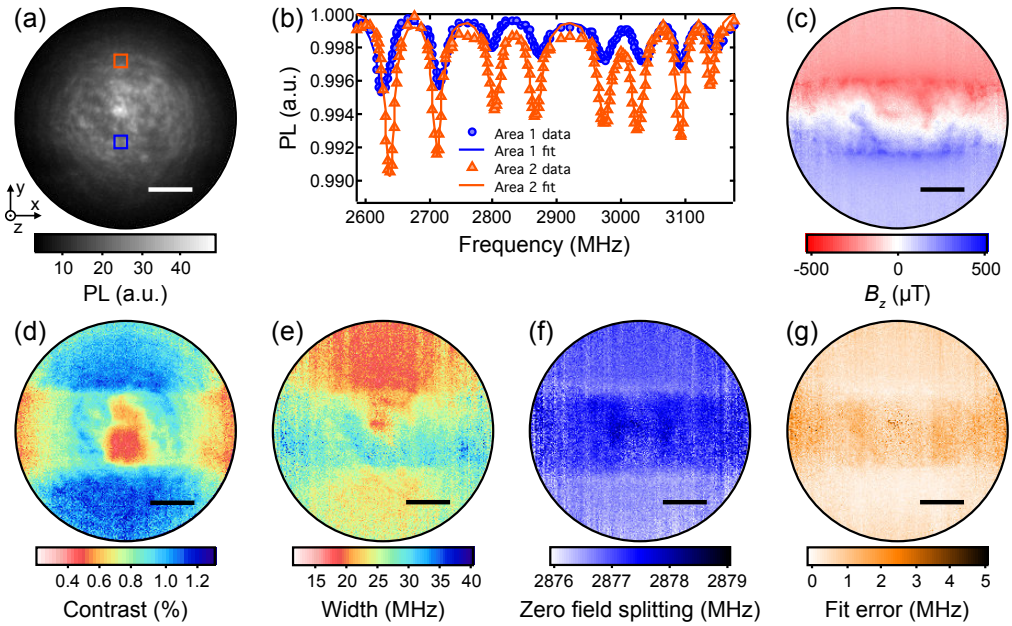

Figure A.11: Vector ODMR analysis for current density imaging. (a) Photoluminescence image of the same Nb channel region measured in figure 5.9. The image is taken under CW illumination at $P_{\text{laser}} = 0.5\,\text{mW}$. (b) ODMR spectra from two areas, one beside the Nb channel (orange), and one under the channel close to the edge (blue), highlighted in (a). (c) B_z map calculated from the analysis described in the text. (d) and (e) show the contrast and width (FWHM), respectively, for the lowest frequency transition of the ODMR spectrum. The equivalent maps for the other seven resonance lines are qualitatively similar. (f) Map of the zero-field splitting parameter, D. (g) Residual error of the fit, ε. The scale bars are $20\,\mu\text{m}$.

of the channel are faintly visible. To begin, we make our vector ODMR measurement under a suitable bias field such that all eight resonance frequencies can be resolved. In this case we apply a magnetic field $\mathbf{B}_{\text{app.}} = (47.5, 97.4, 19.1)\,\text{G}$ expressed in lab frame coordinates, where the xyz axes are defined in figure A.11(a). In this frame the NV axes have unit vectors $\mathbf{u}_{\text{NV}} = (\pm 1, \pm 1, 1)/\sqrt{3}$. Example ODMR spectra recorded under this field are shown in figure A.11(b), highlight significant variation between spectra beneath and adjacent to the Nb channel.

To analyse the ODMR data, we first fit the spectrum at each pixel with a sum-of-eight-Lorentzian function with free frequencies, amplitudes and widths as detailed in section 2.4. These fits to the data are shown in figure A.11(b). The eight resulting resonance frequencies, $\{f_i\}_{i=1\ldots8}$, are then used to find the total magnetic field, $\mathbf{B}_{\text{tot}}$, by

minimising the root-mean-square difference between the fit frequencies and those calculated from a Hamiltonian model, $\varepsilon(D, \mathbf{B}_{\text{tot}})$ defined by equation 2.4. Specifically, in this application we use a simplified Hamiltonian model,

$$\mathcal{H}/h \quad = DS_Z^2 + \gamma_{\text{NV}} \mathbf{S} \cdot \mathbf{B}_{\text{tot}} \ , \tag{A.1}$$

considering only the Zeeman and zero-field-splitting terms. Here $\mathbf{S} = (S_X, S_Y, S_Y)$ are the spin-1 operators, D is the temperature-dependent zero-field splitting, $\gamma_{\text{NV}} = 28.035(3)\,\text{GHz/T}$ is the isotropic NV gyromagnetic ratio, and XYZ is the reference frame specific to each NV orientation, Z being the symmetry axis of the defect [15, 33] with unit vector $\mathbf{u}_{\text{NV}}$ defined previously. The resulting total magnetic field, $\mathbf{B}_{\text{tot}}$, contains both the applied bias field and the field from the Nb film due to its magnetic response as well as the transport current (Ørsted field). Since the applied field is uniform over the field of view, we simply subtract a constant offset to $\mathbf{B}_{\text{tot}}$, taken to be the field measured far from the Nb wire, to obtain the Nb-induced field. Illustrative results of this analysis are shown in figure A.11, including: (c) the background-subtracted B_z map; (d) the contrast and (e) width of a single ODMR resonance, (f) the D parameter, and (g) the residual error function from the Hamiltonian fit, ε. The fit residue seems to correlate with the contrast, with $\varepsilon < 1\,\text{MHz}$ beside the Nb wire but reaching 2 MHz under the Nb where the ODMR contrast is lower. This suggests that ε is dominated by noise in the data and that the model Eq. (A.1) is adequate. In comparison, the shifts induced by the Ørsted field are much larger, up to 10 MHz. The zero-field splitting parameter $D \approx 2877\,\text{MHz}$ is roughly as expected at this temperature [258], with a step of $\sim 0.5\,\text{MHz}$ under the Nb wire attributed to strain [229].

To separate the Ørsted field from the magnetic response of the Nb film, we performed ODMR measurements both before and after applying the transport current. Here we compare B_z and ODMR contrast maps from those measurements alongside the current-on measurement for comparison. Figure A.12(a) shows B_z imaged immediately after cooling the sample below T_c under the same bias field used during acquisition, $\mathbf{B}_{\text{app}} = (47.5, 97.4, 19.1)\,\text{G}$. The field exhibits a small expulsion from the Nb channel as apparent from a reduction of B_z by $\approx 0.4\,\text{G}$ under the Nb. The expected density of vortices due the applied B_z is about 1 vortex/μm^2 [259], hence the weak expulsion is in broad

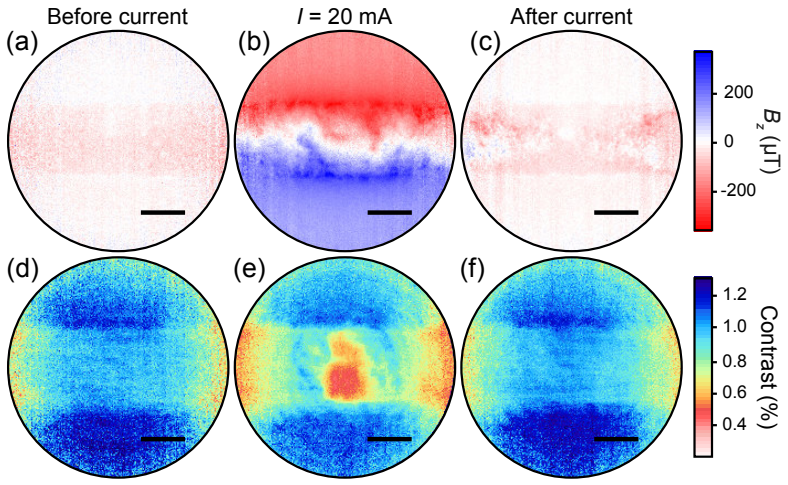

Figure A.12: Magnetic response of the Nb wire. Maps of the background-subtracted B_z magnetic field component (top row) and ODMR contrast (bottom row) measured with $P_{\text{laser}} = 0.5\,\text{mW}$ and $\mathbf{B}_{\text{app.}} = (47.5, 97.4, 19.1)\,\text{G}$. (a) was taken without current just after cooling down, (b) corresponds to the case $I = 20\,\text{mA}$ shown before, (c) was taken just after turning off the current. The scale bars are $20\,\mu\text{m}$.

agreement with the London penetration depth estimated from the device resistance ($\lambda \approx 400\,\text{nm}$). Upon turning the current on, figure A.12(b), the field is dominated by the Ørsted contribution, reaching $B_z \pm 5\,\text{G}$. Turning off the current, the small field expulsion is recovered but additional features appear, figure A.12(c), indicating a rearrangement of vortices due to the current. Given that this field is much smaller than the targeted Ørsted field and that the response may be different while the current is on, we simply ignore it when reconstructing the current density. That is, the reconstructed current density will also include a small contribution from the supercurrent associated with the response to the applied field. This supercurrent is localised near the edges of the wire and has opposite signs for each edge, so that the net current integrated across the width of the wire will be only due to the transport current. The ODMR contrast maps from these same three measurements show a slight but uniform reduction in contrast under the Nb wire in the absence of current as compared to the bare diamond, figure A.12(d) and (f), and a significant reduction at the centre of the image when the current is on, figure A.12(e). Building on our observation of vortex heating in figure 5.5, we tentatively ascribe this drop in contrast to a portion of the Nb wire turning normal, but not extending through the

entire thickness of the film since the resistance remains $R = R_{\mathrm{SC}}$. Although our vortex imaging showed no significant change in local contrast at $P_{\mathrm{laser}} = 0.5\,\mathrm{mW}$, the relatively large current density lowers T_c sufficiently to allow heating at this laser power to locally quench superconductivity, as shown in section A.3.5.

A.3.7 Current reconstruction method analysis

The vector ODMR analysis outlined in the previous section demonstrated that we can reliably extract the Ørsted field. As discussed in the previous chapter, section 4.4, there are several nominally equivalent methods by which the current density can be reconstructed from the Ørsted field. In the previous chapter, all current density images were produced from the B_z field, owing to a slight artefact being present in the reconstruction from the planar field. Here we see such an artefact emerge again, but in a more significant manner, and so we present the analysis in detail. Note that the current density imaged here is the current density projected into a two-dimensional plane, i.e. $\widetilde{\mathbf{J}} = \int \mathbf{J}\, dz$, as our measurement cannot resolve the current distribution in the z direction. This case is distinct from the case for graphene in the previous chapter, which is an intrinsically two-dimensional distribution. In all of the images and terms presented, we drop the projected notation for simplicity, e.g. $\widetilde{J}_i \rightarrow J_i$.

Figure A.13 shows the three Ørsted field components for each of the three conditions imaged in figure 5.9 of the main text, which form the basis of our current reconstruction. In principle, the three magnetic field components, (B_x, B_y, B_z), are related to each other via Ampère's law, $\nabla \times \mathbf{B} = 0$ [260], and there are several ways to use them to reconstruct the current density. Here, we consider two methods that both rely on the Biot-Savart law (equation 4.1) and continuity of current ($\nabla \cdot \mathbf{J} = 0$) as discussed in section 4.4. The first reconstructs current from the in-plane field components, B_x and B_y, using the real-space relations,

$$J_x = -\frac{2}{\mu_0} B_y \tag{A.2}$$

$$J_y = \frac{2}{\mu_0} B_x\,, \tag{A.3}$$

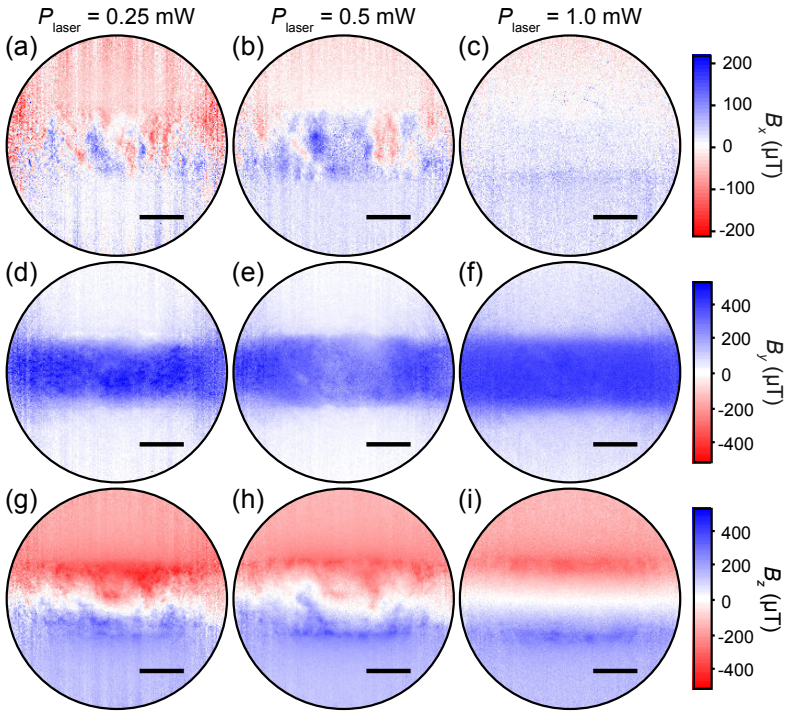

Figure A.13: Vector magnetic field. Background-subtracted vector magnetic field components B_x (a,b,c), B_y (d,e,f), and B_z (g,h,i) for the three cases studied in figure 5.9 of the main text: $P_{\text{laser}} = 0.25\,\text{mW}$ (left column), $P_{\text{laser}} = 0.5\,\text{mW}$ (middle column), $P_{\text{laser}} = 1.0\,\text{mW}$ (right column). The scale bars are $20\,\mu$m.

where we have utilised the fact that the Nb-NV distance (between 0 - 400 nm) is small compared to the lateral spatial resolution of the measurements ($\approx 1\,\mu$m given by the optical resolution) [16, 60]. This method will be referred to below as "planar reconstruction". Alternatively, we can use the B_z component to obtain relations in the Fourier plane,

$$j_x = -\frac{2}{\mu_0}\frac{ik_y}{k}b_z \tag{A.4}$$

$$j_y = \frac{2}{\mu_0}\frac{ik_x}{k}b_z\,. \tag{A.5}$$

Here $f(k_x, k_y)$ denotes the two-dimensional Fourier transform of $F(x, y)$, where $\mathbf{k} = (k_x, k_y)$ is the spatial frequency vector and $k = \sqrt{k_x^2 + k_y^2}$. This method is identical to that used for the current density imaging of graphene in the previous chapter, and recovers the real-space current densities via an inverse Fourier transform as described in section 4.4. We refer to this method below as the "out-of-plane reconstruction".

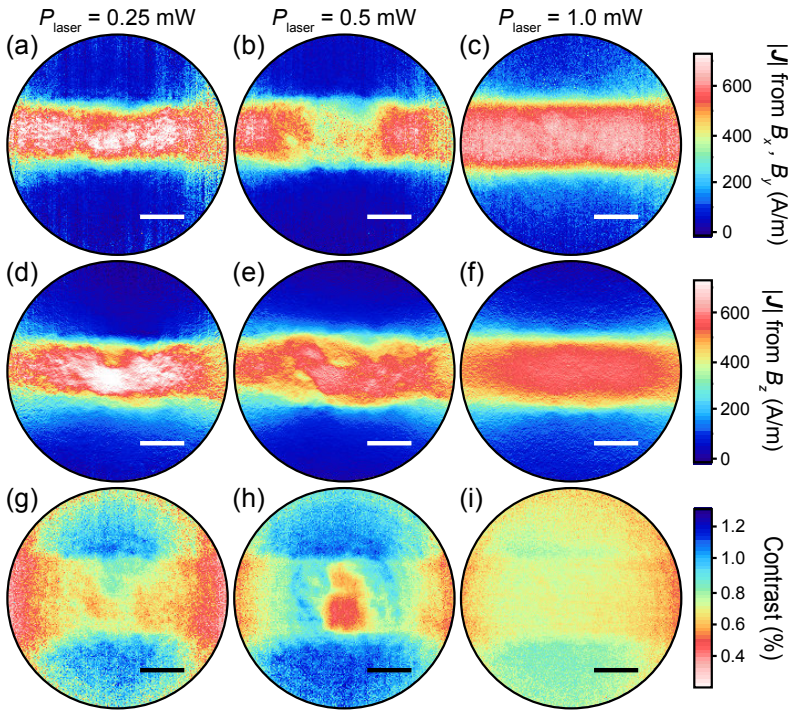

Figure A.14: Reconstructed current density. Norm of the projected current density, $|J|$, reconstructed from equations A.2 and A.3 (a,b,c), and from equations A.4 and A.5 (d,e,f), with their corresponding ODMR contrast maps (g,h,i), for the three cases studied in figure 5.9 of the main text: $P_{\text{laser}} = 0.25\,\text{mW}$ (left column), $P_{\text{laser}} = 0.5\,\text{mW}$ (middle column), and $P_{\text{laser}} = 1.0\,\text{mW}$ (right column). All scale bars are $20\,\mu\text{m}$.

Figure A.14 shows the current densities reconstructed by both the planar and out-of-plane methods for the three P_{laser} conditions studied in figure 5.9. There are several key differences between the two methods. Considering the case where the Nb wire is in the normal state ($P_{\text{laser}} = 1.0\,\text{mW}$, right column in figure A.14), we see that the planar reconstruction method gives a $|\mathbf{J}|$ map that looks sharper and more uniform along the length of the Nb wire as compared to the out-of-plane method, for which the current tapers near the left and right boundaries of the image. This discrepancy is due to the latter method being prone to truncation artefacts when calculating the Fourier transform of B_z, as discussed in section 4.4, which are more pronounced near the boundaries where the B_z data has more noise. In contrast, the planar method bypasses the need for a Fourier transform and so avoids truncation artefacts. The noise in $|\mathbf{J}|$ reconstructed by this method therefore directly mirrors the noise in the B_x and B_y data. While this observation would

normally motivate the use of planar reconstruction method, imaging at $P_{\text{laser}} = 0.5\,\text{mW}$ (middle column of figure A.14) reveals another effect. Here, the planar reconstruction shows a "missing" current near the centre of the image [60]. Integrating the x component of the projected current density across the width of the wire, i.e. $I_{\text{int.}} = \int J_x\,dy$, we approximately recover the electrically measured current of $I = 20\,\text{mA}$ near the boundaries of the image, but the value of $I_{\text{int.}}$ drops to 14 mA (a 30% drop) near the centre. This missing current originates from a drop in B_y measured under these conditions, figure A.13(e), and is somewhat correlated with a drop in ODMR contrast, figure A.14(h), taken previously to indicate local quenching of superconductivity. At $P_{\text{laser}} = 0.25\,\text{mW}$ (left column of figure A.14), the missing current is recovered and the contrast is mostly uniform along the Nb wire. Previous work from our group identified similar missing currents in metals at room temperature, suggesting an apparent delocalisation of current towards the diamond substrate, which decreases $|\mathbf{J}|$ in the in-plane reconstruction method but not the out-of-plane method [60]. A possible explanation for this effect may involve a magnetic response in the diamond itself which can be significant for nitrogen-doped diamond at low temperatures [261], however this requires further investigation. See reference [60] for a more complete discussion. For this reason, we chose to use the out-of-plane reconstruction method in the main text, assuming the resulting $|\mathbf{J}|$ is a good indicator for the transport in the Nb channel. With this method, the integrated current $I_{\text{int.}}$ remains within 10% of the electrically measured value (20 mA) at any point along the wire for all three laser conditions studied.

All current-density imaging presented so far has been of a single location along the narrow Nb channel. In the main text, we asserted that the non-uniform current distribution seen when the Nb conduction path is fully superconducting is due to the temperature profile seeded by our illumination laser. Another possibility is that this non-uniformity is due to local defects across the Nb wire. To investigate this we image the current density in three regions along the narrow Nb channel, under the same laser and current conditions, $I = 20\,\text{mA}$ and $P_{\text{laser}} = 0.5\,\text{mW}$. Figure A.15 shows current density images (reconstructed from the out-of-plane field, B_z) and ODMR contrast maps for two additional locations, (a,d) and (c,f), either side of the region studied initially, (b,e). The current pattern is broadly similar in all cases, supporting the interpretation that it is

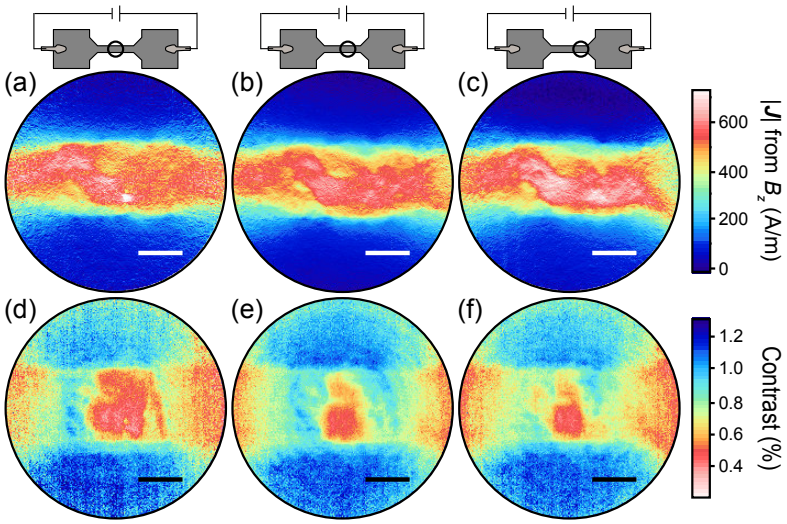

Figure A.15: Current density at different locations along the Nb channel. (a,b,c) Maps of the current density, $|\mathbf{J}|$, and (d,e,f) corresponding ODMR contrasts for three different locations along the Nb strip, indicated on the diagrams (above). The same current, $I = 20\,\text{mA}$, and laser power, $P_{\text{laser}} = 0.5\,\text{mW}$, were used for each image. The scale bar is $20\,\mu\text{m}$.

mostly dictated by temperature profile imprinted by the laser. Moving the sample relative to the laser does not change the temperature profile in the field of view and therefore, the current density pattern is essentially unchanged. The small differences between the current images are somewhat correlated with features seen in the ODMR contrast maps.